The urgent need for a sustainable energetic system to mitigate global warming has increased interest in solar energy as a promising solution. Currently, photoconversion technologies generate only a small fraction of the total energy consumption. There are promising emerging technologies, including perovskite solar cells and photoelectrochemical systems, for hydrogen generation. However, these technologies face stability and performance challenges. The investigation of these technologies using modulated techniques: impedance spectroscopy, intensity-modulated photocurrent and photovoltage spectroscopies, can contribute to identifying their limitations. In this thesis, we have correlated the "negative capacitance" in impedance spectroscopy and the "inverted hysteresis" in current-voltage curves, attributing them in solar cells to an ionic deleterious process. Furthermore, we have developed a methodology to analyse the three modulated techniques in combination, allowing for a deeper analysis. These results allow a better understanding of the performance of photoconversion devices, identifying their limitations, and thereby contributing to their improvement.

Modulated Techniques
to Analyse Photoconversion Devices

Agustin **Alvarez Ojeda**

AGUSTIN ALVAREZ OJEDA 2023

DOCTORAL THESIS

DOCTORAL THESIS

Modulated Techniques to Analyse Photoconversion Devices

AUTHOR
Agustin **Alvarez Ojeda**

SUPERVISORS
Prof. Francisco **Fabregat-Santiago**
Dr. Elena **Mas Marzá**

UNIVERSITAT JAUME I

inam Institute of Advanced Materials and Centers

MARIE CURIE ACTIONS

MAESTRO Making perovskites truly exploitable

Doctoral Thesis

Modulated Techniques to Analyse Photoconversion Devices

Author:

AGUSTIN ALVAREZ - NIF: Y6611214Q

Digitally signed by AGUSTIN ALVAREZ - NIF:Y6611214Q
DN: CN=AGUSTIN ALVAREZ - NIF: Y6611214Q, SERIALNUMBER=Y6611214Q, G=AGUSTIN, SN=ALVAREZ, OU=CIUDADANOS, O=ACCV, C=ES
Reason: I am the author of this document
Location: your signing location here
Date: 2023-07-03 12:03:38
Foxit Reader Version: 9.7.1

Agustin Alvarez Ojeda

Supervisors:

FRANCISCO| FABREGAT|SANTIAGO

Firmado digitalmente por FRANCISCO|FABREGAT|SANTIAGO
Nombre de reconocimiento (DN): cn=FRANCISCO|FABREGAT|SANTIAGO, serialNumber=18972796G, givenName=FRANCISCO, sn=FABREGAT SANTIAGO, ou=CIUDADANOS, o=ACCV, c=ES
Fecha: 2023.07.03 12:23:53 +02'00'

Prof. Francisco Fabregat-Santiago

ELENA| MAS| MARZA

Firmado digitalmente por ELENA|MAS|MARZA
Nombre de reconocimiento (DN): cn=ELENA|MAS|MARZA, serialNumber=20460029B, givenName=ELENA, sn=MAS MARZA, ou=CIUDADANOS, o=ACCV, c=ES
Fecha: 2023.07.03 12:18:09 +02'00'

Dr Elena Mas Marzá

UNIVERSITAT JAUME·I

Report submitted in order to be eligible for a doctoral degree awarded by the Universitat Jaume I, Doctoral School

Doctoral Programme in Sciences

Castelló de la Plana, June 2023

A mis padres, Marta y Daniel

Funding

The source responsible for founding the research carried out in this thesis was:

- Project: MAESTRO: Making Perovskite Truly Exploitable. Funded by the European Union's Horizon 2020 MSCA (Marie Skłodowska-Curie Actions) Innovative Training Network under grant agreement no. 76478

Acknowledgements

First, I would like to thank my thesis supervisor, Prof. Francisco Fabregat-Santiago, for trusting me and allowing me to do this PhD. It has been a privilege to receive all the dedication he has given me, with a noble predisposition to share all his extensive experience and profound knowledge. I am grateful for all the opportunities he has given me, far more than I could ever have imagined. I have grown enormously over these years, professionally and personally, and it all started with his vote of confidence. I am also grateful that he has provided me with the freedom to explore the problems addressed during the thesis scientifically and that he has listened to my ideas and suggestions. His help and support have been indispensable for the completion of this thesis.

I am also deeply grateful to my co-supervisor, Dr Elena Mas Marzá, whose support and drive have been essential for the accomplishment of this thesis. I especially appreciate all her effort, dedication and patience over these years, which shone even brighter in the most challenging moments. It was a fortune to have the opportunity to learn from her extraordinary capabilities of organisation, planning, perseverance and determination.

I would like to express my sincere gratitude to Prof. Germà Garcia-Belmonte for his confidence and support at the end of this doctoral thesis. Furthermore, I would like to thank him for giving me the chance to learn from his extraordinary knowledge and outstanding expertise in scientific research.

It has been an honour to be part of the Institute of Advanced Materials (INAM). In this institute, I had the opportunity to meet and learn from the best scientists worldwide in the research topic of this thesis. I particularly want to thank the principal investigators Prof. Sixto Giménez, Prof. Iván Mora-Seró, Prof Juan Bisquert, Dr Victor Sans Sangorrin and Dr Antonio Guerrero for invaluable discussions and advice throughout this thesis. And last but not least, I would like to thank Loles Merchan Mundina for all the administrative help she has given me.

I have been privileged to have been part of the Marie Curie MAESTRO project. I am very grateful to Prof. Alison Walker of Bath University, coordinator of the project, for her dedication and effort in making sure that all the members of this project grow professionally as much as possible, while at the same time taking care of each one of us personally.

I would like to thank Prof. Thomas Kirchartz for allowing me to join, for several months, his research group IEK5-Photovoltaics at the Forschungszentrum Jülich. During this secondment, I have learned and grown a lot both professionally and personally. I appreciate very much his valuable advice and constructive scientific opinions, which have given me a new perspective on my research.

During this stay, I was fortunate to work continuously with Dr Sandheep Ravishankar, a brilliant young scientist and a great friend. I am very grateful to him for his guidance during this stay and also during my first steps into the modulated techniques. Extensive discussions and his generosity in sharing his knowledge with me have been foundational in this thesis.

I want to especially highlight the importance that Dr Clara Aranda has played in this thesis. From a professional point of view, it is a privilege to work with her, and I dare to say that she is one of the most brilliant scientists I have met. In particular, I am eternally grateful for all the effort and dedication she put into the paper that became the first publication of this thesis. On a personal level, I want to thank her for all the care and support she daily gives to me. All the happy moments we have shared have made all the suffering moments insignificant.

I want to thank my all friends, who make my life happier, as they did in particular during this thesis. To Ramón, Marise and Jesus with whom I have had the privilege of sharing the doctorate path, inside and outside the institute, through whom I could also meet two unconditional friends, Fabi and Yaiza. To Miguel, Osbel, Cam, Carlos and Rafa, magnificent young scientists, who in addition to sharing their friendship have taught and encouraged me whenever I have needed it. To the MAESTRO team, Vivek, Thijs, Nadja, Luigi, Christina, Rene, Sijo, Emily, Phillippe, Naga, Rahul, Lefteris and Sathy, with whom we have grown together as scientists and have made each trip an unforgettable experience, full of knowledge, laughter and fun.

And also to the friends who have been with me since before I started this adventure, and despite the distance are still by my side. To whom I shared my first steps in the scientific world, to Aru, Belu, Li, Andres, Francesco, Dieguito, Santi Maldonado, Lupe, Javi, Sole, Sofi, Eli, Fran Garcia, Fran Ompre, Nati, Andy, Chula, Santi Rosa, Ale and Barbi, who also helped me with the design of the cover of this thesis. To Franco, Julian, Pablo Estofan, Pablo Weber, Toni, Octa, Emilio, Manu and Manu El, with whom, besides enjoying life, I have been able to learn from their curiosity in different areas of knowledge. To Jair, Taty, Ezio, Victor, Durin and Lara, with whom I have been able to grow as a person, for many years now, and who show me how with effort and passion unthinkable goals can be achieved.

To Pocholo, whom I will always carry in my heart, and to Damita and Pampi, who have been patiently by my side, literally, during my endless hours of work, always ready to receive and give a caress.

Finally, I want to thank my family for all their unconditional support and continuous care, knowing that they will always be there gives me all the strength I need to face any challenge. I would like to thank my siblings, Javier, Belén and Pilar, for their constant example in facing life, which fills me with pride and motivation. And to my parents, Marta and Daniel, for having given me, with so much sacrifice, the best opportunities. This thesis is dedicated to both of them, who teach me, with them as examples, that things have to be done with a lot of love and a lot of effort, both as a person and as a scientist.

Abstract - Resumen

Abstract

The greatest threat facing humanity today is global warming, with the generation of energy from fossil fuels being the main cause. Therefore, is urgent the transition to an energetic system based on sustainable energy sources, among which solar energy is the one with the capacity to broadly cover the energy demands. The challenge then is to harness this solar energy to meet energy demand. There have been remarkable advances in photoconversion systems in the last decades, including the massive installation of silicon solar panels around the world. However, the established photoconversion systems only generate a small percentage of the total energy consumed. Fortunately, there are emerging technologies such as perovskite solar cells, which in a few years of development have outperformed in several aspects the other photovoltaic technologies. In addition to the conversion of solar energy into electricity, another challenge is the intermittency of this energy, due to day and night cycles, cloud cover, among others. The generation of hydrogen from photoelectrochemical cells appears as a possible solution to this problem. However, these emerging photoconversion devices have limitations that prevent their mass commercialisation, such as their stability or performance.

The objective of this thesis is to contribute to the understanding of the internal mechanisms involved in the operation of photoconversion devices, and thus to identify their main limitations. By doing so, we aim to contribute to the development and improvement of renewable technologies, mitigating the impact of global warming. To achieve this goal, we have focused on modulated techniques, also known as small perturbation techniques, as they have demonstrated a great capability to identify and study these internal mechanisms.

The most traditional technique used in the characterisation of electronic devices is the current versus voltage curve, from which fundamental performance characteristics such as power conversion efficiency, short-circuit current or open-circuit voltage are usually extracted. Hysteresis is the difference in measured current between the voltage sweeps from short-circuit to open-circuit (Forward scan) and the inverse (Reverse scan). The identification of the hysteresis is therefore essential, otherwise, the performance is often misinterpreted. There are devices, such as those based on silicon, which usually have negligible hysteresis. However, other devices such as perovskite solar cells, have shown remarkable hysteresis effects, which can be classified as: “normal hysteresis” and “inverted hysteresis”, given by a better performance in the Reverse and Forward scan, respectively. Through impedance spectroscopy (IS), the most popular modulated technique, the “normal hysteresis” has been related to the presence of a giant capacitance at low frequencies, which has been attributed to the accumulation of ions/vacancies at the interface between the perovskite and the contacts.

In this thesis, we have been able to correlate, for the first time, the “inverted hysteresis” with the presence of a negative capacitance at low frequencies in the impedance spectra. We also confirmed that this relationship is universal, demonstrating it experimentally for different compositions of perovskite solar cells exposed to different conditions. Furthermore, we have pointed out that these effects are generated by an additional recombination pathway, which consequently reduces the performance of the devices. For the investigated devices, we were able to identify this recombination with the interaction of perovskite ions/vacancies with the contacts interfaces. In fact, we observed that these effects disappeared in optimised devices. In line with our objectives, we hope that this result will be useful for the easy identification of a limiting process when observing the presence of inverted hysteresis, in any photoconversion device. For these cases, we suggest an interfacial optimisation for performance improvement and encourage the study of this process in detail with IS.

These results are a clear example of the great power of IS for the in-operando analysis of devices. However, the use of this technique also has some limitations. To overcome the limitations of IS and gain a better understanding of the performance of photoconversion devices, most of the effort during this thesis has been devoted to developing a methodology to combine IS with two other well-known but less explored modulated techniques: intensity-modulated photocurrent spectroscopy (IMPS) and intensity-modulated photovoltage spectroscopy (IMVS). To do this, we first developed a protocol for obtaining reliable IMPS and IMVS spectra, which involves measuring the modulation of the light used to measure these techniques.

The analysis of IMPS and IMVS spectra is usually limited to the analysis of their characteristic times. On the other hand, the most common way to analyse IS spectra is using an equivalent circuit (EC) model, however, its choice is one of the main problems of this technique, since a given impedance spectrum can be generated by different ECs, resulting in different interpretations of the device’s performance.

One of the main results of this thesis is the development of a procedure to analyse in combination the IS, IMPS and IMVS responses. To achieve this, we have incorporated the effect of the absorbance and the separation efficiency on the IMPS and IMVS transfer functions. We have developed this procedure as general as possible, intending to make it available for its application to any photoconversion device. As a proof of concept, we successfully demonstrate the application of this procedure on a silicon photodiode. We have demonstrated that this procedure allows a more appropriate selection of the EC, solving, at least in part, the main limitation of IS. In addition, we have shown, for the first time, the analysis of the IS, IMPS and IMVS spectra with the same EC. With this analysis, we have demonstrated that the combination of IS, IMPS, and IMVS enables higher accuracy in the obtained parameters, as well as providing additional parameters that cannot be accessed through the separate analysis of these techniques.

Then, we have adapted this procedure to devices where the generation of carriers is distributed along the absorber material and the extraction of these photogenerated charges is limited by diffusion and recombination. For this purpose, we have presented an EC

obtained from the fundamental equations describing these processes. We have shown experimentally that this circuit adjusts appropriately and simultaneously the IS, IMPS and IMVS responses of an electrochemical hydrogen generation cell with a Zr:$BiVO_4$ photoanode. As a result, we have been able to identify how the electron and the hole diffusions limit the charge extraction when the device is illuminated from the hole and the electron collector contacts, respectively. Together with this result, we have also demonstrated that the main performance limitation of this device is the charge separation efficiency of Zr:$BiVO_4$.

These results are a validation of the power of combining IS, IMPS and IMVS, exposing the main limitations of the device, and thus indicating the target for improving its performance. Therefore, in line with our objectives, we are convinced that this combination will be of great help in the development of photoconversion devices.

Resumen

La mayor amenaza que enfrenta la humanidad hoy en día es el calentamiento global, siendo la generación de energía a partir de combustibles fósiles la principal causa. Por lo tanto, es urgente la transición a un sistema energético basado en fuentes de energía sostenibles, entre las cuales la energía solar es la que tiene la capacidad de cubrir ampliamente las demandas energéticas. El desafío, entonces, es aprovechar esta energía solar para satisfacer la demanda energética. En las últimas decadas, se han realizado avances notables en la fotoconversión, incluida la instalación masiva de paneles solares de silicio en todo el mundo. Sin embargo, los sistemas de fotoconversión actuales solo generan un pequeño porcentaje de la energía total consumida. Afortunadamente, existen tecnologías emergentes prometedoras como las células solares de perovskita, que en pocos años de desarrollo han superado en varios aspectos a otras tecnologías fotovoltaicas. Además de la conversión de la energía solar en electricidad, otro desafío es la intermitencia de esta energía, debido a los ciclos de dia y noche, la nubosidad, entre otros. La generación de hidrógeno a partir de células fotoelectroquímicas parece ser una posible solución a este problema. Sin embargo, estos dispositivos emergentes de fotoconversión tienen limitaciones que impiden su comercialización masiva, como su estabilidad o rendimiento.

El objetivo de esta tesis es contribuir a la comprensión de los mecanismos internos involucrados en la operación de dispositivos de fotoconversión, y así identificar sus principales limitaciones. Con ello pretendemos contribuir al desarrollo y mejora de las tecnologías renovables, mitigando el impacto del calentamiento global. Para lograr este objetivo, nos hemos centrado en técnicas moduladas, también conocidas como técnicas de pequeñas perturbaciones, ya que han demostrado una gran capacidad para identificar y estudiar estos mecanismos internos.

La técnica más utilizada tradicionalmente en la caracterización de dispositivos electrónicos es la curva de corriente en función del voltaje, de la cual se suelen extraer características fundamentales de rendimiento, como la eficiencia de conversión de energía, la corriente de cortocircuito o el voltaje de circuito abierto. La histéresis es la diferencia de corriente medida entre los barridos de voltaje de cortocircuito a circuito abierto (escaneo directo) y el inverso (escaneo inverso). La identificación de la histéresis es, por lo tanto, esencial, de lo contrario, el rendimiento a menudo se interpreta incorrectamente. Hay dispositivos, como aquellos basados en silicio, que suelen tener una histéresis despreciable. Sin embargo, otros dispositivos como las células solares de perovskita, han mostrado efectos de histéresis notable, que pueden clasificarse como: “histéresis normal” e “histéresis invertida”, dadas por un mejor rendimiento en el escaneo inverso y directo, respectivamente. A través de la espectroscopía de impedancia (IS), la técnica modulada más popular, se ha relacionado la “histéresis normal” con la presencia de una capacitancia gigante a bajas frecuencias, que se ha atribuido a la acumulación de iones/vacantes en la interfaz entre la perovskita y los contactos.

En esta tesis, hemos sido capaces de correlacionar, por primera vez, la “histéresis invertida” con la presencia de una capacitancia negativa a bajas frecuencias en los espectros de impedancia. También hemos confirmado que esta relación es universal, demostrándola experimentalmente para diferentes composiciones de células solares de perovskita expuestas a diferentes condiciones. Además, hemos señalado que estos efectos son generados por una vía adicional de recombinación, que consecuentemente reduce el rendimiento de los dispositivos. En el caso de los dispositivos investigados, hemos podido identificar esta recombinación con la interacción de los iones/vacantes de perovskita con las interfaces con los contactos. De hecho, hemos observamos que estos efectos desaparecieron en los dispositivos optimizados. En línea con nuestros objetivos, esperamos que este resultado sea útil para la fácil identificación de un proceso limitante al observar la presencia de histéresis invertida en cualquier dispositivo de fotoconversión. Para estos casos, sugerimos una optimización interfacial para la mejora del rendimiento y recomendamos el estudio detallado de este proceso con IS.

Estos resultados son un claro ejemplo del gran poder de la IS para el análisis in-operando de dispositivos. Sin embargo, el uso de esta técnica también tiene algunas limitaciones. Para superar las limitaciones de la IS y conocer mejor el funcionamiento de los dispositivos de fotoconversión, la mayor parte del esfuerzo durante esta tesis se ha dedicado a desarrollar una metodología para combinar la IS con otras dos técnicas moduladas muy conocidas pero menos exploradas: la espectroscopia de fotocorriente de intensidad modulada (IMPS) y la espectroscopia de fotovoltaje de intensidad modulada (IMVS). Para ello, primero hemos desarrollado un protocolo para obtener espectros de IMPS e IMVS fiables, que implica medir la modulación de la luz utilizada para medir estas técnicas.

El análisis de los espectros IMPS e IMVS suele limitarse al análisis de sus tiempos característicos. Por otro lado, la forma más habitual de analizar los espectros de IS es utilizando un modelo de circuito equivalente (EC), sin embargo, su elección es uno de los principales problemas de esta técnica, ya que un espectro de impedancia dado puede ser generado por diferentes ECs, dando lugar a diferentes interpretaciones del funcionamiento del dispositivo.

Uno de los principales resultados de esta tesis es el desarrollo de un procedimiento para analizar de forma combinada las respuesta de IS, IMPS e IMVS. Para ello, hemos incorporado el efecto de la absorbancia y la eficiencia de separación en las funciones de transferencia de IMPS e IMVS. Hemos desarrollado este procedimiento de la forma más general posible, con la intención de que pueda ser aplicado a cualquier dispositivo de fotoconversión. Como prueba de concepto, demostramos con éxito la aplicación de este procedimiento en un fotodiodo de silicio. Hemos demostrado que este procedimiento permite una selección más adecuada del EC, resolviendo, al menos en parte, la principal limitación de la IS. Además, hemos mostrado, por primera vez, el análisis de los espectros de IS, IMPS e IMVS con el misma EC. Con este análisis, hemos demostrado que la combinación de IS, IMPS e IMVS permite obtener parámetros con mayor precisión, así

como también parámetros adicionales que no son accesibles mediante el análisis por separado de estas técnicas.

A continuación, hemos adaptado este procedimiento a dispositivos en los que la generación de portadores se distribuye a lo largo del material absorbente y la extracción de estas cargas fotogeneradas está limitada por la difusión y la recombinación. Para ello, hemos presentado un EC obtenido a partir de las ecuaciones fundamentales que describen estos procesos. Hemos demostrado experimentalmente que este circuito ajusta adecuada y simultáneamente las respuestas de IS, IMPS e IMVS de una celda electroquímica de generación de hidrógeno con un fotoánodo de Zr:$BiVO_4$. Como resultado, hemos podido identificar cómo la difusión de electrones y de huecos limitan la extracción de carga cuando el dispositivo es iluminado desde los contactos colector de huecos y de electrones respectivamente. Junto con este resultado, también hemos demostrado que la principal limitación del rendimiento de este dispositivo es la eficiencia de separación de carga del Zr:$BiVO_4$.

Estos resultados son una validación del poder de la combinación de IS, IMPS e IMVS, exponiendo las principales limitaciones del dispositivo, e indicando así el objetivo para mejorar su rendimiento. Por lo tanto, en línea con nuestros objetivos, estamos convencidos de que esta combinación será de gran ayuda en el desarrollo de dispositivos de fotoconversión.

Contents

Publications

Publications Included in this Thesis

1. Agustin O. Alvarez, Ramón Arcas, Clara A. Aranda, Loengrid Bethencourt, Elena Mas-Marzá, Michael Saliba, and Francisco Fabregat-Santiago. Negative Capacitance and Inverted Hysteresis: Matching Features in Perovskite Solar Cells, *The Journal of Physical Chemistry Letters* **2020**, *11*, 8417. DOI: 10.1021/acs.jpclett.0c02331. Impact Factor 2020: 6.475.
2. Agustin O. Alvarez, Antonio Riquelme, Rosinda Fuentes-Pineda, Lluis F. Marsal, Osbel Almora, Juan A Anta, Francisco Fabregat-Santiago. Correcting unintended changes in electroluminescence perturbation for reliable light intensity modulated spectroscopies, *Measurement Science and Technology* **2023**, *Submitted*. Impact Factor 2023: 2.398.
3. Agustin O. Alvarez, Sandheep Ravishankar, Francisco Fabregat-Santiago. Combining Modulated Techniques for the Analysis of Photosensitive Devices, *Small Methods* **2021**, *5*, 2100661. DOI: 10.1002/smtd.202100661. Impact Factor 2021: 15.367.
4. Agustin O. Alvarez, Miguel García-Tecedor, Laura Montañés, Elena Mas-Marzá, Sixto Giménez, Francisco Fabregat-Santiago. New Views on Carrier Diffusion and Recombination by Combining Small Perturbation Techniques: Application to $BiVO_4$ Photoelectrodes, *Solar RRL* **2022**, 2200826. DOI: 10.1002/solr.202200826. Impact Factor 2021: 9.173.

All the co-authors have agreed to the use of these publications for this PhD thesis and have declined to use them as part of another PhD thesis.

Publications not Included in this Thesis

1. Vivek Babu, Rosinda Fuentes Pineda, Taimoor Ahmad, Agustin O Alvarez, Luigi Angelo Castriotta, Aldo Di Carlo, Francisco Fabregat-Santiago, Konrad Wojciechowski. Improved stability of inverted and flexible perovskite solar cells with carbon electrode, *ACS Applied Energy Materials* **2020**, *3, 6*, 5126–5134. DOI: 10.1021/acsaem.0c00702. Impact Factor 2020: 6.024.

2. Nadja Klipfel, Agustin O. Alvarez, Hiroyuki Kanda, Albertus Adrian Sutanto, Cansu Igci, Cristina Roldán-Carmona, Cristina Momblona, Francisco Fabregat-Santiago, Mohammad Khaja Nazeeruddin. C_{60} Thin Films in Perovskite Solar Cells: Efficient or Limiting Charge Transport Layer? *ACS Applied Energy Materials* **2022**, *5, 2*, 1646-1655. DOI: 10.1021/acsaem.1c03060. Impact Factor 2021: 6.959.

3. Jesús Sanchez-Diaz, Rafael S. Sánchez, Sofia Masi, Marie Krečmarová, Agustín O. Alvarez, Eva M. Barea, Jesús Rodriguez-Romero, Vladimir S. Chirvony, Juan F. Sánchez-Royo, Juan P. Martinez-Pastor, Iván Mora-Seró. Tin perovskite solar cells with >1,300 h of operational stability in N2 through a synergistic chemical engineering approach, *Joule* **2022**, *6, 4*, 861-883. DOI: 10.1016/j.joule.2022.02.014. Impact Factor 2021: 46.048.

4. Gabriela S. Anaya Gonzalez, Jose J. Jeronimo-Rendon, Qiong Wang, Guixiang Li, Agustin O. Alvarez, Francisco Fabregat-Santiago, Hans Köbler, Alberto Alvarado, Hector Juárez-Santiesteban, Silver-Hamill Turren-Cruz, Michael Saliba, Antonio Abate. Large grain size with reduced non-radiative recombination in potassium incorporated methylammonium-free perovskite solar cells, *Solar Energy Materials and Solar Cells* **2022**, *248*, 111964. DOI: 10.1016/j.solmat.2022.111964. Impact Factor 2021: 7.305.

5. Carlos Echeverría-Arrondo, Agustin O. Alvarez, Sofia Masi, Francisco Fabregat-Santiago, Felipe A. La Porta. Electronic, Structural, Optical, and Electrical Properties of CsPbX3 Powders (X = Cl, Br, and I) Prepared Using a Surfactant-Free Hydrothermal Approach, *Nanomanufacturing* **2023**, 3(2), 217-227. DOI: 10.3390/nanomanufacturing3020013.

Appendix

List of Abbreviations and Acronyms

$\bar{\ }$	DC variable
$\sim$	AC variable
A	Largest radius cation
a	Absorptance
ABX_3	Perovskite chemical structure
AC	Alternating current
B	Smallest radius cation
BX_6	Octahedron complex
CdTe	Cadmium Telluride
CIGS	Copper Indium Gallium Selenide
C_g/C_d	Geometrical or Dielectric capacitance
C	Capacitance per unit area/Capacitor
CV	Cyclic voltammetry
d	Thickness of the absorber
D	Diffusion coefficient
DC	Direct current
D_n	Electron diffusion coefficient
D_p	Hole diffusion coefficient
E	Energy
EC	Equivalent Circuit
E_C	Conduction Band
E_F	Fermi Level o Fermi Energy
E_{Fn}	Electron Fermi level
E_{Fp}	Hole Fermi level
EQE	External quantum efficiency
ESC	Electron Selective Contact
E_V	Valence Band
E_g	Bandgaps
E_{ph}	Energy of a photons
E_{vac}	Vacuum Level
f	Frequency
$f(E)$	Probability of occupancy of states
FA	$NH_2CH{=}NH_2$ formamidinium

FF	Fill factor
FTO	Fluorine-doped tin oxide
G	Free charge generation probability by an incident photon
g	Density of states
GaAs	Gallium Arsenide
h	Hole density
HI	Hysteresis index
HSC	Hole Selective Contact
IMPS	Intensity-Modulated Photocurrent Spectroscopy
IMVS	Intensity-Modulated Photovoltage Spectroscopy
IQE	Internal quantum efficiency
IS	Impedance Spectroscopy
ITO	Indium tin oxide
IZO	Indium zinc oxide
j-V curve	External current-voltage curve
j_0	Reverse saturation current
j_{LS}	Light source current
j_{MPP}	MPP current
j_a	Absorbed current
j_{ext}	Extracted current
j_{inj}	Injected current
j_{ph}	Free photogenerated current
j_{rec}	Recombination current
L	Inductance
LED	Light-Emitting Diode
LHE or η_{LHE}	Light-harvesting efficiency
L_n	Electron diffusion length
L_p	Hole diffusion length
m	Ideality factor
MA	CH_3NH_3 methylammonium
$MAPbBr_3$	Methylammonium Lead Bromide
$MAPbI_3$	Methylammonium Lead Iodide
MPP	Maximum power point
ms-$BiVO_4$	Monoclinic scheelite $BiVO_4$
n	Electron density
n-i-p	Standard (or regular) perovskite solar cell structure
OC	Open-circuit
OLED	Organic Light-Emitting Diode
P3HT	Thiophene-based poly(3-hexylthiophene-2,5-diyl)

PC	Photocatalysis
PCBM	[6,6]-phenyl-C-61-butyric acid methyl ester
PCE	Power Conversion Efficiency
PEC	Photoelectrochemical
PEDOT: PSS	Poly(3,4-ethylenedioxythiophene)-poly(styrenesulfonate)
p-i-n	Inverted perovskite solar cell structure
P_{in}	Power of the light reaching a device
P_{max}	Maximum power that can be extracted from a device
P_{out}	Power extracted from a device
PSC	Perovskite Solar Cells
PTAA	Polytriarylamine
PV	Photovoltaics
PV-EC	Photovoltaic-Electrolysis
Q	IMPS transfer function
$\mathbb{Q}$	Charge per unit area
R	Resistance
R_{DC}	Direct current resistance
R_L	Resistance in Series to an Inductance
R_S	Series resistance
R_{rec}	Recombination resistance
R_{sh}	Shunt resistance
SC	Short-circuit
s	Scan-rate
spiro-OMeTAD	N2,N2,N2′,N2′,N7,N7,N7′,N7′-octakis(4-methoxyphenyl)-9,9′-spirobi[9H-fluorene]-2,2′,7,7′-tetramine
SRH	Shockley-Read-Hall recombination
SSC	Silicon Solar Cells
STH	Solar-to-Hydrogen Conversion Efficiency
T	Temperature
t	Time
TCO	Transparent-conducting oxide
V_0	Initial voltage
V_C	Voltage drop in a capacitor
V_L	Voltage drop in an inductor
V_{MPP}	MPP voltage
V_{OC}	Open-circuit voltage
V_{app}	Applied voltage
V_{bi}^{ESC}	Built-in potential at the absorber/ESC interface
V_{bi}^{HSC}	Built-in potential at the absorber/HSC interface

W	IMVS transfer function
X	Anions
Z	IS transfer function
α	Absorption coefficient
δ	Phase shift
η_{col}	Collection efficiency
η_{opt}	Optical efficiency
η_{ph}	Photogeneration efficiency
η_{sep}	Separation efficiency
λ	Wavelength of the light
τ_{rec}	Lifetime
Φ_B	Magnetic flux
ϕ	Photon flux
ϕ_{int}	Internal photon flux
ω	Angular frequency

List of Physical Constants

Quantity	Symbol	Value
Elementary charge	q	1.602×10^{-19} C
Boltzmann's constant	k_B	1.3806×10^{-23} J K^{-1}
Thermal Energy at 300 K	$k_B T$	0.0259 eV
Speed of light in vacuum	c	2.998×10^{8} m s^{-1}
Plank’s constant	h	6.626×10^{-34} J s

Thesis Style

This thesis is divided into eight chapters following the journal articles compilation style. **CHAPTER 1** introduces broadly the field in which this thesis is developed, with its main challenges and recent advances. **CHAPTER 2** describes the experimental techniques employed in this thesis. **CHAPTER 3** provides a critical overview of the thesis, where the general and specific objectives are stated, the state of the art of the specific topics investigated is discussed, the major obstacles encountered are described and the main results obtained are commented. **CHAPTER 4**, **CHAPTER 5**, **CHAPTER 6** and **CHAPTER 7** present, in detail, the results obtained in this thesis in the format of the final version of the manuscript before publication (pre-print version), with a preliminary description of the contributions of the candidate in each manuscript. Finally, **CHAPTER 8** sets out the general conclusions of this thesis, highlighting the contributions that have been made to the area of research, and the implications that these results might have in the future.

CHAPTER 1

Introduction

1.1. Sustainable Energy for the Future

Climate change is probably the biggest challenge currently faced by humanity. In the right axis of **Figure 1.1**a it is presented the change in the average global temperature over the years. Despite the year-to-year fluctuations, it is clear that the temperature has increased more than 1ºC since the industrial revolution,[1] with a sharp rise in the last decades. The main cause of climate change is human emissions of greenhouse gases, primarily CO_2 emissions.[2] **Figure 1.1**a shows also how the CO_2 emissions have increased since 1850,[3] following the trend of the temperature change. From this figure, it can be noted that these increments in temperature and CO_2 emissions are essentially linked to the use of fossil fuels. On the other hand, emissions from land use change (green in **Figure 1.1**a) have been decreasing in recent decades, currently reaching 19th-century values. To meet the goals established in the Paris Agreement, it is calculated that the CO_2 emissions have to be halved by 2030, and net-zero emissions must be achieved by 2050.[4-5]

The overall consumption of energy is continuously increasing and, according to the International Energy Agency, is expected to increase by nearly 50% by 2050.[6] As can be seen in **Figure 1.1**b, so far, energy production has come almost exclusively from fossil fuels. Therefore, to reduce CO_2 emissions, it is necessary to replace fossil fuel energy with sustainable energy, i.e. derived from resources that can maintain current operations without jeopardizing the needs of future generations.[7]

There are many alternative energy sources to fossil fuels. To meet sustainability, the energy sources not only have to address the greenhouse gas emission problem, but they should also address other environmental, social and economic aspects.[8] Nuclear and biofuels have seen their expansion affected by the questioning of their sustainability, due to the generation of radioactive waste[9] and the clearing of forests,[10] respectively. Hydropower has been so far the main alternative to fossil fuels, but its energy production capacity has grown at a slower rate than total energy demand. In contrast, wind and solar energy represent a small portion of the current energy production but they have been growing rapidly in the latest years, as can be seen in **Figure 1.1**b. These three energy sources (hydro, wind and solar) could have a considerable environmental impact, but with proper planning, they have proven to be sustainable sources.[11] The main limitation of these sources is their intermittency because they depend on fluctuating sources such as river flow, wind and sunlight. Therefore, in the transition to sustainable energy, it is essential the implementation and investigation of different energy sources, together with complementary technologies to enable safe and sustainable storage of the exceeding energy.[12] The energy storage could be done through technologies such as batteries or

pumped-storage hydroelectricity, which comes with additional costs and difficulties.[13] An alternative is to use solar energy to split the water molecule (H_2O) and store the resulting molecular hydrogen (H_2). H_2 can then be transported and converted into electrical energy on demand, even within electrical vehicles. This process takes place in clean fuel cells, with water as the combustion product.

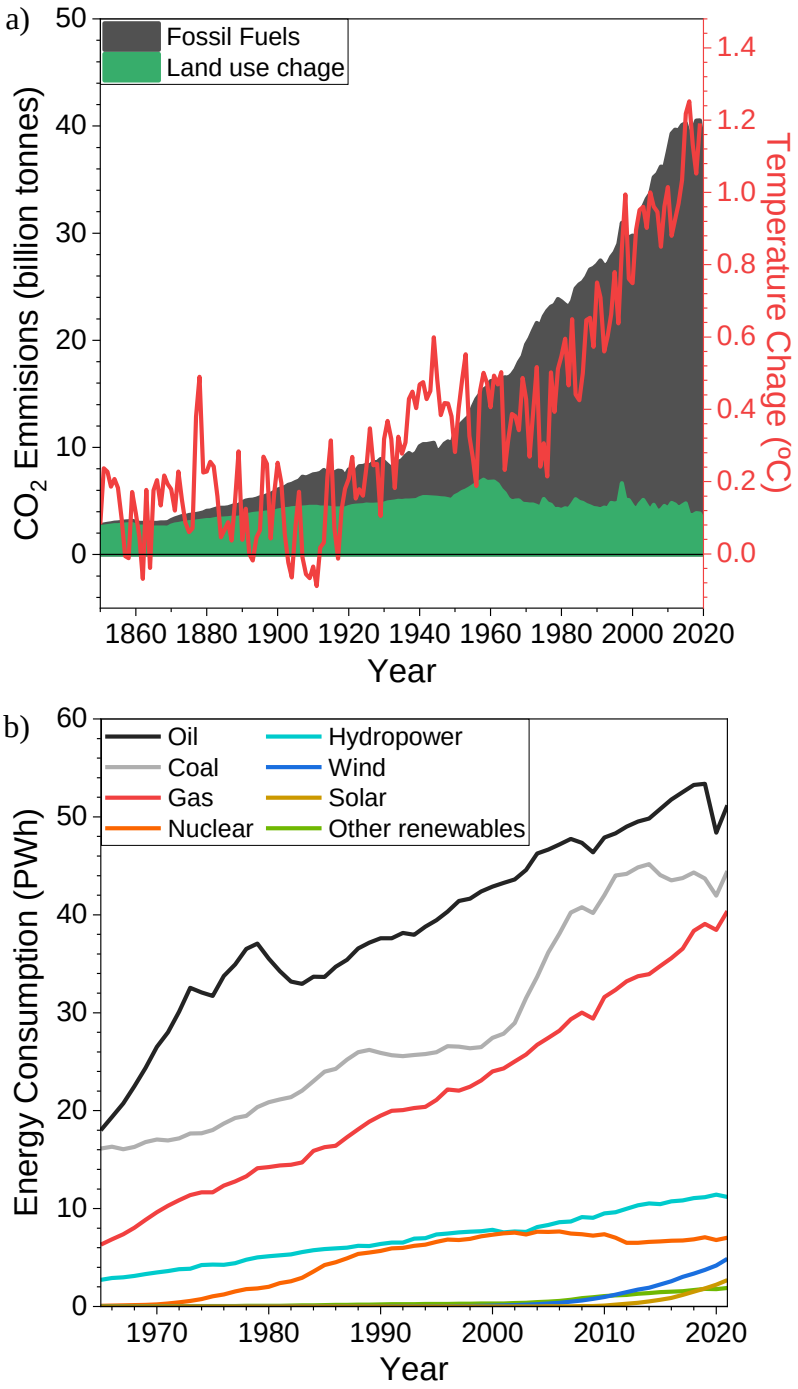

Figure 1.1. a) Global CO_2 emissions from fossil fuels and land use change[3] compared with the change in the global average land-sea temperature,[14] over time. b) World energy consumption by source over time.[15]

1.1.1. Photovoltaics

The World Energy Assessment estimated, in 2000, that the potential solar energy that could be used annually by humans could reach 14000 PWh, taking into account factors such as cloud cover and the land available to humans.[16] This amount is far beyond the consumption of energy in 2021 (approximately 160 PWh). Therefore, solar energy could largely cover the energy demand, the current limitation then lies in the application of technologies to harness this energy. Solar Water Heating is frequently used in residences and some industries, reaching a capacity of 472 GW in 2017.[17] On the other hand, to convert solar energy into electrical energy, there are two options, either directly with Photovoltaics (PV) or indirectly with Concentrated Solar Power. The capability of Concentrated Solar Power was only 6.8 GW in 2021,[18] being the technical difficulties and high prices the main limitations of this technology.[19]

Many photovoltaic technologies have been extensively investigated in the last decades. **Figure 1.2** shows the maximum efficiency reached by the different solar cells over time.[20] As can be seen, there are solar cells that successfully convert almost half of the solar energy into electrical energy. Some of these technologies have particular applications, such as detectors and space applications. The highest efficiencies are achieved by multijunction cells, made by the combination of several materials that absorb different wavelengths of the solar spectrum. The high cost of these devices has been the main limitation to their wider use.[21] To reach the global mass production of energy, photovoltaic technology needs more than high efficiencies.

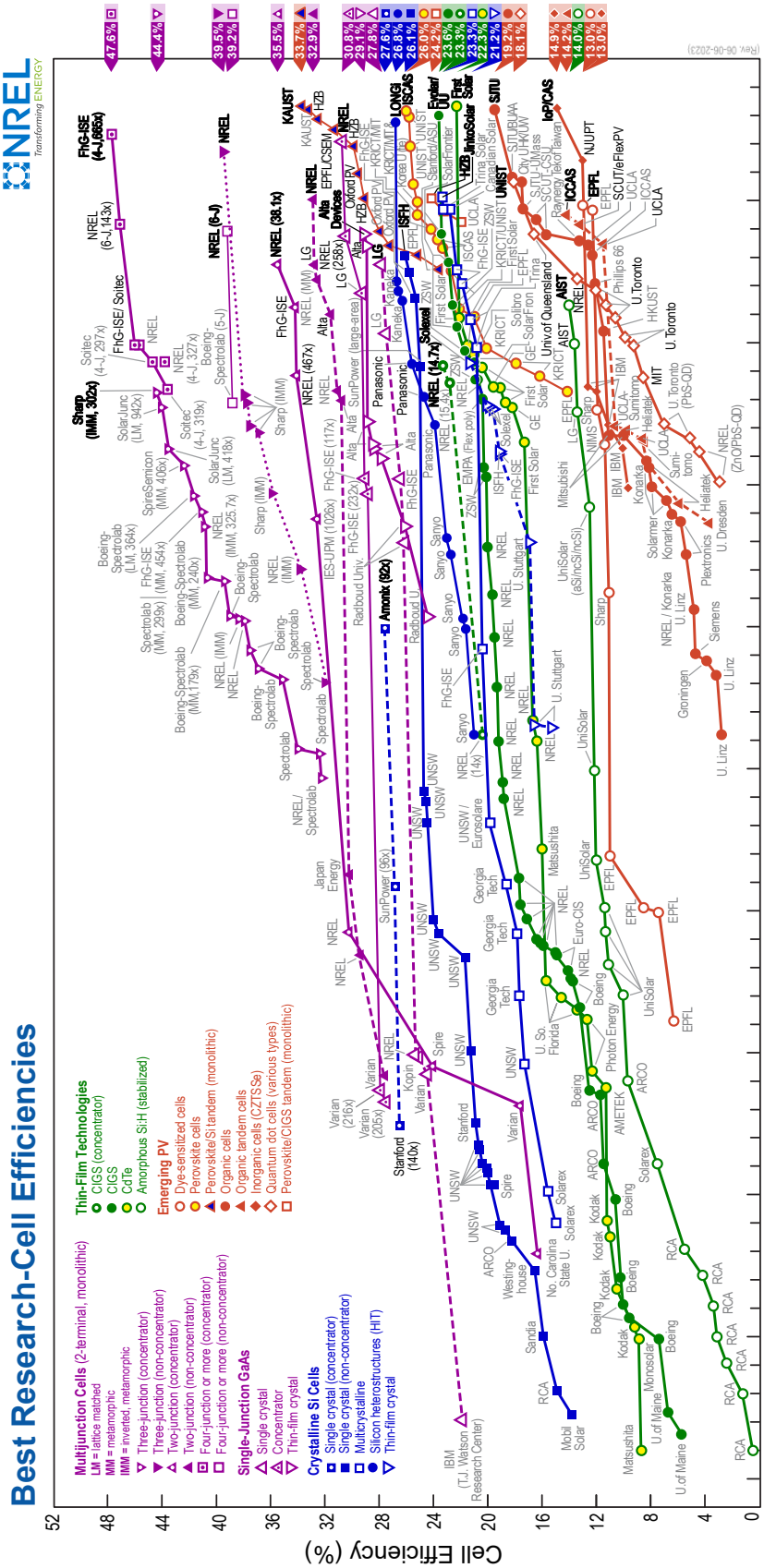

Figure 1.2. Temporal evolution of the efficiencies of the different photovoltaic technologies. Reproduced with permission from Ref. [20]. Copyright 2023, NREL.

The theoretical maximum power conversion efficiency (PCE) for a single-junction cell is 33.16% according to Shockley–Queisser limit.[22] Surprisingly, many solar cell technologies have overpassed the 20% in the last years (see **Figure 1.2**). While the main limitations among these technologies ate the efficiency, stability and cost, some of them face other drawbacks such as toxicity, in the case of cadmium telluride (CdTe) cells or the presence of scarce elements, in copper indium gallium selenide (CIGS) and gallium arsenide (GaAs) cells.[23-24] For many years, the solar cell market has been dominated by silicon solar cells (SSCs), as can be seen in **Figure 1.3**, overpassing 94% of the total market.[25] Silicon has obvious advantages, such as abundance and non-toxicity. But its dominance in the market is mainly because it has proven to last for more than 25 years with PCE above the 20%, with continuously declining prices, as can be seen in **Figure 1.3**.[24, 26] On the other hand, it is clear from this graph that the reduction in prices of SSCs is being followed by the prices of other thin-film technologies.

Perovskite solar cells (PSCs) emerged in 2009 with a PCE of only 3.8%,[27] and since then they have experienced an explosive improvement, exceeding 25% (orange and yellow circles in **Figure 1.2**).[20] In addition to their efficiency, PSCs have attracted interest for their simple manufacturing from solutions involving low-cost materials.[28] Furthermore, these devices have capabilities that differentiate them from the SSCs, such as the possibility to easily tunned their absorption spectra[29] and to prepare flexible devices with this material.[30] These properties allow PSCs many applications, including indoor cells[31] and tandem cells with other solar cells or even with themselves. The tandem application, positions the PSCs as allies rather than competitors to the SSCs, considering that the Si/perovskite tandem cell has already achieved over 32% PCE, as can be seen in the red and blue triangles in **Figure 1.2**.

Two main issues prevent the widespread commercialisation of PSCs. One of them is the toxicity related to the presence of lead, but there are perovskite lead-free alternatives that have already demonstrated impressive performances.[32-33] The other issue, more determinant, is the reduced stability of PSCs compared to market-available SSCs.[34] It is, therefore, necessary to understand the causes behind the lack of stability of the PSCs. A detailed understanding of the internal processes that occur during their operation would shed light on the degradation processes, paving the way to possible solutions.

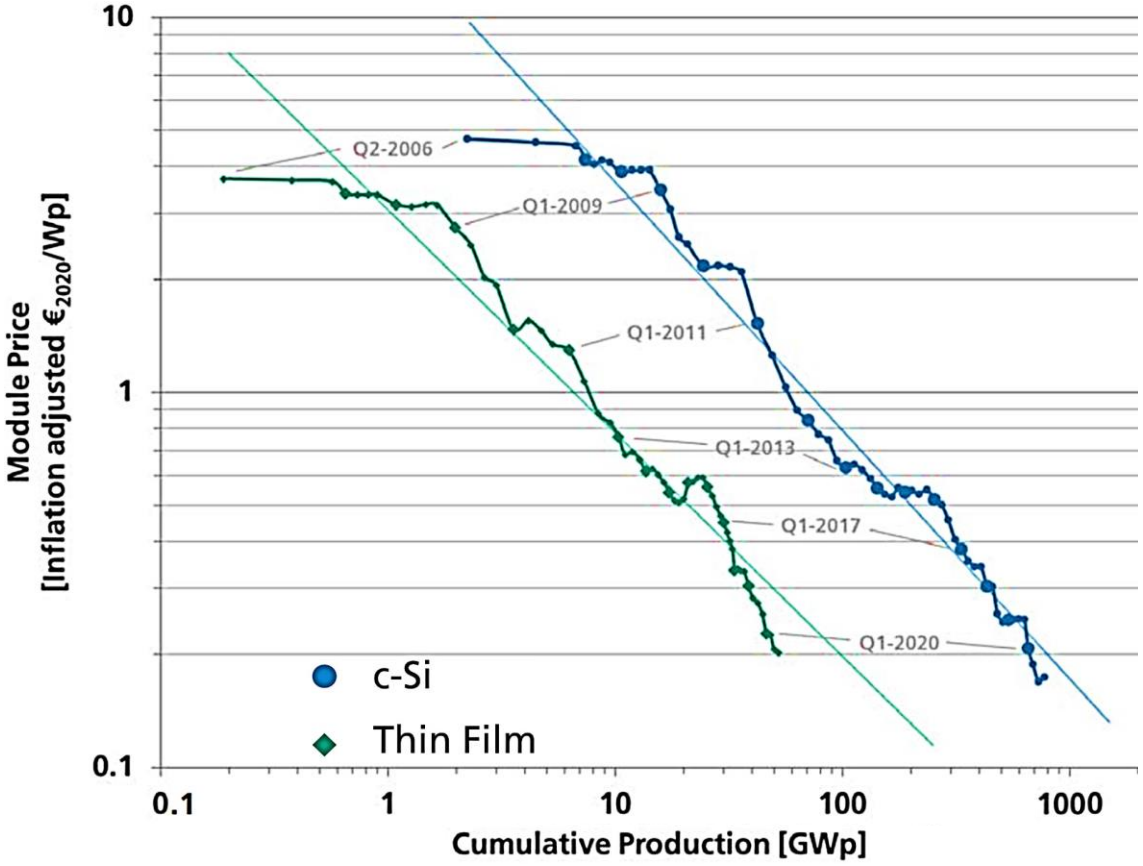

Figure 1.3. Evolution of the price as a function of the accumulated production by photovoltaic technology. c-Si accounts for monocrystalline and polycrystalline silicon, while Thin Films contain cells such as CdTe, amorphous silicon and CIGS. Different periods are remarked, from the second quarter of 2006 to the fourth quarter of 2020. GWp is the maximum electrical power (in GW) under standard conditions. Adapted from ref. [25], Copyright 2022, Fraunhofer ISE.

1.1.2. Solar to Fuel

As discussed in the previous section, photovoltaics has enormous potential to replace fossil fuel energy with solar energy. But as mentioned before, the inherent problem with this technology is the intermittency of the sunlight, which can lead to a mismatch between energy generation and demand. The water molecule (H_2O) splitting from solar energy to generate hydrogen (H_2) is an attractive solution to this problem, as mentioned above. H_2 has also other applications, such as atmospheric CO_2 reduction or as feedstock in some industries.[35]

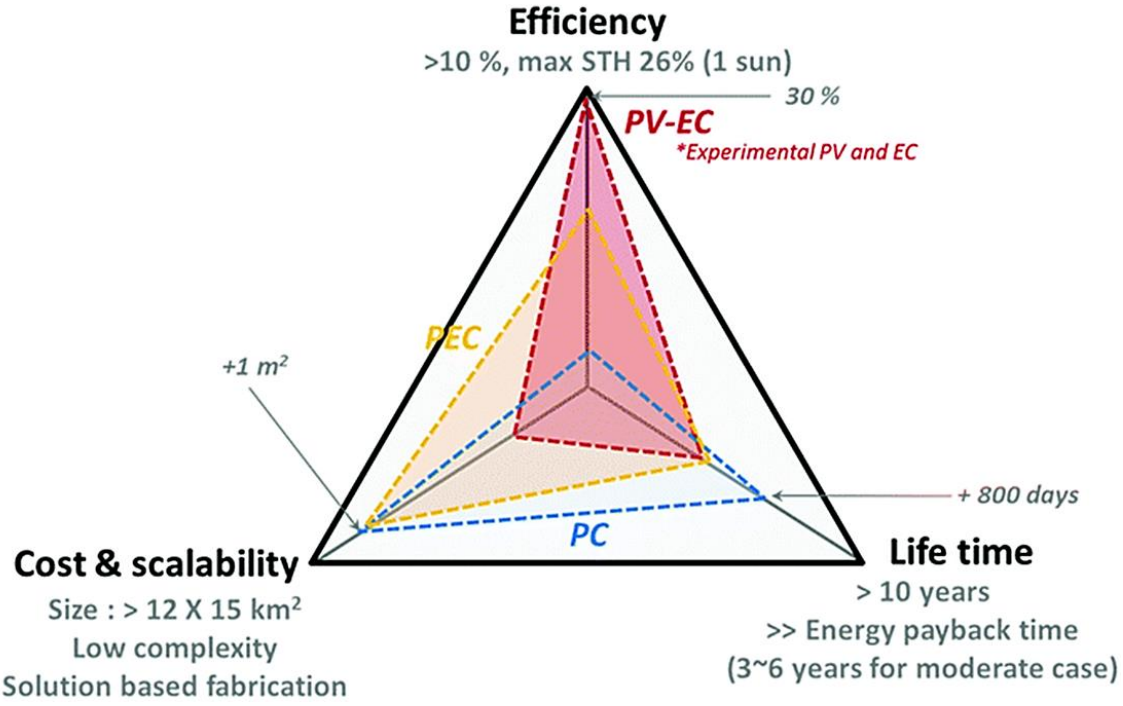

Figure 1.4. A comparison between a potential commercialization goal of hydrogen generation from solar energy and the different technologies available: photovoltaic-electrolysis (PV-EC), photoelectrochemical (PEC) system and particulate photocatalysis (PC). Adapted from ref. [36], Copyright 2019, The Royal Society of Chemistry.

Nowadays, about 96% of H_2 is produced from fossil fuels because, despite the availability of many technologies to generate H_2 from solar energy, they are much more expensive than methane reforming.[37] There is great interest in making these technologies commercially available, as evidenced by the multi-millionaire projects around the world.[38-39] This interest is not only to reduce global warming but also to reduce the H_2 price low enough to make viable other technologies such as hydrogen electric vehicles.[40]

The solar-to-hydrogen technologies can be grouped into three categories:[41]

- Photovoltaic–electrolysis (PV-EC): electricity generated from a solar cell is used to split the water molecule in an electrolyzer.
- Photoelectrochemical (PEC) system: a similar working mechanism to PV-EC but the absorber material is in direct contact with the electrolyte (water).
- Particulate photocatalysis (PC): the light is absorbed by particles that can use this energy to split the water molecules.

Each of these approaches has its advantages and disadvantages, **Figure 1.4** shows a simplified comparison, among them and with a potential commercialization goal.[36] The main metric for these technologies is the solar-to-hydrogen conversion efficiency (STH), defined as the fraction of incident solar energy that is stored as chemical energy in the H_2 produced.[42] As can be seen, the PV-EC have reached outstanding values of around 30% STH. However, to exceed 10% efficiency with PV-EC it is necessary to use multi-junction solar cells,[43] associated with high costs, limiting their scalability. By contrast, PC water splitting is the simplest solar hydrogen production system with just light and water. The downside of PC is that they have a theoretical maximum of 10% STH.[44] In practice, most reported efficiencies are less than 3%,[45-47] but an astonishing 9.4% has recently been reported.[48] At an intermediate level of complexity is the PEC, which has achieved efficiencies of 19%.[49] While PV-ECs may be closer to commercialisation by adapting existing technologies, the simplicity of PEC could lead to lower costs.[50] In any case, to achieve the commercialisation of any of these technologies, significant improvement is needed, especially in understanding the processes involved in the transformation of light to hydrogen.

1.2. Working Principles of Photoconversion Devices

The working principles for photovoltaic and photoelectrochemical cells are almost the same. Simplistically, both systems consist of absorber material and selective contacts. The main difference is that in the photovoltaic cells the selective contacts extract the charges to generate electrical energy, while in the photoelectrochemical cells at least one of the selective contacts is an electrolyte (water), where the chemical energy is generated (O_2 or H_2). For this reason, in this section, we will employ the term "photoconversion device" to refer to both photovoltaic and photoelectrochemical cells. In the next sections, both cells will be described in detail, separately.

1.2.1. Semiconductors and Energy Levels

The first step to understand the working principles of a photoconversion device is to comprehend the properties of the absorber materials. The materials most traditionally employed as absorbers in these devices are the semiconductors, but other materials such as molecular absorbers are also used.[51] In this section, we will explore the properties of semiconductors.

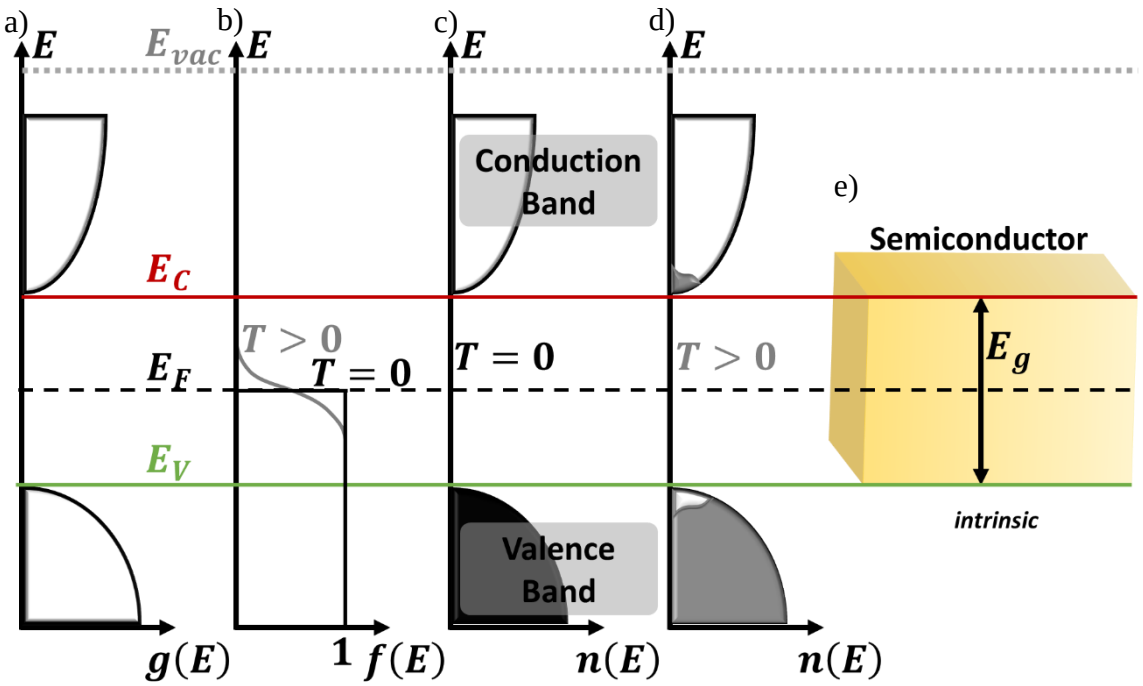

Figure 1.5. Scheme of different functions depending on the energy (E) typical for a semiconductor: a) the density of states ($g(E)$), b) the probability of occupancy of states ($f(E)$) and b) the electron density ($n(E)$), at temperatures equal to cero ($T = 0\ K$) and higher than zero ($T > 0\ K$). The energy (E) grows upwards, as indicated by the arrow. In these figures are represented: the Fermi level (E_F), the valence band energy (E_V), the conduction band energy (E_C), the vacuum level (E_{vac}) and the bandgap of the semiconductor (E_g). e) is a simplified representation of such a semiconductor.

Each material has available energy ranges to its electrons, known as energy bands. In other words, there cannot be an electron within the material with an energy outside these bands (in principle, we will discuss the "traps" in the next subsection). **Figure 1.5**a shows a diagram of a possible density of states available as a function of energy, $g(E)$, in a material. In the zero temperature limit ($T = 0\ K$), the electrons will fill the lowest energy states. The valence band is the highest range of occupied states, while the conduction band is the lowest range of unoccupied states, both at $T = 0\ K$. E_V is the higher energy of the valence band and E_C is the lower energy of the conduction band. The difference between these energies is defined as the bandgap: $E_g = E_C - E_V$.[52]

The Fermi level (E_F) is defined as the energy for which, at $T = 0\ K$, the probability of occupancy of states ($f(E)$) with lower energy is one and with higher energies is cero. At temperatures higher than zero ($T > 0\ K$), some of the electrons have kinetic energies that could allow them to move to states of higher energies, which modifies $f(E)$ around E_F, as shown in **Figure 1.5**b.[53] **Figure 1.5**c and d show the number density of electrons as a function of energy ($n(E)$) for the case shown in **Figure 1.5**a at $T = 0\ K$ and $T > 0\ K$, respectively.

Materials can be classified according to their different E_g. Semiconductors have a bandgap wider than conductors ($E_g \cong 0$) but narrower than insulators ($E_g > 3\ eV$).[54] **Figure 1.5**e shows the simplified scheme for a semiconductor that we will employ in this thesis.

The E_g can also be defined as the minimum energy needed to excite an electron from E_V to E_C, see **Figure 1.6**a. This energy can be provided externally, for example applying a voltage high enough to the material. Another option is by illuminating the material, with the wavelength of the light (λ) low enough to result in the energy of the photons ($E_{ph} = hc/\lambda$) higher than E_g, where c is the speed of light in vacuum and h the Plank's constant. The resulting electrons in the conduction band, and the holes in the valence band, can move in the semiconductor similarly to the charges on a conductor. In this sense, semiconductors are considered as having the property of behaving similarly to both conductors and insulators, depending on the external conditions.[55-56]

Figure 1.6a shows an absorber material and other two materials, with different E_F, when they are separated. **Figure 1.6**b illustrates that when the three materials are in contact, the Fermi levels align, resulting in the differences and bending in the conduction and valence bands. For the proper functioning of a photoconversion device is needed a ladder-like energy diagram for the conduction and the valence bands, as shown in **Figure 1.6**b. This implies that the free electrons and holes in the absorber will energetically prefer to go to the materials at the left and right, respectively. The ideal selective contact for a photoconversion device allows a resistance-free flow of one type of carrier while completely blocking the other, and is reversible for both injection and extraction of carriers.

Thus, in **Figure 1.6**b, the left material is acting as the electron selective contact (ESC) while the material on the right is acting as the hole selective contacts (HSCs) of the

photoconversion device. This energy diagram causes the photoconversion devices to have a diode-like behaviour, where the current has a preferred direction of flow. This figure also shows how the vacuum level (E_{vac}) keeps the contuinity after contacting the absorber with the contacts, it a displacement in this level is generated as a consequence of the alignment of the Fermi levels. This is known as the vacuum level alignment rule or the Mott–Schottky rule.[57] These displacements are known as building potential (V_{bi}), in grey in **Figure 1.6**, for both interfaces of the absorber, with the ESC (V_{bi}^{ESC}) and HSC (V_{bi}^{HSC}). For simplicity, the energy levels are shown as squares, a more realistic scenario will be desciussed in **Subsection 2.1.3**.

The Femi level of an intrinsic semiconductor (without impurities) can be increased or reduced by doping the material with donor (n-type doping) or acceptor (p-type doping) atoms, which provide additional free electrons or holes, respectively.[58] This surplus of free charges in n- and p-type semiconductors increases the conductivity of electrons in the conduction band and holes in the valence band, respectively. For this reason, n- and p-type semiconductors are normally used as ESCs and HSCs, respectively.

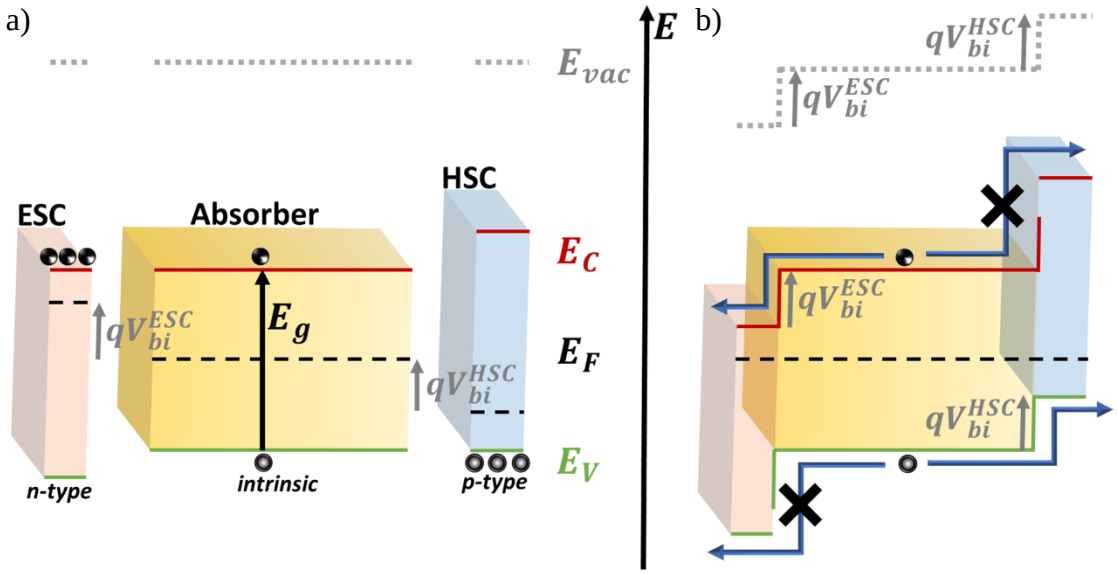

Figure 1.6. a) Scheme of the basic materials needed in a photoconversion device: absorber, electron selective contact (ESC) and hole selective contact (HSC). These materials are presented as examples of intrinsic, n-type and p-type semiconductors. The arrow points in the direction of the growing energy (E), and are represented: the Fermi level (E_F), the valence band (E_V), the conduction band (E_C), the vacuum level (E_{vac}) and the bandgap of the absorber (E_g). In greay are shown the built-in potentials for the interfaces of the absorber with the ESC (V_{bi}^{ESC}) and the HSC (V_{bi}^{HSC}). b) The result of contacting these materials and the resulting energetical preferable direction for the electrons and holes.

1.2.2. Fundamental Mechanisms

There are three fundamental mechanisms required for the proper working of a photoconversion device:

a) *Photon absorption*: a photon is absorbed to create an exciton.
b) *Charge separation*: the exciton is separated into a free electron and a free hole.
c) *Charge collection*: the free charges are extracted to generate electrical energy (photovoltaics cells) or they generate a chemical reaction in the electrolyte (photoelectrochemical cells).

These three steps are illustrated in **Figure 1.7** a, b and c, respectively.

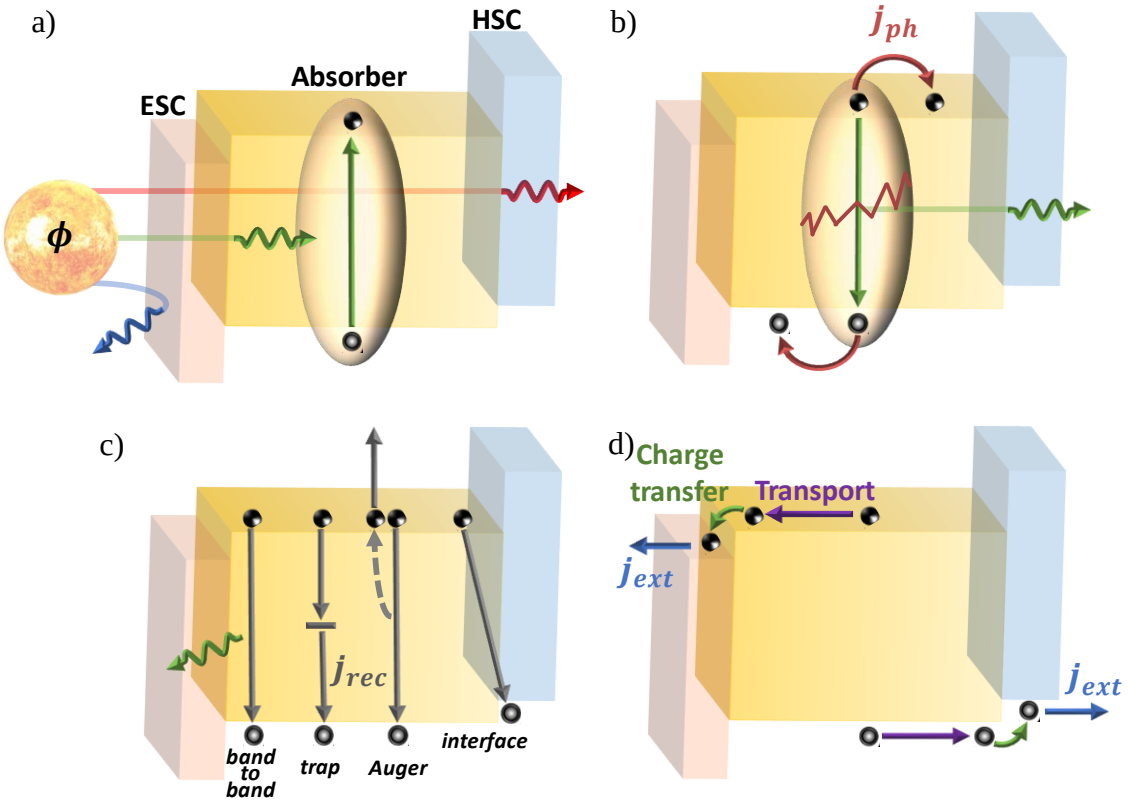

Figure 1.7. Scheme of the basic processes occurring in a photoconversion device, composed of an absorber material, sandwiched by an electron selective contact (ESC) and hole selective contact (HSC). a) A photon flux (ϕ) composed of different wavelengths (arrows of different colours) reaches the device, a part can be reflected (schematized with a blue arrow), and the remaining is the internal photon flux (ϕ_{int}) from which part can be transmitted (schematized with a red arrow) or absorbed (schematized with a green arrow), generating an electron-hole pair. b) This pair can recombine (geminate) or be separated, generating free-photogenerated charges (j_{ph}). c) These charges can recombine (j_{rec}) through many pathways: "band to band", "traps", "Auger" or "interfacial". d) The charges that do not recombine can be transported and transferred to the contacts to be extracted (j_{ext}).

As depicted in **Figure 1.7**a, when a photon flux (ϕ) impacts the cell, part of these photons will be lost before reaching the absorber material, for example by reflectance at the contacts. We can define the photons that reach the absorber material as the internal photon flux

$$\phi_{int} = \eta_{opt}\phi \tag{1.1}$$

where η_{opt} is the optical efficiency. **Figure 1.7**a shows the light reaching the device from the ESC, but in practice, it could also arrive from the HSC, this depends on the design of the device, as we will discuss in the next section.

Part of the ϕ_{int} will be absorbed, which means that these photons will transfer their energy to electrons in the valence band and excite them to the conduction band, by the photoelectric effect,[59] leaving holes, with positive effective charges, at their initial energy states. The photons that are not absorbed can be detected as transmitted light (schematized with a red arrow in **Figure 1.7**a). An absorbed photon then results in a bound electron-hole pair or exciton. The absorbed current is defined by

$$j_a = a\ q\ \phi_{int} \tag{1.2}$$

where q is the elementary charge and a is the absorptance, also called light-harvesting efficiency (LHE or η_{LHE}), defined as the fraction of photons that generate an exciton.

As mentioned in the previous section, to generate an exciton it is required that the energy of the photon is larger than the bandgap. But this is a requirement that does not ensure effective absorption. In fact, the absorptance can be written as

$$a = e^{-\alpha d} \tag{1.3}$$

with d the thickness of the absorber and α the absorption coefficient, which depends on the photon wavelength and the type of absorber. In general, the low-energy photons have lower probabilities to be absorbed, requiring a thicker absorber layer.[57]

Figure 1.7b shows that after the electron-hole pair is formed, it has two options, either it separates or it recombines. The recombination of this exciton emits a photon with the same energy as the absorbed photon, returning the system to the same state as before the photon absorption. This recombination is known as geminate recombination.[57] To avoid this recombination the electron-hole pair have to be dissociated, generating in this way a free electron and a free hole in the conduction and valence band, respectively. The free-photogenerated current is defined as

$$j_{ph} = \eta_{sep} j_a = \eta_{ph} q \phi \tag{1.4}$$

where η_{sep} is the separation efficiency, defined as the fraction of exciton that is successfully separated. In this thesis, we are introducing the photogeneration efficiency, given by

$$\eta_{ph} = \eta_{sep}\ a\ \eta_{opt} \tag{1.5}$$

As schematized in **Figure 1.7**b the charge separation takes place usually in the absorbing material, although there are some devices where more than one material is

involved in the charge separation process. The specific mechanisms involved in the charge separation depend on the type of absorber, for example, the separation efficiency may depend highly on the dielectric permeability of the material.[57] These mechanisms, in turn, may also depend on external factors, such as the temperatures, that can provide the thermal energy to overcome the binding energy.[52]

It has been observed that the separation efficiency can be very high in homogeneous semiconductors with high-dielectric permittivities and low-exciton binding energies. In particular, silicon-based devices have proven to be able to achieve near-ideal separation efficiencies.[60-61] Similar results were found in thin film technologies, in particular in perovskite solar cells. For the latter, it was observed that the population of excitons at room temperature can be very low, with a separation time in the order of ps.[62-64] In contrast, other semiconductors can present separation efficiencies below 10%, such as bismuth vanadate ($BiVO_4$), which is used as an absorber in electrochemical cells for water splitting.[65]

After the generation of the free charges in the absorber material, the free electrons and holes have again two options: they can recombine with each other or they can be collected at the contacts. **Figure 1.7**c shows the four different pathways of non-geminate recombination. It has to be kept in mind that the recombination of an electron in the conduction band with a hole in the valence band implies the release of energy. In the case of recombination "band to band" this energy is transformed into a photon, there is a possibility that this photon is reabsorbed by the material, leading to what is known as a photon-recycling event.[66]

The semiconductors can present, to a lesser or greater extent, energy states in the bandgap, known as "traps". Then, charges can recombine through these states, resulting in the fragmented release of the recombination energy, which can be dissipated to the lattice. This is described by the so-called Shockley-Read-Hall (SRH) recombination model.[67-68]

Another option, known as Auger recombination, is that the recombination energy is transferred as kinetic energy to a carrier. In **Figure 1.7**c the energy difference between the electron and the hole is transferred to another electron in the conduction band, but it could also be transferred to another hole in the valence band.

If the absorber were isolated, all photogenerated charges would recombine through one of these three processes. When contacts are attached to the absorber, **Figure 1.7**d shows that the free charges can be extracted (blue arrows), after some transport within the absorber material (purple arrows) and a charge transfer to the contacts (green arrows). However, the attachment of the contacts can generate new recombination paths at the interfaces, both radiative or mediated by traps (**Figure 1.7**c). This recombination pathway can be reduced by surface engineering. The recombination current (j_{rec}) is defined by considering the sum of all four recombination paths:

$$j_{rec} = j_{rec}^{band\ to\ band} + j_{rec}^{trap} + j_{rec}^{Auger} + j_{rec}^{interface} \quad (1.6)$$

Then, in a steady-state condition, by conservation of charge, the extracted current has to be given by

$$j_{ext} = j_{ph} - j_{rec} = \eta_{col} j_{ph} = EQE\ q\ \phi \tag{1.7}$$

where η_{col} is the collection efficiency, defined as the fraction of free photogenerated electrons and holes that are successfully extracted. Considering Equations (1.4) and (1.5), the external quantum efficiency is then given by

$$EQE = \eta_{col}\eta_{ph} = \eta_{col}\ \eta_{sep}\ a\ \eta_{opt} \tag{1.8}$$

Finally, the internal quantum efficiency is defined by

$$IQE = \frac{EQE}{\eta_{opt} a} = \eta_{col}\eta_{sep} \tag{1.9}$$

1.2.3. Operating Conditions

Considering the concepts introduced in the previous sub-sections, we can describe the operating conditions of a photoconversion device in terms of three currents: the photogeneration (j_{ph}), the recombination (j_{rec}) and the extraction (j_{ext}). In this subsection, we will consider different steady-state conditions, whereby the three currents will be linked, i.e. the sum of the last two has to be equal to the photogeneration, see Equation (1.7). **Figure 1.8** shows three different conditions where the balance fluctuates between these currents, but it is always fulfilled the relationship that links them.

As mentioned at the end of the previous subsection, if the material is not attached to the contacts, all the photogenerated charges will recombine. However, if the absorber is contacted to the ESC and the HSC but the whole device is isolated, the photogenerated charges are still unable to leave ($j_{ext} = 0$), this is known as open-circuit condition. Whereby, as shown in **Figure 1.8**a, all charges will also recombine ($j_{ph} = j_{rec}$), through some of the pathways depicted in **Figure 1.7**c. Nonetheless, the recombination of the charges requires time, which in the steady-state condition, results in an accumulation of electrons and holes in the conduction and valence band, respectively. This accumulation generates what is known as the splitting of the quasi-Fermi Levels. Here, the electron density does not follow the occupancy probability given by E_F (see **Figure 1.5**), instead the electron density in the conduction band and the hole density in the valence band follow the occupancy probability given by the "Electron Fermi level" (E_{Fn}) and the "Hole Fermi level" (E_{Fp}), respectively. Since electrons in the conduction band and holes in the valence band can only flow into the ESL and HSC, respectively, E_{Fn} is aligned with the E_F in the ESL and E_{Fp} is aligned with the E_F in the ESL.[57]

The external voltage of the cell, also known as the applied voltage (V_{app}), is the voltage difference measured externally between the ESC and HSC. In the ideal case where there is no additional potential drop, which could be due to e.g. the presence of series resistance, the external voltage will be equal to the difference between the quasi-Fermi levels of the absorber

$$V_{app} = \left(E_{Fn} - E_{Fp}\right)/q \tag{1.10}$$

In the case of **Figure 1.8**a, where light is reaching the device and there is no current extracted, the corresponding external voltage is defined as the open-circuit voltage (V_{OC}). This voltage depends on the photogenerated current, as more charges are generated per unit of time, the total cumulative charges can increase. But the open-circuit voltage depends strongly on the absorber material and the selective contacts, for example, the bandgap of the absorber and Fermi energy of the selective contacts limit the V_{OC}. However, approaching the theoretical limit of a device is always a challenge, involving the minimisation of the recombination processes.

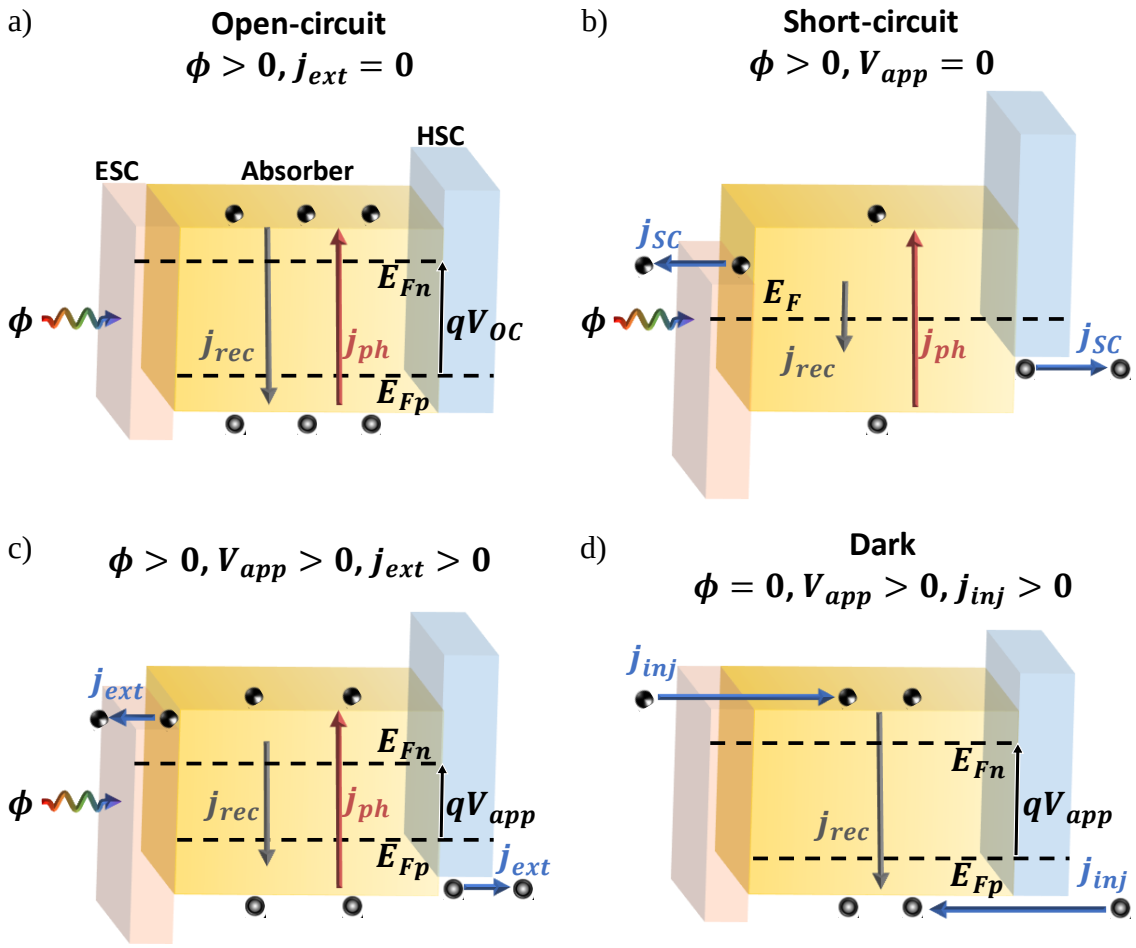

Figure 1.8. Scheme of different operating conditions of a photoconversion device, composed of an absorber material, sandwiched by an electron selective contact (ESC) and hole selective contact (HSC). a) A photon flux (ϕ) generates free-photogenerated charges (j_{ph}) in the absorber that recombines (j_{rec}) and generate an external voltage V_{app}, E_{Fn} and E_{Fp} are the electron and hole Fermi levels. In this particular case, the generated voltage is known as open-circuit voltage V_{OC}. b) By making $V_{app} = 0$, part of j_{ph} will be extracted (j_{ext}), and the Fermi level (E_F) of the three materials is aligned. c)An intermediate situation between the previous two cases. d) No light is externally applied, known as the "dark" condition, and an external voltage is applied, requiring the injection of external current (j_{inj}) to compensate for the recombination current.

The external voltage in the photoconversion device can be controlled independently of the incident light, either by connecting the device to an external resistor, to limit j_{ext}, or using a potentiostat to control either V_{app} or j_{ext}. **Figure 1.8**b shows the case where this voltage is equal to zero, this is known as short-circuit condition. As discussed in **Figure 1.6** this corresponds to the alignment of the Fermi levels, and the resulting ladder-like of conduction and valence energy bands allows photogenerated charges to flow outwards. To keep $V_{app} = 0$ when the device is illuminated, it is necessary to connect externally the contacts, which allows the electrons to exit from the ESC and enter again through the HSC to recombine with the holes. It should be noted that, although charges are allowed to flow out of the device, some of the photogenerated charges will recombine by some of the pathways depicted in **Figure 1.7**c.

Figure 1.8a and b show that the photogenerated current can be converted into extracted current or external voltage. The external control of this voltage regulates the balance between the extracted current and the recombination current. Usually, an intermediate point between these two cases is desired, as shown in **Figure 1.8**c, because the power extracted from the device is the product of both

$$P_{out} = j_{ext} V_{app} \tag{1.11}$$

Finally, **Figure 1.8**d shows the case where no light is reaching the device, known as the "dark" condition. Strictly speaking, there will always be light reaching the device, it will at least receive the light corresponding to black body radiation. But at room temperature for most photoconversion devices, this current is negligible in comparison with the operating currents. This figure shows that when we apply an external potential, recombination is generated inside the device (as we saw in **Figure 1.8**a), which necessarily has to be accompanied by the same injection of an electric current into the device ($j_{inj} = -j_{ext}$), in this particular case become $j_{inj} = j_{rec}$.

1.3. Perovskite Solar Cells

In this section, we will introduce the main concepts related to perovskite solar cells (PSCs). We will start presenting the perovskite material itself, including its chemical structure and some optoelectronic properties. Then, we will address the configurations and materials employed to manufacture functional solar cells. Finally, we will discuss the main challenge faced by this technology, namely stability issues.

1.3.1. Perovskite Thin Film

The term "perovskite" refers to a wide variety of materials with a chemical structure given by ABX_3, **Figure 1.9**a shows this type of structure.[69] Where A and B are cations, having A a compound radius greater than B. X are anions that six-coordinate B to form a BX_6 octahedron, which can be seen as grey rhombuses in **Figure 1.9**a.

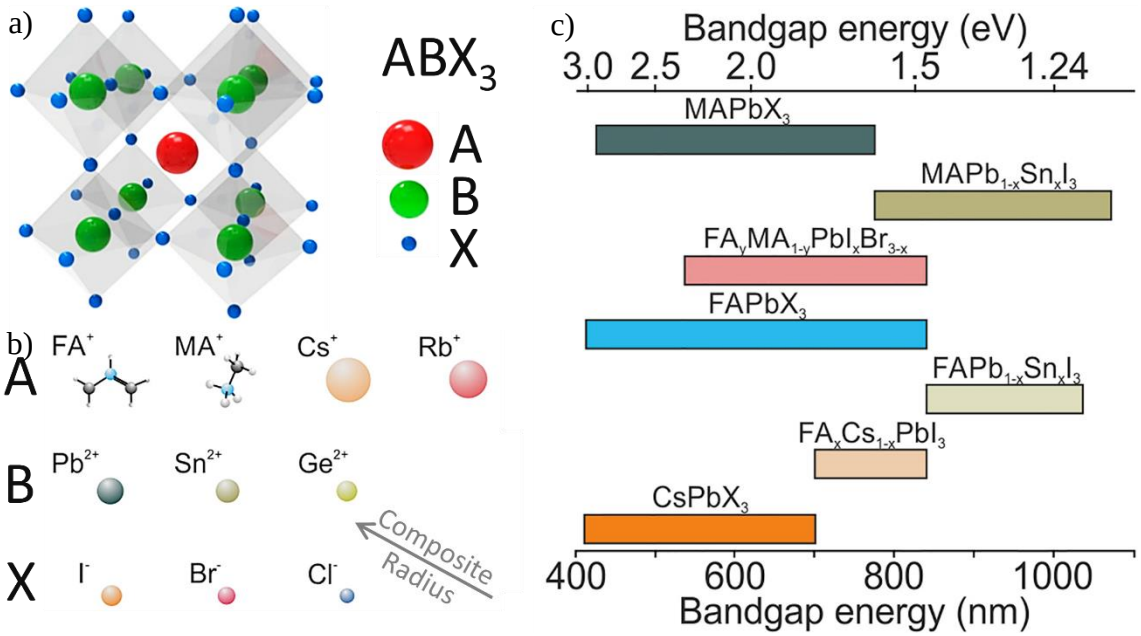

Figure 1.9. a) Schematic illustration of a perovskite (ABX_3) crystal structure. Adapted from ref. [69], Copyright 2021, MDPI Journals. b) Typical elements occupying the different positions in the structure. c) Bandgap energies that can be attained with the different combinations of elements in an ABX_3 perovskite strcucture. Adapted from ref. [70], Copyright 2017, Elsevier.

In 1839, Gustav Rose investigated calcium titanate ($CaTiO_3$) and employed the term “perovskite” for the first time in recognition of Lev Perovski.[71] However, the perovskites typically employed nowadays as absorber material have other compositions, as shown in **Figure 1.9**b.[70] In the hybrid-halide perovskite, the A-site is a monovalent organic cation, mainly $CH_3NH_3^+$ (methylammonium, MA^+) or $NH_2CH{=}NH_2^+$ (formamidinium, FA^+), but the use of monovalent alkali metals, primarily Caesium (Cs^+) and Rubidium (Rb^+), is also

investigated. The B-site is a divalent metal, the most studied has been Lead (Pb^{2+}) but, because of the concerns about its toxicity, Tin (Sn^{2+}) is gaining attention in the last few years. Another option for the B-site is Germanium (Ge^{2+}). The X-site are halogen elements such as Chloride (Cl^-), Bromide (Br^-) and Iodide (I^-). It is needed to consider that to design a stable perovskite material, the Goldschmidt tolerance factor and octahedral factor are the main criteria. While additional compounds could satisfy these relationships, there are further requirements for the resulting material, such as defect tolerance and exciton binding.[72-73]

As different compounds can be used in the three sites (A, B and X), or even combine different elements at the same site, with a wide variety of properties, such as for example their bandgap. **Figure 1.9**c shows the bandgap variation, from around 1.2 to 3 eV, for several perovskite compositions. The possibility to tune the bandgap of this material by only changing the elements makes perovskites particularly attractive for tandem applications, where a combination of materials that absorb different ranges of the solar spectrum is required.[70]

In addition to the tunable bandgap, perovskite exhibits excellent optoelectronic properties, such as high absorption coefficients, low exciton binding energies, good charge carrier mobility, long charge carrier diffusion lengths and defect tolerance.[74] These properties make this material very useful for developing devices other than solar cells, such as light-emitting diodes (LEDs), lasers, photodetectors, X-ray detectors, and field-effect transistors.

The wide, and continuously growing, variety of perovskites can be overwhelming when first studied, but fortunately, many of their optoelectronic properties are similar.[75] Methylammonium Lead Iodide ($MAPbI_3$) is probably the most investigated perovskite, due to its band gap (around 1.61 eV)[76] which is near the ideal for perovskite solar cells according to the Shockley-Queisser limit.[77] In addition, the synthesis of the material has shown to be relatively easy and cheap.[78-79] $MAPbI_3$ presents a high absorption coefficient ($\sim 10^5$ cm^{-1}) in the visible range,[80], which allows the absorption of this light with just a thin film (~300 nm).[81] The binding energy of this material at room temperature was determined to be between 2 to 60 meV, which is very low in comparison with the thermal energy at room temperature, which is around 26 meV. Consequently, this perovskite composition has a very high separation efficiency.[82] In addition to its excellent optical properties, perovskite has proven to be a mixed electronic-ionic conductor, being the Iodide (I^-) the dominant mobile ionic specie in $MAPbI_3$, with a diffusion coefficient of around 10^{-8} cm^2 s^{-1}.[83-84]

1.3.2. Device Configuration and Materials

The perovskite solar cell configurations can be separated into two groups: the standard (or regular) structure also called “n-i-p” and the inverted structure called “p-i-n”. Schemes of both configurations are shown respectively in **Figure 1.10**a and b. The difference between these two configurations is that the light is reaching the device from the electron selective contact (ESC) and the hole selective contact (HSC) for the n-i-p and p-i-n

configurations, respectively. In **Section 1.2** we have introduced the working principles of general photoconversion devices. In particular, we introduced the selective contacts and mention that ESCs are often n-type semiconductors, while HSCs are often p-type semiconductors. This is the origin of the designations "n-i-p" and "p-i-n", where the "i" refers to the perovskite as an intrinsic semiconductor, although the doping of perovskites is still under discussion.[85]

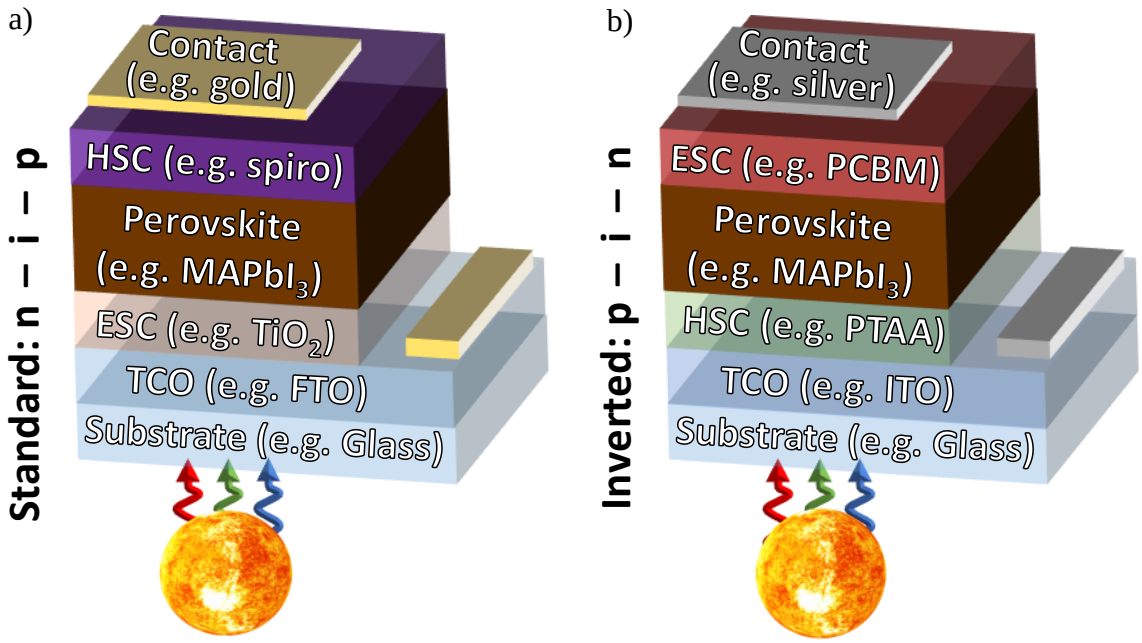

Figure 1.10. Schematic illustration of a) standard (n-i-p) and b) inverted (p-i-n) structures for perovskite solar cells, where ESC refers to electron selective contact, HSC to hole selective contact and TCO to transparent-conducting oxide.

Therefore, for the n-i-p configuration, the ESC has to be as transparent as possible, thus usually metal oxides such as TiO_2, SnO_2 or ZnO are employed. Whereas for the p-i-n configuration, fullerenes such as [6,6]-phenyl-C-61-butyric acid methyl ester (PCBM) are often used, which do not have to be transparent and may have other properties, such as hydrophobicity that can protect the perovskite.[86] For HSCs is the opposite, being N^2,N^2,$N^{2\prime}$,$N^{2\prime}$,N^7,N^7,$N^{7\prime}$,$N^{7\prime}$-octakis(4-methoxyphenyl)-9,9′-spirobi[9H-fluorene]-2,2′,7,7′-tetramine (spiro-OMeTAD) and Polytriarylamine (PTAA) the most common for n-i-p and p-i-n configuration, respectively. Thiophene-based poly(3-hexylthiophene-2,5-diyl) (P3HT) and poly(3,4-ethylenedioxythiophene)-poly(styrenesulfonate) (PEDOT:PSS) have also been widely studied and applied as HSCs alternatives for n-i-p and p-i-n configuration, respectivelly.[87]

On top of the HSC in the n-i-p configuration and the ESC in the p-i-n configuration, it is placed a good conductor to extract the separated holes and electrons, respectively. Typically gold or silver have been used for this purpose. Recently, carbon has also shown to successfully fulfil this role, which is very promising for its lower cost, among other

qualities.[88] However, these materials can not be directly used to extract the charges separated by the ESC in the n-i-p configuration and the HSC in the p-i-n configuration, as transparent conducting materials are needed. Transparent-conducting oxides (TCOs) such as indium tin oxide (ITO), fluorine-doped tin oxide (FTO) and, to a lesser extent, indium zinc oxide (IZO), are typically used for this function.[89] Independently of the structure, these TCOs are a thin film on top of a substrate, typically glass, for rigid (and more stable) configurations, or polymeric foils (PET, PEN) for flexible applications.[88]

1.3.3. Stability Issues

As discussed above perovskite solar cells have an enormous potential to be the next generation of photovoltaics. However, their widespread use is still limited, mainly due to their poor stability. **Figure 1.11** summarize the stability factors and the degradation mechanisms.[90]

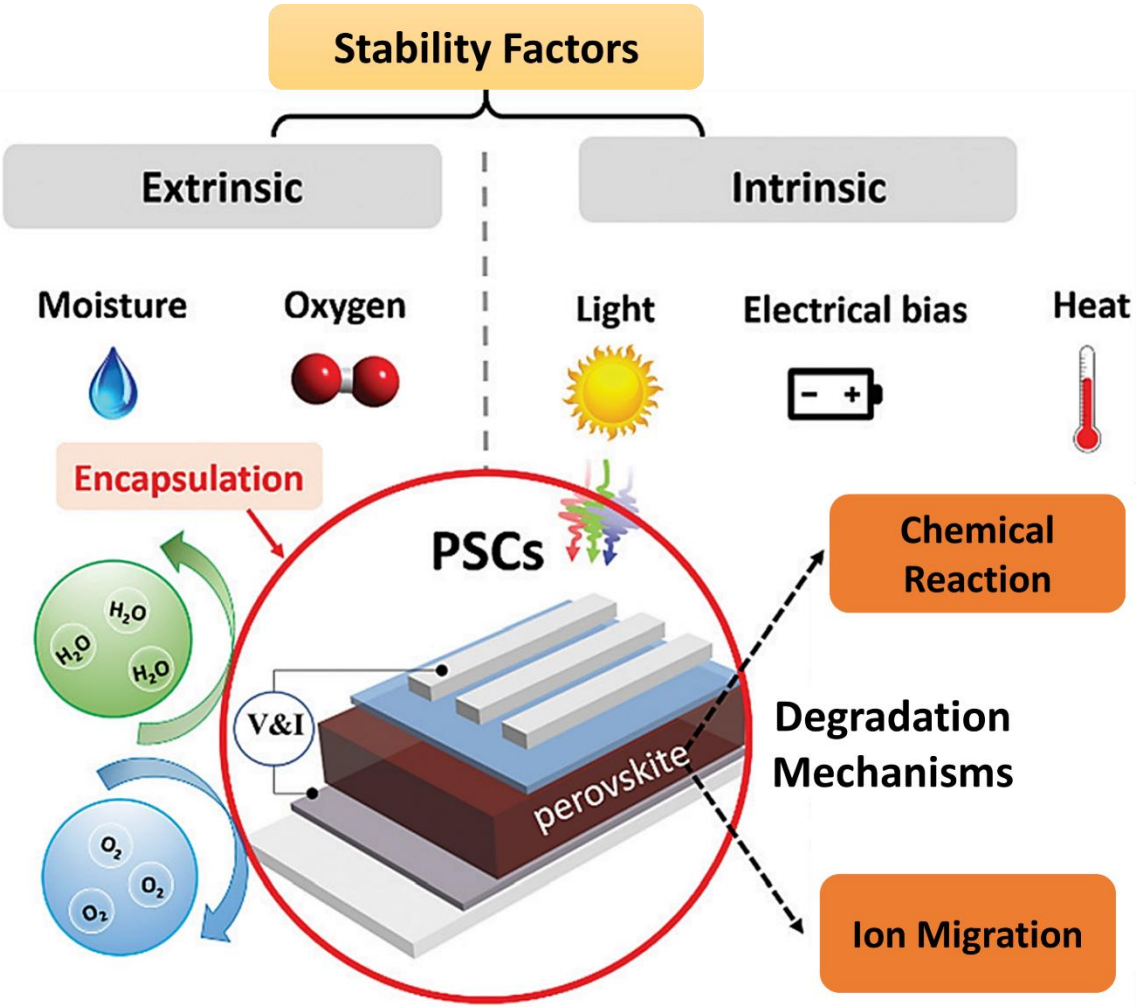

Figure 1.11. Illustration of the stability factors that can affect the perovskite solar cells (PSCs), differentiated as extrinsic and intrinsic, with the corresponding degradation mechanisms: chemical reactions and ion migration. Adapted from ref. [90], Copyright 2021, Royal Society of Chemistry.

The stability factors can be separated into two categories, the extrinsic and the intrinsic. Extrinsic factors are those that are not related to the functioning of PSCs, they are induced by the environmental conditions of the device. The most common extrinsic factors are moisture and oxygen. These factors can be, at least in theory, completely eliminated by correctly encapsulating the solar cells.[91] Conversely, intrinsic factors are inherent to the functioning of PSCs, and, although they could be reduced, they cannot be eliminated. Among these factors are the incident light to be absorbed, the electrical bias needed to generate the electrical power and the heat that is produced due to operational factors such as the electrical current.

These factors have the risk to accelerate the degradation of the perovskite. In this material, the degradation can be separated into two mechanisms. The most evident is the destruction of the perovskite by reacting chemically with other species. Probably the most harmful factor in this sense is the high levels of humidity, which proved to be able to generate a fast degradation.[92] It has also been shown that chemical degradation can occur with high levels of oxygen or even with species such as silver from the contacts.[93-94] In addition to the chemical degradation mechanism, which is suffered by all solar cells to a greater or lesser extent, PSCs have an additional degradation mechanism, associated with ionic migration. For this mechanism, the electric field is probably the most harmful factor, which can increase the migration of ions such as Iodine (I^-), or even MA.[95-97] Both degradation mechanisms are correlated, i.e. the chemical reaction of the perovskite can free ions that can migrate, and in turn, these ions can promote further chemical reactions. To successfully enhance the stability of PSCs is crucial a clear understanding of these mechanisms and their consequences in the operation of the device.

1.4. Photoelectrochemical Cells for Water Splitting Systems

In this section, we will introduce the other system investigated in this thesis, namely photoelectrochemical cells (PECs) for water splitting. We will start presenting the operation of PECs, including the basic concepts for water splitting, and the possible configurations of these devices. We will finish this section with a brief discussion of the possible absorber materials that may be used for these cells.

1.4.1. Photoelectrochemical Cells: Configuration and Operation

Water splitting is the chemical reaction where the water molecules (H_2O) are broken to generate oxygen (O_2) and hydrogen (H_2):

$$2H_2O \rightarrow O_2 + 2H_2 \tag{1.12}$$

Figure 1.12a shows an electrochemical water splitting cell, composed of an anodeand a cathode, in an electrolyte (water). As can be noted, the chemical reaction in Equation (1.12) is carried out through two half-reactions. One is the oxidation of water

$$2H_2O \rightarrow O_2 + 4H^+ + 4e^- \tag{1.13}$$

where the charge of the electrons resulting from the reaction is compensated with the holes provided by the anode. The other half-reaction is the reduction of the protons

$$2H^+ + 2e^- \rightarrow 2H_2 \tag{1.14}$$

where the electrons are provided by the cathode.

The complete water splitting reaction, Equation (1.12), theoretically requires a minimum voltage of 1.23 V, but in practice, a higher voltage is needed to improve the kinetics of the processes.[98-99] **Figure 1.12**a shows this reaction in an electrochemical water splitting cell, where the required voltage (or energy) is provided by an external voltage. This external voltage could be generated for example by a photovoltaic cell or fossil fuels, as discussed in **Subsection 1.1.2**.

Figure 1.12b and c show two photoelectrochemical cells (PECs) where the same reactions take place. The main difference with **Figure 1.12**a is that at least part of the energy required for the chemical reaction is provided by the light (e.g., the sun). The sun could provide all the energy needed to generate the complete water splitting reaction as occurs in the photosynthesis in the plants and some particulate photocatalysis (PC) as discussed in **Subsection 1.1.2**.[100] However, PECs generally employ a material to absorb part of this energy and the remaining is provided externally.[101]

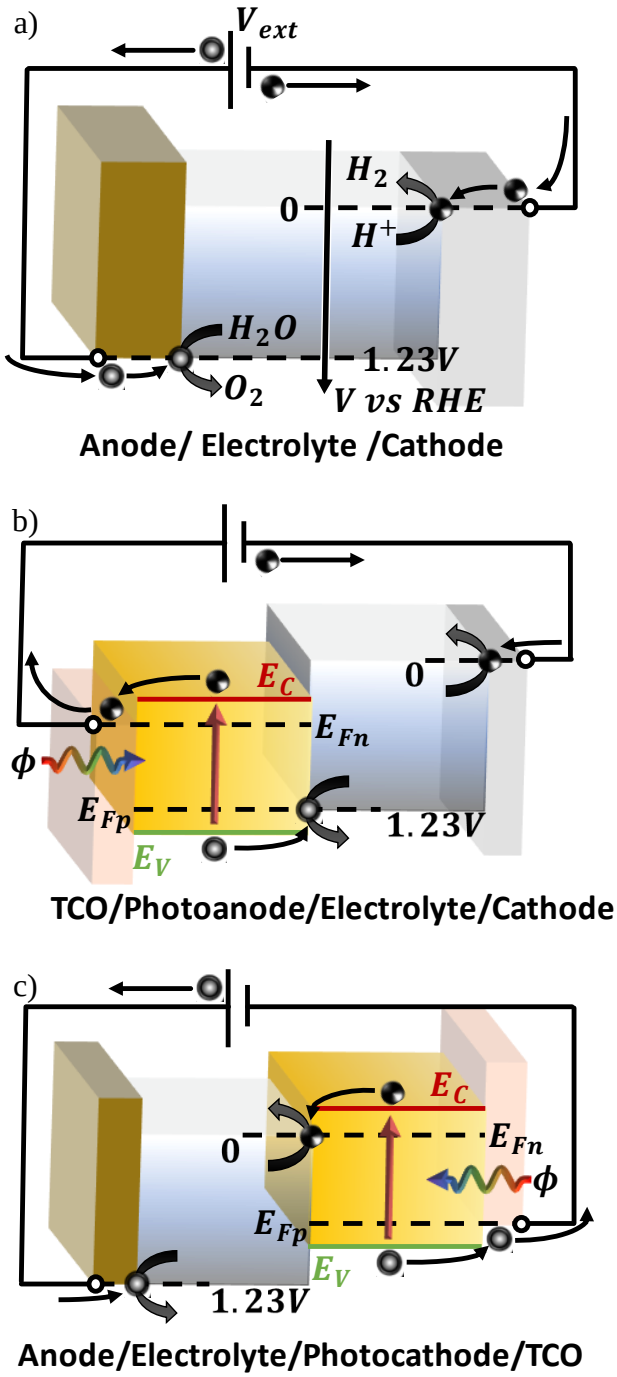

Figure 1.12. Schemes of water splitting in: a) an electrochemical cell composed of an anode and a cathode, in an electrolyte (water); b) a photoelectrochemical cell (PEC) composed of a photoanode, deposited on a transparent-conducting oxide (TCO), and a cathode, in an electrolyte (water); c) a PEC composed of an anode and a photocathode, deposited on a TCO, in an electrolyte (water). Both half-reactions of water splitting are depicted in energy and place. For the absorber semiconductors, are shown the conduction band (E_C), the valence band (E_V), the electron Fermi level (E_{Fn}) and the hole Fermi level (E_{Fp}).

On one hand, in **Figure 1.12**b the light is absorbed by the photoanode, which implies that the photogenerated holes are given to the electrolyte to generate the oxidation half-reaction in Equation (1.13). The photogenerated electrons are collected externally and injected into the cathode, through an electrical connection, to generate the reduction half-reaction in Equation (1.14). If extra energy is needed to complete the reaction, it may be provided by an external power source connected to the electrodes. On the other hand, in **Figure 1.12**c the light is absorbed by the photoanode, which will provide the photogenerated electrons to the electrolyte to make the reduction half-reaction in Equation (1.14). The photogenerated holes will be collected through the external electrical circuit and transported to the anode to generate the oxidation half-reaction in Equation (1.13).

In the PECs in **Figure 1.12**b and c, the light reaches from the collector side, which forces this collector to be as transparent as possible. As in the case of perovskite solar cells discussed in the previous section, usually transparent-conducting oxides (TCOs) such as fluorine-doped tin oxide (FTO) are used as collectors. However, if the light strikes the absorber material from the electrolyte side, the collector does not need to be transparent. Note that all the schemes in **Figure 1.12** are simplified models, more sophisticated models can consider additional features such as band-bending and charge transfer.[102] Finally, it is worth mentioning that the configurations in **Figure 1.12**b and c could be combined to generate a PEC with a photoanode and a photocathode.[103]

1.4.2. Metal Oxide Photoelectrodes

With the discussion in the previous subsection, the challenges faced by the materials to be a good photoelectrode can be guessed. First of all, as in any photoconversion device (including solar cells), the material has to be a good light absorber, which requires properties such as good photon absorption, high separation efficiency and good charge transport that allows their collection. The photoelectrodes also require a suitable band energy alignment with the redox energies of the reaction that is performed in the cell, as shown in **Figure 1.12**b and c. **Figure 1.13** shows the band energy of several semiconductors investigated as photoanodes (blue) and photocathodes (red). Note that the photoanodes have the valence band below the water oxidation energy, allowing the material to give the photogenerated holes to the electrolyte to generate this chemical reaction. By contrast, the conduction band of the photocathodes are above the water redox energy. But all these requirements are not enough, the photoelectrodes are submerged in the electrolyte, so stability under these conditions is necessary. With all these restrictions it is not surprising that there is still no photoelectrode for large-scale water splitting.

The current investigations could be separated into two categories: the search for new materials and the improvement of available materials. The second category can be approached by methods such as doping or changing the morphology. In any case, to improve the material it is necessary to identify its limitations, for which it is essential to understand the processes that occur during the operation of the device.

The first demonstration of a photoelectrochemical cell (PEC) for water splitting was reported in 1972 by Fujishima and Honda, where TiO_2 was employed as photoanode.[104]

As can be seen in **Figure 1.13** this material has a suitable band structure to be a good photoanode, but it has a bandgap wider than 3 eV, being able to absorb only ultra violet light. Since then, many photoanodes have been investigated, among which $BiVO_4$ and Fe_2O_3 have attracted a lot of attention lately. As can be noted in **Figure 1.13** these two materials have similar band structures, with a narrowed bandgap compared with TiO_2, allowing additional absorption of part of the visible spectrum. However, in both cases, their poor electronic properties limit their performance.[105] Many photocathodes have also been investigated, being the combination of absorbing materials an area of growing interest.[106]

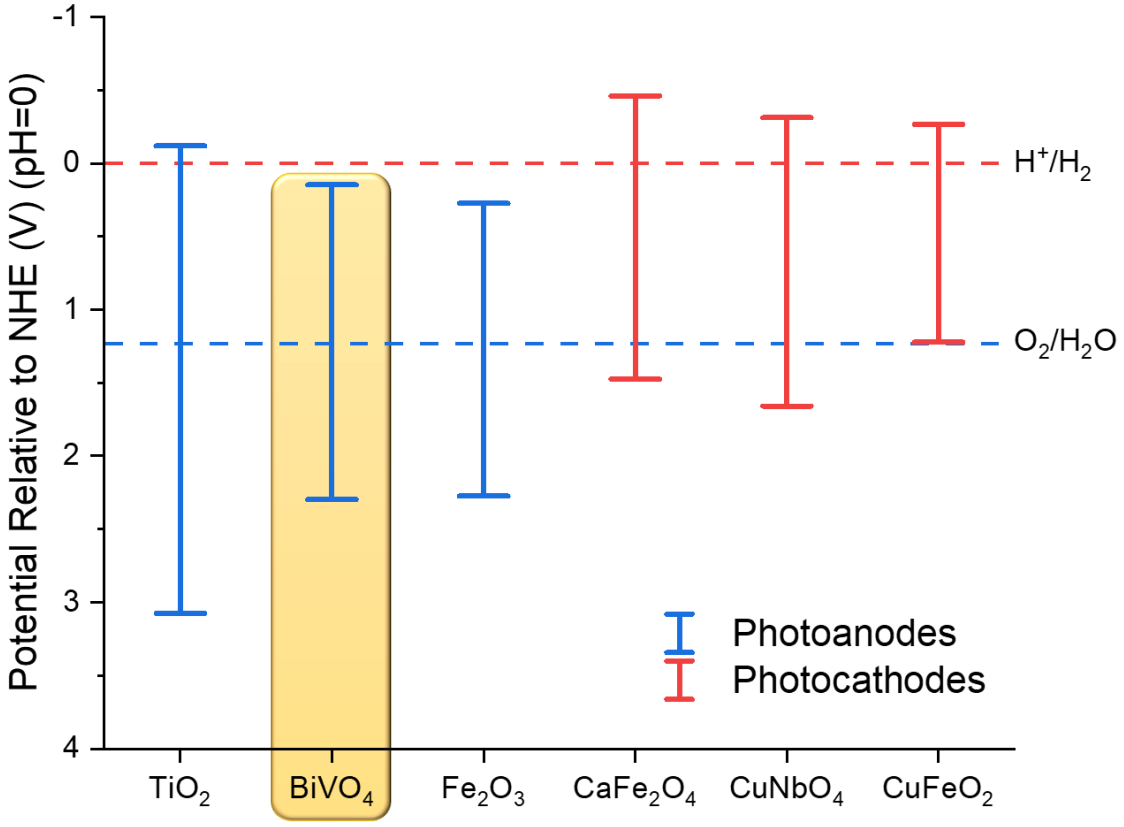

Figure 1.13. Band structure illustration of several semiconductors, where the lines represent the bandgap of the material so that the bottom and top of the bars correspond to the valence and conduction bands, respectively. The blue and red bar colours are distinguishing if the semiconductors are suitable for photoanodes or photocathodes, respectively. The potentials for water oxidation (O_2/H_20) and reduction (H^+/H_2) are respectively represented in blue and red dashed lines. Data obtained from ref.[107-108]

1.4.3. $BiVO_4$ as photoanode

This thesis is focused on the study of $BiVO_4$, as photoanode. Nevertheless, the results obtained are intended to be as general as possible so that they can be easily adapted to all types of electrochemical cells and even to other photoconversion devices.

Figure 1.14 shows the crystal structure of monoclinic scheelite $BiVO_4$ (ms-$BiVO_4$), which is mainly desired for photoelectrochemistry applications, other possibilities are tetragonal zircon-type and tetragonal scheelite structure.[109] Calcination of the tetragonal-zircon type at temperatures ranging from 400-500°C is the most common synthetic strategy for the preparation of ms-$BiVO_4$, as an irreversible transition occurs at these temperatures.[110] The monoclinic scheelite crystal structure, the V is tetrahedrally coordinated to oxygen with two different bond lengths and the Bi is coordinated to eight oxygens with four different bond lengths, as shown in **Figure 1.14**.[111]

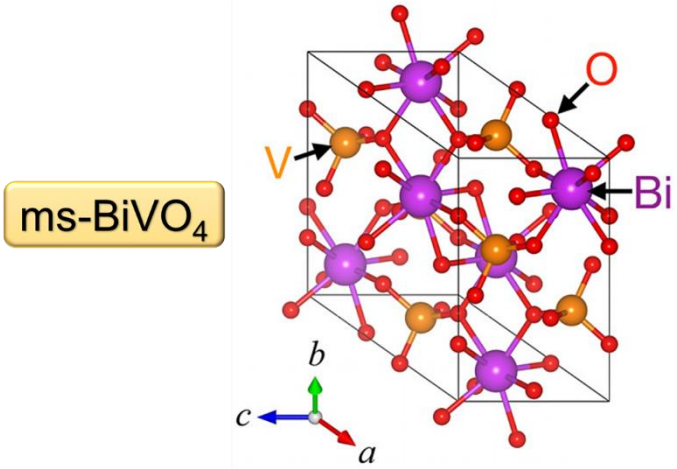

Figure 1.14. Crystal structure of monoclinic scheelite $BiVO_4$ (ms-$BiVO_4$). Adapted from ref. [112], Copyright 2021, AIP Publishing LLC.

Among the properties of this material, probably the most interesting are its low synthesis costs and its non-toxicity.[113] The bandgap of $BiVO_4$ has been reported around 2.4 eV, which results in a theoretical maximum photocurrent density of 7.5 mA cm^{-2}, implying a 9.2% solar to hydrogen efficiency (STH).[114] The stability of this material is continuously improving, with recent research having surpassed 100 hours of continuous stable operation.[115] As mentioned above, the main limitation of $BiVO_4$ seems to be its poor extraction of the photogenerated charge, which has been attributed to its electronic properties.[116-117] For this material, has been observed low electron mobility, of around 0.01 cm^2 V^{-1} s^{-1}.[118] In addition, a relatively short diffusion length, of about 70 nm, has been reported as a consequence of a characteristic recombination time of 40 ns.[117]

The limitations of the $BiVO_4$ as photoanode have been addressed mainly by three different approaches: by controlling the morphology and size of the material, by the deposition of co-catalyst layers or (nano)particles at the surface of the material, and by the doping of the material.[119] This thesis is focused on the study of Zircon-doped $BiVO_4$

(Zr:$BiVO_4$). The doping of $BiVO_4$ with Molybdenum (Mo) and Tungsten (W) has been extensively studied and shown to be effective in improving its performance as photoanode.[120-122] This improvement has been linked to doping at the V site, introducing an excess of electrons, which increases the n-type conductivity.[123] It has been shown that doping $BiVO_4$ with Zirconium (Zr) also leads to an improvement in its performance as photoanode.[124] This improvement has also been linked to the enhancement in n-type conductivity by introducing an excess of electrons, but in this case by doping at the Bi site. [125]

References

[1] T. L. Delworth, F. Zeng, G. A. Vecchi, X. Yang, L. Zhang, R. Zhang, *Nat. Geosci.* **2016**, 9, 509.

[2] A. A. Lacis, G. A. Schmidt, D. Rind, R. A. Ruedy, *Science* **2010**, 330, 356.

[3] P. Friedlingstein, M. W. Jones, M. O'Sullivan, R. M. Andrew, D. C. E. Bakker, J. Hauck, C. Le Quéré, G. P. Peters, W. Peters, J. Pongratz, S. Sitch, J. G. Canadell, P. Ciais, R. B. Jackson, S. R. Alin, P. Anthoni, N. R. Bates, M. Becker, N. Bellouin, L. Bopp, T. T. T. Chau, F. Chevallier, L. P. Chini, M. Cronin, K. I. Currie, B. Decharme, L. M. Djeutchouang, X. Dou, W. Evans, R. A. Feely, L. Feng, T. Gasser, D. Gilfillan, T. Gkritzalis, G. Grassi, L. Gregor, N. Gruber, Ö. Gürses, I. Harris, R. A. Houghton, G. C. Hurtt, Y. Iida, T. Ilyina, I. T. Luijkx, A. Jain, S. D. Jones, E. Kato, D. Kennedy, K. Klein Goldewijk, J. Knauer, J. I. Korsbakken, A. Körtzinger, P. Landschützer, S. K. Lauvset, N. Lefèvre, S. Lienert, J. Liu, G. Marland, P. C. McGuire, J. R. Melton, D. R. Munro, J. E. M. S. Nabel, S. I. Nakaoka, Y. Niwa, T. Ono, D. Pierrot, B. Poulter, G. Rehder, L. Resplandy, E. Robertson, C. Rödenbeck, T. M. Rosan, J. Schwinger, C. Schwingshackl, R. Séférian, A. J. Sutton, C. Sweeney, T. Tanhua, P. P. Tans, H. Tian, B. Tilbrook, F. Tubiello, G. R. van der Werf, N. Vuichard, C. Wada, R. Wanninkhof, A. J. Watson, D. Willis, A. J. Wiltshire, W. Yuan, C. Yue, X. Yue, S. Zaehle, J. Zeng, *Earth Syst. Sci. Data* **2022**, 14, 1917.

[4] J. Hilaire, J. C. Minx, M. W. Callaghan, J. Edmonds, G. Luderer, G. F. Nemet, J. Rogelj, M. del Mar Zamora, *Clim. Change* **2019**, 157, 189.

[5] J. Rogelj, M. Meinshausen, M. Schaeffer, R. Knutti, K. Riahi, *Environ. Res. Lett.* **2015**, 10, 075001.

[6] IEA (2021), *World Energy Outlook 2021*, IEA, Paris https://www.iea.org/reports/world-energy-outlook-2021. Accessed 21.08.2022.

[7] I. Gunnarsdottir, B. Davidsdottir, E. Worrell, S. Sigurgeirsdottir, *Renewable Sustainable Energy Rev.* **2021**, 141, 110770.

[8] I. Galarraga, M. González-Eguino, A. Markandya, *Handbook of Sustainable Energy*, Edward Elgar Publishing, **2011**.

[9] B. Martin, *Soc. Alternatives* **2007**, 26, 43.

[10] E. Bryngemark, *For. Policy Econ.* **2019**, 109, 102022.

[11] United Nations Economic Commission for Europe (UNECE), *Pathways to Sustainable Energy*, https://unece.org/sustainable-energy/pathways-sustainable-energy. Accessed 21.08.2022.

[12] World Energy Scenarios, *Composing energy futures to 2050*, https://www.worldenergy.org/publications/entry/world-energy-scenarios-composing-energy-futures-to-2050. Accessed 21.08.2022.

[13] T. R. Cook, D. K. Dogutan, S. Y. Reece, Y. Surendranath, T. S. Teets, D. G. Nocera, *Chem. Rev.* **2010**, 110, 6474.

[14] C. P. Morice, J. J. Kennedy, N. A. Rayner, P. D. Jones, *J. Geophys. Res.* **2012**, 117.

[15] BP, *Statistical Review of World Energy*, https://www.bp.com/en/global/corporate/energy-economics/statistical-review-of-world-energy.html. Accessed 21.08.2022.

[16] World Energy Assessment, *Energy and the Challenge of Sustainability*, https://www.undp.org/publications/world-energy-assessment-energy-and-challenge-sustainability. Accessed 28.06.2022.

[17] REN21, *Renewables Global Status Report*, https://www.ren21.net/reports/global-status-report/. Accessed 22.08.2022.

[18] China Solar Thermal Aliance (CSTA), *Blue Book of China's Concentrating Solar Power Industry 2021*, https://www.solarpaces.org/wp-content/uploads/Blue-Book-on-Chinas-CSP-Industry-2021.pdf. Accessed 16.02.2023.

[19] S. Pfenninger, P. Gauché, J. Lilliestam, K. Damerau, F. Wagner, A. Patt, *Nat. Clim. Change* **2014**, 4, 689.

[20] National Renewable Energy Laboratory (NREL), *Best Research-Cell Efficiency Chart*, https://www.nrel.gov/pv/assets/pdfs/best-research-cell-efficiencies.pdf. Accessed 17.04.2023.

[21] A. Luque, S. Hegedus, *Handbook of photovoltaic science and engineering*, John Wiley & Sons, **2011**.

[22] S. Rühle, *Sol. Energy* **2016**, 130, 139.

[23] N. Mufti, T. Amrillah, A. Taufiq, Sunaryono, Aripriharta, M. Diantoro, Zulhadjri, H. Nur, *Sol. Energy* **2020**, 207, 1146.

[24] R. Singh, *J. Nanophotonics* **2009**, 3, 032503.

[25] Fraunhofer Institute for Solar Energy Systems, *Photovoltaics Reportcite*, https://www.ise.fraunhofer.de/de/veroeffentlichungen/studien/photovoltaics-report.html. Accessed 29.08.2022.

[26] P.-J. Ribeyron, *Nat. Energy* **2017**, 2, 17067.

[27] A. Kojima, K. Teshima, Y. Shirai, T. Miyasaka, *J. Am. Chem. Soc.* **2009**, 131, 6050.

[28] N. L. Chang, A. W. Yi Ho-Baillie, P. A. Basore, T. L. Young, R. Evans, R. J. Egan, *Prog. Photovolt: Res. Appl.* **2017**, 25, 390.

[29] F. Hao, C. C. Stoumpos, R. P. H. Chang, M. G. Kanatzidis, *J. Am. Chem. Soc.* **2014**, 136, 8094.

[30] I. K. Popoola, M. A. Gondal, T. F. Qahtan, *Renewable Sustainable Energy Rev.* **2018**, 82, 3127.

[31] B. Li, B. Hou, G. A. J. Amaratunga, *InfoMat* **2021**, 3, 445.

[32] J. Sanchez-Diaz, R. S. Sánchez, S. Masi, M. Krecmarová, A. O. Alvarez, E. M. Barea, J. Rodriguez-Romero, V. S. Chirvony, J. F. Sánchez-Royo, J. P. Martinez-Pastor, I. Mora-Seró, *Joule* **2022**, 6, 861.

[33] Y. Rong, Y. Hu, A. Mei, H. Tan, M. I. Saidaminov, S. I. Seok, M. D. McGehee, E. H. Sargent, H. Han, *Science* **2018**, 361, eaat8235.

[34] J.-P. Correa-Baena, M. Saliba, T. Buonassisi, M. Grätzel, A. Abate, W. Tress, A. Hagfeldt, *Science* **2017**, 358, 739.

[35] N. S. Lewis, *Science* **2016**, 351, aad1920.

[36] J. H. Kim, D. Hansora, P. Sharma, J.-W. Jang, J. S. Lee, *Chem. Soc. Rev.* **2019**, 48, 1908.

[37] A. Körner, C. Tam, S. Bennett, J.-F. Gagné, International Energy Agency, *Technology roadmap-hydrogen and fuel cells*, https://www.aeh2.org/images/stories/PDF/DOCS_SECTOR/technologyroadmaphydrogenandfuelcells.pdf. Accessed 30.06.2023. 2015.

[38] Iberdrola, *Puertollano Green Hydrogen Plant*, https://www.iberdrola.com/about-us/lines-business/flagship-projects/puertollano-green-hydrogen-plant. Accessed 25.08.2022.

[39] Siemens Energy, *Green Hydrogen Project: clean fuel from solar power in Dubai*, https://www.siemens-energy.com/mea/en/company/megaprojects/dewa-green-hydrogen-project.html. Accessed 25.08.2022.

[40] B. A. Pinaud, J. D. Benck, L. C. Seitz, A. J. Forman, Z. Chen, T. G. Deutsch, B. D. James, K. N. Baum, G. N. Baum, S. Ardo, H. Wang, E. Miller, T. F. Jaramillo, *Energ. Environ. Sci.* **2013**, 6, 1983.

[41] A. C. Nielander, M. R. Shaner, K. M. Papadantonakis, S. A. Francis, N. S. Lewis, *Energ. Environ. Sci.* **2015**, 8, 16.

[42] Z. Chen, H. N. Dinh, E. L. Miller, *Photoelectrochemical Water Splitting: Standards, Experimental Methods, and Protocols*, Springer, **2013**.

[43] K. Sivula, *Advanced Device Architectures and Tandem Devices* in *Photoelectrochemical Solar Fuel Production: From Basic Principles to Advanced Devices*, (Eds: S. Giménez, J. Bisquert), Springer International Publishing, Cham **2016**.

[44] T. Hisatomi, J. Kubota, K. Domen, *Chem. Soc. Rev.* **2014**, 43, 7520.

[45] F. A. Chowdhury, M. L. Trudeau, H. Guo, Z. Mi, *Nat. Commun.* **2018**, 9, 1707.

[46] Q. Wang, T. Hisatomi, Q. Jia, H. Tokudome, M. Zhong, C. Wang, Z. Pan, T. Takata, M. Nakabayashi, N. Shibata, Y. Li, I. D. Sharp, A. Kudo, T. Yamada, K. Domen, *Nat. Mater.* **2016**, 15, 611.

[47] K. Maeda, K. Teramura, D. Lu, N. Saito, Y. Inoue, K. Domen, *Angew. Chem. Int. Ed.* **2006**, 45, 7806.

[48] P. Zhou, I. A. Navid, Y. Ma, Y. Xiao, P. Wang, Z. Ye, B. Zhou, K. Sun, Z. Mi, *Nature* **2023**, 613, 66.

[49] W.-H. Cheng, M. H. Richter, M. M. May, J. Ohlmann, D. Lackner, F. Dimroth, T. Hannappel, H. A. Atwater, H.-J. Lewerenz, *ACS Energy Lett.* **2018**, 3, 1795.

[50] R. Van de Krol, M. Grätzel, *Photoelectrochemical hydrogen production*, Vol. 90, Springer, **2012**.

[51] J. Bisquert, F. Fabregat-Santiago, *Impedance spectroscopy: a general introduction and application to dye-sensitized solar cells* in *Dye-sensitized solar cells*, EPFL Press, **2010**.

[52] J. A. Nelson, *The physics of solar cells*, World Scientific Publishing Company, **2003**.

[53] N. W. Ashcroft, N. D. Mermin, *Solid state physics*, Harcourt College Publishers, **2022**.

[54] *Introduction to Inorganic Chemistry*, Penn State University, LibreTexts, **2020**.

[55] S. M. Sze, Y. Li, K. K. Ng, *Physics of semiconductor devices*, John wiley & sons, **2021**.

[56] Y. Peter, M. Cardona, *Fundamentals of semiconductors: physics and materials properties*, Springer Science & Business Media, **2010**.

[57] J. Bisquert, *The Physics of Solar Energy Conversion*, CRC Press, **2020**.

[58] S. Giménez, J. Bisquert, *Photoelectrochemical solar fuel production: From basic principle to advanced devices*, Springer, **2016**.

[59] A. Einstein, *Annalen der Physik* **1905**, 322, 549.

[60] J. Bisquert, *The physics of solar cells: perovskites, organics, and photovoltaic fundamentals*, CRC press, Boca Raton **2017**.

[61] T. Kirchartz, J. Bisquert, I. Mora-Sero, G. Garcia-Belmonte, *PCCP* **2015**, 17, 4007.

[62] J. S. Manser, P. V. Kamat, *Nat. Photonics* **2014**, 8, 737.

[63] Y. Yamada, T. Nakamura, M. Endo, A. Wakamiya, Y. Kanemitsu, *J. Am. Chem. Soc.* **2014**, 136, 11610.

[64] K. Chen, A. J. Barker, F. L. C. Morgan, J. E. Halpert, J. M. Hodgkiss, *J. Phys. Chem. Lett.* **2015**, 6, 153.

[65] J. Song, M. J. Seo, T. H. Lee, Y.-R. Jo, J. Lee, T. L. Kim, S.-Y. Kim, S.-M. Kim, S. Y. Jeong, H. An, S. Kim, B. H. Lee, D. Lee, H. W. Jang, B.-J. Kim, S. Lee, *ACS Catal.* **2018**, 8, 5952.

[66] J. E. Parrott, *Sol. Energ. Mat. Sol. C.* **1993**, 30, 221.

[67] W. Shockley, W. T. Read, *Phys. Rev.* **1952**, 87, 835.

[68] R. N. Hall, *Phys. Rev.* **1952**, 87, 387.

[69] S. Rhee, K. An, K.-T. Kang, *Crystals* **2021**, 11, 39.

[70] M. Anaya, G. Lozano, M. E. Calvo, H. Míguez, *Joule* **2017**, 1, 769.

[71] E. A. Katz, *Helv. Chim. Acta* **2020**, 103, e2000061.

[72] M. Saliba, J.-P. Correa-Baena, M. Grätzel, A. Hagfeldt, A. Abate, *Angew. Chem. Int. Ed.* **2018**, 57, 2554.

[73] D. Yang, J. Lv, X. Zhao, Q. Xu, Y. Fu, Y. Zhan, A. Zunger, L. Zhang, *Chem. Mater.* **2017**, 29, 524.

[74] W.-J. Yin, T. Shi, Y. Yan, *Appl. Phys. Lett.* **2014**, 104, 063903.

[75] J. S. Manser, J. A. Christians, P. V. Kamat, *Chem. Rev.* **2016**, 116, 12956.

[76] K. Tvingstedt, O. Malinkiewicz, A. Baumann, C. Deibel, H. J. Snaith, V. Dyakonov, H. J. Bolink, *Sci. Rep.* **2014**, 4, 6071.

[77] W. Shockley, H. J. Queisser, *J. Appl. Phys.* **1961**, 32, 510.

[78] S. Luo, W. A. Daoud, *J. Mater. Chem. A* **2015**, 3, 8992.

[79] T.-B. Song, Q. Chen, H. Zhou, C. Jiang, H.-H. Wang, Y. Yang, Y. Liu, J. You, Y. Yang, *J. Mater. Chem. A* **2015**, 3, 9032.

[80] W.-J. Yin, T. Shi, Y. Yan, *Adv. Mater.* **2014**, 26, 4653.

[81] N.-G. Park, *Mater. Today* **2015**, 18, 65.

[82] K. Galkowski, A. Mitioglu, A. Miyata, P. Plochocka, O. Portugall, G. E. Eperon, J. T.-W. Wang, T. Stergiopoulos, S. D. Stranks, H. J. Snaith, R. J. Nicholas, *Energ. Environ. Sci.* **2016**, 9, 962.

[83] C. Li, A. Guerrero, S. Huettner, J. Bisquert, *Nat. Commun.* **2018**, 9, 5113.

[84] W. Peng, C. Aranda, O. M. Bakr, G. Garcia-Belmonte, J. Bisquert, A. Guerrero, *ACS Energy Lett.* **2018**, 3, 1477.

[85] L. A. Frolova, N. N. Dremova, P. A. Troshin, *Chem. Commun.* **2015**, 51, 14917.

[86] S. Sun, T. Buonassisi, J.-P. Correa-Baena, *Adv. Mater.* **2018**, 5, 1800408.

[87] B. Roose, Q. Wang, A. Abate, *Advanced Energy Materials* **2019**, 9, 1803140.

[88] V. Babu, R. Fuentes Pineda, T. Ahmad, A. O. Alvarez, L. A. Castriotta, A. Di Carlo, F. Fabregat-Santiago, K. Wojciechowski, *ACS Appl. Energy Mater.* **2020**, 3, 5126.

[89] Y.-H. Chiang, C.-K. Shih, A.-S. Sie, M.-H. Li, C.-C. Peng, P.-S. Shen, Y.-P. Wang, T.-F. Guo, P. Chen, *J. Mater. Chem. A* **2017**, 5, 25485.

[90] Y. Cheng, L. Ding, *Energ. Environ. Sci.* **2021**, 14, 3233.

[91] C. A. Aranda, L. Caliò, M. Salado, *Crystals* **2021**, 11, 519.

[92] C. Aranda, A. Guerrero, J. Bisquert, *ChemPhysChem* **2019**, 20, 2587.

[93] G. Niu, X. Guo, L. Wang, *J. Mater. Chem. A* **2015**, 3, 8970.

[94] Y. Kato, L. K. Ono, M. V. Lee, S. Wang, S. R. Raga, Y. Qi, *Adv. Mater.* **2015**, 2, 1500195.

[95] A. Guerrero, J. You, C. Aranda, Y. S. Kang, G. Garcia-Belmonte, H. Zhou, J. Bisquert, Y. Yang, *ACS Nano* **2016**, 10, 218.

[96] J. Carrillo, A. Guerrero, S. Rahimnejad, O. Almora, I. Zarazua, E. Mas-Marza, J. Bisquert, G. Garcia-Belmonte, *Advanced Energy Materials* **2016**, 6, 1502246.

[97] C. C. Boyd, R. Cheacharoen, K. A. Bush, R. Prasanna, T. Leijtens, M. D. McGehee, *ACS Energy Lett.* **2018**, 3, 1772.

[98] X. Li, J. Yu, J. Jia, A. Wang, L. Zhao, T. Xiong, H. Liu, W. Zhou, *Nano Energy* **2019**, 62, 127.

[99] X. Li, L. Zhao, J. Yu, X. Liu, X. Zhang, H. Liu, W. Zhou, *Nano Micro Lett.* **2020**, 12, 131.

[100] J. Barber, *Nat. Plants* **2017**, 3, 17041.

[101] N. Nandal, S. L. Jain, *Coord. Chem. Rev.* **2022**, 451, 214271.

[102] L. Bertoluzzi, P. Lopez-Varo, J. A. Jiménez Tejada, J. Bisquert, *J. Mater. Chem. A* **2016**, 4, 2873.

[103] A. J. Nozik, *Appl. Phys. Lett.* **1977**, 30, 567.

[104] A. Fujishima, K. Honda, *Nature* **1972**, 238, 37.

[105] K. Sivula, *J. Phys. Chem. Lett.* **2013**, 4, 1624.

[106] J. Brillet, J.-H. Yum, M. Cornuz, T. Hisatomi, R. Solarska, J. Augustynski, M. Graetzel, K. Sivula, *Nat. Photonics* **2012**, 6, 824.

[107] K. Sivula, R. van de Krol, *Nat. Rev. Mater.* **2016**, 1, 15010.

[108] C. A. Mesa, L. Francàs, K. R. Yang, P. Garrido-Barros, E. Pastor, Y. Ma, A. Kafizas, T. E. Rosser, M. T. Mayer, E. Reisner, M. Grätzel, V. S. Batista, J. R. Durrant, *Nat. Chem.* **2020**, 12, 82.

[109] C. Martinez Suarez, S. Hernández, N. Russo, *Appl. Catal., A* **2015**, 504, 158.

[110] K. R. Tolod, S. Hernández, M. Castellino, F. A. Deorsola, E. Davarpanah, N. Russo, *Int. J. Hydrogen Energy* **2020**, 45, 605.

[111] X. Liang, P. Wang, F. Tong, X. Liu, C. Wang, M. Wang, Q. Zhang, Z. Wang, Y. Liu, Z. Zheng, Y. Dai, B. Huang, *Adv. Funct. Mater.* **2021**, 31, 2008656.

[112] M. Choi, *Appl. Phys. Lett.* **2021**, 118, 161901.

[113] M. Tayebi, B.-K. Lee, *Renewable Sustainable Energy Rev.* **2019**, 111, 332.

[114] Y. Pihosh, I. Turkevych, K. Mawatari, J. Uemura, Y. Kazoe, S. Kosar, K. Makita, T. Sugaya, T. Matsui, D. Fujita, M. Tosa, M. Kondo, T. Kitamori, *Sci. Rep.* **2015**, 5, 11141.

[115] R.-T. Gao, L. Wu, S. Liu, K. Hu, X. Liu, J. Zhang, L. Wang, *J. Mater. Chem. A* **2021**, 9, 6298.

[116] C. Zachäus, F. F. Abdi, L. M. Peter, R. van de Krol, *Chem. Sci.* **2017**, 8, 3712.

[117] F. F. Abdi, T. J. Savenije, M. M. May, B. Dam, R. van de Krol, *J. Phys. Chem. Lett.* **2013**, 4, 2752.

[118] Z. Zhao, Z. Li, Z. Zou, *PCCP* **2011**, 13, 4746.

[119] D. Cárdenas Morcoso, *Advanced semiconductors for photo-electrocatalytic solar fuel production*, Universitat Jaume I, **2020**.

[120] H. S. Park, K. E. Kweon, H. Ye, E. Paek, G. S. Hwang, A. J. Bard, *J. Phys. Chem. C* **2011**, 115, 17870.

[121] H. Ye, H. S. Park, A. J. Bard, *J. Phys. Chem. C* **2011**, 115, 12464.

[122] S. P. Berglund, A. J. E. Rettie, S. Hoang, C. B. Mullins, *PCCP* **2012**, 14, 7065.

[123] I. Grigioni, K. G. Stamplecoskie, E. Selli, P. V. Kamat, *J. Phys. Chem. C* **2015**, 119, 20792.

[124] S. Ikeda, T. Kawaguchi, Y. Higuchi, N. Kawasaki, T. Harada, M. Remeika, M. M. Islam, T. Sakurai, *Front. Chem.* **2018**, 6.

[125] W.-J. Yin, S.-H. Wei, M. M. Al-Jassim, J. Turner, Y. Yan, *Physical Review B* **2011**, 83, 155102.

CHAPTER 2

Characterization and Modelling

With the general introduction of the previous chapter, we hope to have made clear how essential it is the proper optoelectronic characterization of photoconversion devices, including solar cells and photoelectrochemical cells. In this chapter, we will discuss the toolkit used in this thesis to characterize and model the working processes of such devices. We will discuss the primary characterisation technique, i.e. current-voltage characteristic, where the hysteresis behaviour will be addressed. Then, the modulated techniques will be introduced, beginning with impedance spectroscopy (IS) and followed by intensity-modulated photocurrent (IMPS) and photovoltage (IMVS) spectroscopies.

2.1. Device Models

2.1.1. Diode Equation

In **Section 1.2** we have introduced the working principles of photoconversion devices, discussing the operation conditions of such devices in **Subsection 1.2.2**. In particular, we have highlighted the need for selective contacts in the device to generate an asymmetry that allows the proper extraction of the photogenerated charges. In this section, we will discuss the relationship between the current and the voltage in these devices. A more detailed explanation can be found in textbooks, such as the main references to the physics of these devices.[1-4]

For photoconversion devices, the simplest description of the relationship between the injected current (j_{inj}) and the applied voltage (V_{app}) is the ideal diode law, described by the Shockley equation.[5] When no light is reaching the device,

$$j_{inj}(V_{app}, \phi = 0) = j_0\left(e^{qV_{app}/k_BT} - 1\right) \tag{2.1}$$

where k_B is Boltzmann's constant, T is the temperature and j_0 is the reverse saturation current, which is independent of V_{app} and the incident light (ϕ). **Figure 2.1** shows the resulting curve in grey for $j_0 = 10^{-14}\ mA\ cm^{-2}$ and $T = 300\ K$ which results in $k_BT = 25.9\ meV$. At this point, it is worth highlighting that the current sign is a convention: with j_{inj} we are employing a convention where the sign is positive when the charges are injected in the device where they recombine (**Figure 1.8**d) and negative when the photogenerated charges are extracted from the device (**Figure 1.8**c). As commented in **Subsection 1.2.3**, the opposite convention is also common and, in this thesis, we will refer to it as the extracted current: $j_{ext} = -j_{inj}$. In the rest of the thesis we will employ j_{inj} as this is the current that it is measured when an external voltage (V_{app}) is applied.

Returning to the definitions in **Section 1.2** (Equation (1.7)), when light is reaching the device (ϕ), the injected current can be written as

$$j_{inj}(V_{app}, \phi) = j_{rec}(V_{app}) - j_{ph}(\phi) \quad (2.2)$$

Figure 2.1 shows the corresponding light *j-V curve* for $j_{ph} = 23\ mA\ cm^{-2}$. By comparing this equation with Equation (2.1) we have the recombination current as

$$j_{rec}(V_{app}) = j_0 e^{qV_{app}/k_B T} \quad (2.3)$$

and photogeneration current (see Equation (1.4)) as

$$j_{ph}(\phi) = j_0 + \eta_{ph} q\phi \approx \eta_{ph} q\phi \quad (2.4)$$

where j_0 is negligible compared to the free charges generated by the incident light in the typical working conditions of a photoconversion device (around 1 sunlight). **Figure 2.1** shows that in dark conditions and reverse bias j_0 can be extracted, however, this current is generally several orders of magnitude lower than the current extracted at the same voltages under illumination.

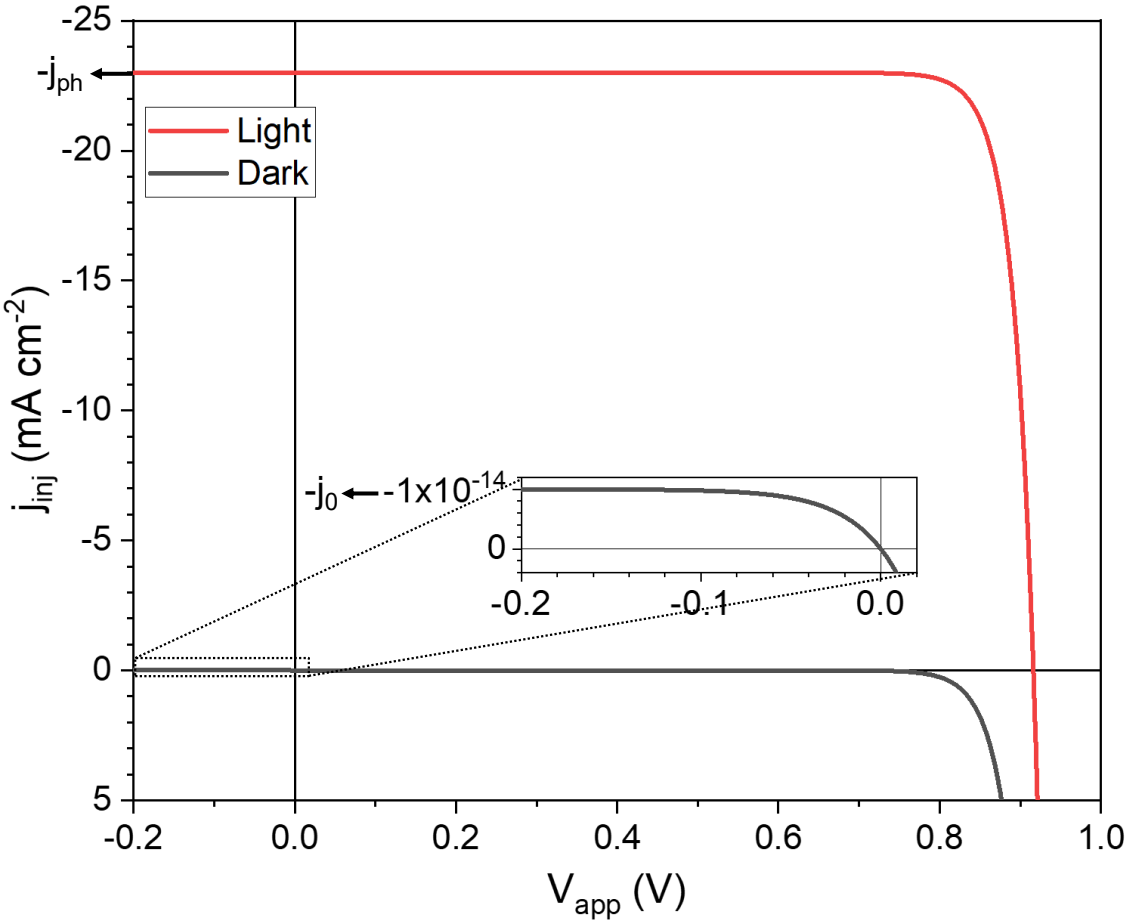

Figure 2.1 Characteristic *j-V* curve, given by the injected current density (j_{inj}) as a function of the applied voltage (V_{app}) for a photoconvertion device, in the dark condition given by the Shockley ideal diode equation, Equation (2.1), and under illumination, Equation (2.2), where j_0 is the reverse saturation current. The parameters where defined as $j_0 = 10^{-14}\ mA\ cm^{-2}$, $j_{ph} = 23\ mA\ cm^{-2}$ and $T = 300\ K$ which results in $k_B T = 25.9\ meV$

Many factors can separate the experimental external current-voltage curve (*j*-*V* curve) of a photoconversion device from the theoretical value, given by Equation (2.1). Based on what we have discussed so far, probably the most evident limitation is the description of the recombination current with a single equation (Equation (2.3)) since we have seen that there are several competing recombination processes (**Figure 1.7**c). To take into account this processes the recombination current in Equation (2.3) is modified by

$$j_{rec}(V_{app}) = j_0 e^{qV_{app}/mk_BT} \tag{2.5}$$

where m is the ideality factor. This parameter is usually between 1 and 2, depending on the dominant recombination process, which may in turn depend on the applied voltage.

2.1.2. Equivalent Circuit

In this section, we will begin the discussion of modelling photoconversion devices with an equivalent circuit (EC). This approach has proven to be especially useful for the analysis of the impedance spectroscopy (IS) responses, as we will discuss in **Subsection 2.3.1**. In this thesis, we will exploit this modelling tool, taking it beyond IS, i.e. employing it also to analyse the responses of light modulated techniques (IMPS and IMVS), as will be discussed in **Section 3.42.3**.

2.1.2.1. Ideal Diode

Figure 2.2 shows the equivalent circuits corresponding to the diode models discussed in the previous subsection. **Figure 2.2**a shows the diode element together with the injected current (j_{inj}) and the applied potential (V_{app}). The diode element is an arrow, pointing in the preferential direction of the current flow, followed by a line, symbolising the obstruction of the current flow in the opposite direction.

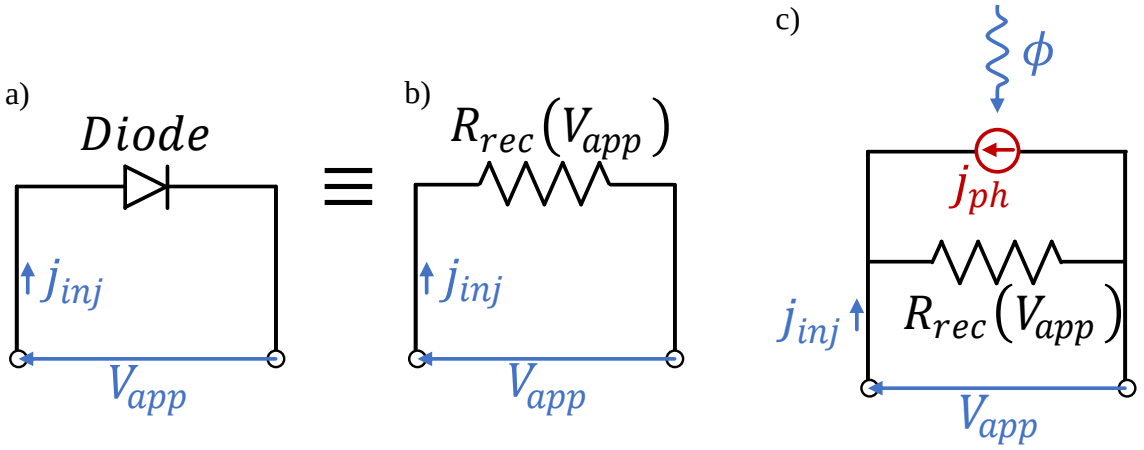

Figure 2.2 a) Equivalent circuits for the diode in the dark, where the injected current (j_{inj}) depends on the applied voltage (V_{app}) through Equation (2.1). b) This equation is equivalent to a recombination resistance (R_{rec}) that depends on the V_{app}, given by Equation (2.8). c) Under an incident light (ϕ), the photodiode is represented by R_{rec} and a photogeneration current source (j_{ph}), described by Equation (2.2). The blue color indicates the variables that can be directly measured and in red is j_{ph} to enphasize that this variable can not be directly measured, unless R_{rec} is very large.

The resistance of the whole device, also known as total resistance or direct current (DC) resistance, is defined as

$$R_{DC}(V_{app}) = \left(\frac{dj_{inj}}{dV_{app}}\right)^{-1} \tag{2.6}$$

which corresponds to the slope of the *j-V* curve, as shown in grey in **Figure 2.3**. Substituting Equation (2.2), the simplest case, into Equation (2.6) is equivalent to substitute j_{inj} for j_{rec} (because j_{ph} do not depend on V_{app}), wich by definition is the recombination resistance

$$R_{rec}(V_{app}) = \left(\frac{dj_{rec}}{dV_{app}}\right)^{-1} \tag{2.7}$$

Then, in this case $R_{DC} = R_{rec}$, which can be calculated from Equation (2.5) as

$$R_{rec}(V_{app}) = R_{rec0}e^{-qV_{app}/mk_BT} \tag{2.8}$$

with

$$R_{rec0} = \frac{mk_BT}{j_0 q} \tag{2.9}$$

Therefore, in practice, the diode can be considered a resistance with an exponential dependence on the applied voltage, as shown in **Figure 2.2**b. Finally, **Figure 2.2**c takes into account the photogenerated current (j_{ph}) produced when light reaches the device, appearing in parallel in the EC as it is a term added in Equation (2.2). Technically, **Figure 2.2**c is also the appropriate equivalent circuit for the dark condition, where j_{ph} is reduced to j_0, which is negligible in the vast majority of working conditions. This R_{rec} is, therefore, an inherent resistance of photoconversion devices, present in all of them.

2.1.2.1. Series and Shunt Resistances

In practice, photoconversion devices present additional limitations. The two main parasitic effects that are observed in such devices can be modelled in the EC as series resistance (R_S) and shunt resistance (R_{sh}), see **Figure 2.3**a. Considering these resistances the diode equation becomes

$$j_{inj} = j_0 e^{\frac{qV_{int}}{mk_BT}} + \frac{V_{int}}{R_{sh}} - j_{ph} \tag{2.10}$$

Where the internal voltage is given by

$$V_{int} = V_{app} - j_{inj}R_S \tag{2.11}$$

From this equation, it is clear that the effect of the series resistance (R_S) is the shift of the applied voltage (V_{app}) with respect to the internal voltage (V_{int}), as can be seen in **Figure 2.3**b. This displacement is proportional to R_S but also to the j_{inj}, so the V_{OC} is not modified by the series resistance, but the shape of the *j-V* curve may be strongly modified. R_S represents the sum of all the limitations to the flow of the injected (or extracted) current, such as finite conductivity at the selective contacts and charge transfer barriers at the interfaces, among others. The optimum device should reduce this resistance as much as possible.

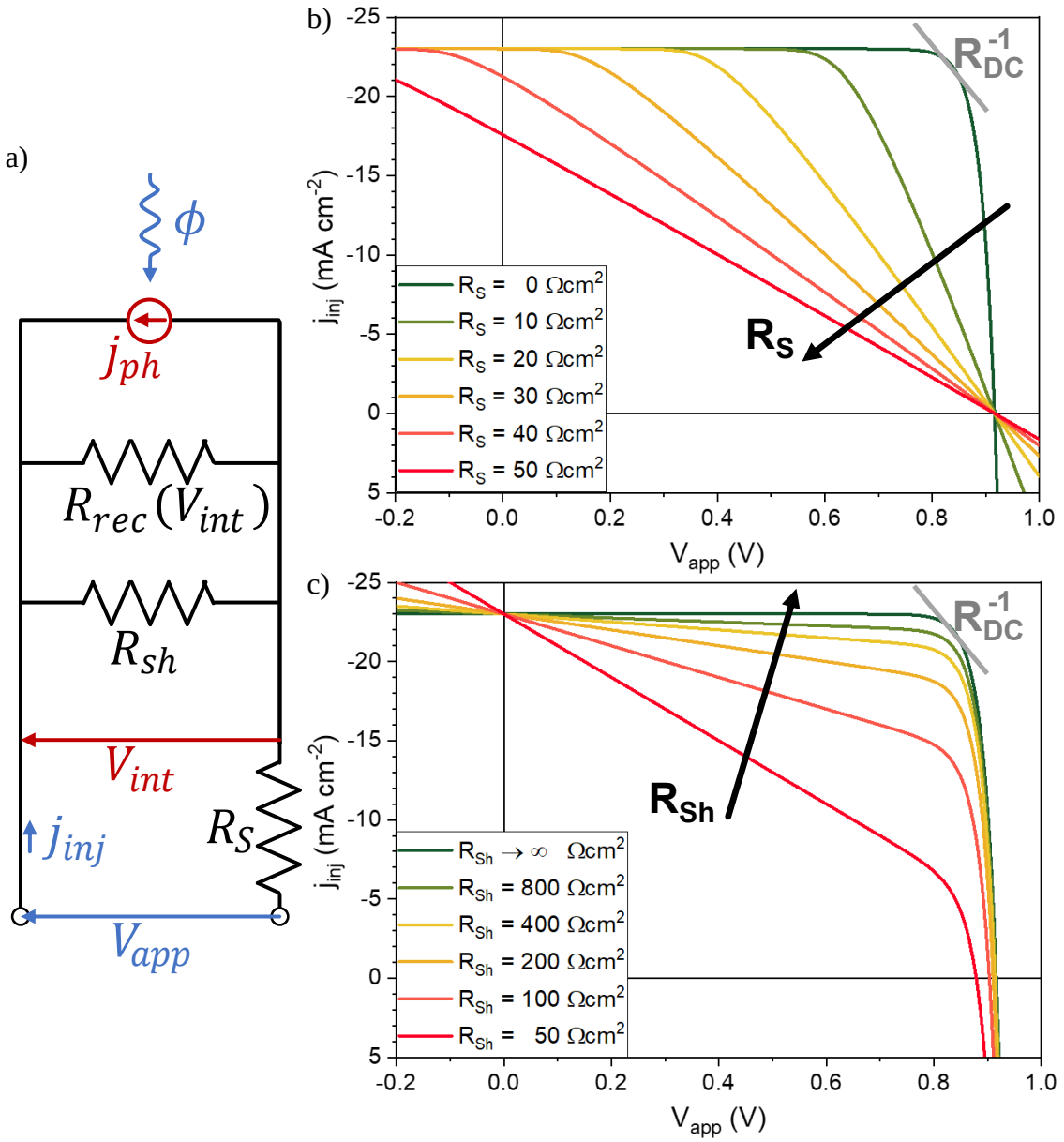

Figure 2.3 a) Equivalent circuit for a photoconversion device with shunt resistance (R_{sh}) and series resisntance (R_S), where R_{rec} and R_{DC} is the recombination and DC resistances, respectively, depending on the applied voltage (V_{app}), j_{inj} is the injected current, ϕ is the incident light and j_{ph} is the photogeneration current. The blue and red colours symbolise respectively the variables that can and cannot be directly measured. j-V curves for b) different R_S considering $R_{sh} \to \infty$ and c) different R_{sh} considering $R_S = 0$. The parameters where defined as $j_0 = 10^{-14}\ mA\ cm^{-2}$, $j_{ph} = 23\ mA\ cm^{-2}$ and $T = 300\ K$ which results in $k_B T = 25.9\ meV$.

Contrarily, the parallel or shunt resistance accounts for a leakage of current, which in practice results in an extra pathway for the charges to recombine, so in an optimum device this resistance should be as large as possible. Therefore, when this resistance is present, appears in parallel to R_{rec} in the EC (see **Figure 2.3**), and the total recombination resistance is given by

$$R_{recT} = \left(\frac{1}{R_{rec}} + \frac{1}{R_{sh}}\right)^{-1} \tag{2.12}$$

Unlike R_{rec}, R_{sh} is in general considered independent of V_{app}. If this is the case, R_{sh} will dominate R_{recT} at low enough voltages, where R_{rec} tends to infinity, as can be seen in **Figure 2.3**c. On the other hand, close to V_{OC}, R_{recT} will be dominated by R_{rec}, which tends to zero, however the values of V_{OC} can be considerably reduced due to the presence of R_{sh}.

2.1.2.1. Time-Dependent EC: Capacitor and Inductor

So far we have only considered the *j-V* curve under steady-state, defined as "A characteristic of a condition, such as value, rate, periodicity, or amplitude, exhibiting only negligible change over an arbitrarily long period of time.".[6] In practice, this steady-state *j-V* curve could be obtained by measuring for each V_{app} the corresponding j_{ext} after waiting enough time for it to stabilise. In this state, the photoconvertion device processes can be modelled with an equivalent circuit composed only of resistances, as in **Figure 2.3**a. But the operation of photoconversion devices involves processes that depend on time. Then, to consider the time dependence of the processes, additional elements such as capacitors and inductors have to be incorporated into the equivalent circuit model.

The capacitor is the most common element employed in the equivalent circuits to model time-dependent processes. A capacitor is a device that can store electrical charge, so any process within photoconversion devices that involves charge accumulation can in principle be modelled into the equivalent circuit with a capacitor.

The capacitance per unit area of a capacitor is defined by

$$C = \frac{\mathbb{Q}}{V_C} \tag{2.13}$$

where $\mathbb{Q}$ is the charge per unit area stored in the capacitor in steady-state condition under a certain voltage (V_C).

Figure 2.4a shows a simple equivalent circuit with a capacitor (C) in series with a resistance (R). The differential equation describing the extracted current is

$$j_{inj}(t) = \frac{d\mathbb{Q}}{dt} = C\frac{dV_C}{dt} = \frac{V_{app}(t) - V_C(t)}{R} = \frac{1}{R}\left[V_{app}(t) - \frac{\mathbb{Q}(t)}{C}\right] \tag{2.14}$$

If we consider that the applied voltage is modified with a scan-rate (s), then

$$V_{app}(t) = V_0 + s\,t \tag{2.15}$$

Where V_0 is the initial voltage. Considering also that the system starts from the equilibrium condition, i.e.

$$\mathbb{Q}(t = 0) = C\,V_0 \tag{2.16}$$

Then, the solution of Equation (2.14) is

$$j_{inj}(t) = sC\left[1 - e^{-t/\tau_C}\right] \tag{2.17}$$

where

$$\tau_C = RC \tag{2.18}$$

Figure 2.4b shows these solutions for $V_0 = 0$ with scan-rates from 0 to $10\,V/s$ ("Forward", dashed lines) and also the solutions for $V_0 = 1\,V$ with the same scan-rates but negative ("Reverse", solid lines). The resistance and capacitance were constant in all the simulations with values $R = 10\,\Omega\,cm^2$ and $C = 1\,m\text{F}\,cm^{-2}$. The limit case of $s \to 0$ corresponds to the stady-state condition, so it is reasonable that the Foward and Reverse coincide in that limit. In this condition, there is no extracted current for any applied voltage, after the capacitor is charged or discharged fulfilling Equation (2.13) it is equivalent to an open-circuit. But when the scan-rate is increased negative and positive currents appear in the Forward and Reverse scan, as a result of the continuous charging and discharging of the capacitor, respectively.

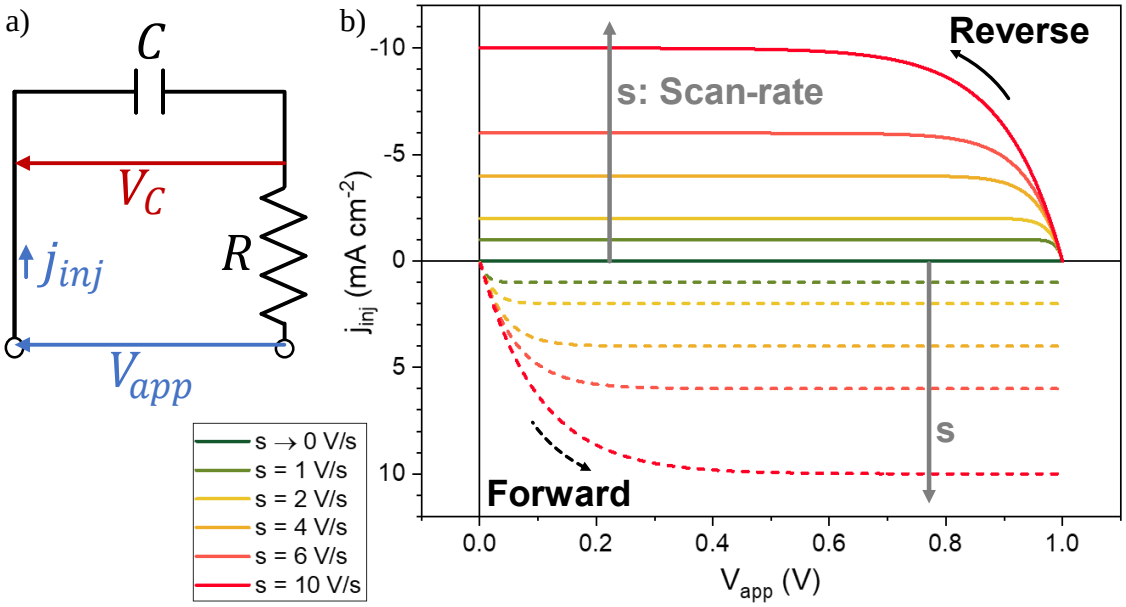

Figure 2.4 a) Simple equivalent circuit composed of a resistance (R) in series with a capacitor (C), where V_C is the corresponding voltage drop, the red colour indicates that it is a variable that can not be directly measured, whereas the blue variables can be directly measured: applied voltage (V_{app}), and the extracted current (j_{ext}). b) Simulations of the j_{inj} as a function of V_{app} for the equivalent circuit in a), starting from an equilibrium condition, Forward and Reverse correspond to positive and negative scan-rates (s), respectively. The resistance and capacitance were constant in all the simulations with values $R = 10\,\Omega\,cm^2$ and $C = 1\,m\text{F}\,cm^{-2}$.

The inductor is an element employed to model another type of time-dependent process, far less common. The voltage drop in the inductor is

$$V_L = L\frac{dj_{inj}}{dt} \tag{2.19}$$

Where L is the inductance. The flow of current (j_{inj}) in any material generates a magnetic flux (Φ_B), the inductance of such material is then defined by

$$L = \frac{\Phi_B}{j_{inj}} \tag{2.20}$$

In general, Φ_B is negligible in photoconversion devices. Sometimes long and tangled cables, employed to connect externally the device, generate an appreciable inductance, but this is not of great concern and usually can be easily reduced.

In photoconversion devices such as perovskite solar cells, the inductor has been employed to model processes that are not related to magnetic flux, this will be discussed in detail in **CHAPTER 4**.[7-8] The inductor is a suitable element to model those processes because of the relationship between the voltage and current with time.

Figure 2.5a shows a simple equivalent circuit with an inductor (L) in series with a resistance (R). The differential equation describing the applied voltage (V_{app}) as a function of the injected current (j_{inj}) become

$$V_{app}(t) = L\frac{dj_{inj}}{dt} + Rj_{inj}(t) \tag{2.21}$$

Considering again that V_{app} is modified at a scan-rate (s), described by Equation (2.15), and the system starts from the equilibrium condition, which in this case means no voltage drop in the inductor, see Equation (2.19), so the initial injected current becomes

$$j_{inj}(t=0) = \frac{V_0}{R} \tag{2.22}$$

Then, the solution of Equation (2.21) is

$$j_{inj}(t) = \frac{s\,\tau_L\left[e^{-t/\tau_L} - 1\right] + (V_0 + s\,t)}{R} \tag{2.23}$$

where

$$\tau_L = L/R \tag{2.24}$$

Similar to **Figure 2.4**b, **Figure 2.5**b shows simulations of j_{inj} as function of V_{app}, using the same intial values, $V_0 = 0$ for Forward curves (positive scan-rates) and $V_0 = 1\ V$ for Reverse curves (negative scan-rates). For all these simulations, the resistance and inductance were also constant with values $R = 100\ \Omega\ cm^2$ and $L = 10\ H\ cm^2$. In contrast to the capacitor circuit, the steady-state ($s \to 0$) of the inductor circuit results in a j_{inj} linear with V_{app}. As mentioned before, in this condition, there is no voltage drop along the inductor, therefore in the steady-state condition the inductor is equivalent to a short-circuit, then in **Figure 2.5**a the j_{inj} is only limited by R. Another important feature of the inductor is that the generated voltage (V_L) is proportional to the change of the current, so the inductor can be interpreted as a resistance to current changes. When the scan-rate is increased, this effect generates a separation from the linear behaviour of j_{ext} vs V_{app}, as can be seen in **Figure 2.5**b. In the limit of fastest scan-rate ($s \to \infty$) the current will not change, for all the voltages will remain equal to the starting values, 0 and $10\ mA\ cm^{-2}$ for the Forward and Reverse scan, respectively. This results in an extra positive and negative current, with respect to the steady-state, for the Forward and Reverse scans, which has the opposite sign to the results obtained for the capacitor circuit, shown in **Figure 2.4**.

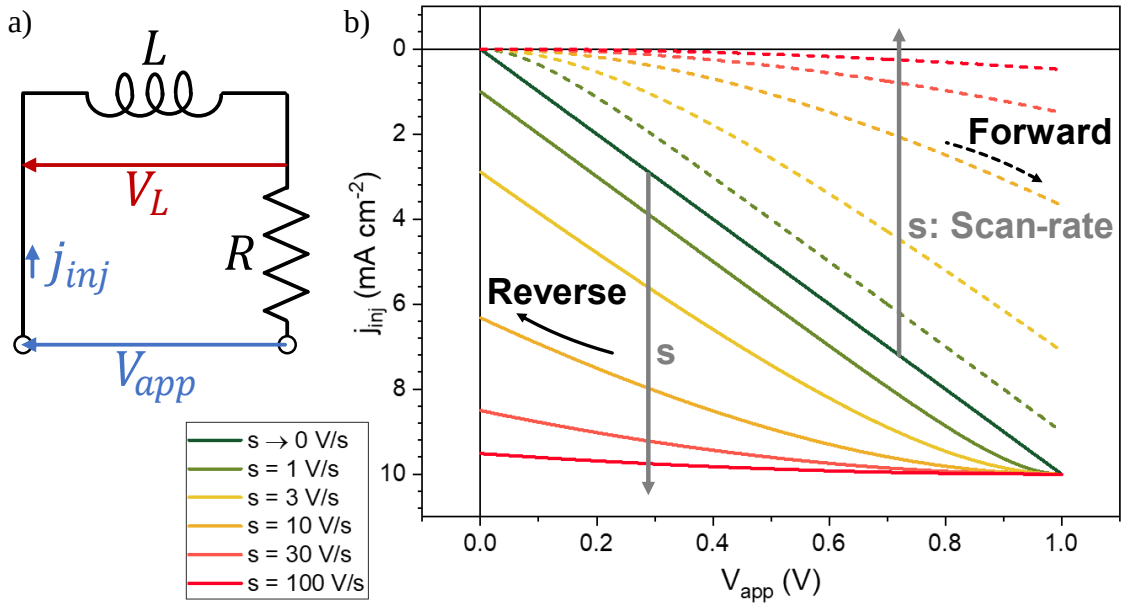

Figure 2.5 a) Simple equivalent circuit composed of a resistance (R) in series with an inductor (L), where V_L is the corresponding voltage drop, the red colour indicates that it is a variable that can not be directly measured, whereas the blue variables can be directly measured: applied voltage (V_{app}), and the injected current (j_{inj}). b) Simulations of the j_{inj} as a function of V_{app} for the equivalent circuit in a), starting from an equilibrium condition, Forward and Reverse correspond to positive and negative scan-rates (s), respectively. The resistance and inductance were constant in all the simulations with values $R = 100\ \Omega\ cm^2$ and $L = 10\ H\ cm^2$.

2.1.3. Drift-Diffusion

So far we have not discussed the transport in the absorber material, i.e. it was assumed that the transport of the photogenerated charges towards the contacts was not a limitation. In many cases this assumption is a good approximation, for example, there are materials with high diffusion coefficients that only need a thin layer to make an efficient photoconversion device. But in other cases, this assumption is not good enough, and this transport could represent a major limitation in the performance of the devices.

Two processes determine the transport into the absorber, drift and diffusion. These two processes are illustrated in **Figure 2.6**, for simplicity in all the cases is considered $V_{app} = 0$ and is analysed the transport of photogenerated charges. If the device is also in dark condition, then the Fermi levels of the absorber, the electron selective contact (ESC) and the hole selective contact (HSC) have to be in equilibrium, as discussed in the previous chapter. And as shown in **Figure 1.6**, this displacement is followed by a displacement in the vacuum level, which has to be continuous according to the vacuum level alignment rule or the Mott–Schottky rule.[1] In that figure, for simplicity, we considered that after the contact of the three materials, there was an abrupt energy jump at the contacts, but this is not usually the case. To illustrate the drift and the diffusion we will discuss in this section two more realistic scenarios.

Figure 2.6a shows the ideal case of an intrinsic semiconductor with a very low density of defects, such that the voltage difference between the vacuum levels of the ESC and the HSC is not perturbated by the absorber material. This results in a linear drop of the potential across the absorber, which means that there is a constant electric potential in the absorber material. The potential difference is equal to $V_{bi}^{ESC} + V_{bi}^{HSC}$, the sum of the differences between the Fermi levels in the vacuum of the absorber with the ESC and the HSC. **Figure 2.6**b shows that if some light is absorbed by this material, the photogenerated charges will be transported to the contacts by the force generated by the electric potential. This is the transport by drift. An example of this is the amorphous silicon (a-Si) p-i-n structure solar cell, which requires a low impurity level to ensure an electric field in the absorber to extract the photogenerated charges.[2]

If we consider that charged defects are added to the absorber material in **Figure 2.6**a, these charges will be transported to the right or to the left, if they are negativle or positively charged, respectively. These charges will eventually reach the interface and accumulate there, assuming that they are blocked by the selective contacts. As a result, the potential drop will take place in short regions near the interfaces, known as *Depletion Layers*. Then, as a consequence of the field screening of these accumulated charges, there will not be an electrostatic field in the centre of the absorber, known as the *Neutral Region*. This situation is represented in **Figure 2.6**b, where is shown that the voltage drops in the depletion layers are V_{bi}^{ESC} and V_{bi}^{HSC} in the interfaces of the absorber with the ESC and the HSC, respectively.

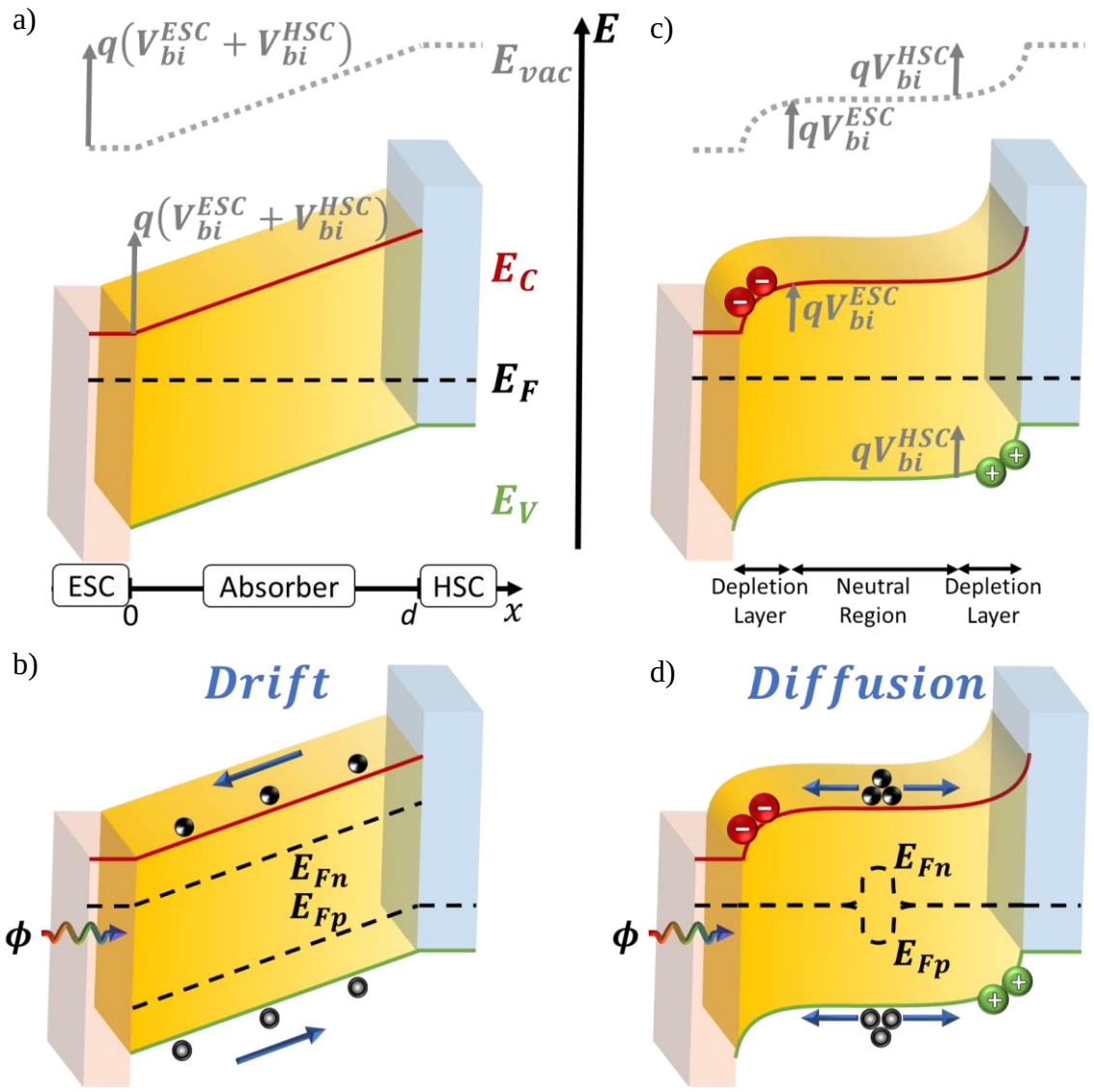

Figure 2.6 Schemes of p-i-n photoconversion devices composed of an absorber sandwiched by an electron selective contact (ESC) and a hole selective contact (HSC). The four situations are under cero external voltage. The central arrow points in the direction of the growing energy (E), and are drawn: the valence bands energy (E_V), the conduction bands energy (E_C), the vacuum levels (E_{vac}), the Fermi level (E_F) and the the elctron (E_{Fe}) and (E_{Fh}) hole Fermi levels. In grey are sown the built-in potential for the interfaces of the absorber with the ESC (V_{bi}^{ESC}) and the HSC (V_{bi}^{HSC}). a) shows the generation of an electric field into the absorber which generates a b) drift force in photogenerated charges. On the other hand, c) shows the screening of this electric field in the *Neutral Region* by the accumulation of anions (red) and cations (green) in the *Depletion Layers*. d) The absence of electric potential limits to diffusion transport of the photogenerated charges in the neutral region.

If we consider that some light is absorbed by the device in **Figure 2.6**c, in particular in the *Neutral Region*, these charges will not be transported by drift, because there is no electric field. Then, as shown in **Figure 2.6**d, the only possibility for the photogenerated charges to reach the selective contacts, where they can finally be extracted, is the transport by diffusion. The diffusion process is the movement of particles from high-concentration to lower-concentration regions, as a consequence of their random thermal motion. In this case, the carrier densities of the electrons (n) and the holes (p) are described by

$$\frac{dn}{dt} = D_n \frac{d^2n}{dx^2} - \frac{n}{\tau_{rec}} + G \tag{2.25}$$

$$\frac{dp}{dt} = D_p \frac{d^2p}{dx^2} - \frac{p}{\tau_{rec}} + G \tag{2.26}$$

Where τ_{rec} is the lifetime of the diffusion carriers, G is the free charge generation probability by an incident photon and D is the diffusion coefficient, where the subindexes n and p refer to electrons and holes. An important parameter is the diffusion length, defined as

$$L_n = \sqrt{D_n \tau_{rec}} \tag{2.27}$$

$$L_p = \sqrt{D_p \tau_{rec}} \tag{2.28}$$

With the clarifications made in this section, the case shown in **Figure 1.6**b can be interpreted as an absorber with extremely high doping, generating a depletion layer so thin that can be considered a step in the interface. This in fact is the usual assumption for the selective contacts, and the reason we do not show any depletion region on this material in **Figure 2.6**.

2.2. Current-Voltage Characteristic

In this section, we will discuss the measurements of the injected current (j_{inj}) as a function of the externally applied voltage (V_{app}). In **Section 2.1** we have discussed, for an ideal photoconversion device, the *j-V* curve under steady-state. We will start by showing a typical *j-V* curve analysis of a solar cell. Then, we will discuss a typical *j-V* curve of a photoanode. To conclude this section we will discuss the effect of measuring these curves outside the steady-state, in cyclic voltammetry (CV), and we will introduce the concept of "hysteresis".

2.2.1. Solar Cells

The characteristic *j-V* curve of a solar cell under illumination is generally represented as shown in **Figure 2.1**. In **Figure 2.7** the points of particular interest for their characterization are highlighted. At open-circuit (OC), which corresponds to $j_{inj} = 0$, it is defined the open-circuit voltage (V_{OC}). At short-circuit (SC), which corresponds to $V_{app} = 0$, it is defined the short-circuit current (j_{SC}). **Figure 1.8**a and b show simplified schems of the OC and SC conditions, respectively, including the internal distribution of the Fermi levels.

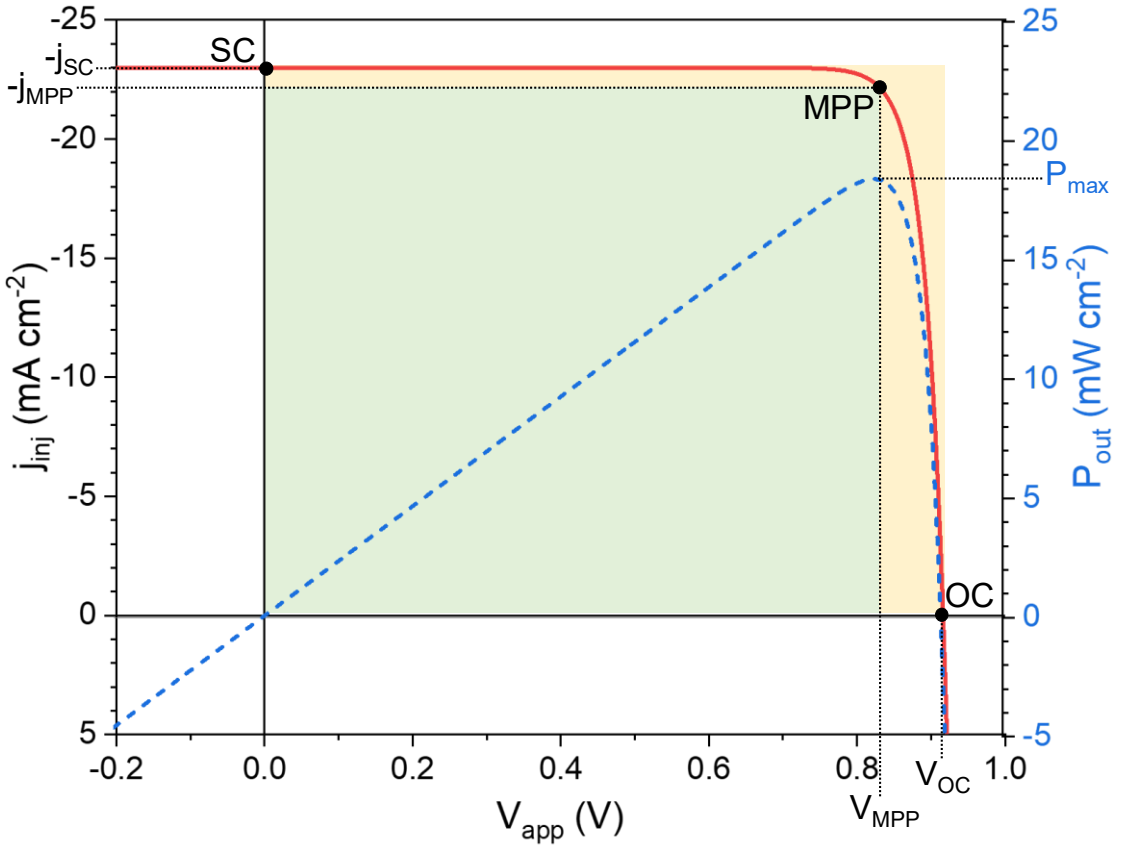

Figure 2.7 Left axis, scheme of a characteristic injected current (j_{inj}) as a function of the applied voltage (V_{app}) for a solar cell under illumination. j_{SC} is the short-circuit current and V_{OC} is the open-circuit voltage. In blue dashed line at the right axis is show the power generated by the device, reaching a maximum at P_{max}, where j_{MPP} and V_{MPP} are defined as the current and voltage at maximum power point (MPP).

From this *j-V* curve, the power generated by the device, i.e the product of the current and the voltage, see Equation (1.11), is calculated. This power, scaled at the right axis of **Figure 2.7** and represented as a dashed blue line, presents a peak, which is known as the maximum power point (MPP), where is defined the MPP voltage (V_{MPP}) and current (j_{MPP}),

$$P_{max} = j_{MPP} V_{MPP} \tag{2.29}$$

Another parameter of interest for solar cells is the fill factor (FF). This parameter measures the 'squareness' of the *j-V* curve

$$FF = \frac{P_{max}}{j_{SC} V_{OC}} = \frac{j_{MPP} V_{MPP}}{j_{SC} V_{OC}} \tag{2.30}$$

which geometrically corresponds to the ratio between the green and yellow square areas in **Figure 2.7**.

The power conversion efficiency (PCE) of the device is then given by

$$PCE = \frac{P_{max}}{P_{in}} = \frac{j_{MPP} V_{MPP}}{P_{in}} = FF \, \frac{j_{SC} V_{OC}}{P_{in}} \tag{2.31}$$

where P_{in} is the power of the light reaching the device. For a solar cell, the standard test condition is the Air Mass 1.5 spectrum, corresponding to $P_{in} = 1000 \, W \, m^{-2}$, at 25 ºC. These are the condition under which the efficiencies in **Figure 1.2** were measured.[9]

2.2.2. Photoelectrochemical Cells

Figure 2.8a shows a typical *j-V* curve obtained for a photoanode (i.e $BiVO_4$) in a photoelectrochemical cell as illustrated in **Figure 1.12**b, under dark and illumination conditions (red and blue solid lines respectively). In photoelectrochemistry, the applied voltage is usually represented versus reversible hydrogen electrode (RHE), as shown in **Figure 2.8**a. The RHE has the advantage, in contrast to other reference electrodes, of following changes in the hydrogen potential caused by changes in the pH of the electrolyte (water). Experimental measurements of the potential are usually made using a silver/silver chloride electrode (Ag/AgCl), which required the voltage transformation

$$V_{RHE} = V_{Ag/AgCl} + V^0_{Ag/AgCl} + \frac{RT}{nF} \times pH \tag{2.32}$$

where V_{RHE} is the potential versus RHE, $V_{Ag/AgCl}$ is the recorded potential versus the reference, $V^0_{Ag/AgCl}$ is the standard potential of the Ag/AgCl redox couple, RT/nF at room temperature is a constant value (0.0591), and the pH is that of the buffer solution used as the electrolyte.[10-11]

Figure 2.8b shows the same curves as **Figure 2.8**a but with the voltage inverted in sign and shifted. The resulting voltage corresponds to the difference between the applied voltage in the TCO and the water oxidation, which is equivalent to the difference between the ESC and the HSC in **Figure 1.8**. In this figure are added the *j-V* curves of a solar cell under dark (dashed grey line) and illumination conditions (dashed red light). Note that for the comparison the open-circuit voltage for the solar cell is 1.23 V, see **Figure 2.8**b.

The blue line in **Figure 2.8**, corresponding to the dark current of the photoelectrochemical cells, is similar to the response of a solar cell in dark, for voltages

lower than 1.23 V vs RHE. As shown in **Figure 1.12**a, at higher voltages water-splitting can be generated without the need for an absorber layer. For this reason, above 1.23 V vs RHE a positive current may appear in the dark *j-V* curve. This exceeding current then is also present in the light *j-V* curve (red solid lines). In addition to this exceeding current, there is a clear separation from the *j-V* curve of the diode under light at lower voltages, as the arrow signals ("Charge Transfer") in **Figure 2.8**b. This reduction in the extracted current has been attributed to a large recombination of the photogenerated charges, caused by a limitation in the transfer of the holes from the absorber material to the electrolyte.[12] But as can be seen in **Figure 2.8**, this process is better overcome for higher voltages.

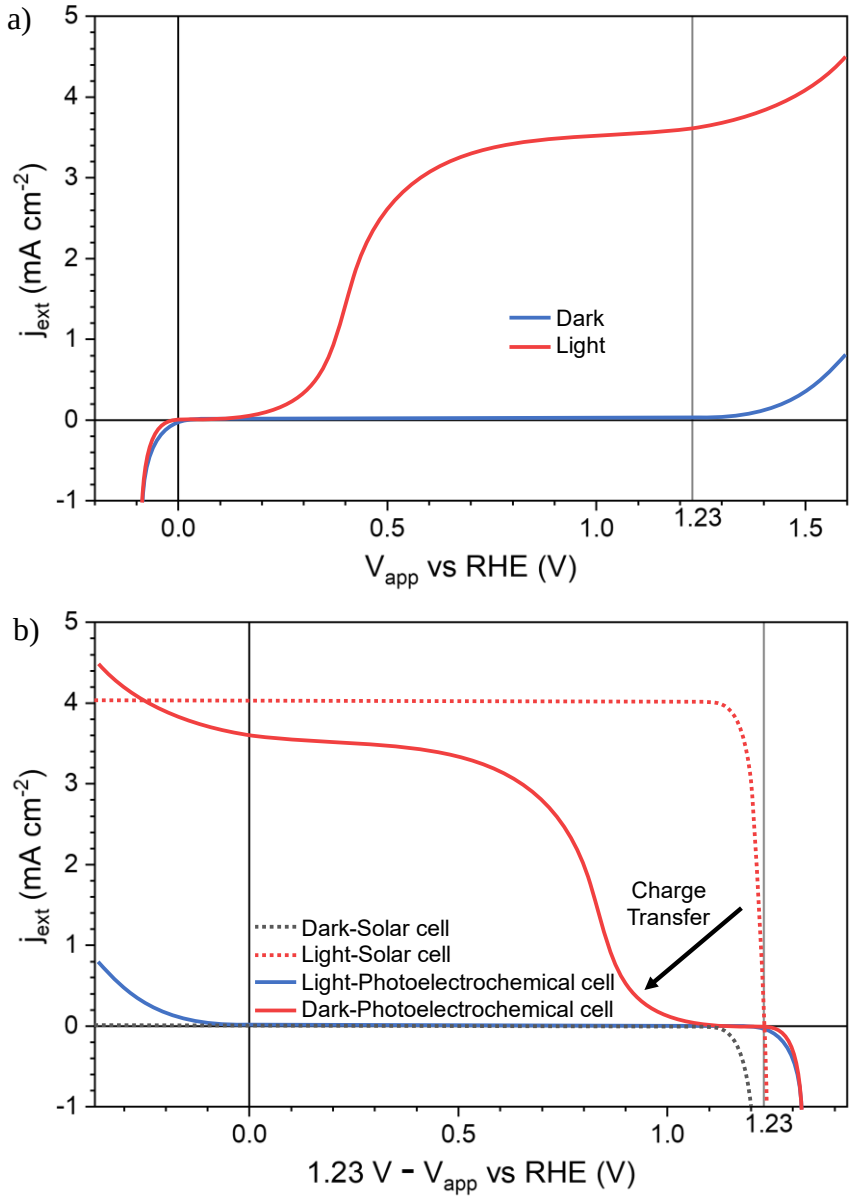

Figure 2.8 Scheme of the typical *j-V* curves of a photoanode in a photoelectrochemical cell as shown in **Figure 1.12**b under light (solid red line) and dark (solid blue line), b) compared with the *j-V* curves of an ideal diode under dark (dashed grey line) and illumination conditions (rashed red light), with open-circuit voltage equal to 1.23 V. The arrow indicates a reduction in the extracted current caused by a limitation in the transfer of the photogenerated charges.

2.2.3. Cyclic Voltammetry and Hysteresis

Cyclic voltammetry (CV) is the linear sweep from an initial voltage to a final voltage followed by the sweep in the opposite direction back to the initial voltage. The Forward and Reverse scans have been defined as the curves corresponding to increasing and decreasing voltages. The presence of time-dependent processes in the devices generates displacements in the *j-V* curves that depend on the scan-rates. Then, the Hysteresis can be defined as the difference between the Forward and Reverse scans. In **Subsection 2.1.2** we have presented different examples where we could note that the steady-state *j-V* curve can be obtained by slowing down enough the scan-rate, eliminating the hysteresis.

In **Figure 2.9** two possible hysteresis responses of solar cells, are plotted for a given scan-rate. By comparing this figure with **Figure 2.1** it is clear that the Forward and Reverse scans have different apparent maximum powers, and therefore, provide different estimations of the power conversion efficiencies (PCE). This is the main issue of hysteresis, the measurement of the current by sweeping the voltage at a certain scan-rate can lead to erroneous conclusions by misinterpreting this result as the steady-state *j-V* curve. In fact, the resulting parameters of this measurement will depend on the scan-rate and direction (Forward or Reverse).

To quantify the hysteresis, it can be defined the hysteresis index as[13]

$$HI = 1 - \frac{PCE_{FS}}{PCE_{RS}} = 1 - \frac{j_{MPP-FS}V_{MPP-FS}}{j_{MPP-RS}V_{MPP-RS}} = 1 - \frac{FF_{FS}j_{SC-FS}V_{OC-FS}}{FF_{RS}j_{SC-RS}V_{OC-RS}} \tag{2.33}$$

where FS and RS account for the Forward and Reverse scans respectively. With this definition, these hysteresis features can be grouped into two categories, positive and negative HI. Positive HI is known as Normal Hysteresis, which corresponds to a higher fill factor and PCE for the Reverse scan, in comparison with the Forward scan. On the other hand, negative HI are known as Inverted Hysteresis, which corresponds to higher FF and PCE for the Forward scan, see **Figure 2.9**.

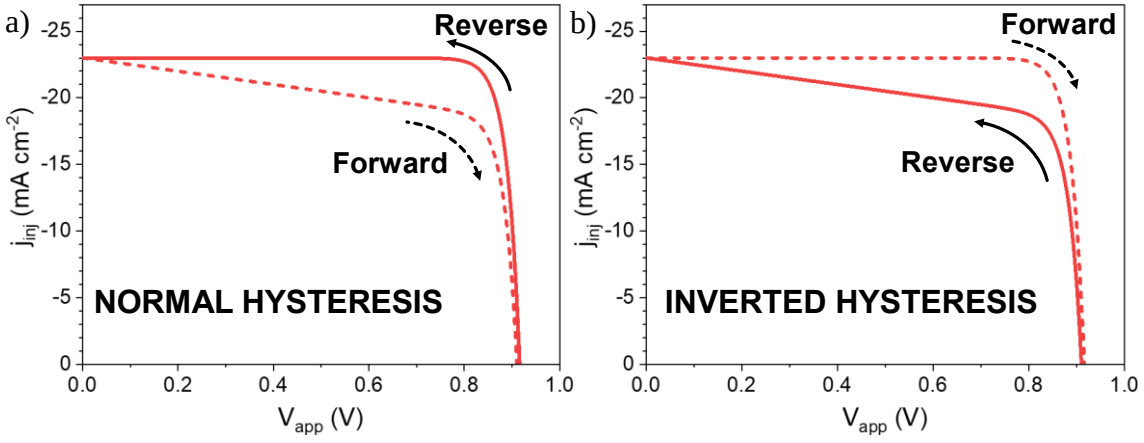

Figure 2.9 Scheme of the two categories of hysteresis: a) Normal Hysteresis, corresponding to a Reverse scan (solid lines) with a higher absolute value of the current, $|j_{inj}|$ than the Forward Scan (dashed lines). And b) Inverted Hysteresis, corresponding to a Forward scan with higher $|j_{inj}|$ compared with the Reverse scan.

2.3. Modulated Techniques

In this section, we will introduce the modulated techniques, also known as small perturbation techniques, evidencing their great power to differentiate and characterise the internal processes in photoconversion devices. We will start presenting Impedance Spectroscopy (IS). Then, we will present light perturbation techniques: Intensity-Modulated Photocurrent Spectroscopy (IMPS) and Intensity-Modulated Photovoltage Spectroscopy (IMVS).

2.3.1. Impedance Spectroscopy

Impedance Spectroscopy (IS) has been widely developed since the first presentation at the end of the XIX century by Heaviside.[14] This technique is not only useful for photoconversion devices but can be applied to characterize any electronic device. Among the advantages of this technique, one of the most relevant is that the measurements are done under real operation conditions. These conditions include dark or light and any applied voltage (V_{app}) or injected current (j_{inj}). **Figure 2.10** shows a shceme of the IS measurement procedure at a given light, voltage and current.

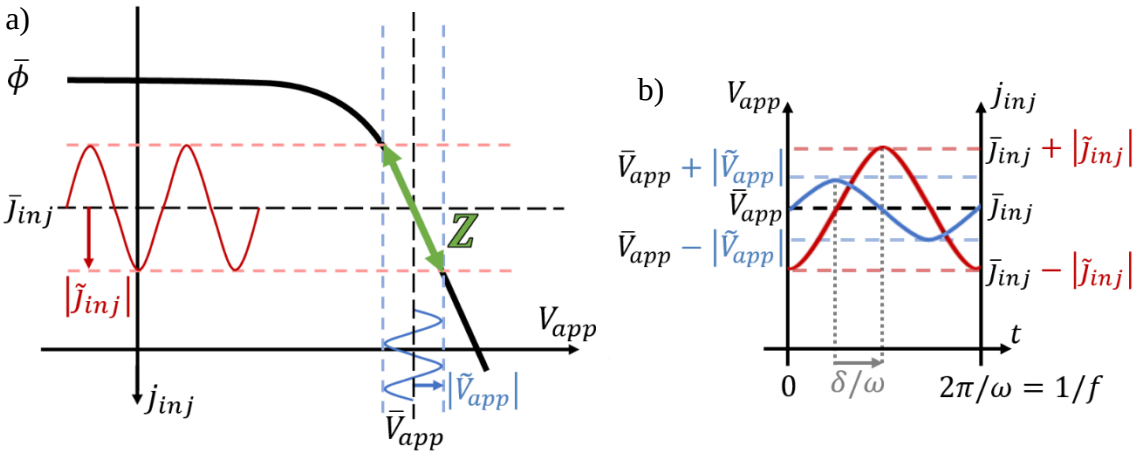

Figure 2.10 Schemes of the impedance spectroscopy (Z) measurement procedure: a) on top of a *j-V* curve and b) as a function of the frequency (f), where ω is the angular frequency and δ is the phase shift. The overbars ($\bar{}$) indicate DC signals and the tilde ($\tilde{}$) indicate the AC perturbation and response. Is applied a voltage perturbation ($\tilde{V}_{app}$, in blue) and is measured the current response ($\tilde{J}_{inj}$ in red). The same measurement can be performed by applying the perturbation in the current and measuring the voltage response.

There are two ways to measure IS: in potentiostatic or galvanostatic mode, where the external control is performed over the V_{app} or the j_{inj}, respectively. Probably the most common mode is the potentiostatic. In this mode, the applied voltage for a given angular frequency (ω) can be written as

$$V_{app}(t,\omega) = \bar{V}_{app} + \tilde{V}_{app}(t,\omega) \tag{2.34}$$

where the overbar ($\bar{}$) indicates a DC signal, it does not depend on time (t), and the variable with the tilde ($\tilde{}$) indicate an AC perturbation, given by

$$\tilde{V}_{app}(t,\omega) = \left|\tilde{V}_{app}\right| e^{i\omega t} \tag{2.35}$$

If the voltage perturbation is small enough, the extracted current will respond linearly, so it will also be as

$$j_{inj}(t,\omega) = \bar{J}_{inj} + \tilde{j}_{inj}(t,\omega) \tag{2.36}$$

with

$$\tilde{j}_{inj}(t,\omega) = \left|\tilde{j}_{inj}\right| e^{i(\omega t-\delta)} \tag{2.37}$$

where the phase (δ) is the delay between the voltage perturbations and the current response. The difference with the Galvanostatic mode is that the current is the perturbation and the voltage is the response, but the equations are equivalent. Then, the impedance transfer function is defined as

$$Z(\omega) = \frac{\tilde{V}_{app}(t,\omega)}{\tilde{j}_{inj}(t,\omega)} = |Z(\omega)|e^{i\delta} = Z'(\omega) + iZ''(\omega) \tag{2.38}$$

It is worth recalling that we are employing the convention in which the current is positive when it flows, through the device, from the positive to the negative of the externally applied voltage from the potentiostat/galvanostat. The opposite convention ($j_{ext} = -j_{inj}$) results in a change of sign in the definition of Z. It is also important to notice that this function does not depend on the time, it only depends on the frequency. By comparing Equation (2.38) with Equation (2.6) it can be noted that the low-frequency limit ($\omega \to 0$) of Z correspond to the total or DC resistance (R_{DC}).

Figure 2.11a shows an impedance spectrum in a *Nyquist Plot*, where each dot corresponds to one frequency. This is probably the most common way of representing impedance spectra, but it should be noted that the relationship of Z with the frequency is not evident in this graph. A common alternative is the use of *Bode Plots*, where a variable is represented as a function of the frequency, as is the case of **Figure 2.11**b. The frequency in this graph is related to the angular frequency (ω) by

$$f = \frac{\omega}{2\pi} \tag{2.39}$$

The capacitance transfer function is also an imaginary function and it is related to the impedance transfer function by

$$C(\omega) = \frac{1}{i\omega Z(\omega)} = \frac{-Z'' - iZ'}{\omega(Z'^2 + iZ''^2)} = C' + iC'' \tag{2.40}$$

Usually, the real part of this imaginary function is simply called the Capacitance, as in **Figure 2.11**b. The units of impedance are Ohms (Ω), but it is very convenient to use the normalized units $\Omega\ cm^2$, as in **Figure 2.11**a, accounting for the current density in Equation (2.38), which allows easier comparison between different samples. Similarly, while the units of the capacitance are Farads (F), it is very common to normailize the units to $F\ cm^{-2}$, as in **Figure 2.11**b.

The analysis of the impedance spectrum is not so simple, as it is necessary to propose a model to extract relevant information. The use of models based on an equivalent circuit (EC) are the most common analysis method because they allow the extraction of many parameters and their implementation is straightforward thanks to specialised software. However, this ease of use can be misleading as there may be many equivalent circuits that fit equally well a given impedance spectrum, but each circuit provides a different interpretation of the parameters obtained. So the equivalent circuit must have a justification from the physicochemical processes on the device under investigation. In that way, the resulting parameters will be related to the real internal processes dominating the response of the device.

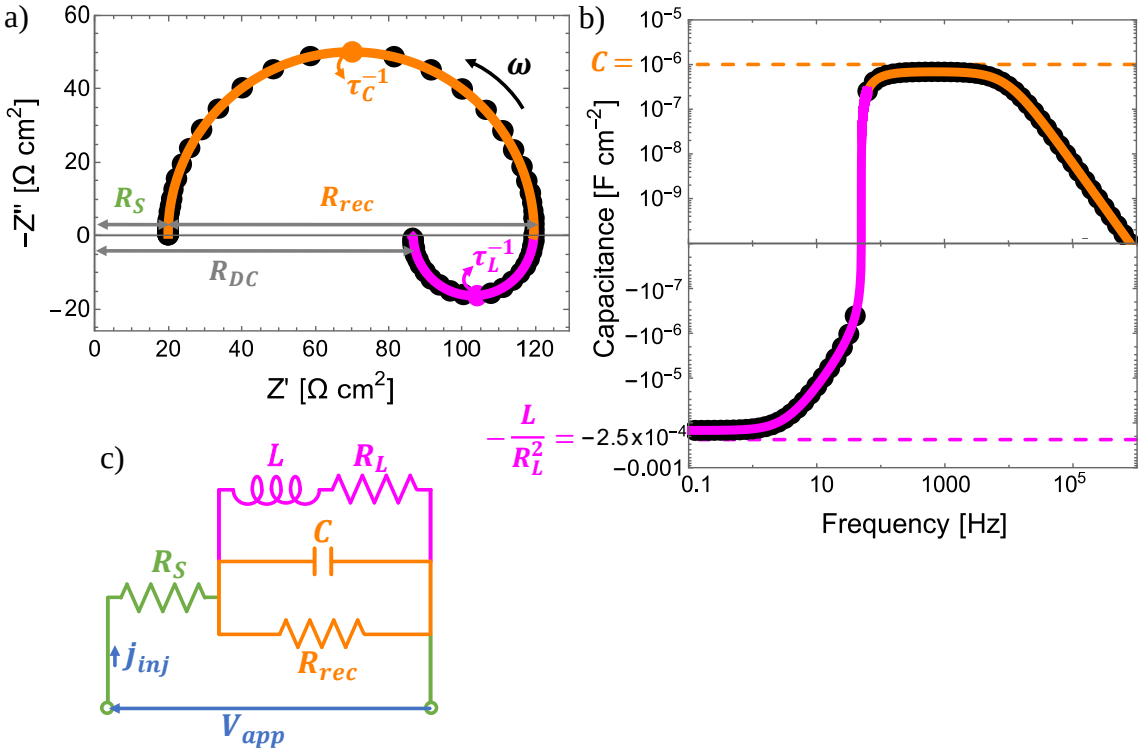

Figure 2.11 Impedance spectrum represented in a) a Nyquist plot and b) the capacitance (real part of the capacitance transfer function) in a Bode Plot, where each dot corresponds to one frequency. c) Equivalent circuit employed to simulate impedance spectra (both the dots and lines are the same spectra) with the parameters in **Table 2.1**. The colours of the elements correspond to the portion of the spectrum with the corresponding colour.

Table 2.1 Values of the equivalent circuit parameters in **Figure 2.11**c employed to make the simulation shown with solid lines in **Figure 2.11**a and b.

R_S [$\Omega\ cm^2$]	R_{rec} [$\Omega\ cm^2$]	C [$F\ cm^{-2}$]	R_L [$\Omega\ cm^2$]	L [$H\ cm^2$]	τ_C [s]	τ_L [s]
20	100	1×10^{-6}	200	10	1×10^{-4}	5×10^{-2}

Although the black dots in **Figure 2.11**a and b were obtained from a simulation, let us consider for a moment that they were obtained experimentally and that we wish to extract information from this spectrum. **Figure 2.11**c shows an equivalent circuit (EC) suitable for the analysis of this impedance spectrum. Here the dots and lines are the same spectra simulated from the EC with the parameter values in **Table 2.1**, but if the points were an experimental spectrum, the values in this table would be the result of the fitting with this EC. To understand the compatibility of the impedance spectrum with the EC, we divide the EC into different colours in **Figure 2.11**c, and next, we will discuss the IS response generated by each of these parts, represented by solid lines with the same colours in **Figure 2.11**a and b.

The impedance transfer function can be calculated from the EC employing Kirchhoff's circuit laws, described for the first time in 1845 by the German physicist Gustav Kirchhoff.[15] For the EC in **Figure 2.11**c, the impedance transfer function is

$$Z = R_S + \left(i\omega C + \frac{1}{R_{rec}} + \frac{1}{R_L + i\omega C}\right)^{-1} \tag{2.41}$$

The series resistance (R_S) generates a displacement in the whole spectrum, see **Figure 2.11**a, and corresponds to the high-frequency limit of Z. The recombination resistance (R_{rec}) and the capacitance (C) generates the orange arc at high frequencies. This process has a characteristic time given by the inverse of the frequency corresponding to the maximum of $-Z''$ (the top of the arc) and is related to the recombination resistance and the capacitance by

$$\tau_C = R_{rec}C \tag{2.42}$$

which we have already obtained in Equation (2.17) when analysing the linear sweep for a resistor and capacitor circuit.

At lower frequencies, in magenta, appears an arc at the bottom of **Figure 2.11**a and the capacitance becomes negative in **Figure 2.11**b. These features are generated by the inductor (L) (or negative capacitance) and its associated resistance (R_L). The characteristic time of this process is the inverse of the frequency corresponding to the minimum of $-Z''$, given by

$$\tau_L = \frac{L}{R_L} \tag{2.43}$$

which we have also already obtained, see Equation (2.24), when analysing the linear sweep for a resistor and inductor circuit.

Finally, as mentioned above, the low-frequency limit of Z is equal to the DC resistance, in this case, equal to

$$R_{DC} = R_S + \left(\frac{1}{R_{rec}} + \frac{1}{R_L}\right)^{-1} \tag{2.44}$$

Figure 2.11b shows in orange and magenta dashed lines the values of C and $-L/R_L^2$, respectivelly. These are the values that the capacitance would take if the circuit were composed only of the elements of these colours. The fact that the maximum and minimum values of the capacitance do not completely reach the dashed lines is due to the effect of the other elements in the circuit.

2.3.2. Light-Modulated Techniques: IMPS and IMVS

Intensity-Modulated Photocurrent Spectroscopy (IMPS) and Intensity-Modulated Photovoltage Spectroscopy (IMVS) are also modulated techniques, similar to Impedance Spectroscopy (IS). But instead of applying a perturbation in the voltage (V_{app}) and measuring the injected current (j_{inj}) (or vice versa) as in the IS measurement, in these two techniques the perturbation is applied in the incident light or photon flux (ϕ) and the response is measured j_{inj} for IMPS or V_{app} for IMVS. This is shown in **Figure 2.12**.

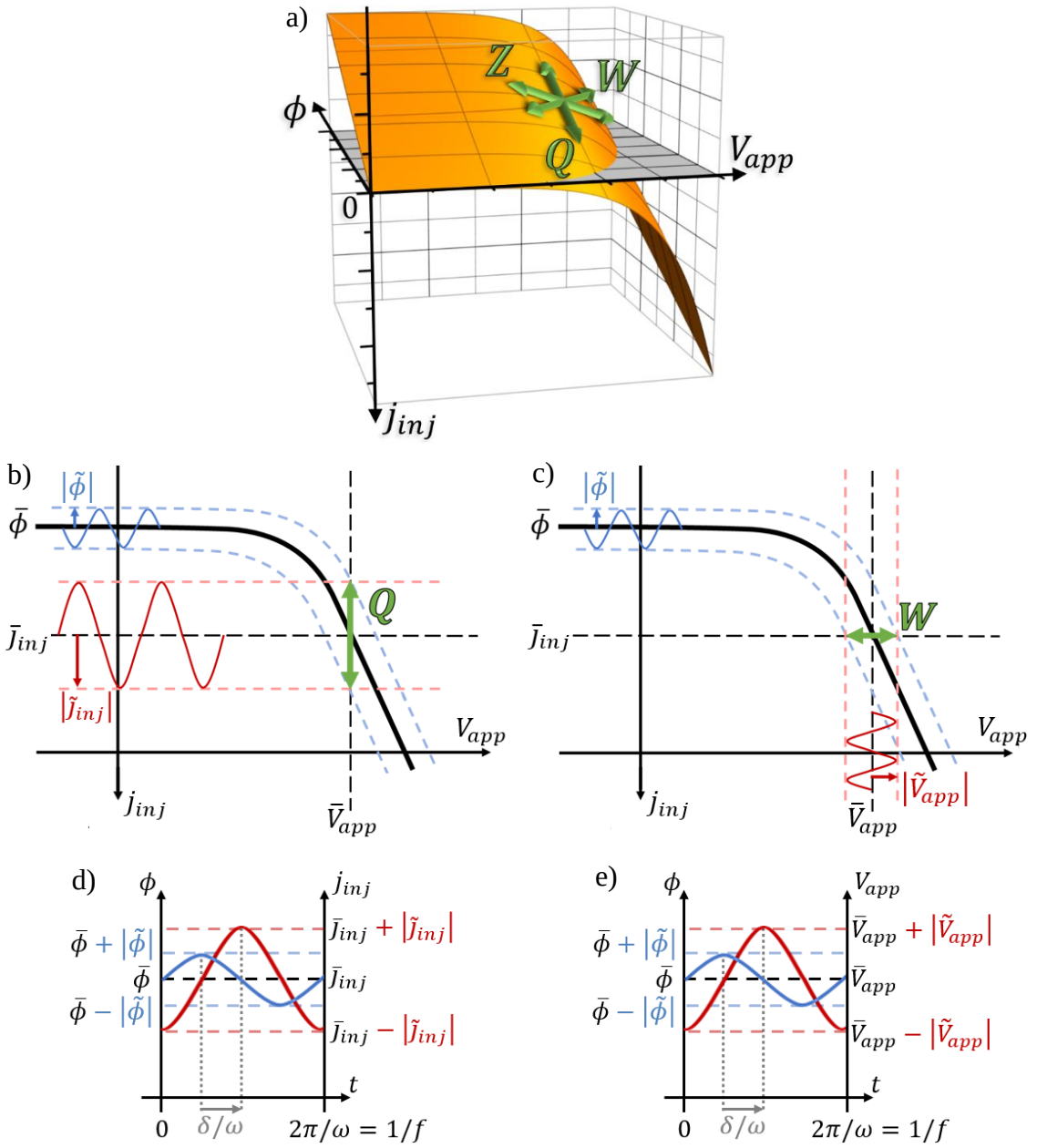

Figure 2.12 a) Scheme of a tridimensional *j-V* curve, where the third axis is the photon flux reaching the device (ϕ), where is shown the IS, IMPS and IMVS transfer functions, Z, Q and W, respectivelly. Measurements procedures for b)-d) Q and c)-e) W.

Figure 2.12a shows the extension of the *j*-*V* curve to a tridimensional surface, where the third axis is the photon flux (ϕ), as shown by Bertoluzzi et al.[16] On a given point of this surface, defined by the DC values ($\bar{J}_{inj}$,$\bar{V}_{app}$,$\bar{\phi}$), is shown with a green arrow the IS response as in **Figure 2.10**, where the light is kept constant. Also with green arrows and at the same point in the surface are shown the IMPS transfer function (Q) and the IMVS transfer function (W), wich are defined in the planes of constante voltage and constant current, respectively.

Equivalent to the equations presented in the previous subsection describing the measurement of IS, to measure IMPS or IMVS the photon flux will be the sum of a DC light ($\bar{\phi}$) and an AC perturbation ($\tilde{\phi}$)

$$\phi(t,\omega) = \bar{\phi} + \tilde{\phi}(t,\omega) \tag{2.45}$$

where

$$\tilde{\phi}(t,\omega) = \left|\tilde{\phi}\right| e^{i\omega t} \tag{2.46}$$

To measure IMPS the voltage is kept constant, while the current will have the form of Equation (2.36) where the AC response to the perturbation will be given by Equation (2.37). Similar to the impedance transfer function in Equation (2.38), the IMPS transfer function is defined as

$$Q(\omega) = -\frac{\tilde{J}_{inj}}{q\tilde{\phi}} = |Q(\omega)|e^{i\delta} = Q'(\omega) + iQ''(\omega) \tag{2.47}$$

Finally, to measure IMVS, the current is kept constant and the voltage will have the form of Equation (2.34), where the AC voltage will be given by

$$\tilde{V}_{app}(t,\omega) = \left|\tilde{V}_{app}\right| e^{i(\omega t-\delta)} \tag{2.48}$$

with δ now the phase difference between the incident AC light flux and the measured voltage. The IMVS transfer function is defined as

$$W(\omega) = \frac{\tilde{V}_{app}}{q\tilde{\phi}} = |W(\omega)|e^{i\delta} = W'(\omega) + iW''(\omega) \tag{2.49}$$

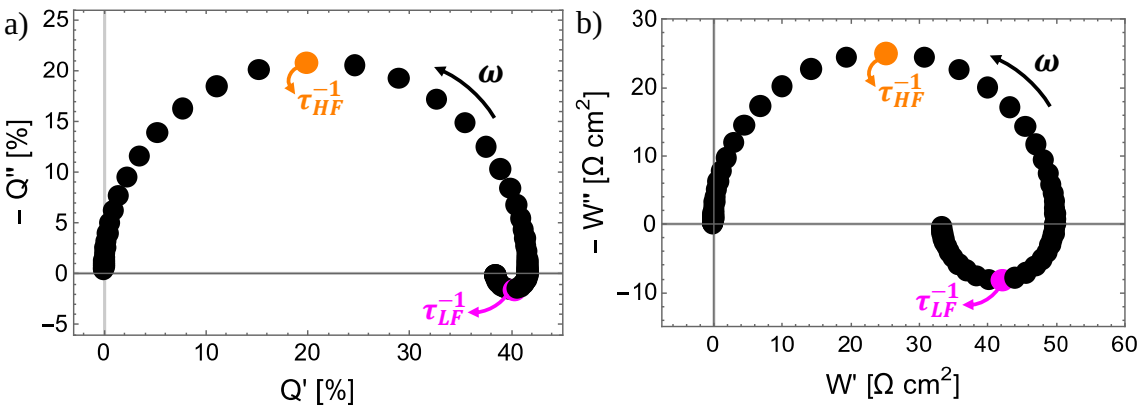

Figure 2.13 a) IMPS and b) IMVS spectra represented in Nyquist Plots, where each dot corresponds to one frequency. The high-frequency (orange) and low-frequency (magenta) characteristic times are highlighted.

Figure 2.13 shows an IMPS and an IMVS spectrum in Nyquist Plots, where again each dot corresponds to one frequency. Unlike IS spectra which are generally analysed through an equivalent circuit, the analysis of IMPS and IMVS spectra is usually limited to the characteristic times. These times are taken from the maximum and minimum of the different arcs observed, as shown in **Figure 2.13** and as discussed in the previous subsection for the IS case.

2.4. Instrumentation for Modulated Techniques

The instruments and techniques employed to achieve the results of this thesis are specified in each chapter, at the end of the publication. Here we take the opportunity to show the basic setup needed to measure IS, IMPS and IMVS, see **Figure 2.15**.[17]

Figure 2.14 shows a schematic setup for the measurement of IS, IMPS and IMVS. To measure IS, this module applies the voltage V_{app} (or current j_{inj}) perturbation required and j_{inj} (or V_{app}) response is measured. In **Figure 2.14** the light ϕ reaching the photoconversion device comes from an LED, for the IS measurement the requirement is a constant light, so any other light source can be used for this technique, including a solar simulator or even complete darkness. On the other hand, as described above, the measurement of IMPS and IMVS implies the application of an AC light in addition to the DC light. This perturbation in the light is generated by the measuring instrument by modifying the current reaching the LED, indicated as j_{LS} in red in **Figure 2.14**. Other setups involve two lights, one for the DC and the other for the AC lights.

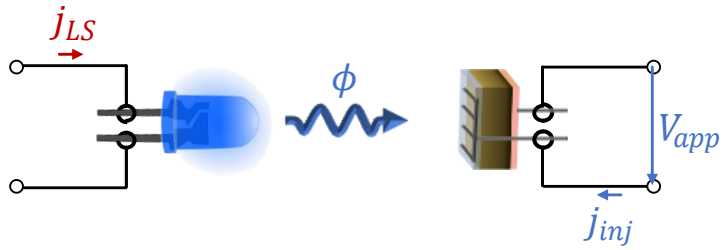

Figure 2.14 Schematic setup for the measurement of IS, IMPS and IMVS. j_{LS} is the light source current, controlling the photon flux ϕ that reach the photoconvertion device under investigation, from which it can be measured the applied voltage (V_{app}) and the injected current (j_{inj}).

The measurements of the three techniques were carried out in this thesis with a Potentiostat/Galvanostat Autolab PGSTAT302 equipment. This equipment is controlled with the NOVA software. To measure modulated techniques, the PGSTAT302 is equipped with a FRA32M module. To measure IMPS and IMVS with this instrument, the external accessory called “LED Driver” is also required, which can be seen in **Figure 2.15**.

The use of monochromatic light is preferable for several reasons. First, different wavelengths may interact differently with the device under investigation, so modulating a light composed of a broad spectrum may result in the superposition of the different responses. In addition, the use of a monochromatic light simplifies the calculations, e.g. the incident light power is linearly related to the photon flux, rather than being an integral.

A detailed description of the measurement procedure is detailed in the LED Driver User Manual from Methrohm Autolab.[17]

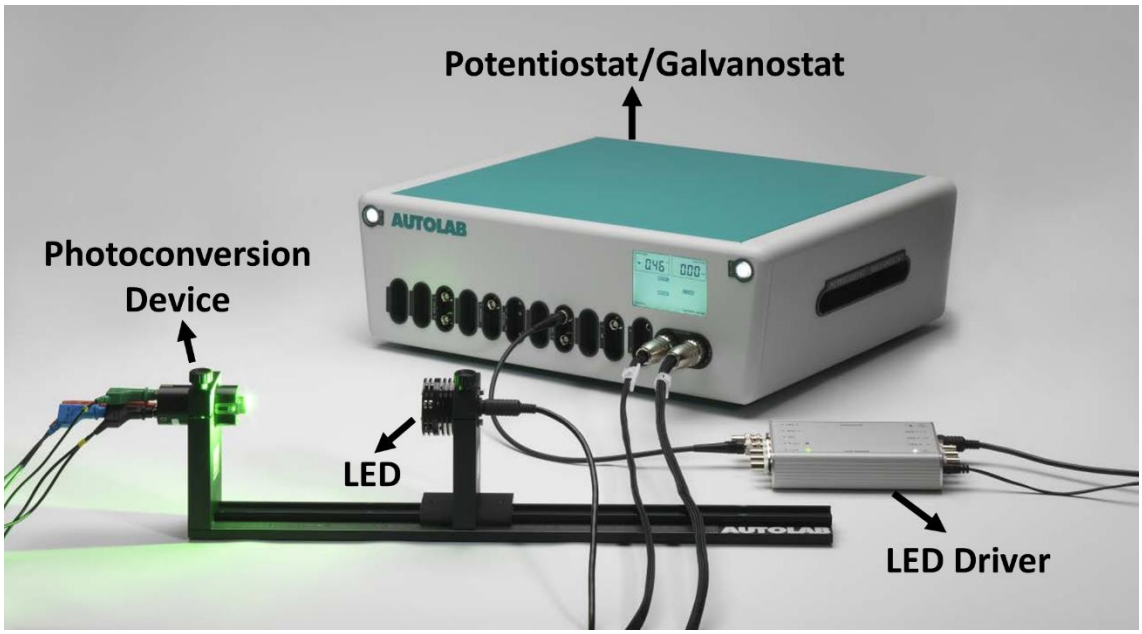

Figure 2.15 Autolab setup to measure IS, IMPS and IMVS, involving a Potentionstat/Galvanostat, a LED Driver, a LED and the photoconversion device under investigation. Adapted from ref. [17], Copyright 2022, Metrohm AG.

2.4.1. Tools and Procedures Used for the Analysis of Experimental Data

For the analysis of the data resulting from the measurements, we mainly use the following computer programs:

- Zview: It has allowed us to analyse IS spectra quickly, easily and reliably.[18]
- SigmaPlot: It is a graphing and data analysis software, which was very useful for us, especially at the beginning of the PhD, for two main reasons: we had templates previously developed in our group and also it contains a function to make pseudo-codes that were very practical for us.[19]
- OriginLab: We started to use this graphing and data analysis software more frequently until it completely displaced SigmaPlot. This was mainly because for our purpose we find OriginLab more user-friendly and thus allowed us a faster and more versatile analysis of our data.[20]
- Mathematica: We used this software to develop codes that, among other things, allowed us to: perform simulations of the experimental techniques, analyse and fit experimental data, solve systems of differential equations and make various graphs. One function provided by this software that was particularly crucial for us was: the possibility to fit simultaneously several experimental data sets (IS, IMPS and IMVS spectra, in our case) with the same parameters (resistances, capacitances, etc.) within different functions (IS, IMPS and IMVS transfer functions, obtained for example from the same EC).[21]

References

[1] J. Bisquert, *The Physics of Solar Energy Conversion*, CRC Press, **2020**.

[2] J. A. Nelson, *The physics of solar cells*, World Scientific Publishing Company, **2003**.

[3] J. Bisquert, F. Fabregat-Santiago, *Impedance spectroscopy: a general introduction and application to dye-sensitized solar cells* in *Dye-sensitized solar cells*, EPFL Press, **2010**.

[4] F. Fabregat-Santiago, E. Barea, S. Giménez, J. Bisquert, *Impedance Spectroscopy in Molecular Devices* in *Molecular Devices for Solar Energy Conversion and Storage*, **2018**.

[5] W. Shockley, *Bell Syst. Tech. J.* **1949**, 28, 435.

[6] S. Keith, P. Victoria, L. Suzanne, A. Marshall, H. Adam, National Institute of Standards and Technology (NIST), *Guide to Industrial Control Systems (ICS) Security*, https://nvlpubs.nist.gov/nistpubs/SpecialPublications/NIST.SP.800-82r2.pdf. Accessed 30.06.2023.

[7] A. O. Alvarez, R. Arcas, C. A. Aranda, L. Bethencourt, E. Mas-Marzá, M. Saliba, F. Fabregat-Santiago, *J. Phys. Chem. Lett.* **2020**, 11, 8417.

[8] E. Ghahremanirad, A. Bou, S. Olyaee, J. Bisquert, *J. Phys. Chem. Lett.* **2017**, 8, 1402.

[9] National Renewable Energy Laboratory (NREL), *Best Research-Cell Efficiency Chart*, https://www.nrel.gov/pv/assets/pdfs/best-research-cell-efficiencies.pdf. Accessed 17.04.2023.

[10] R. Van de Krol, M. Grätzel, *Photoelectrochemical hydrogen production*, Vol. 90, Springer, **2012**.

[11] D. Cárdenas Morcoso, *Advanced semiconductors for photo-electrocatalytic solar fuel production*, Universitat Jaume I, **2020**.

[12] L. Bertoluzzi, P. Lopez-Varo, J. A. Jiménez Tejada, J. Bisquert, *J. Mater. Chem. A* **2016**, 4, 2873.

[13] H.-S. Kim, I.-H. Jang, N. Ahn, M. Choi, A. Guerrero, J. Bisquert, N.-G. Park, *J. Phys. Chem. Lett.* **2015**, 6, 4633.

[14] D. D. Macdonald, *Electrochim. Acta* **2006**, 51, 1376.

[15] K. T. S. Oldham, *The doctrine of description: Gustav Kirchhoff, classical physics, and the "purpose of all science" in 19 th-century Germany*, University of California, Berkeley, **2008**.

[16] L. Bertoluzzi, J. Bisquert, *J. Phys. Chem. Lett.* **2017**, 8, 172.

[17] Metrohm Autolab B.V., *LED Driver User Manual*, https://www.metrohm.com/en.html. Accessed 25.10.2022.

[18] Scribner Associates, *ZView*, https://www.scribner.com/software/68-general-electrochemistr376-zview-for-windows/. Accessed 02.03.2023.

[19] Systat, *SigmaPlot*, https://systatsoftware.com/sigmaplot/. Accessed 02.03.2023.

[20] OriginLab, https://www.originlab.com/. Accessed 02.03.2023.

[21] Wolfram, *Mathematica*, https://www.wolfram.com/mathematica/. Accessed 02.03.2023.

CHAPTER 3

Critical Overview

3.1. Motivation and General Goals of the Thesis

Figure 3.1 summarises the objectives of this thesis, describing the chosen path that has led us from the global objective, to which we have intended to make a small contribution, to the specific objectives of this thesis.

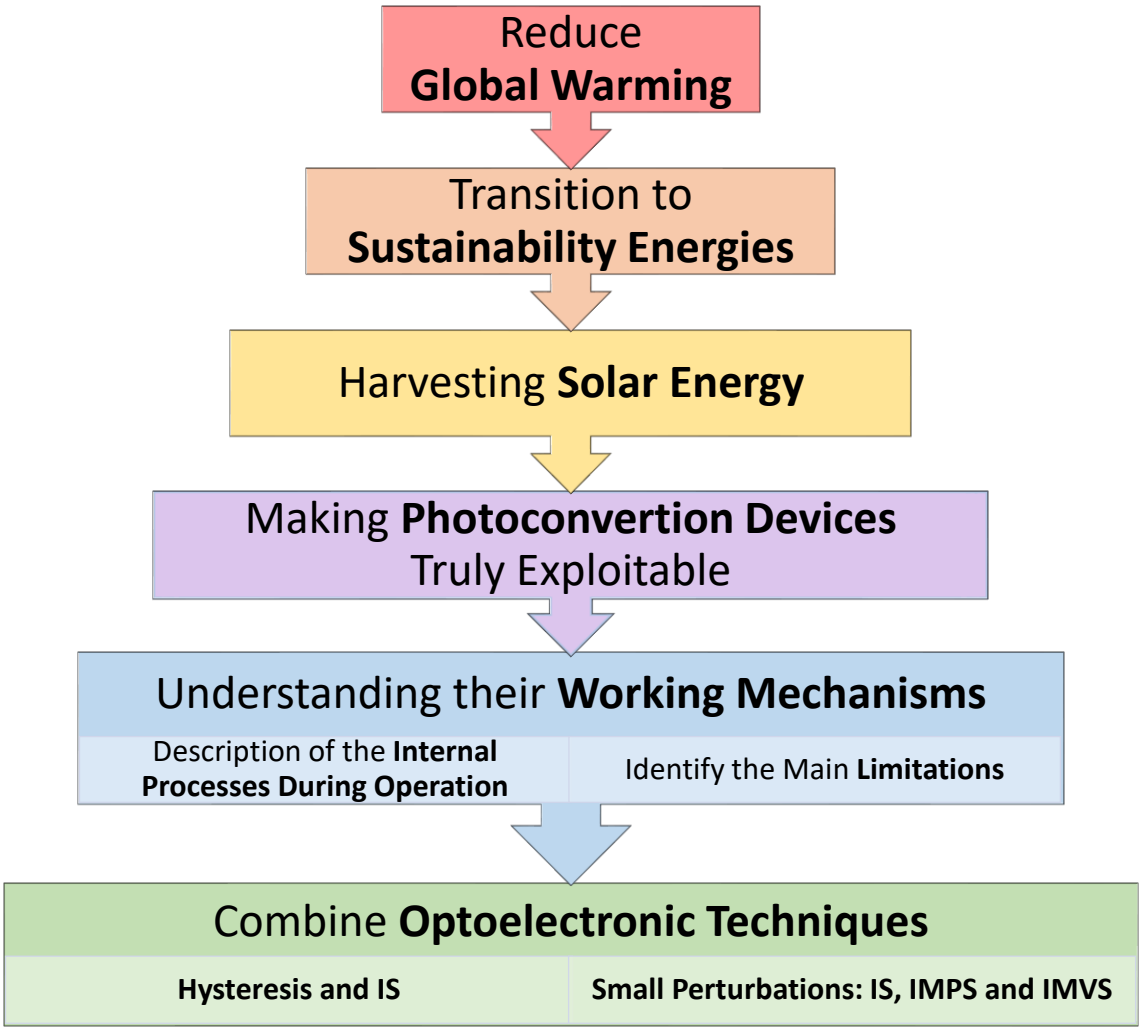

Figure 3.1 Thesis goals: describing the motivation global objectives that lead to the specific objectives of this thesis.

This thesis has joined the worldwide efforts to reduce global warming. We have intended to contribute to the transition toward sustainable energies, to reduce fossil fuel consumption, therefore CO_2 emissions, and therefore global warming. With this thesis, we have worked on making truly exploitable novel technologies that transform solar

energy into electrical or chemical energy. Within this specific approach, we have focused our efforts on understanding the constraints of these devices that are limiting their massive use. To achieve this particular objective we have combined different techniques trying to generate a more accurate and reliable description of the internal processes during the operation of the photoconversion devices. Two combinations of techniques that we have studied in this thesis can be separated:

- Hysteresis and IS
- Modulated techniques: IS, IMPS and IMVS

In this chapter, we will give an overview of this thesis. We will present the state of the art of the research areas in which this thesis is developed. The starting hypotheses, based on those previous results, will be presented. We will discuss some of the obstacles we have overcome during the research, including technological limitations. And also we will highlight the main results we have obtained. The details of the results we have obtained in this thesis will be presented in **CHAPTER 4**, **CHAPTER 5**, **CHAPTER 6** and **CHAPTER 7.**

3.2. Hysteresis and Impedance Spectroscopy in Perovskite Solar Cells

In line with the goals of this thesis, we have explored the relationship between hysteresis and Impedance Spectroscopy (IS), focused on perovskite solar cells (PSCs). PSCs present unique properties that make them a very promising technology to transform solar energy into electrical energy. However, the stability of these devices is the main limitation that prevents them from being used on a massive scale, see **Section 1.3** for further details. As we will expose in this section, this lack of stability results in a wide variety of hysteresis and IS responses that are challenging to fully understand, making PSCs a convenient system for investigating the relationship between these responses. Following our objectives, we have approached this investigation with the aim of providing further insight into these photoconversion devices, with the hope that it could be useful for the improvement of their performance

3.2.1. Hysteresis Features

As mentioned above, the hysteresis effect occurs when there is a difference in the current measured when the applied voltage is sweeped from short-circuit to open-circuit (Forward scan) and vice versa (Reverse scan). In perovskite solar cells, it has been shown that these currents vs voltage curves, and therefore the hysteresis, could depend on many external parameters such as the scan-rate, prebiasing voltage, temperature and light intensity.[1-3] The hysteresis may also depend on the device design, such as the perovskite composition or the external contacts.[4-5] Considering, in addition, the instability of these devices, it is not surprising that there are many hysteresis features reported in the literature, some of which are presented in **Figure 3.2**.[6-7] As can be noted in this figure, the hysteresis in general appears as a clear difference in the short-circuit currents, open-circuit voltages or fill factors between the Forward and Reverse curves. As discussed in **Section 2.2.3**, hysteresis can be grouped into two categories: Normal Hysteresis (NH) and Inverted Hysteresis (IH), corresponding to more current (absolute value) in the Reverse and the Forward scan, respectively (as shown in **Figure 2.9**). Other more peculiar effects have been observed, such as a "Bumbp" effect in the Forward curve (**Figure 3.2**b) or an intersection between the Forward and Reverse curves, but these effects are usually interpreted as extreme cases or combinations of the NH and IH.[6, 8-10]

Several mechanisms have been proposed to explain the different hysteresis features, including ferroelectric polarization, charge trapping and detrapping, unbalanced distribution of electrons and holes, capacitive effects, charge accumulation at the interfaces, space-charge buildup and unfavourable energy level alignment.[4, 6, 11-15] The Forward or Reverse scans are generally measured at scan-rates between 10 and 200 mV/s from around 0 to 1 or 2 Volts, thus it takes approximately between 5 and 200 seconds to measure each scan. It has been reported that halide vacancy diffusion and the response of ions accumulated at the perovskite/selective contacts interfaces have characteristic times in the range of 10^{-1} and 10^{0}-10^{2} seconds, respectively.[16] Since the measurement times of each scan is in the range of ionic movements, the hysteresis in PSCs is usually related to the mixed ionic-electronic nature of the perovskite, with a critical dependence on the perovskite/selective contacts interfaces.

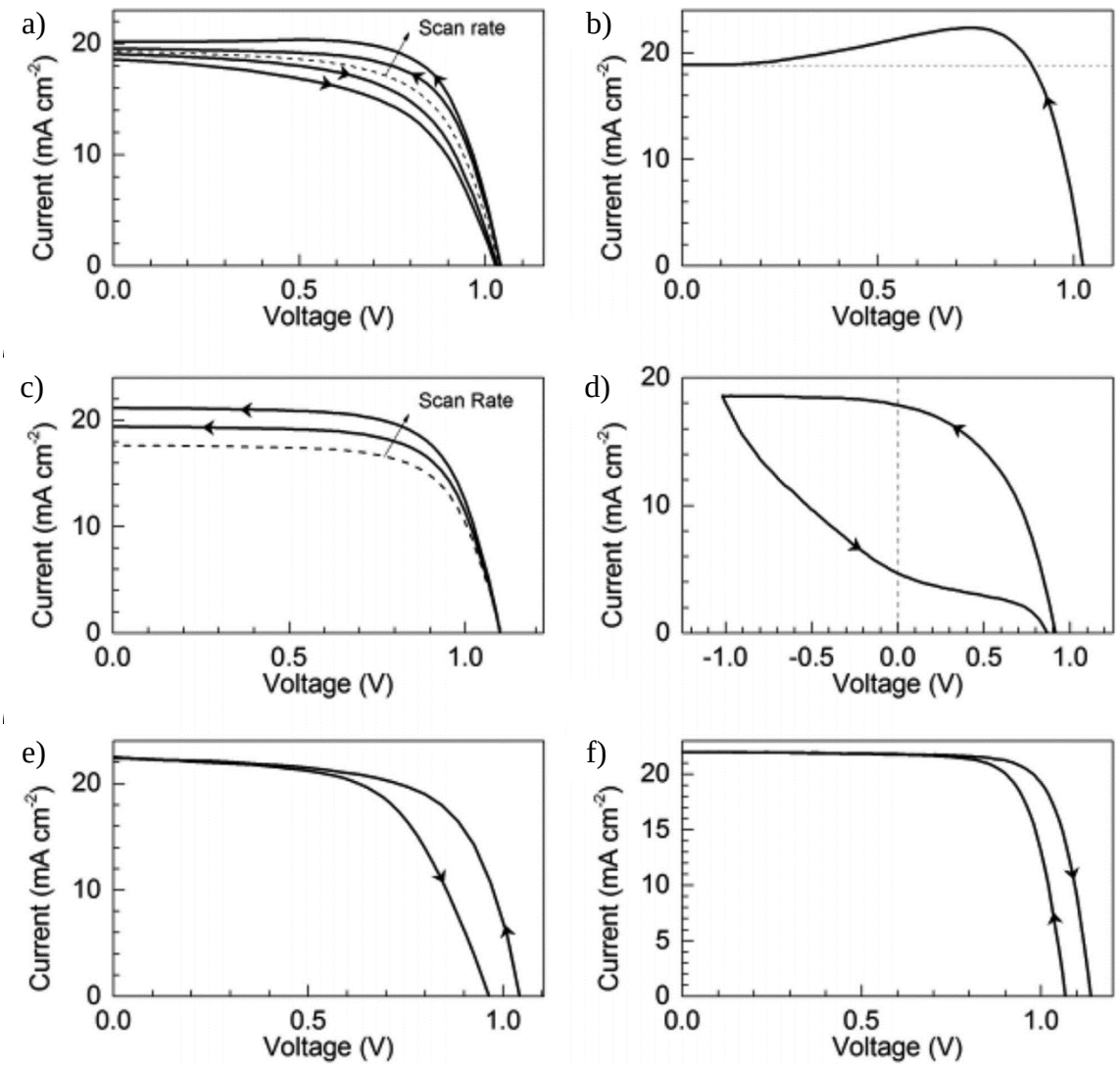

Figure 3.2 Scheme of some of the hysteresis features observed in PSCs. The arrows show the direction of the sweep. Dashed lines indicate in a) and b) the steady-state curve, and in b) and d) the short-circuit current and the zero bias, respectively. Adapted from ref. [7], Copyright 2018, WILEY-VCH Verlag GmbH & Co. KGaA, Weinheim.

3.2.2. Impedance Spectroscopy Responses

Impedance Spectroscopy (IS) is a powerful technique because the application of modulations (also known as small perturbations) with different frequencies allows the separation and the study of the limiting processes with different characteristic times. This technique is very useful when the processes that limit the performance of the device under study are known in advance. In these cases, a simple analysis of the resulting spectra through an equivalent circuit (EC), allows the extraction of quantitative parameters of these limiting processes, including recombination lifetimes, diffusion coefficients and charge-transfer resistances, to name a few.[17-19] This is the case for many photoconversion devices, such as organic solar cells[18] and dye-sensitized solar cells.[19] However, in the case of perovskite solar cells, their instability and susceptibility to a large number of variables discussed above, capable of generating different hysteresis behaviours, can also generate a large variety of IS responses. These seemingly unpredictable outcomes are the main reason behind the ongoing discussions about the interpretation of the IS responses of PSCs.

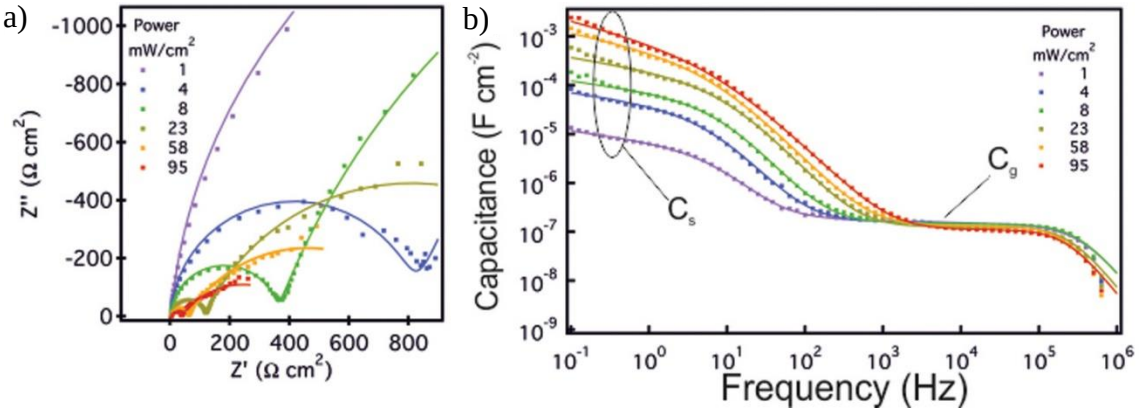

Figure 3.3 Typical two-arc IS response of PSCs in a) a Nyquist Plot and b) the capacitance in a Bode Plot. The measurements were performed under short-circuit conditions at different irradiation intensities in a PSC of planar structure FTO/TiO_2/$MAPbI_3$/spiro-OMeTAD/Au. Adapted from ref. [20], Copyright 2016, American Chemical Society.

Despite the wide variety of IS responses reported, **Figure 3.3** is an example of the most common response observed in highly efficient and reproducible PSCs.[20-23] In the Nyquist Plot (**Figure 3.3**a) two arcs are observed, the high-frequency one in the left and the low-frequency on the right, see also **Figure 2.11**. These two arcs are correlated with the two plateaus in the Bode Plot of the capacitance (**Figure 3.3**b). There is a fairly widespread consensus that the capacitance observed at high frequencies is related to the geometrical capacitance (C_g). This is mainly because it has been observed to be thickness-dependent according to its dielectric constant, while being independent of light and frequency, as shown in **Figure 3.3**.[20] On the other hand, the low-frequency capacitance has been found to depend on the illumination, reaching gigantic values (~10^{-2} F cm^{-2}).[24-25] Moreover, this capacitance is observed at very low frequencies, approximately in the range between 10^1 and 10^{-2} Hz, i.e. times between 10^{-1} and 10^2 seconds, that corresponds

to ionic transport and accumulation at interfaces, as discussed above.[16] These are the main reasons why this capacitance has been related to electrode polarization (C_s).[26]

In contrast to the apparent consensus on the interpretation of capacities, the interpretation of resistances has been less clear. Probably the most popular way to extract resistance values for the IS responses as in **Figure 3.3** is by analyzing them with the EC proposed by Garcia-Belmonte and co-workers.[20] However, the two resulting resistances have been shown to have a similar dependence on illumination and voltage, suggesting that they are related in some way that has not yet been fully clarified. Many other ECs have been proposed to analyze this typical two-arc IS response of PSCs, which may even result in exactly the same spectrum with different values for their corresponding resistances, which will be discussed in more detail in **Section 3.3.1**.[27-30] As already discussed, this is one of the main limitations of IS spectra analysis and we will discuss this issue in detail in the next sections and chapters.

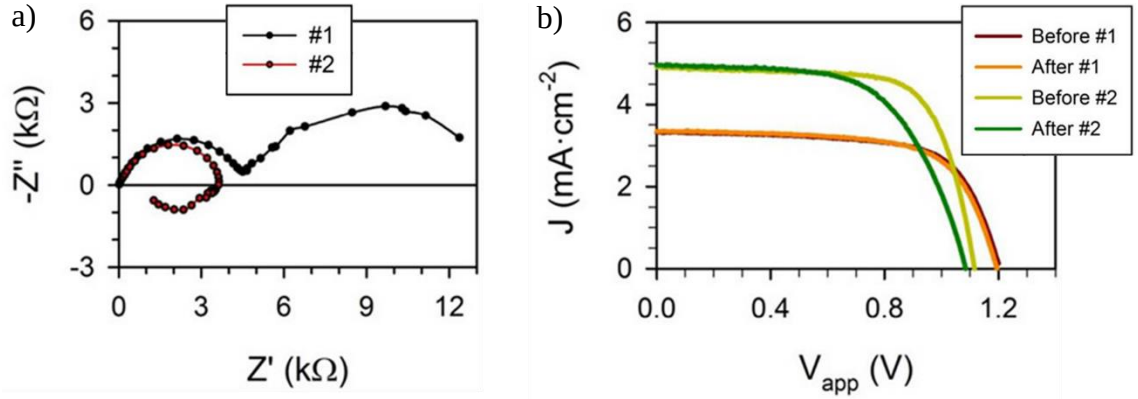

Figure 3.4 a) IS response of samples #1 and #2 taken at a fixed voltage of 0.7 V and under 1 sun illumination. A prominent arc below the x-axis appears at low frequencies for sample #2. b) Comparison of the *j-V* curves before and after the IS measurement of each sample, measured as a Reverse scan, from positive to zero potential. Adapted from ref. [31], Copyright 2017, American Chemical Society.

In addition to this typical response of two arcs with a giant capacitance at low frequencies, PSCs have also repeatedly presented negative capacitances.[22, 31-35] Fabregat-Santiago et al. characterized two PSCs with $CsPbBr_3$ as the absorber and TiO_2 and polytriaryl amine (PTAA) as electron and hole selective layers, see **Figure 3.4**.[31] Sample #1 presented the typical arcs discussed above, while Sample #2 presented a similar arc at high-frequency but an arc in the fourth quadrant at low frequencies, as can be seen in black and red dots in **Figure 3.4**a. As shown in **Figure 2.11**, the arc in the fourth quadrant of the Nyquist plot is correlated with the negative values of the capacitance at low frequencies. **Figure 3.4**b compares the *j-V* curves before and after the IS measurement of each sample, it is clear that Sample #1 presents approximately the same performance, while Sample #2 with the negative capacitance presents a loss in FF and V_{OC}.[31] This effect has also been observed in other devices such as organic light-emitting diodes (OLEDs)[36] and dye-sensitized solar cells (DSSCs).[37] Over the last few decades, several different explanations have been proposed to explain this phenomenon, making it one of

the most challenging phenomena to understand.[36, 38-40] Despite the different explanations, there seems to be a fairly general agreement on the unfavourable effect of this feature on the performance of the device.[31, 37]

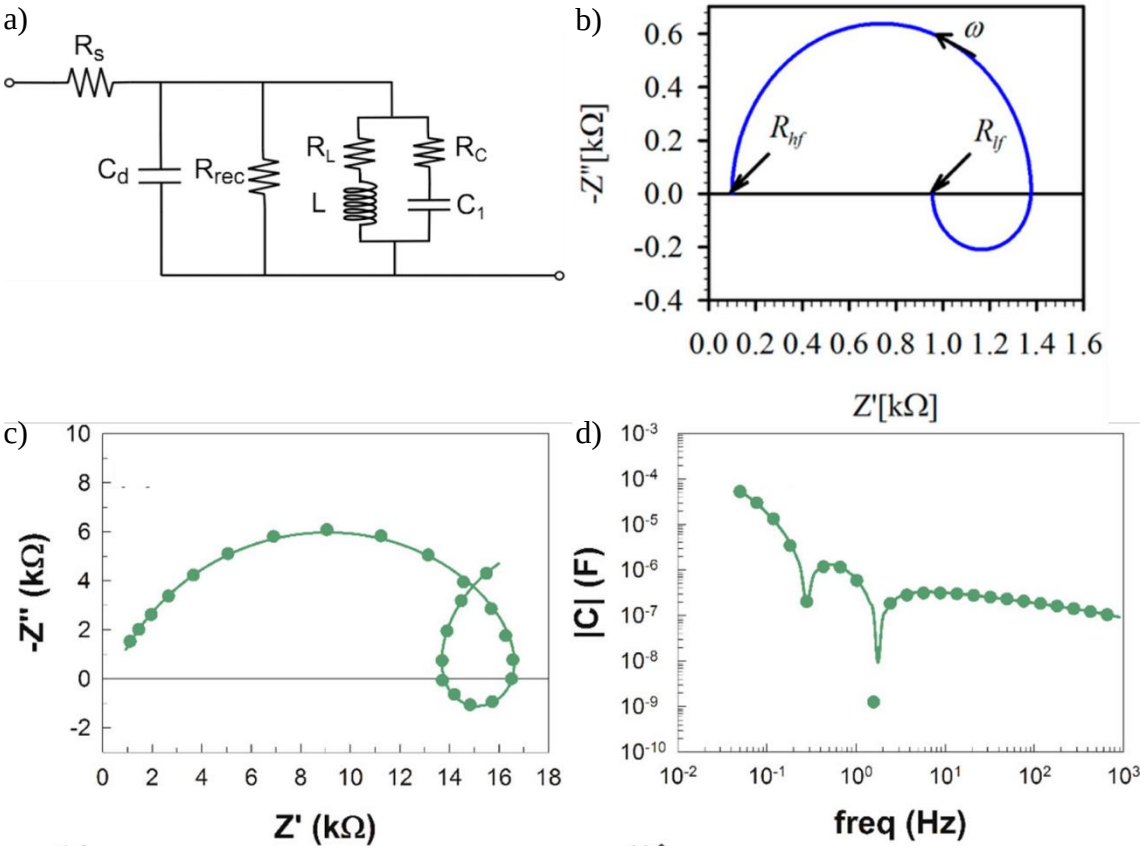

Figure 3.5 a) Equivalent circuit (EC) obtained through the surface polarization model (SPM). In this circuit, R_S is the series resistance, C_d is the dielectric o geometrical capacitance (C_g), R_{rec} is the recombination resistance, R_L is the series resistance with the inductance L, and R_C is the series resistance with the surface charging capacitance C_1. b) Simulation of this EC resulting in a negative capacitance. c) Nyquist and d) capacitance−frequency spectra obtained under illumination and with an applied bias of 0.7 V. The circles represent the experimental points, while solid lines are the fitting curves using the EC. See [38] for de values of the elements in the EC corresponding to b), c) and d). Adapted from ref. [38], Copyright 2017, American Chemical Society.

Bisquert et al. have suggested that the negative capacitance observed in OLEDs is caused by electron injection through interfacial states.[36] Anaya et al. suggested that this could also be the cause of the negative capacitances they observed in their PSCs.[32] Another explanation for the negative capacitance was later given by Bisquert and co-workers by means of the surface polarization model (SPM).[38] The SPM is based on the idea that the huge electronic and ionic charges accumulated at the perovskite/selective contact interface, produce a surface voltage.[6] **Figure 3.5**a shows the EC they obtained from the SPM. As can be seen, it presents an inductance element that can generate the negative capacitance in **Figure 3.5**b. The inductance element in **Figure 3.5**a, and

therefore the resulting negative capacitance, is the result of the delay of the surface voltage, proposed in the SPM, and depends on a certain kinetic relaxation time. This time is proposed theoretically in the SPM, therefore, its value is unknown and depends on the process in the device that generates this response. Jacobs et al. showed drift-diffusion simulations where the negative capacitance at low frequencies could be generated by the phase-delayed recombinations due to the ionic movement and accumulation at the interfaces.[41] We will continue this discussion in **Subsection 3.2.4** and **CHAPTER 4**.

In addition to the IS responses of PSCs we have discussed, the typical two arcs and the negative capacitance, other less often phenomena have been reported. The inductive loop is a feature that has been reported several times.[32, 38, 42-43] As its name indicates, it consists of a loop at intermediate frequencies, as can be seen in **Figure 3.5**c. This feature is closely related to the negative capacitance at low frequencies, the crossover to the fourth quadrant generates a range of intermediate frequencies in which the capacitance becomes negative, in the plot of the absolute value of the capacitance (**Figure 3.5**d) corresponds to the region between the two valleys. Bisquert and co-workers showed that the EC deduced from the SPM can also reproduce this phenomenon, see the solid lines in **Figure 3.5**c and d.[38] Finally, it is worth mentioning that the presence of a third arc has also been reported, both at high and intermediate frequencies.[28, 41, 43-44] However, both the inductive loop and the third arc in PSCs are phenomena that have generally been associated with the lack of optimization of the device, which has been disappearing as PSCs have been optimised.

3.2.3. Normal Hysteresis and Giant Capacitance

Normal Hysteresis is the most common feature for PSCs and has been observed since the first devices under investigation.[1-2, 45] As discussed in the previous subsections, this hysteresis is associated with the electronic and ionic accumulation at the perovskite interfaces with the selective contacts, which also generates the giant capacitance at low frequencies in the IS measurements. In fact, this relationship between these two features has been reported several times for different PSCs.[9, 14, 23, 41, 46] To easily understand the generation of normal hysteresis by the presence of a huge capacitance in PSCs, it is sufficient to compare the charge and discharge curves of a capacitor as shown in **Figure 2.4** with a typical normal hysteresis response as shown in **Figure 2.9**.

The relationship between these two features was demonstrated by Park and co-workers, as shown in **Figure 3.6**.[47] The authors compared two types of PSCs, a normal structure using TiO_2 as ESL and an inverted structure with PCBM as ESL, see the insets of **Figure 3.6**a and b, respectively. The normal structure presented a pronounced normal hysteresis, while the inverted structure presented almost no hysteresis, as evidenced in **Figure 3.6**a and b. When comparing the IS responses of these two devices, they found that at low frequencies, the normal structure had a capacitance of more than one order of magnitude higher than the inverted structure, both in darkness and under illumination, as can be seen in **Figure 3.6**c and d respectively.

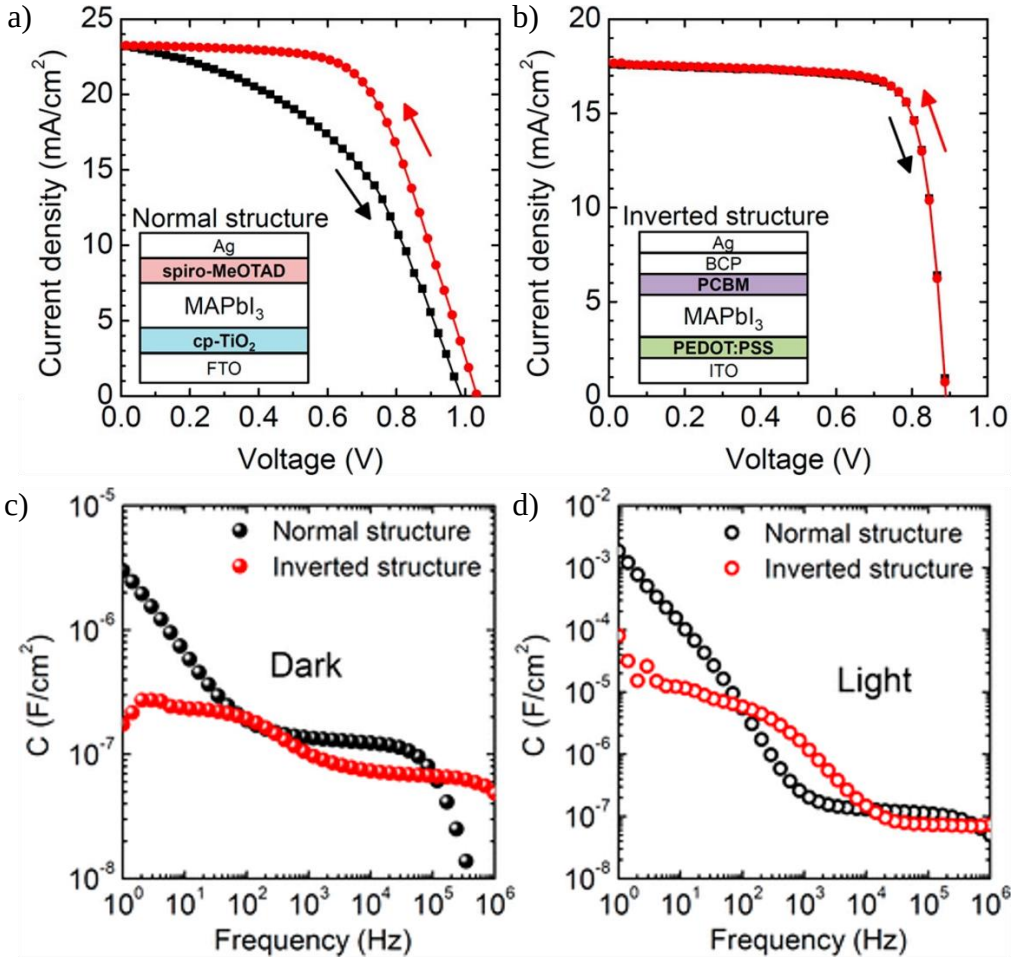

Figure 3.6 Forward (black) and Reverse (red) $j-V$ curves of the a) cp-TiO_2/$MAPbI_3$/spiroMeOTAD (normal) structure and b) the PEDOT:PSS/$MAPbI_3$/PCBM (inverted) structure. Respective capacitance-frequency curves c) under dark and d) under one sun illumination at short-circuit condition (bias voltage = 0 V). Adapted from ref. [47] , Copyright 2015, American Chemical Society.

3.2.4. Inverted Hysteresis and Negative Capacitance

Based on the state of the art presented in this section, our hypothesis was that inverted hysteresis had to be related to the presence of negative capacitance. The details of the results published to prove this hypothesis are presented in **CHAPTER 4**. The first proof of our hypothesis was found while investigating the effect of humidity on PSCs, see **Figure 3.7**a, b and c. For this investigation, we exposed a $MAPbI_3$ PSC progressively to different relative humidities. We observed a systematic reduction of hysteresis with humidity, starting from a positive value (normal hysteresis), for the fresh device under dry working conditions, and reaching negative values (inverted hysteresis), at high values of relative humidities values, as can be seen in **Figure 3.7**b. When comparing the capacity values at low frequencies, obtained through IS measurements, as a function of the relative humidity, we observed a similar trend in **Figure 3.7**c, under dry working conditions we obtained the maximum capacity and this value decreased with the relative humidities, reaching negative values at high relative humidities values. The relationship between the

presence of a negative capacitance (or inductance) with inverted hysteresis could be clarified by comparing the current response of a simple circuit with an inductor under different scan-rates, as shown **Figure 2.5**, with a typical inverted hysteresis response as shown in **Figure 2.9**.

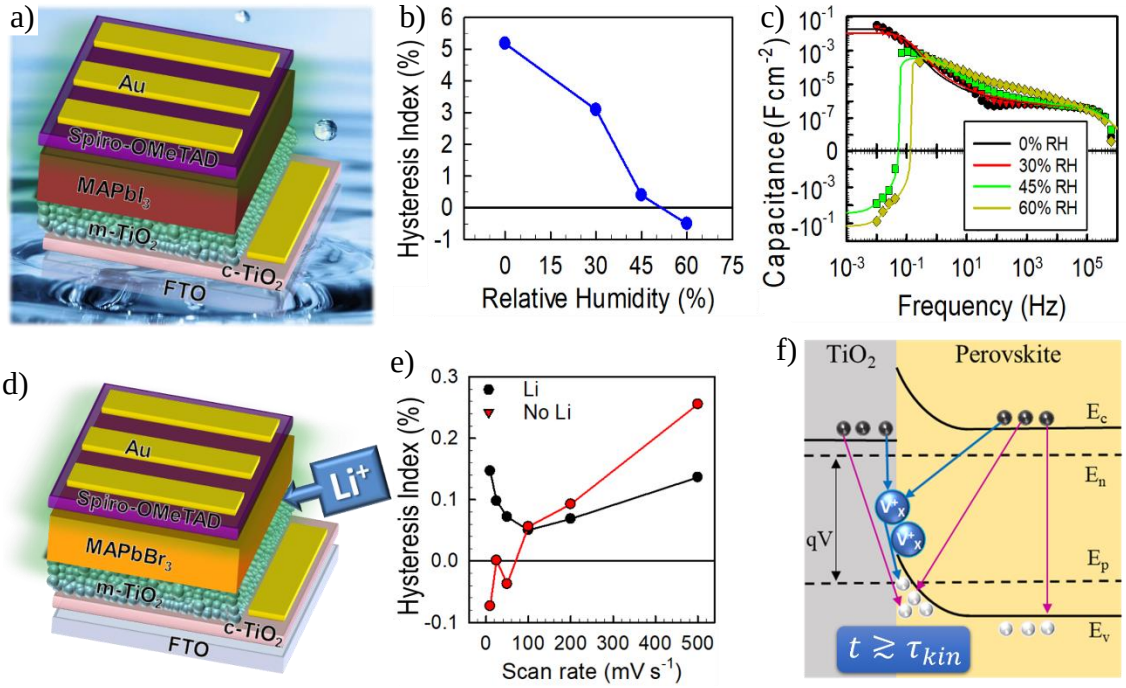

Figure 3.7 The scheme of the a) $MAPbI_3$ devices exposed at different relative humidities with the resulting b) hysteresis and c) capacitance-frequencies measured at 0.95 applied voltage. And the scheme of the b) $MAPbBr_3$ devices with and without Li treatment with the resulting e) hysteresis. f) Schematic diagram of the surface accumulation and binding of ions/vacancies responsible for the large kinetic relaxation time (τ_{kin}), favouring interfacial electronic recombination processes shown with blue arrows. Black and white spheres represent electrons and holes, respectively. Blue spheres represent ionic vacancies.

These experimental results seemed conclusive about the connection between inverted hysteresis and negative capacity, but we wanted to go further. To show that this effect was not only related to $MAPbI_3$ devices under humidity, we studied $MAPbBr_3$ devices that Aranda and co-workers had optimised in a previous work. In that work, they showed, employing PL measurements, that the introduction of Li in the perovskite/TiO_2 interface reduced the non-radiative interfacial recombination, resulting in a record open circuit voltage, see **Figure 3.7**d.[48] In **Figure 3.7**e we show that when we measure cyclic voltammetries (CVs) at different scan-rates the optimized PSCs (with Li) always present normal hysteresis, while in the cells without Li we observe inverted hysteresis if the scan-rate is low enough.

In addition, we employed the equivalent circuit in **Figure 3.5**a from the surface polarization model (SPM) to analyze the IS spectra.[38] We obtained characteristic times for the process related to the negative capacitance in the order of 10^0-10^2 s, for both the

$MAPbI_3$ cells at high humidities and the $MAPbBr_3$ cells without the Li treatment. As mentioned above, these times have been related to ionic accumulation and interaction at the perovskite/selective contacts interfaces.[16] Therefore with this work, in addition to demonstrating experimentally the relationship between negative capacitance and inverted hysteresis, we were able to show that these effects can be generated by delayed recombination caused by the surface accumulation and interactions of ions/vacancies at the perovskite/selective contacts interface.

We claim that the relationship established between the inverted hysteresis and the negative capacitance (or inductance) is universal. In fact, Bisquert and co-workers have afterwards shown the validity of this relationship for memristor devices.[49]

3.3. Individual Analysis of Modulated Techniques

In the previous section, we have illustrated the great capability of IS to study the internal processes involved during device operation, but we could also note the limitations of this technique. As we will see in the next section, a promising idea to overcome these limitations is the combination of IS with IMPS and IMVS. But before exploring such a combination, in this section, we will intend to state the main limitations that arise from the typical individual analysis of each modulated technique.

It is worth noting that these three techniques are used to extract parameters indirectly. For all three techniques, it is necessary to propose a model that allows transforming the measured parameters, such as resistances, capacitances or characteristic frequencies/times, into parameters describing the internal processes of the device under investigation, such as recombinations, charge accumulations or lifetimes.

3.3.1. Impedance Spectroscopy

As mentioned above, the most typical analysis of the impedance spectroscopy (IS) responses is through an equivalent circuit (EC). This approach has proven to be very useful in a wide variety of systems, such as dye-sensitized solar cells[19] and organic solar cells.[18] In those cases, it was found a consensus in the appropriate EC, with a clear relationship between their elements and the properties of the systems. However, when the EC for the system is not clearly established, the analysis of the corresponding IS responses is more challenging, as is the case for perovskite solar cells (PSCs) discussed in the previous section. To clarify this problem, in **Figure 3.8** we show three EC that has been proposed for the analysis of the typical two arcs IS responses of PSCs. [20, 28, 50] The problem is that these three ECs can reproduce a two-arc spectrum in exactly the same way, so it is a challenge to distinguish which of the three is the one that most adequately describes the system under study. Although all three ECs can generate the same spectrum, the corresponding values of the elements will be different. Distinguishing the most appropriate EC is crucial, since each element is related to a different process and according to their position they have a different physicochemical meaning, as can be noted from the names assigned in each EC in **Figure 3.8**. This limitation of IS spectra analysis is well known, in 1994 Fletcher published a paper showing groups of analogous ECs, i.e. capable of generating the same response.[30]

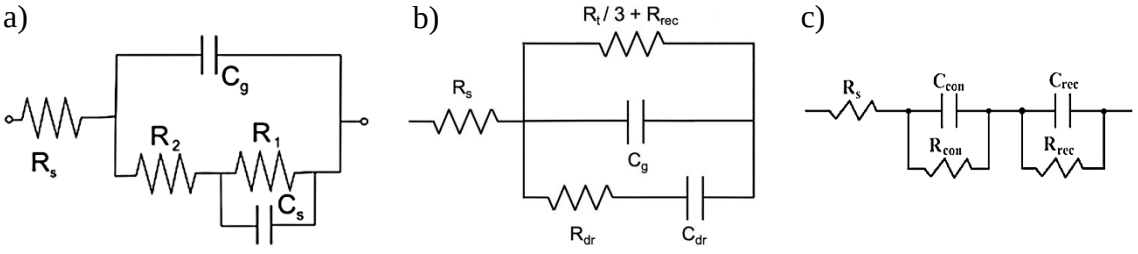

Figure 3.8 Analoguee equivalent circuits proposed for the analysis of the typical two arcs IS responses obtained for PSCs. a) Adapted from ref. [20], Copyright 2016, American Chemical Society. b) Adapted from ref. [28], Copyright 2019, Elsevier. c) Adapted from ref. [50], Copyright 2020, Elsevier.

Other information that can be extracted from the IS response is the characteristic times of the different processes observed, as shown in **Figure 2.11**. As we pointed out in **Subsection 2.3.1**, from the point of view of the equivalent circuit, this characteristic time will be related to the involved elements, such as the product between the resistance and the capacitance or the quotient between the inductance and the resistance, as in the case corresponding to Equation (2.42) and (2.43) respectively. However, from the point of view of the internal process in the device under investigation, the analysis of these times can be challenging as it will depend on the interpretation of the involved elements. For example, if the resistance and the capacitance in the EC are related to the recombination resistance and the chemical capacitance of the absorber material, then the corresponding characteristic time can be interpreted as the recombination lifetime.[51] On the other hand, the combination of other resistances with other capacities can result in characteristic times with a less clear physicochemical interpretation. As shown in **Figure 2.11**, to obtain the characteristic times of the processes observed in the IS spectra, it is not necessary to analyse the spectra through an EC, these times can be calculated as the inverse of the frequency corresponding to the maximum or minimum of the corresponding arc. However, the interpretation of the characteristic time obtained in this way can be even more difficult.

3.3.2. Light Intensity Modulated Techniques

IMPS and IMVS have been employed to analyse many photoconversion devices, such as dye-sensitized solar cells,[52-53] photoelectrodes for water oxidation,[54-56] and even perovskite solar cells (PSCs).[57-58] IMPS was extensively developed by Peter and co-workers[59-60] and primarily used for the characterisation of carrier transport processes,[61-62] while IMVS has been used mainly for the study of recombination processes.[63] Despite their growing popularity, these techniques have been less explored than IS. This is probably the main reason why the analysis of IMPS and IMVS spectra is usually limited to the characteristic times, obtained from the maximum and minimum of the arcs in the Nyquist plots, as shown in **Figure 2.13**. As discussed in the previous subsection for the IS case, the characteristic times contain only a small part of all the information that can be extracted from a given spectrum, so limiting the analysis to these parameters implies a loss of information. Finally, it must be kept in mind that the spectra analysis limited to characteristic times also implies the imposition of a model on the system under analysis. Therefore, the extraction of more information allows for a more reliable assessment of the model.

As an example of the individual analysis, **Figure 3.9** shows the characterisation that Peter and co-workers did in 2015 on a group of PSCs using IS, IMPS and IMVS.[64] Although they used the three techniques, the analysis of each technique was done separately. **Figure 3.9**a shows the EC they proposed to analyse the IS spectra shown in **Figure 3.9**b.

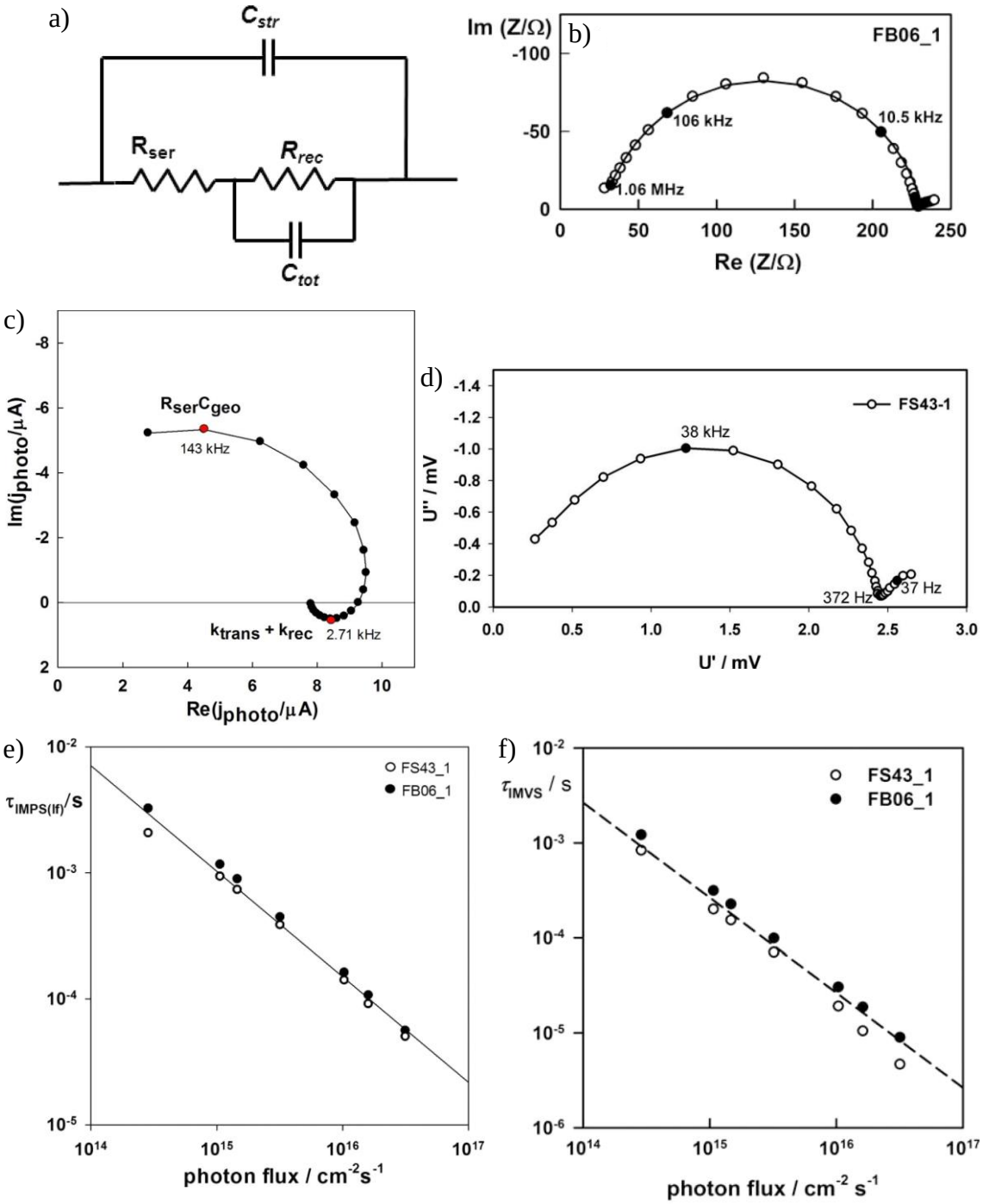

Figure 3.9 Typical separate analysis of modulated techniques, applied to a group of PSCs. A) Equivalent circuit, to analyse the b) IS responses, with elements representing the recombination resistance, R_{rec}, cell capacitance, C_{tot}, series resistance, R_{ser}, and the stray capacitance C_{str}. c) IMPS response showing the RC time constant at high-frequency and a low-frequency semicircle which is related to transport and recombination. d) IMVS response. Intensity dependence of the lifetimes measured by e) IMVS and f) IMPS, for two PSCs. Adapted from ref. [64], Copyright 2015, American Chemical Society.

Figure 3.9c shows one of the IMPS responses they measured, where they highlighted the two characteristic times with their corresponding interpretation, identified as the minimum, $\tau_{IMPS(hf)}{}^{-1} = R_{ser}C_{geo}$, and maximum, $\tau_{IMPS(lf)}{}^{-1} = k_{trans} + k_{rec}$, of the high- and low-frequency arc respectively. In addition to these two values, they correlate the IMPS low-frequency limits with the charge transfer efficiency. Defining this efficiency as a function of the charge transfer rate (k_{trans}) and recombination rate (k_{rec}) allows them to calculate both rates, by also using τ_{IMPS}. **Figure 3.9**d shows one of the IMVS responses, where two arcs are observed, but only the high-frequency (on the left) is completed, from which they extract their characteristic time (τ_{IMVS}).

Figure 3.9e and f show τ_{IMVS} and τ_{IMPS} as a function of the photon flux, this plot is in gerall very usuful to evaluate the model as different processes could depend differently on the light. The authors propose that τ_{IMVS} is related to the product $R_{rec}C_{tot}$ which, as can be seen in **Figure 3.9**a, will also correspond to a characteristic time of IS. This analysis is a good example of the large amount of information that can be extracted from IMPS and IMVS, and in turn, shows the complementarity between the three techniques, these two and IS.

3.4. Combination of Modulated Techniques

As discussed in the two previous subsections the modulated techniques have an enormous potential to identify and analyse the internal processes that limit the performance of different photoconversion devices. However, each of these techniques used separately gives limited information about the device under investigation. Fortunately, the information from the techniques is complementary, so their combination would result in a more accurate and detailed analysis. We can make the analogy that each of these techniques is a photograph of the device from a particular angle, then to know what the device looks like we must combine the photographs from different angles.

3.4.1. State of the Art

From the definitions of the transfer functions, Equations (2.38), (2.47) and (2.49), and from **Figure 2.12**a it is clear that the three techniques (IS, IMPS and IMVS) are closely related. The main relationship between them is

$$Z = \frac{W}{Q} \tag{3.1}$$

This relationship was suggested and confirmed experimentally for a dye-sensitized solar cell in 2011 by Halme, one of the first researchers to study in detail the combination of IS, IMPS and IMVS.[65] Afterwards, this relationship was also confirmed experimentally in other devices such as hematite photoanodes for water splitting[66] and perovskite solar cells.[67] In 2017, Bertoluzzi and Bisquert derived Equation (3.1) by describing **Figure 2.12**a as a surface into the tridimensional space current-voltage-light, and defining the IS, IMPS and IMVS transfer functions through the partial derivatives of this surface.[68] Despite all this, in 2020 Almora et al. presented measurements on different devices where Equation (3.1) was not entirely valid.[69-70] The discussion about this equation will continue through the following subsections and chapters.

While Equation (3.1) could be considered as the fundamental relationship between the three techniques, it does not provide information about how they can be combined to extract further information. On the contrary, this equation turns out to be mainly a constraint. Different approaches have been used to combine these techniques. This is the main topic of this thesis, so we will extend this discussion through the rest of the thesis. In the remainder of this subsection, we will highlight the main results on which this thesis is founded.

Halme, in his 2011 publication, in addition to confirming Equation (3.1), presented an equivalent circuit model for dye-sensitized solar cells for the three techniques, based on earlier results by himself and by Bay with West.[65, 71-72] However, in none of these works the models were implemented to analyse the IS, IMPS and IMVS experimental spectra. A different approach was presented in 2016 by Klotz and co-workers based on the use of the distribution of relaxation times function. This method was used by the authors to analyse a thin film hematite photoanode, showing its potential to separate polarization processes.[66] The disadvantage of this approach is that the implementation is not straightforward.

Bertoluzzi and Bisquert, in addition to derived Equation (3.1), in their 2017 publication, proposed an equivalent circuit for a water-splitting system, see **Figure 3.10**a.[68] As can be seen, this equivalent circuit incorporates the photogenerated current because it is extended to the three transfer functions. A simulation of each transfer function was also presented, as can be seen in **Figure 3.10**b, c and d, evidencing that the same processes in the device can generate different features in the spectrum of each technique. Despite they did not show an experimental implementation of this model, they proposed the extraction of further information by using special frequencies, such as the low- and high-frequency limits, in addition to the characteristic times, see **Figure 3.10**b, c and d.

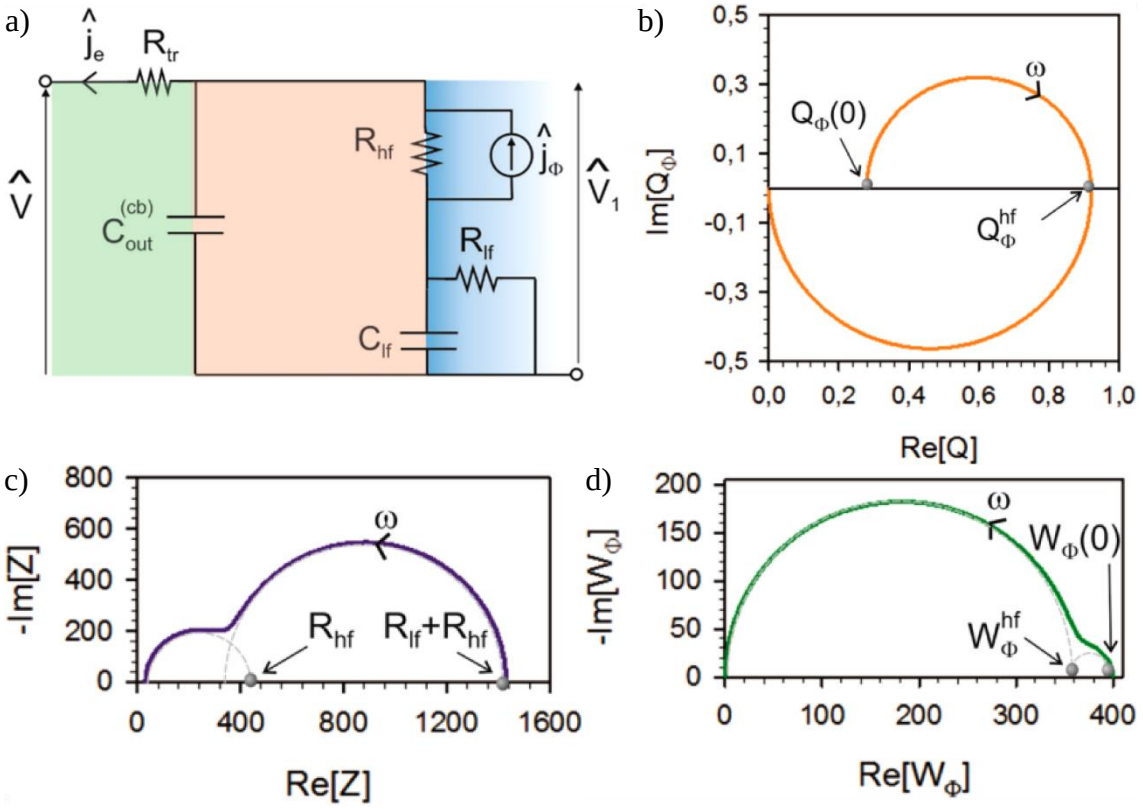

Figure 3.10 a) Equivalent circuit model for water-splitting systems, with the corresponding simulations of the b) IMPS, c) IS and d) IMVS transfer functions. Adapted from ref.[68], Copyright 2017, American Chemical Society.

Following these results, in 2019, Ravishankar et al. proposed the equivalent circuit model shown in **Figure 3.11**a for perovskite solar cells.[62] They presented the experimental IS and IMPS spectra for a PSC and they showed that their model can reproduce the features observed with both techniques, see **Figure 3.11**b and c. Even more, following the methodology proposed by Bertoluzzi and Bisquert of extracting the values of the parameters in the EC for critical frequencies, they were able to extract two sets of parameters, one from IS and the other from IMPS. However, while some of the parameters were in good agreement between the two techniques, other parameters differed significantly.

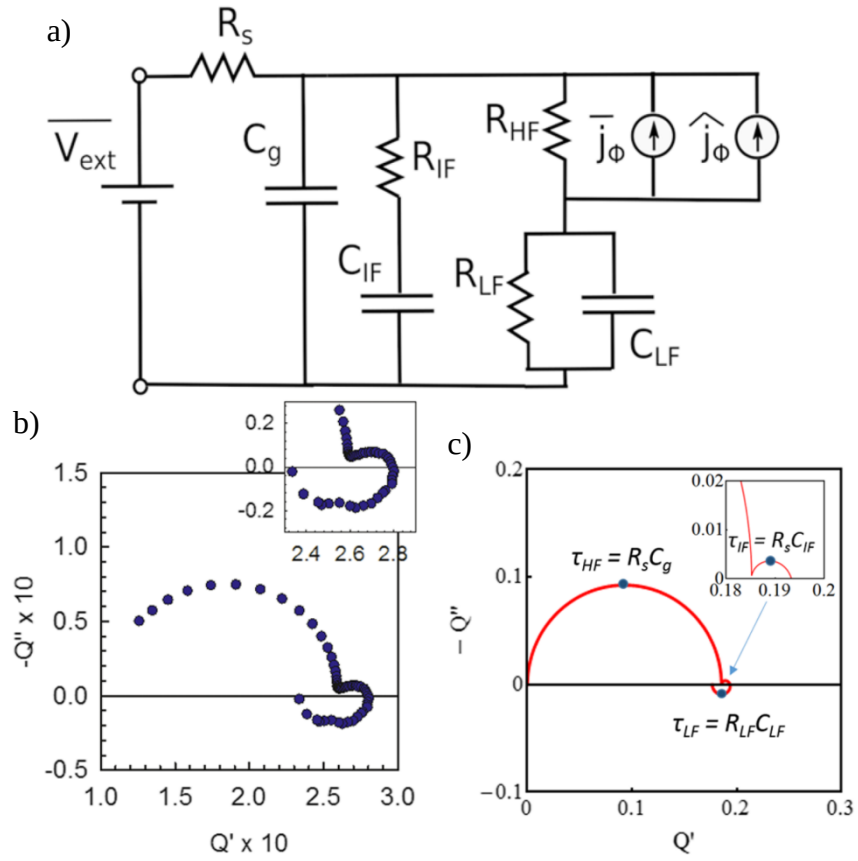

Figure 3.11 a) Equivalent circuit model for perovskite solar cells, with the comparison between b) the experimental IMPS spectrum of a perovskite solar cell and c) the corresponding simulation of the IMPS transfer function. Adapted from ref. [62], Copyright 2019, American Chemical Society.

3.4.2. Hypothesis and Goals

Our initial hypothesis was that there should be a way to analyse IS, IMPS and IMVS using a single model, and that this combined analysis should provide more information than the separate analysis of the techniques. Our general goal, therefore, was to develop a methodology to analyse the three techniques in combination and to use the resulting additional information to answer some of the questions that the separate analysis of the techniques has not been able to address.

As we saw in the previous subsection, before this thesis, papers had been published that made important advances in the combination of IS, IMPS and IMVS. However, these works exposed some of the difficulties in combining these techniques for the practical analysis of photoconversion devices. In the next subsections, we will discuss the specific problems that had to be solved to combine these techniques, and we will present the main results we have achieved.

3.4.3. Measurement Protocol

The first step to make the combination of the techniques is a proper measurement of each of them. As mentioned, IS is the most developed of the three techniques, the instruments have been extensively developed over decades to make proper measurements of this technique. On the other hand, while there are several instruments capable of measuring IMPS and IMVS, they are all comparatively newer, with the measurement procedures still under development, so far mainly focused on individual spectrum analysis and limited to characteristic times. Furthermore, we have found that some measurement equipment present errors in their configuration that may introduce some misunderstanding of the results. As described in **Section 2.4**, we have measured the three techniques with a Potentiostat/Galvanostat Autolab PGSTAT302 equipped with a FRA32M and a LED Driver.

The first consideration to take into account before combining the three techniques may seem a bit obvious: they have to be measured under the same steady-state, i.e. under the same DC parameters: same applied potential, same injected current and same incident light, as shown in **Figure 2.12**a. The time required for each measurement depends mainly on the low-frequency limit up to which it is measured. In our case, we typically measure up to 100 or 10 mHz, and then a measurement of each technique usually takes approximately between 1 to 10 minutes. Therefore, procedures must be applied that allow the investigated sample to reach such a steady-state and then the sample must remain stable during all measurements. This is not always easy, since in certain devices, such as PSCs, irreproducible measurements are often observed, due to their lack of stability. For this reason, we have first focused on silicon photodiodes (SiPhs), whose stability has been well demonstrated.

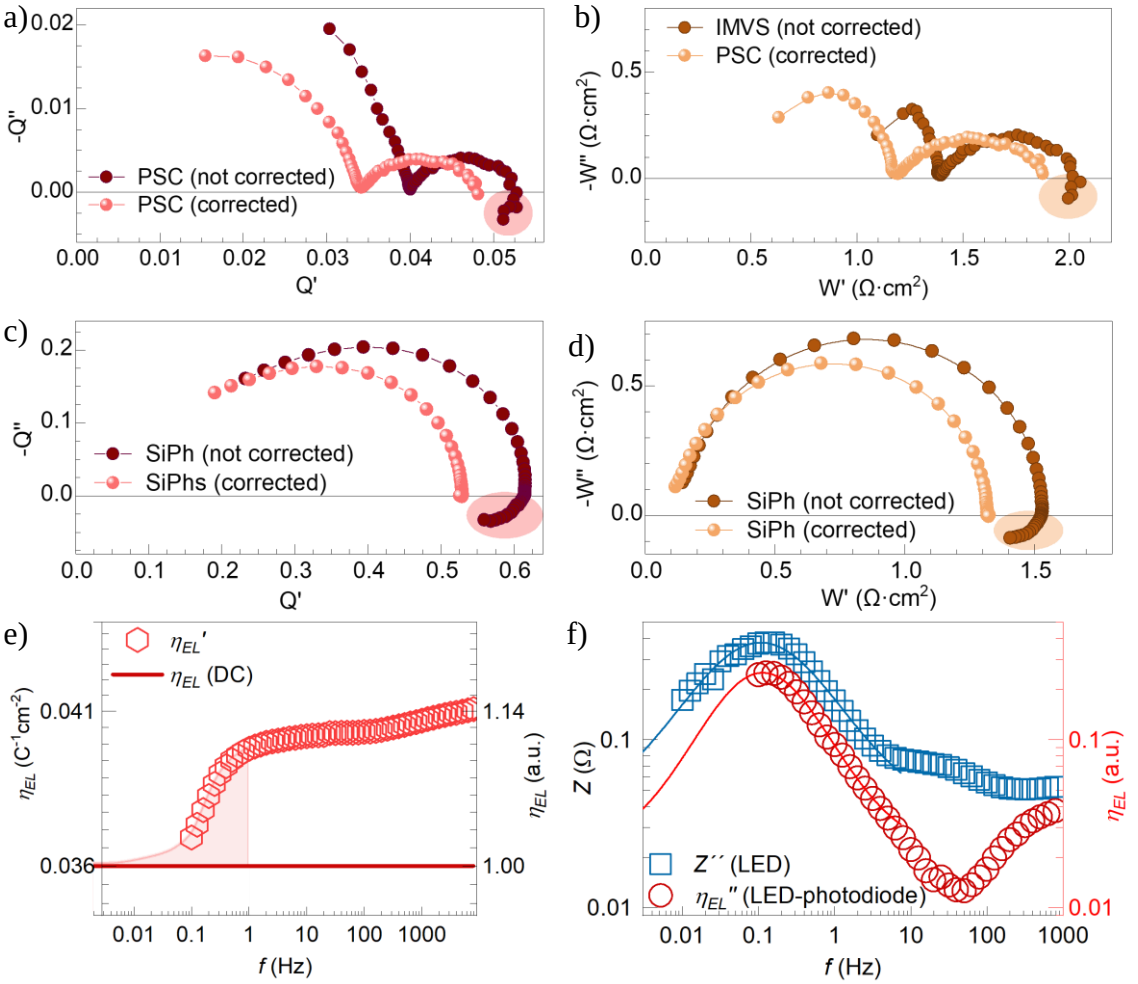

Figure 3.12 IMPS and IMVS response for a perovskite solar cell (PSC), a) and b) respectively, and for a silicon photodiode (Hamamatsu S1133), c) and d) respectively. The measurements were performed from 200 kHz to 0.1 Hz, at open-circuit conditions (980 and 544 mV for PSC and SiPH respectively) under a DC light intensity of 89 mW cm^{-2} from a blue LED (600mA, LXML-PB01-0040 Philips LUMILEDS).[73] The "corrected" spectra indicate a correction of the photon flux by considering the variations in the electroluminescence modulation of the LED used to perturbe the illumination on the sample. e) The modulated electroluminescence rate after calibration compared to the DC estimation. f) Comparison between the impedance and electroluminescence rate spectra of the LED.

The second aspect to take into account is to ensure that the light modulation behaves as required by the model or, alternatively, that it is measured correctly. **Figure 3.12** shows the IMPS (dark red) and IMVS (dark yellow) results of a PSC (**Figure 3.12**a and b respectively) and a SiPh (**Figure 3.12**c and d respectively). By comparing the results from both devices it can be noticed that they have a suspiciously similar process at low-frequencies, which was not expected for the SiPhs, so we have investigated this process in detail.

We discovered that the origin of this artefact is an unexpected fluctuation in the modulated light, with the frequency. This fluctuation is shown with empty hexagons in

Figure 3.12e, as a rate of electroluminescence (η_{EL}), and is compared with the constant assumption in the measurement protocol, obtained from a calibration under DC conditions. Furthermore, we were able to demonstrate that this fluctuation is due to an internal process within the LED used to illuminate the sample, see the comparison of η_{EL} and the IS response of this LED in **Figure 3.12**f and **CHAPTER 5** for more details. Therefore, the solution that we have proposed is to use the properly measured η_{EL} to calculate the appropriate IMPS and IMVS measurements, as can be seen, respectively in pink and light yellow, in **Figure 3.12**a, b, c and d. We see that by correcting these spectra the feature at low frequencies is eliminated, confirming that it is an artefact. These results are presented in **CHAPTER 5.** where we present the details of how to carry out this correction to obtain the appropriate IMPS and IMVS spectra.

3.4.4. Three Techniques, One Equivalent Circuit

Once we manage to achieve reliable measurements of the three techniques we focus on the combined analysis. To do that we continue the approach of the publications of Bertoluzzi and Bisquert[68] and Ravishankar et al.[62] In these two papers, the authors proposed equivalent circuits that can generate the IS, IMPS and IMVS spectra. However, these authors did not implement the circuits proposed to analyse the three spectra simultaneously.

To focus on the development of the methodology for the combined analysis of the spectra, we employed a SiPh, as this is a well-known and stable system. The fundamental relationship between these techniques is given by Equation (3.1) ($Z = W/Q$). We assumed this relationship to be true, so we discarded any set of spectra that did not satisfy this relation. To progress in the analysis of IMPS and IMVS spectra we noted that was essential to incorporate properly the relationship between the photon flux (ϕ) and the free photogenerated charges (j_{ph})

$$j_{ph} = q\,\eta_{sep}\,a\,\phi \tag{3.2}$$

where q is the elementary charge, a is the absorptance, defined as the fraction of ϕ that is absorbed by the device, and η_{sep} is the separation efficiency, defined as the fraction of the absorbed photons that are separated to generate j_{ph}. This relationship was crucial to achieve the analysis of IMPS and IMVS spectra with an EC, because with these techniques, ϕ is measured, but only the fraction given by the product of η_{sep} and a generate free charges (j_{ph}) inside the device. In **Figure 3.13**, as well as in all the other ECs presented in this thesis, it can be noticed how j_{ph} is inside the ECs, while ϕ is only represented as a reference. Therefore, this relationship allowed us to develop a general methodology for the combined analysis of IS, IMPS and IMVS through a common equivalent circuit for all of them. We present these results in **CHAPTER 6**, where we provide all the details of the procedure needed to perform such analysis. To facilitate the application of this methodology to different photoconversion devices, we developed an equivalent circuit considering all elements as general as possible.

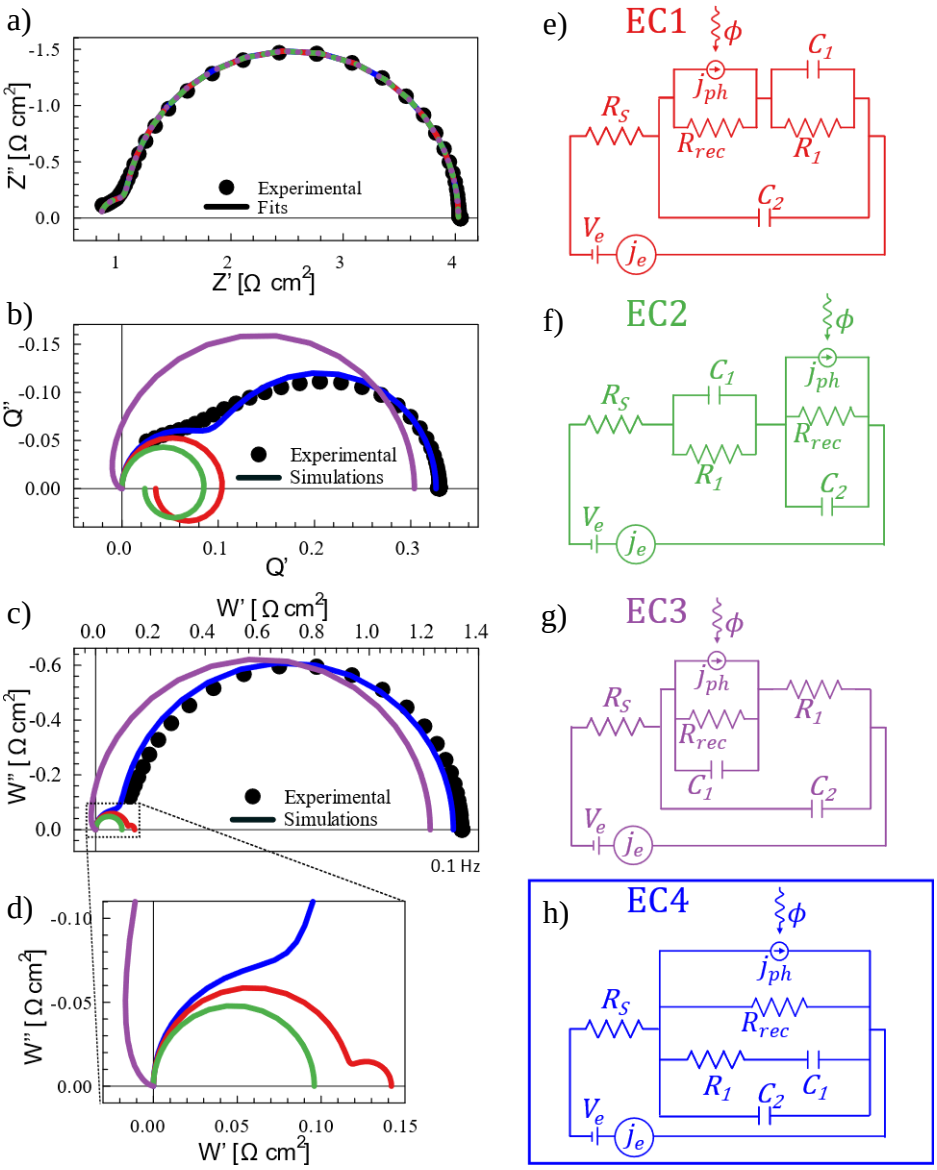

Figure 3.13 Black dots show measured a) IS, b) IMPS, and c) IMVS for a silicon photodiode, under OC condition and 89 mW cm^{-2} blue light (470 nm peak). The different lines in a) are the resulting fits employing the equivalent circuits in e), f), g), and h), respectively with the colour. Following the same colour pattern, the lines in b), c), and d) are the IMPS and IMVS simulations corresponding to the IS fitting results and the absorption measured externally.

By experimentally applying this analysis procedure, to IS, IMPS and IMVS spectra obtained with the protocol explained in the previous subsection, we were able to demonstrate that the combination of the three techniques allows for a more detailed and in-depth analysis compared with the analysis of the techniques separately. Among the descriptions that are accessible by the combination of the three techniques but not for each one alone, we can highlight the more accurate identification of the equivalent circuit model (needed to fit the data) and therefore the internal processes of the device.

We used a SiPh to illustrate these results, **Figure 3.13**a, b, c and d show the measured IS, IMPS and IMVS for this device. The lines in **Figure 3.13**a are the fitting of this

spectrum with the EC in **Figure 3.13**e, f g and h. Note that if the photogenerated current is eliminated from them, which is the case for IS, then these circuits are the same as those in **Figure 3.8**. Therefore, it is not surprising that all these circuits can fit the IS spectrum equally well. However, when we use the results of each fit to simulate the IMPS and IMVS spectra we see that only EC 4 (**Figure 3.8**h) matches the measured spectra. This result corroborates one of our main hypotheses and objectives: the combination of the three techniques has the power to help in the determination of the most appropriate EC. Once the most appropriate EC was determined, we used it to analyse the three techniques, obtaining a good matching for the three spectra, as can be seen in **CHAPTER 6**. In particular, we can highlight that this combined analysis allowed us the quantification of parameters, such as separation efficiencies, inaccessible through the separate analysis of the techniques.

We consider the results obtained in this publication to be of crucial relevance, as they evidence the possibility of combining the techniques, and make clear some of the advantages of the combination compared to each technique separately.

3.4.5. $BiVO_4$ Photoelectrodes: Carrier Diffusion and Recombination

As discussed in **Section 1.4**, the photoelectrochemical cells (PECs) for water splitting are a very promising technology. Especially, $BiVO_4$ used as a photoanode has very interesting properties, such as low synthesis costs and non-toxicity.[74] As discussed, the main limitation of this material seems to be its poor extraction of the photogenerated charge, the causes of which seem to be not entirely clear.[75-76] In particular, it has been shown that the analysis that can be performed on these systems with IS is limited, as a single arc is mainly observed.[77-80] For these reasons, we decided to apply the combined analysis of IS, IMPS and IMVS in a photoelectrochemical cell for water splitting with a photoanode based on $BiVO_4$ doped with Zircon (Zr:$BiVO_4$). This doping is a promising strategy to improve their performance, as mentioned above. The results of this study are shown in detail in **CHAPTER 7**.

As mentioned in **Subsection 1.4.2** and **Subsection 2.2.2**, this device presents many internal processes that limit its performance. These processes depend on the applied voltage, so by choosing the appropriate voltage we can consider that the processes that are mainly limiting the performance of the device are the diffusion and recombination of the electronic carriers. Previous research has made important developments in modelling these processes to interpret the responses of IS, IMPS and IMVS. However, no work used these models for the combined analysis of the three techniques. It was therefore a great challenge, both from a theoretical and practical point of view.

To analyse the IS, IMPS and IMVS spectra of such a photoconversion device, with distributed photogeneration, diffusion and recombination, we extended the procedure described in the previous subsection. First, we generalised Equation (3.2) to a distributed absorption along the absorber material. Then, taking also into account the recombination and diffusion equations as a function of the position in the material, we calculated the IS, IMPS and IMVS transfer functions. Finally, we derive the appropriate EC, i.e. whose transfer functions correspond to those obtained from the fundamental equations, shown

in **Figure 3.14**a. **Figure 3.14**b shows the simulated IS spectrum with this EC that is independent of the absorptance (a), the diffusing species (electrons or holes) and the side from which the device is illuminated, either from the electron selective contact (ES illumination) or from the hole selective contact (HS illumination). **Figure 3.14**c, d, e and f show that the IMPS and IMVS spectra depend on a and the illimination side, so they can be used to extract information on these aspects.

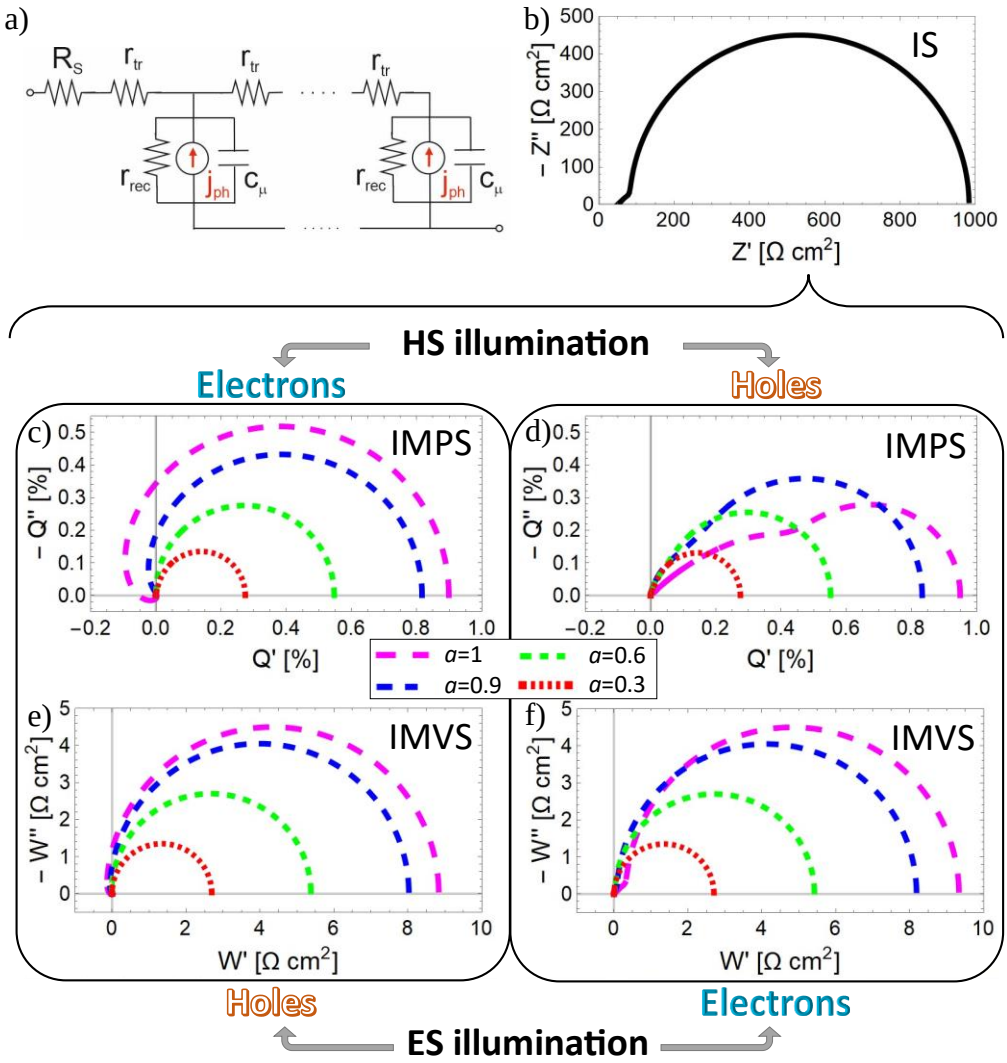

Figure 3.14 a) EC model for single-carrier transport and recombination with distributed absorption, used to simulate b) IS, c,d) IMPS, and e,f) IMVS spectra, with $R_S = 50\ \Omega\ cm^2$, $R_{tr} = 100\ \Omega\ cm^2$, $\omega_D = 450\ rad\ s^{-1}$, $\omega_D = 50\ rad\ s^{-1}$, and $\eta_{sep}\eta_{opt} = 100\ \%$. Consider either electrons or holes as diffusing species, with light reaching the device from the electron selective contact (ES illumination) or the hole selective contact (HS illumination). Each line in the IMVS and IMPS plots corresponds to different absorptance (a) as indicated in the legend.

Furthermore, we have demonstrated that it is possible to use this EC to analyse simultaneously the IS, IMPS and IMVS spectra resulting from the PEC based on Zr:$BiVO_4$. As a result, we have identified the electrons as the limitation of the photogenerated charges extraction of this device, when light reaches from the hole collector contact. Conversely, when the sample is illuminated from the electron collector contact, holes take this role. Additionally, we have been able to obtain a detailed and accurate quantitative analysis of the photoconversion parameters, which has led us to identify the separation efficiency as the main limitation on the performance of this device.

References

[1] H. J. Snaith, A. Abate, J. M. Ball, G. E. Eperon, T. Leijtens, N. K. Noel, S. D. Stranks, J. T.-W. Wang, K. Wojciechowski, W. Zhang, *J. Phys. Chem. Lett.* **2014**, 5, 1511.

[2] E. L. Unger, E. T. Hoke, C. D. Bailie, W. H. Nguyen, A. R. Bowring, T. Heumüller, M. G. Christoforo, M. D. McGehee, *Energ. Environ. Sci.* **2014**, 7, 3690.

[3] G. A. Nemnes, C. Besleaga, V. Stancu, D. E. Dogaru, L. N. Leonat, L. Pintilie, K. Torfason, M. Ilkov, A. Manolescu, I. Pintilie, *J. Phys. Chem. C* **2017**, 121, 11207.

[4] Y. Rong, Y. Hu, S. Ravishankar, H. Liu, X. Hou, Y. Sheng, A. Mei, Q. Wang, D. Li, M. Xu, J. Bisquert, H. Han, *Energ. Environ. Sci.* **2017**, 10, 2383.

[5] W. Tress, J. P. Correa Baena, M. Saliba, A. Abate, M. Graetzel, *Advanced Energy Materials* **2016**, 6, 1600396.

[6] S. Ravishankar, O. Almora, C. Echeverría-Arrondo, E. Ghahremanirad, C. Aranda, A. Guerrero, F. Fabregat-Santiago, A. Zaban, G. Garcia-Belmonte, J. Bisquert, *J. Phys. Chem. Lett.* **2017**, 8, 915.

[7] P. Lopez-Varo, J. A. Jiménez-Tejada, M. García-Rosell, S. Ravishankar, G. Garcia-Belmonte, J. Bisquert, O. Almora, *Advanced Energy Materials* **2018**, 8, 1702772.

[8] R. S. Sanchez, V. Gonzalez-Pedro, J.-W. Lee, N.-G. Park, Y. S. Kang, I. Mora-Sero, J. Bisquert, *J. Phys. Chem. Lett.* **2014**, 5, 2357.

[9] B. Chen, M. Yang, X. Zheng, C. Wu, W. Li, Y. Yan, J. Bisquert, G. Garcia-Belmonte, K. Zhu, S. Priya, *J. Phys. Chem. Lett.* **2015**, 6, 4693.

[10] G. Richardson, S. E. J. O'Kane, R. G. Niemann, T. A. Peltola, J. M. Foster, P. J. Cameron, A. B. Walker, *Energ. Environ. Sci.* **2016**, 9, 1476.

[11] B. Chen, M. Yang, S. Priya, K. Zhu, *J. Phys. Chem. Lett.* **2016**, 7, 905.

[12] P. Calado, A. M. Telford, D. Bryant, X. Li, J. Nelson, B. C. O'Regan, P. R. F. Barnes, *Nat. Commun.* **2016**, 7, 13831.

[13] I. Levine, P. K. Nayak, J. T.-W. Wang, N. Sakai, S. Van Reenen, T. M. Brenner, S. Mukhopadhyay, H. J. Snaith, G. Hodes, D. Cahen, *J. Phys. Chem. C* **2016**, 120, 16399.

[14] O. Almora, I. Zarazua, E. Mas-Marza, I. Mora-Sero, J. Bisquert, G. Garcia-Belmonte, *J. Phys. Chem. Lett.* **2015**, 6, 1645.

[15] F. Wu, B. Bahrami, K. Chen, S. Mabrouk, R. Pathak, Y. Tong, X. Li, T. Zhang, R. Jian, Q. Qiao, *ACS Appl. Mater. Inter.* **2018**, 10, 25604.

[16] H. Wang, A. Guerrero, A. Bou, A. M. Al-Mayouf, J. Bisquert, *Energ. Environ. Sci.* **2019**, 12, 2054.

[17] J. Bisquert, *J. Phys. Chem. B* **2002**, 106, 325.

[18] F. Fabregat-Santiago, G. Garcia-Belmonte, I. Mora-Seró, J. Bisquert, *PCCP* **2011**, 13, 9083.

[19] J. Bisquert, F. Fabregat-Santiago, *Impedance spectroscopy: a general introduction and application to dye-sensitized solar cells* in *Dye-sensitized solar cells*, EPFL Press, **2010**.

[20] I. Zarazua, G. Han, P. P. Boix, S. Mhaisalkar, F. Fabregat-Santiago, I. Mora-Seró, J. Bisquert, G. Garcia-Belmonte, *J. Phys. Chem. Lett.* **2016**, 7, 5105.

[21] G. S. Anaya Gonzalez, J. J. Jeronimo-Rendon, Q. Wang, G. Li, A. O. Alvarez, F. Fabregat-Santiago, H. Köbler, A. Alvarado, H. Juárez-Santiesteban, S.-H. Turren-Cruz, M. Saliba, A. Abate, *Sol. Energ. Mat. Sol. C.* **2022**, 248, 111964.

[22] N. Klipfel, A. O. Alvarez, H. Kanda, A. A. Sutanto, C. Igci, C. Roldán-Carmona, C. Momblona, F. Fabregat-Santiago, M. K. Nazeeruddin, *ACS Appl. Energy Mater.* **2022**, 5, 1646.

[23] I. Zarazua, J. Bisquert, G. Garcia-Belmonte, *J. Phys. Chem. Lett.* **2016**, 7, 525.

[24] E. J. Juarez-Perez, M. Wuβler, F. Fabregat-Santiago, K. Lakus-Wollny, E. Mankel, T. Mayer, W. Jaegermann, I. Mora-Sero, *J. Phys. Chem. Lett.* **2014**, 5, 680.

[25] E. J. Juarez-Perez, R. S. Sanchez, L. Badia, G. Garcia-Belmonte, Y. S. Kang, I. Mora-Sero, J. Bisquert, *J. Phys. Chem. Lett.* **2014**, 5, 2390.

[26] A. Guerrero, J. Bisquert, G. Garcia-Belmonte, *Chem. Rev.* **2021**, 121, 14430.

[27] A. Pockett, G. E. Eperon, N. Sakai, H. J. Snaith, L. M. Peter, P. J. Cameron, *PCCP* **2017**, 19, 5959.

[28] S.-M. Yoo, S. J. Yoon, J. A. Anta, H. J. Lee, P. P. Boix, I. Mora-Seró, *Joule* **2019**, 3, 2535.

[29] L. Yang, F. Cai, Y. Yan, J. Li, D. Liu, A. J. Pearson, T. Wang, *Adv. Funct. Mater.* **2017**, 27, 1702613.

[30] S. Fletcher, *J. Electrochem. Soc.* **1994**, 141, 1823.

[31] F. Fabregat-Santiago, M. Kulbak, A. Zohar, M. Vallés-Pelarda, G. Hodes, D. Cahen, I. Mora-Seró, *ACS Energy Lett.* **2017**, 2, 2007.

[32] M. Anaya, W. Zhang, B. C. Hames, Y. Li, F. Fabregat-Santiago, M. E. Calvo, H. J. Snaith, H. Míguez, I. Mora-Seró, *J. Mater. Chem. C* **2017**, 5, 634.

[33] F. Ebadi, N. Taghavinia, R. Mohammadpour, A. Hagfeldt, W. Tress, *Nat. Commun.* **2019**, 10, 1574.

[34] A. Zohar, N. Kedem, I. Levine, D. Zohar, A. Vilan, D. Ehre, G. Hodes, D. Cahen, *J. Phys. Chem. Lett.* **2016**, 7, 191.

[35] D. Moia, I. Gelmetti, P. Calado, W. Fisher, M. Stringer, O. Game, Y. Hu, P. Docampo, D. Lidzey, E. Palomares, J. Nelson, P. R. F. Barnes, *Energ. Environ. Sci.* **2019**, 12, 1296.

[36] J. Bisquert, G. Garcia-Belmonte, Á. Pitarch, H. J. Bolink, *Chem. Phys. Lett.* **2006**, 422, 184.

[37] I. Mora-Seró, J. Bisquert, F. Fabregat-Santiago, G. Garcia-Belmonte, G. Zoppi, K. Durose, Y. Proskuryakov, I. Oja, A. Belaidi, T. Dittrich, R. Tena-Zaera, A. Katty, C. Lévy-Clément, V. Barrioz, S. J. C. Irvine, *Nano Lett.* **2006**, 6, 640.

[38] E. Ghahremanirad, A. Bou, S. Olyaee, J. Bisquert, *J. Phys. Chem. Lett.* **2017**, 8, 1402.

[39] J. Bisquert, *PCCP* **2011**, 13, 4679.

[40] D. Klotz, *Electrochem. Commun.* **2019**, 98, 58.

[41] D. A. Jacobs, H. Shen, F. Pfeffer, J. Peng, T. P. White, F. J. Beck, K. R. Catchpole, *J. Appl. Phys.* **2018**, 124, 225702.

[42] Y. Feng, J. Bian, M. Wang, S. Wang, C. Zhang, Q. Dong, B. Zhang, Y. Shi, *Mater. Res. Bull.* **2018**, 107, 74.

[43] A. Guerrero, G. Garcia-Belmonte, I. Mora-Sero, J. Bisquert, Y. S. Kang, T. J. Jacobsson, J.-P. Correa-Baena, A. Hagfeldt, *J. Phys. Chem. C* **2016**, 120, 8023.

[44] M. Ulfa, T. Zhu, F. Goubard, T. Pauporté, *J. Mater. Chem. A* **2018**, 6, 13350.

[45] H.-S. Kim, N.-G. Park, *J. Phys. Chem. Lett.* **2014**, 5, 2927.

[46] G. Garcia-Belmonte, J. Bisquert, *ACS Energy Lett.* **2016**, 1, 683.

[47] H.-S. Kim, I.-H. Jang, N. Ahn, M. Choi, A. Guerrero, J. Bisquert, N.-G. Park, *J. Phys. Chem. Lett.* **2015**, 6, 4633.

[48] C. Aranda, A. Guerrero, J. Bisquert, *ACS Energy Lett.* **2019**, 4, 741.

[49] J. Bisquert, A. Guerrero, C. Gonzales, *ACS Phys. Chem. Au* **2021**, 1, 25.

[50] S. M. Seyed-Talebi, I. Kazeminezhad, *J. Colloid Interface Sci.* **2020**, 562, 125.

[51] J. Bisquert, F. Fabregat-Santiago, I. Mora-Seró, G. Garcia-Belmonte, S. Giménez, *J. Phys. Chem. C* **2009**, 113, 17278.

[52] L. Dloczik, O. Ileperuma, I. Lauermann, L. M. Peter, E. A. Ponomarev, G. Redmond, N. J. Shaw, I. Uhlendorf, *J. Phys. Chem. B* **1997**, 101, 10281.

[53] J. Bisquert, V. S. Vikhrenko, *J. Phys. Chem. B* **2004**, 108, 2313.

[54] H. Cachet, E. M. M. Sutter, *J. Phys. Chem. C* **2015**, 119, 25548.

[55] J. E. Thorne, J.-W. Jang, E. Y. Liu, D. Wang, *Chem. Sci.* **2016**, 7, 3347.

[56] D. Cardenas-Morcoso, A. Bou, S. Ravishankar, M. García-Tecedor, S. Gimenez, J. Bisquert, *ACS Energy Lett.* **2020**, 5, 187.

[57] A. Todinova, J. Idígoras, M. Salado, S. Kazim, J. A. Anta, *J. Phys. Chem. Lett.* **2015**, 6, 3923.

[58] L. Contreras, J. Idígoras, A. Todinova, M. Salado, S. Kazim, S. Ahmad, J. A. Anta, *PCCP* **2016**, 18, 31033.

[59] J. Li, R. Peat, L. M. Peter, *J. Electroanal. Chem. Interfacial Electrochem.* **1984**, 165, 41.

[60] L. M. Peter, *Chem. Rev.* **1990**, 90, 753.

[61] P. E. de Jongh, D. Vanmaekelbergh, *Phys. Rev. Lett.* **1996**, 77, 3427.

[62] S. Ravishankar, A. Riquelme, S. K. Sarkar, M. Garcia-Batlle, G. Garcia-Belmonte, J. Bisquert, *J. Phys. Chem. C* **2019**, 123, 24995.

[63] J. Krüger, R. Plass, M. Grätzel, P. J. Cameron, L. M. Peter, *J. Phys. Chem. B* **2003**, 107, 7536.

[64] A. Pockett, G. E. Eperon, T. Peltola, H. J. Snaith, A. Walker, L. M. Peter, P. J. Cameron, *J. Phys. Chem. C* **2015**, 119, 3456.

[65] J. Halme, *PCCP* **2011**, 13, 12435.

[66] D. Klotz, D. S. Ellis, H. Dotan, A. Rothschild, *PCCP* **2016**, 18, 23438.

[67] A. Bou, A. Pockett, D. Raptis, T. Watson, M. J. Carnie, J. Bisquert, *J. Phys. Chem. Lett.* **2020**, 11, 8654.

[68] L. Bertoluzzi, J. Bisquert, *J. Phys. Chem. Lett.* **2017**, 8, 172.

[69] O. Almora, Y. Zhao, X. Du, T. Heumueller, G. J. Matt, G. Garcia-Belmonte, C. J. Brabec, *Nano Energy* **2020**, 75, 104982.

[70] O. Almora, D. Miravet, G. J. Matt, G. Garcia-Belmonte, C. J. Brabec, *Appl. Phys. Lett.* **2020**, 116, 013901.

[71] J. Halme, K. Miettunen, P. Lund, *J. Phys. Chem. C* **2008**, 112, 20491.

[72] L. Bay, K. West, *Sol. Energ. Mat. Sol. C.* **2005**, 87, 613.

[73] Metrohm Autolab B.V., *LED Driver User Manual*, https://www.metrohm.com/en.html. Accessed 25.10.2022.

[74] M. Tayebi, B.-K. Lee, *Renewable Sustainable Energy Rev.* **2019**, 111, 332.

[75] C. Zachäus, F. F. Abdi, L. M. Peter, R. van de Krol, *Chem. Sci.* **2017**, 8, 3712.

[76] F. F. Abdi, T. J. Savenije, M. M. May, B. Dam, R. van de Krol, *J. Phys. Chem. Lett.* **2013**, 4, 2752.

[77] X. Shi, I. Herraiz-Cardona, L. Bertoluzzi, P. Lopez-Varo, J. Bisquert, J. H. Park, S. Gimenez, *PCCP* **2016**, 18, 9255.

[78] M. Zhou, J. Bao, Y. Xu, J. Zhang, J. Xie, M. Guan, C. Wang, L. Wen, Y. Lei, Y. Xie, *ACS Nano* **2014**, 8, 7088.

[79] D. Cardenas-Morcoso, R. Ifraemov, M. García-Tecedor, I. Liberman, S. Gimenez, I. Hod, *J. Mater. Chem. A* **2019**, 7, 11143.

[80] F. S. Hegner, I. Herraiz-Cardona, D. Cardenas-Morcoso, N. López, J.-R. Galán-Mascarós, S. Gimenez, *ACS Appl. Mater. Inter.* **2017**, 9, 37671.

CHAPTER 4

Publication 1: Negative Capacitance and Inverted Hysteresis: Matching Features in Perovskite Solar Cells.

Agustin O. Alvarez, Ramón Arcas, Clara A. Aranda, Loengrid Bethencourt, Elena Mas-Marzá, Michael Saliba, and Francisco Fabregat-Santiago.

The Journal of Physical Chemistry Letters **2020**, *11*, 8417.
DOI: 10.1021/acs.jpclett.0c02331.
Impact Factor 2020: 6.475.

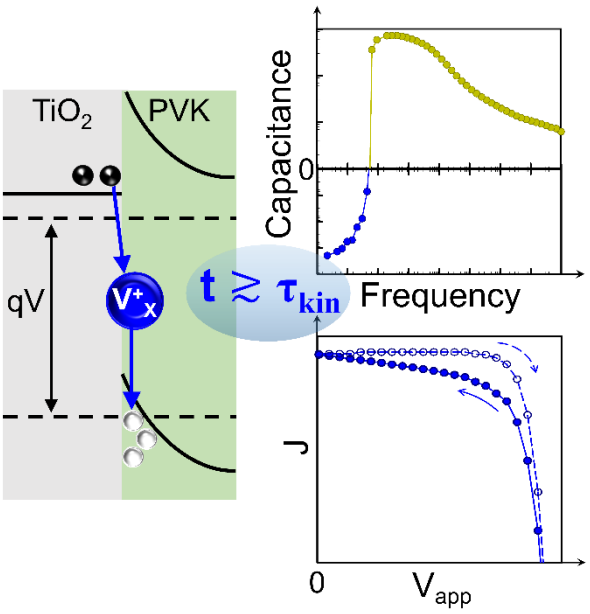

4.1. Candidate's contribution

Nature of Contribution	Extent of Contribution
✓ Carried out part of the measurements ✓ Analysed all the measurements ✓ Contribute to the interpretation of the results ✓ Prepared all the figures ✓ Assisted in the writing of the manuscript ✓ Contribute to the reply to the referees	50%

4.2. Thesis context

The identification of the hysteresis is fundamental for the proper characterisation of the photoconverter devices. Within this work, we have connected the observation of inverted hysteresis with the presence of negative capacitance in the impedance spectroscopy (IS) response. This work is an example of the great power of IS. This technique has allowed us to identify, for different perovskite solar cells under different conditions, that these effects are caused by an additional recombination path that reduced the overall performance. Furthermore, by analysing the IS responses, especially the characteristic time of the negative capacitance process, we have been able to relate this process with the transport of ions/vacancies in the perovskite and their interaction with the interfaces with the contacts. In addition, we have shown that the inverted hysteresis and the negative capacitance disappeared in optimised devices. Therefore, in line with our general objective, our results allow the identification of a limitation in the studied device and suggest a path for its optimisation.

4.3. Published Manuscript

Negative Capacitance and Inverted Hysteresis: Matching Features in Perovskite Solar Cells

Agustin O. Alvarez[1]; Ramón Arcas[1]; Clara A. Aranda[2,3*]; Loengrid Bethencourt[1,4]; Elena Mas-Marzá[1]; Michael Saliba[2,3]; Francisco Fabregat-Santiago[1*]

[1]*Institute of Advanced Materials (INAM), Universitat Jaume I, 12006 Castelló, Spain*

[2]*IEK-5 Photovoltaics, Forschungzentrum Jülich, 52425 Jülich, Germany*

[3]*Institute für Photovoltaik (IPV), Universität Stuttgart, 70569 Stuttgart, Germany*

[4]*Grupo de Desarrollo de Materiales y Estudios Ambientales, Departamento de Desarrollo Tecnológico, CURE, Universidad de la República, Ruta 9 Km 207, Rocha, Uruguay*

Email: fabresan@uji.es; caranda@uji.es

Abstract

Negative capacitance at the low-frequency domain and inverted hysteresis are familiar features in perovskite solar cells, where the origin is still under discussion. Here we use Impedance Spectroscopy to analyse these responses in methylammonium lead bromide cells treated with lithium cation at the electron selective layer/perovskite interface and in iodide devices exposed to different relative humidity conditions. Employing the *Surface Polarization Model*, we obtain a time constant associated to the kinetics of the interaction of ions/vacancies with the surface, τ_{kin}, in the range of 10^0 - 10^2 s for all the cases exhibiting both features. These interactions lead to a decrease in the overall recombination resistance, modifying the low-frequency perovskite response and yielding to a flattening of the cyclic voltammetry. As consequence of these results we find that that negative capacitance and inverted hysteresis lead to a decrease in the fill factor and photovoltage values.

The progress of lead halide perovskite solar cells (PSCs) in the photovoltaic field has been astoundingly rapid.[1] However, the current impressive power conversion efficiency (PCE) approaching 26% in the lab scale, is accompanied by a wide range of features during device operation that still needs to be solved.[2] Hysteretic behaviour is one of them, representing a bottle-neck in the reporting of PSCs performance for high-efficiency values, slowing down the overall development.[3],[4],[5] This feature consists of a delay between the change of the system properties under variation of an external electric field. The consequence is a difference in the J-V curves during the sweeping in the two directions from short-circuit towards open-circuit (Forward scan, FS) and *vice versa* (Reverse scan, RS). A noteworthy manifestation of this phenomenon depends on the external parameters affecting the J-V curve: i.e. temperature, light intensity, scan-rate, pre-biasing voltage and external contacts. These perturbations lead to a wide range of hysteresis responses including: photocurrent decay in RS, apparent V_{oc} shift in FS, capacitive hysteresis and *bump* (maximum current close to V_{oc} at the FS).[6],[7],[8] The hysteretic behaviour most commonly observed in PSCs is the *normal hysteresis* (NH) which performs with an improved fill factor (FF) and photovoltage (V_{oc}) for the RS, while the FS brings lower values. In this process, the cell behaves as a capacitor. During the FS, an accumulation of charge occurs ("capacitor filling"), while in the RS this charge is realised ("capacitor emptying") leading to an excess of current in the external circuit. On the other hand, an *inverted hysteresis* (IH) can also be present in certain samples and/or under specific preconditions. In this case, the RS displays lower photovoltage and FF values than the FS. Several mechanisms have been proposed for the different hysteretic features, including charge trapping and de-trapping, ferroelectric polarization, ion migration, capacitive effects, charge accumulation at the interfaces and unbalanced distribution of electrons and holes.[9],[10],[11],[12] All of them are connected with the mixed ionic-electronic nature of PSCs, bringing out the perovskite/selective contact interfaces as the main character controlling charge extraction capability, accumulation and recombination mechanisms.[13] Additionally, the accumulation mechanisms reported for the IH involve unfavourable energy level alignment, ionic accumulation and space-charge buildup.[14],[15]

Tress and co-workers observed a NH for simple $MAPbI_3$ while an IH for mixed-cation perovskite devices. After including an isolating layer onto the mesoporous titanium dioxide (m-TiO_2) in the simple perovskite device, they concluded that the process responsible for the IH was an energetic extraction barrier at the TiO_2 interface.[16] On the other hand, Nemnes et. al showed that pre-poling bias (in particular negative pre-poling) can produce the switching from NH to IH for the same structure device. They also analysed by a *dynamic electrical model* (DEM) the influence of the scan rate in terms of the time evolution of electronic and ionic charge accumulated at the interfaces. This DEM model includes a capacitor accounting for nonlinear polarization effects in the equivalent circuit.[17] This theory is in perfect agreement with the *Surface Polarization Model* (SPM) proposed by Bisquert and coworkers.[13] This model is based on the formation of a surface

potential, V_s, at the electron selective layer (ESL)/perovskite interface due to the arrival of positively charged ions under large injection or illumination conditions, creating an accumulated density of both ionic and electronic holes, increasing recombination dynamics. An experimental work reported by Bisquert and co-workers provided evidence of the surface polarization of the ESL/perovskite interface.[15] In their work, a switch from NH to IH is shown when the thickness of the c-TiO_2 material is diminished, attributing this evolution to an interaction between charge accumulation and recombination mechanisms. The charge accumulation at the TiO_2/perovskite interface has been related with an atypically high capacitive feature (mF cm^{-2}) in the low-frequency domain (LF) (< 1 Hz), measured using Impedance Spectroscopy (IS) and being also present under dark conditions, which brings out the strong influence of slow ionic dynamic on the hysteretic behaviour.[12] This relation was demonstrated in the work of Park and co-workers.[18] They systematically compared the hysteretic behaviour between a regular perovskite configuration, using TiO_2 as ESL and an inverted configuration with PCBM as ESL. In the case of inverted structure, a hysteresis-free performance of the J-V curve was observed together with a much lower value of capacitive response in the LF domain. They established the origin of this reduction as a decreased polarization of the device electrode.

Beyond the giant capacitive response, even in dark conditions, a negative capacitance has also been measured under a wide range of external conditions and in many different perovskite devices, becoming one of the hardest features to decode.[19],[20],[21],[22] The only thing in which there seems to be some agreement in literature is the unfavourable effect on the optoelectronic response of the cells.[23],[24] An electron injection through interfacial states was attributed to the origin of negative capacitance in light-emitting diodes (LEDs), assigned as well as the main cause in PSCs by Anaya et. al.[25] Bisquert and co-workers analysed the IS response of samples with negative capacitance by SPM,[26] matching the negative capacitance to an inductive element included in their equivalent circuit (EC). This negative capacitance was attributed to a delay of the surface voltage depending on a certain kinetic relaxation time, controlling the equilibration of the ESL/perovskite interface governed by the ionic dynamic. The value of that kinetic relaxation time depends on the process governing the slow response. To this respect, a recent review summarizes the kinetic relaxation time values for halide vacancy diffusion and the response of ions accumulated at the perovskite surface; being in the range of 10^{-1} s and 10^{0} – 10^{2} s, respectively.[27]

The next question lies then if there is any relation between the negative capacitance and hysteresis response. A recent work reported by Tress and co-workers correlates the negative capacitance with a stronger scan rate dependence of hysteresis behaviour, considering a change in the charge injection as the cause of this effect.[28] Contrary, Jacobs et.al reported an ion-drift-diffusion (IDD) theory to simulate the negative capacitive process and its dependence on scan rate, pointing to a phase-delayed recombination mechanism due to mobile ions.[29]

In this work we demonstrate experimentally how negative capacitance and inverted hysteresis are related and the common origin by which both effects are produced. We apply the SPM to analyse the impedance response of a batch of $MAPbBr_3$ devices with lithium treatment at the ESL[30] and $MAPbI_3$ devices exposed to moisture. Matching results are obtained for all the cells. Samples with IH and strong negative capacitive response present higher kinetic relaxation times and lower recombination resistance values than the ones with lower IH or NH and low/null negative capacitances. We correlate these results with a surface ionic interaction, leading to a delayed recombination mechanism. These insights provide a concise explanation about the origin of these two features, confirming the direct relationship between them and advancing forward to a deeper knowledge about PSCs dynamics.

We evaluate in the first place the hysteretic behaviour of two representative champion devices of well-known $MAPbBr_3$ solar cells with and without lithium treatment at the ESL (Li and No-Li samples, respectively).[30] As previously demonstrated, this Li^+ treatment leads to an increased photovoltage value, enhancing the electroluminescence (EL) emission of the perovskite bulk, due to a reduction of undesired non-radiative and surface recombination mechanisms by reducing the density of holes in the charge accumulation zone. The ionic nature of this effect may have a strong influence on the cyclic voltammetry (CV) measurement at different scan rates.[4],[6] Then, CV from 10 mV s^{-1} to 500 mV s^{-1} under illumination conditions are developed in order to force the ionic effect into the photogenerated electronic carriers.

In Fig. 1a and 1b we show the corresponding hysteretic behaviour for champion cells with a without lithium at the ESL, respectively. The strong differences between them are clear determining the hysteresis index calculated from eq.1:[18]

$$HI = 1 - \frac{PCE_{FS}}{PCE_{RS}} \quad (1)$$

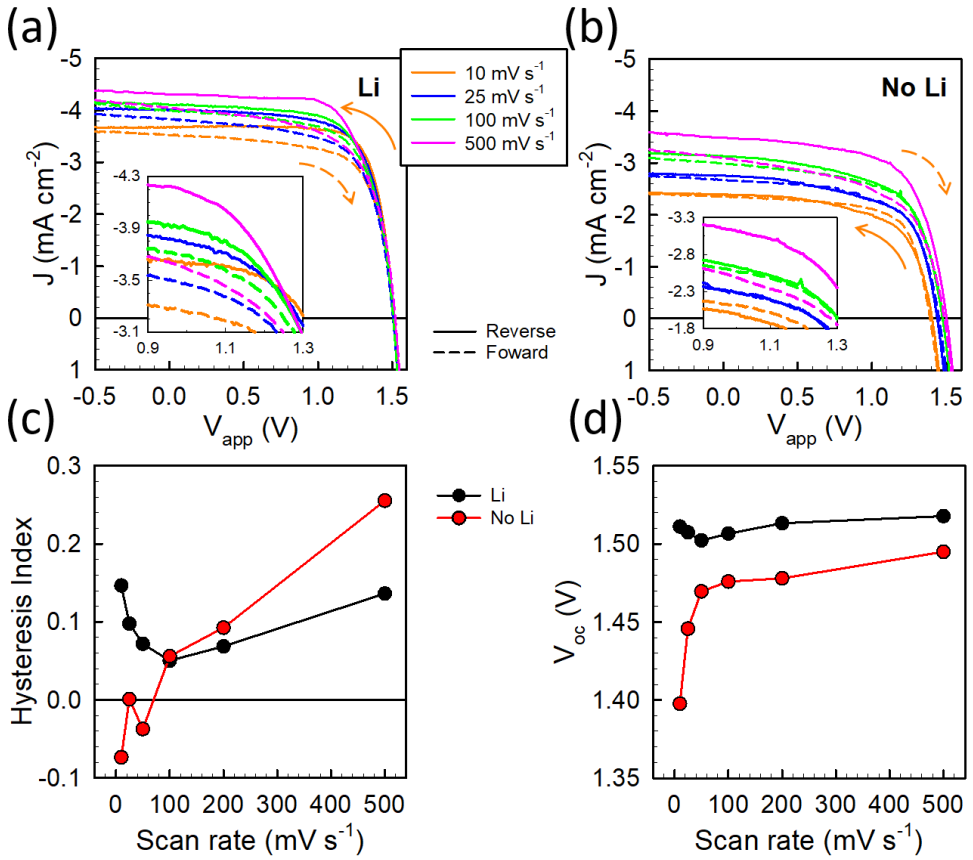

Figure 1. Cyclic voltammetry of Li (a) and No-Li $MAPbBr_3$ cells (b) devices performed at different scan rates from 10 mV s^{-1} to 500 mV s^{-1}. (c) Hysteresis index and (d) photovoltage *versus* scan rate comparing both samples: black dots for doped and red dots for un-doped samples.

As it can be observed in Figs. 1a and 1c, the Li device presents NH independently of the scan rate applied (positive hysteresis index). However, the No-Li device (Figs 1b and 1c) exhibits a more pronounced NH at high scan rates (bigger hysteresis index) and IH at low scan rates (negative hysteresis index). The variations of the photovoltage with the scan rate are also notorious comparing both type of samples (Fig. 1d and Fig. S1 in SI). While the open circuit potential of the Li sample is almost constant with the scan rate, in the absence of lithium the photovoltage increases sharply for scan rates from 10 to 50 mV s^{-1} and then presents little variations. Furthermore, the photovoltage value is lower for the No-Li device at any scan-rate. This is due to the major surface recombination, previously reported.[30] Comparing Figs. 1c and 1d, it can be noted that, in general terms, when the HI diminishes, so does the V_{oc} (see Figure S1 in SI). Besides, for both cases, an improvement of photocurrent proportional to the scan rate is found (see Fig. 1 a, b and S1 in SI). This effect has been attributed previously to a slow process related to the build-up of the space charge close to the contacts, due to ionic displacement and associated with a capacitor-like discharge of current.[7],[31]

The negative capacitance feature has been considered as a deleterious effect for the PSCs performance.[24],[20] Then, to evaluate the nature of this dynamic, we performed an analysis of the impedance response and the hysteretic behaviour of samples presenting moderate PCE. In this context, we consider moderate PCE for devices with photovoltages below 1.5 V for Li samples and below 1.4 V for the No-Li devices. All the good cells (high PCE) are considered above these values respectively. We establish these limits taking into account the record photovoltage value of 1.56 V reported for $MAPbBr_3$ by Aranda et. al[30]. The cyclic voltammetry of the two devices (Li and No-Li) performed at 50 mV s^{-1} are shown in Fig. 2a.

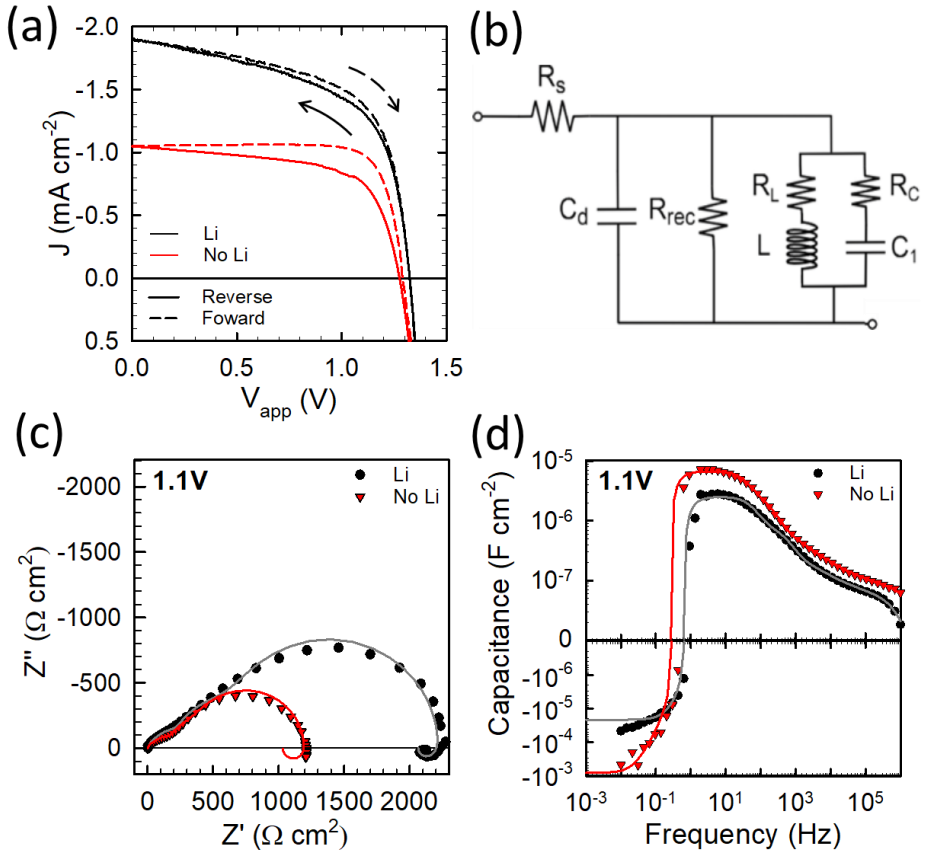

Figure 2. Black and red colours correspond to the Li and No-Li devices respectively. (a) CV measures showing inverted hysteresis for both configurations. The dashed lines correspond to forward scans, while the solid lines represent the reverse ones. (b) EC established by the SPM and used here to fit our experimental impedance results. R_s is the series resistance, C_d is de dielectric capacitance, R_{rec} is the recombination resistance, R_L is a resistance associated to the inductance L and R_C is the series resistance associated to the interfacial charging capacitance C_1. (c) Impedance plot and corresponding (d) capacitance spectra, measured under dark conditions and at 1.1V. Solid lines correspond to fits using the equivalent circuit showed in (b).

As it can be observed, both samples present an inverted hysteretic behaviour, but clearly this effect is much stronger in the case of the No-Li device. Capacitance and hysteretic phenomena have already been correlated with slow transients, specifically to ionic electrode polarization. Therefore, we performed the IS analysis at different potentials towards open-circuit and under dark conditions to prevent further complexity due to photogeneration mechanisms (see Fig.S4).[12] In Fig. 2c it is shown the fitting of the impedance spectra measured at 1.1 V (where the effect is more clear due to the greater polarization of the sample) and in a wide range of frequencies from 1 MHz to 10 mHz, to ensure the low-frequency ionic contribution. As it can be observed, pronounced differences in the recombination resistance are presented comparing both samples (Z' axis cross). This is in complete agreement with our previous results, confirming that lithium decreases the surface recombination dynamics. Together with that, a negative capacitance appears for both samples, being much more pronounced for the No-Li device, (Fig. 2d). This negative capacitance is represented as the inductance in the R_L-L line of the EC proposed by Bisquert and coworkers in their SPM (Fig.2b), used as well in other works[32]. This new line produces the low frequency arc below the real axis which is the clearest signature on impedance of this phenomena or, in other situations, a loop that makes two arcs in the impedance to cross each other.[33],[34] The extracted parameters from the impedance spectra corresponding to both samples, using the EC of Fig.2b, are detailed in Table 1 (See Table S1 for the complete fitting parameters).

Table 1. Extracted parameters from dark IS measurements for the samples with and without Li^+ at the ESL.

Cells	R_{rec} (Ω·cm²)	L (H·cm²)	R_L (Ω·cm²)	$\tau_{kin}=L/R_L$ (s)
Li	2.2×10^3	2.1×10^4	2.9×10^4	**0.7**
No Li	1.2×10^3	5.6×10^4	9.9×10^3	**5.7**

The SPM establishes that the surface potential (V_s), created by the ionic accumulation at the ESL, cannot follow immediately the external voltage (V) variations.[13],[26] The relaxation equation defining this behaviour was described by the SPM as follows:

$$\frac{dV_s}{dt} = -\frac{V_s-(V-V_{bi})}{\tau_{kin}} \quad (2)$$

where V_{bi} is the built-in potential (see SI for the definition of the EC elements corresponding to the model, equations S1-S5). Here τ_{kin} represents the characteristic kinetic relaxation time of this delay which is governed by the ionic movement speed and their possible accumulation to the surface. This induces an increase of the recombination processes and generates the negative capacitance (modulated by the inductance) (see SI for further explanation).

The recombination resistance value (R_{rec}) for the Li device almost doubles the No-Li device (Table 1), confirming a reduction of recombination losses due to lithium effect.

According to the model, R_L and R_{rec} are both inversely proportional to $\bar{J}_{rec}$ (see eq. S2 and S3). In the EC they are in parallel, consequently, R_L reduces the total recombination resistance at low frequency. The smaller R_L is, the smaller total recombination resistance will be. In Table 1 can be noted that R_L and R_{rec} are smaller in the case of the No-Li sample, what provides the smaller low-frequency resistance limit in Fig. 2c. Additionally, the τ_{kin} value for the No-Li sample is one order of magnitude bigger than Li sample. Large values of the kinetic relaxation time are attributed to slower ionic dynamics and long delays to reach the equilibrium state after an external voltage is applied (V). For the No-Li device, the kinetic time value is in the order of 10^0 - 10^2 s, which agrees with a response of accumulated ions at the perovskite surface interacting with contacts (Ref. 26). In fact, the reactivity of migrating ions with TiO_2 defects (Ti^{3+}) have been discreetly reported in the literature as other cause of instability and hysteretic responses.[35],[36],[37] A large intrinsic accumulation of ions (or vacancies) at the ESL/perovskite interface could facilitate their interaction at the surface, yielding larger kinetic relaxation times and increasing surface recombination processes. On the other hand, the sample with Li at the ESL/perovskite interface shows a kinetic time value in the range of 10^{-1} s, which agrees with halide vacancy diffusion time, indicating "free" bulk ionic movement.[27] When ions/vacancies move freely, negative capacitance and inverted hysteresis are very limited (usually not observed). The presence of lithium at that interface could reduce the accumulation of these bulk ions, avoiding their interactions with the surface, as indicated by the small value of τ_{kin} obtained.

Besides, it has recently been reported the photoluminescence (PL) quenching as an effect of the ion drift-diffusion.[38] The origin of this phenomenon is attributed to the creation of non-radiative recombination centres in the perovskite bulk. To reduce this non-radiative recombination mechanism, potassium doping of the perovskite material has been used to avoid the ionic attachment to the surface.[39] Similar effect was found in our previous work, where lithium cation at the ESL generates an additional effect enhancing the PL and electroluminescence (EL) response of the $MAPbBr_3$ bulk material.[30] This phenomenon could explain the recombination decrease when associated with vacancy diffusion kinetics, obtained for the Li sample.

These results are not only a consequence of the specific conditions of bromide cells and we prove it performing the same analysis in the most widely used perovskite device: $MAPbI_3$. In these standard cells under dry working conditions, there is no presence of IH or negative capacitance, thus we induced it in a controlled way. Moisture is one of the main degradation factors in PSCs, closely related to hysteretic behaviours.[40] Thus, several IS and CVs measurements were performed on $MAPbI_3$ cells under different relative humidity (%RH) conditions (see Fig. 3 and the experimental part in SI).

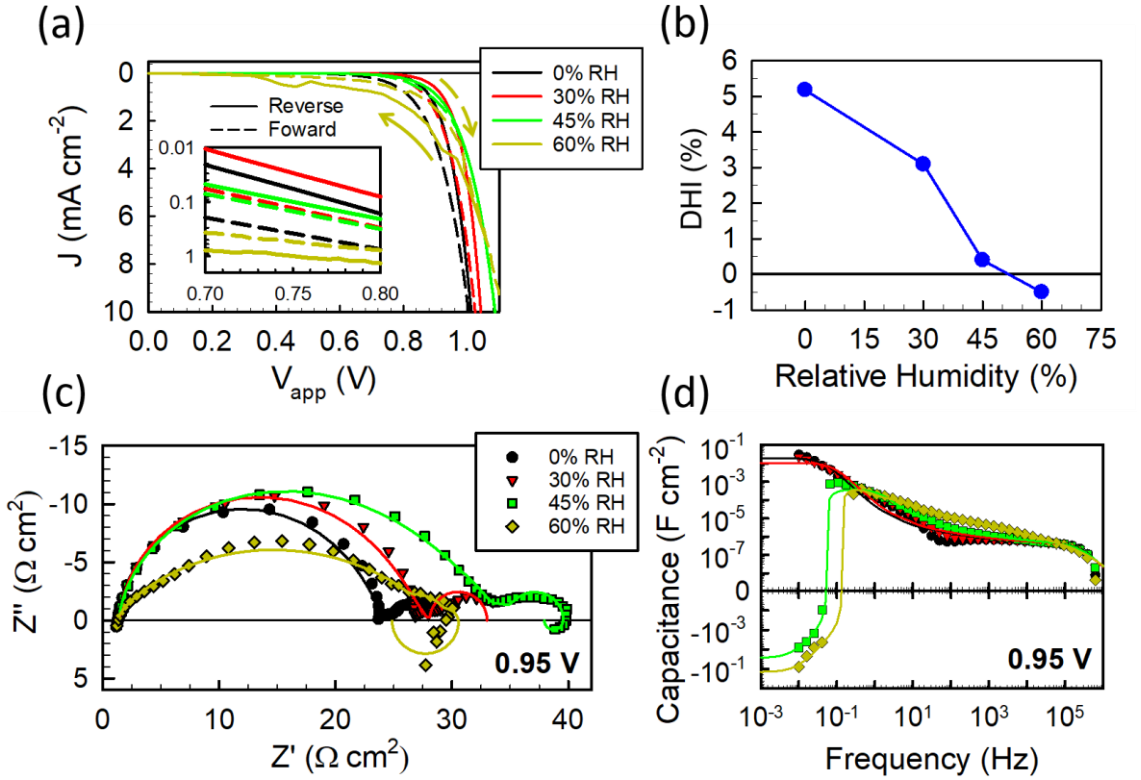

Figure 3. Measurements of regular $MAPbI_3$ solar cells (FTO/TiO_2/m-TiO_2/$MAPbI_3$/*spiro*-OMeTAD/Au) at different relative humidity (0, 30, 45 and 60 %), under dark conditions (see also Fig. S2) (a) Cyclic voltammetry curves and (b) their respective hysteresis index defined by eqn. (1), calculated at 0.75 V. (c) Impedance plots with (d) the corresponding capacitance spectra, at 0.95 applied voltage. Solid lines correspond to fits using the equivalent circuit detailed in Fig 1c.

In Fig. 3a we show the cyclic voltammetry corresponding to the different %RH exposure. From Fig. 3a the evolution of hysteretic behaviour is clear: a switching from NH to IH is produced when moving from dry conditions to high humidity. For the best of our knowledge, there is not an equivalent definition of hysteresis index for dark conditions in literature, at least in the perovskite field. Then, an approach has been made following eq. 3 for dark hysteresis index (DHI):

$$DHI(V_R) = \frac{J_{RS}(V_R)}{J_{FS}(V_R)} - 1 \qquad (3)$$

were J_{RS} and J_{FS} are the current-density in the reverse and forward scan directions respectively, at the reference voltage V_R, established here in 0.75 V because is close to the maximum power point voltage under 1 sun. As it can be observed in Fig. 3b, a decrease in the DHI takes place with increasing %RH, i.e. from high positive values at 0% RH corresponding to NH until reaching a negative value at 60% RH corresponding to an IH.

In Fig. 3c (see Fig. S3b for zoom at low frequency region) it is shown the impedance response of the different cells measured at 0.95V. The impedance spectra corresponding to 0 and 30% RH do not present an arc below the Z' axis. However, when we increase the humidity above 45% RH an arc below the Z' axis appears, evidencing the signature of the negative capacitance (Fig. 3d). The quantification of these results applying the EC of Fig. 1b is shown in Table S1 in the SI. Here we focus on 45 and 60 % RH which are the conditions where the samples present negative capacitance, see Table 2.

Table 2. Extracted parameters from IS for the samples under moisture conditions showing negative capacitance.

Cells	R_{rec} (Ω·cm²)	L (H·cm²)	R_L (Ω·cm²)	$\tau_{kin}=L/R_L$ (s)
45% RH	38	2.1×10^4	860	**24**
60% RH	29	3.0×10^3	69	**44**

In both conditions, the kinetic constant present values in the range of ~10^0 - 10^2 s, similar to the case of the bromide perovskite without Li, which agrees with large interactions between accumulated ions and the surface.[6] For these two moisture conditions, the R_{rec} and R_L parameters show clear differences. The lower values correspond to the higher %RH, which agrees with higher recombination rates. Therefore, as in the case of the bromide perovskite, the increase in negative capacitance yields to both, larger inverted hysteresis and an increment in recombination, suggesting both phenomena are related. The origin of this behaviour may be associated here to the chemical degradation of the TiO_2 and perovskite interfaces by moisture exposure, leading to a major density of defects, which can interact with the accumulated ions at the ESL/perovskite interface. This interaction might lead to the generation of an intermediate recombination state yielding to an additional recombination path, produced at the interface between the TiO_2 and the perovskite material. This new mechanism would yield a reduction in the overall recombination resistance.

To provide direct comparison between our bromide and iodide results we compare in Fig. 4 the results obtained for both series of data. In Fig.4a and 4b the kinetic times and the associated recombination resistances are represented for all samples respect to the applied bias. The kinetic times are in the same range for No-Li and moisture exposed devices, indicating that in these cases accumulated ions have strong interactions at the ESL/perovskite interface, dominating the hysteretic response of the CV. For Li devices, τ_{kin} is one order of magnitude lower, yielding to a behaviour dominated by ionic diffusion.

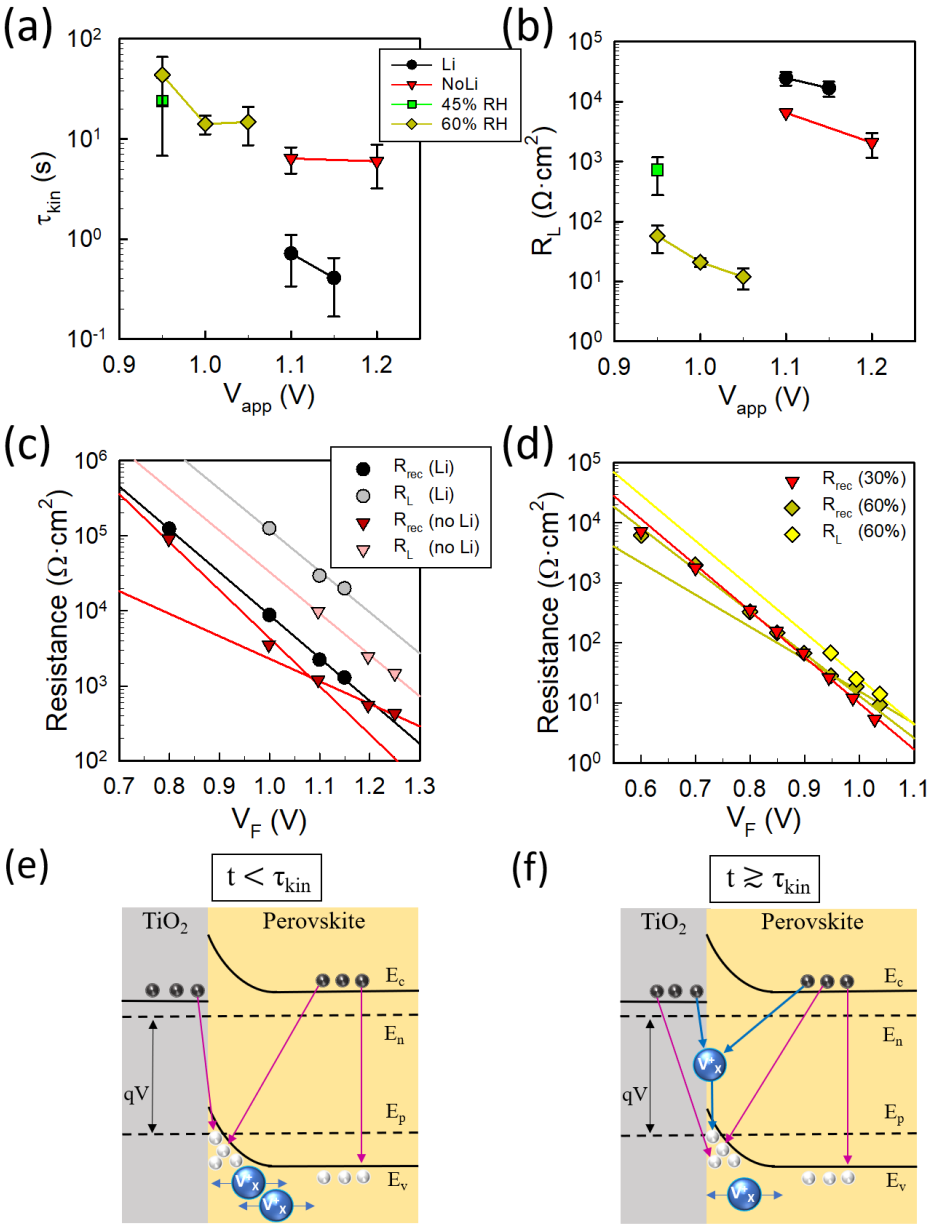

Figure 4. Kinetic relaxation times (a) and recombination values (b) versus applied bias corresponding to all samples analysed. It is shown how the kinetic relaxation time values and recombination resistances decrease with the applied voltage. Black circles and red triangles correspond to Li and No-Li samples, respectively; green squares and yellow diamonds to iodide samples under 45 %RH 65 %RH, respectively. (c) Evolution of R_{rec} and R_L with voltage corrected from the voltage drop at series resistance ($V_F = V\text{-}V_{drop}$). (d) The same for samples with 30 and 60% relative humidity. (e) Schematic diagram of the mechanisms occurring at times lower than τ_{kin}. Black and white spheres represent electron and holes, respectively. Blue spheres represent ionic vacancies migrating towards the ESL/perovskite interface. (f) Shows the surface accumulation and binding of ions responsible for the large τ_{kin}, favouring interfacial electronic recombination processes as well.

When we attend to the evolution of recombination resistance with voltage in Figs 4c and 4d, we observe that R_{rec} is smaller than R_L in all cases. This means that despite the overall recombination resistance (which is obtained as the parallel combination of R_{rec} and R_L), is smaller than both, its behaviour is dominated by R_{rec}. Figs 4c and 4d show that for samples with low τ_{kin} or without negative capacitance, R_{rec} presents a single exponential decrease with increasing voltage. The slope founded for R_{rec} is similar to the one founded for R_L (see table S2: m_β and m_γ, ideality factors, defined in equations S6 and S7 in the SI). However, in samples showing negative capacitance, and precisely at the moment R_L it starts to be observable, R_{rec} diminishes its slope, increasing the ideality factors (see Table S2). This result suggests a change in the recombination mechanism that could move from being dominated by direct recombination of electrons with accumulated holes at the interface (Fig. 4e), to a recombination mediated by the interfacial states created by ionic vacancies (fig. 4f). A direct effect of the increasing in the ideality factor is a decrease of the J-V curve slope in the region of high voltages, leading to a lower FF (See eqs. S2 and S3).[41] In the Li samples this effect is minimal due to the fact that the final ideality factor is very similar. Contrary, for the samples with higher %RH, the flattening of the J-V curve is clearly appreciated in Fig. 3a and may be associated to the increased ideality factor yielding to the negative capacitance due to surface interactions.

As depicted in Fig. 4e when the kinetic relaxation time is small, the intrinsic ions can migrate towards the ESL/perovskite interface and accumulate, but not interact. This brings normal hysteresis and positive capacitive responses. However, when charges present large τ_{kin}, the accumulated ions are allowed to interact with the surface and therefore, their movement to follow changes in the applied potential becomes delayed.

In summary, we have shown experimentally the intimate relationship between negative capacitance and IH. Employing the SPM, we get a kinetic relaxation time in the range of 10^0 - 10^2 s, which is associated to surface interactions with ions/vacancies at the ESL/perovskite interface. These interactions lead to a decrease in the overall recombination resistance, dominating low-frequency perovskite behaviour and yielding to negative capacitance response. Besides, the changes in recombination mechanisms and its values provoke a flattening of the cyclic voltammetry and the inverted hysteresis response. These combined effects yield to a decrease in *FF* and V_{oc} (and thus in the performance of perovskite solar cells). We also have shown that this process is common in different type of perovskites (bromide and iodide) and under different treatments such as cation addition, which limits NC and thus IH, or humidity control, which acts the opposite way.

Supporting Information: Additional measurements, experimental part and further analysed recombination parameters.

Acknowledgements

This project has received funding from the European Union's Horizon 2020 research and innovation programme under the Marie Sklodowska-Curie grant agreement No 764787. Authors want to acknowledge Ministerio de Economía y Competitividad (MINECO) from Spain under project, ENE2017-85087-C3-1-R.

References

[1] I. Mora-Seró, M. Saliba, Y. Zhou, *Solar RRL* **2020**, 4, 1900563.

[2] NREL, **2020**.

[3] H. J. Snaith, A. Abate, J. M. Ball, G. E. Eperon, T. Leijtens, N. K. Noel, S. D. Stranks, J. T.-W. Wang, K. Wojciechowski, W. Zhang, *The Journal of Physical Chemistry Letters* **2014**, 5, 1511.

[4] W. Tress, N. Marinova, T. Moehl, S. M. Zakeeruddin, M. K. Nazeeruddin, M. Gratzel, *Energy & Environmental Science* **2015**, 8, 995.

[5] G. Garcia-Belmonte, J. Bisquert, *ACS Energy Letters* **2016**, 683.

[6] R. S. Sanchez, V. Gonzalez-Pedro, J.-W. Lee, N.-G. Park, Y. S. Kang, I. Mora-Sero, J. Bisquert, *J. Phys. Chem. Lett.* **2014**, 5, 2357.

[7] B. Chen, M. Yang, X. Zheng, C. Wu, W. Li, Y. Yan, J. Bisquert, G. Garcia-Belmonte, K. Zhu, S. Priya, *J. Phys. Chem. Lett.* **2015**, 6, 4693.

[8] G. Richardson, S. E. J. O'Kane, R. G. Niemann, T. A. Peltola, J. M. Foster, P. J. Cameron, A. B. Walker, *Energ. Environ. Sci.* **2016**, 9, 1476.

[9] B. Chen, M. Yang, S. Priya, K. Zhu, *J. Phys. Chem. Lett.* **2016**, 7, 905.

[10] P. Calado, A. M. Telford, D. Bryant, X. Li, J. Nelson, B. C. O'Regan, P. R. F. Barnes, *Nature Communications* **2016**, 7, 13831.

[11] I. Levine, P. K. Nayak, J. T.-W. Wang, N. Sakai, S. Van Reenen, T. M. Brenner, S. Mukhopadhyay, H. J. Snaith, G. Hodes, D. Cahen, *J. Phys. Chem. C* **2016**, 120, 16399.

[12] O. Almora, I. Zarazua, E. Mas-Marza, I. Mora-Sero, J. Bisquert, G. Garcia-Belmonte, *J. Phys. Chem. Lett.* **2015**, 6, 1645.

[13] S. Ravishankar, O. Almora, C. Echeverría-Arrondo, E. Ghahremanirad, C. Aranda, A. Guerrero, F. Fabregat-Santiago, A. Zaban, G. Garcia-Belmonte, J. Bisquert, *The Journal of Physical Chemistry Letters* **2017**, 8, 915.

[14] F. Wu, B. Bahrami, K. Chen, S. Mabrouk, R. Pathak, Y. Tong, X. Li, T. Zhang, R. Jian, Q. Qiao, *ACS Appl. Mater. Inter.* **2018**, 10, 25604.

[15] Y. Rong, Y. Hu, S. Ravishankar, H. Liu, X. Hou, Y. Sheng, A. Mei, Q. Wang, D. Li, M. Xu, etal., *Energy & Environmental Science* **2017**, 10, 2383.

[16] W. Tress, J. P. Correa Baena, M. Saliba, A. Abate, M. Graetzel, *Advanced Energy Materials* **2016**, 6, 1600396.

[17] G. A. Nemnes, C. Besleaga, V. Stancu, D. E. Dogaru, L. N. Leonat, L. Pintilie, K. Torfason, M. Ilkov, A. Manolescu, I. Pintilie, *J. Phys. Chem. C* **2017**, 121, 11207.

[18] H.-S. Kim, I.-H. Jang, N. Ahn, M. Choi, A. Guerrero, J. Bisquert, N.-G. Park, *The Journal of Physical Chemistry Letters* **2015**, 6, 4633.

[19] J. Bisquert, G. Garcia-Belmonte, Á. Pitarch, H. J. Bolink, *Chem. Phys. Lett.* **2006**, 422, 184.

[20] J. Bisquert, *PCCP* **2011**, 13, 4679.

[21] Y. Feng, J. Bian, M. Wang, S. Wang, C. Zhang, Q. Dong, B. Zhang, Y. Shi, *Mater. Res. Bull.* **2018**, 107, 74.

[22] D. Klotz, *Electrochem. Commun.* **2019**, 98, 58.

[23] I. Mora-Seró, J. Bisquert, F. Fabregat-Santiago, G. Garcia-Belmonte, G. Zoppi, K. Durose, Y. Proskuryakov, I. Oja, A. Belaidi, T. Dittrich, etal., *Nano Letters* **2006**, 6, 640.

[24] F. Fabregat-Santiago, M. Kulbak, A. Zohar, M. Vallés-Pelarda, G. Hodes, D. Cahen, I. Mora-Seró, *ACS Energy Lett.* **2017**, 2, 2007.

[25] M. Anaya, W. Zhang, B. C. Hames, Y. Li, F. Fabregat-Santiago, M. E. Calvo, H. J. Snaith, H. Míguez, I. Mora-Seró, *J. Mater. Chem. C* **2017**, 5, 634.

[26] E. Ghahremanirad, A. Bou, S. Olyaee, J. Bisquert, *The Journal of Physical Chemistry Letters* **2017**, 8, 1402.

[27] H. Wang, A. Guerrero, A. Bou, A. M. Al-Mayouf, J. Bisquert, *Energy & Environmental Science* **2019**.

[28] F. Ebadi, N. Taghavinia, R. Mohammadpour, A. Hagfeldt, W. Tress, *Nat. Commun.* **2019**, 10, 1574.

[29] D. A. Jacobs, H. Shen, F. Pfeffer, J. Peng, T. P. White, F. J. Beck, K. R. Catchpole, *Journal of Applied Physics* **2018**, 124, 225702.

[30] C. Aranda, A. Guerrero, J. Bisquert, *ACS Energy Letters* **2019**, 741.

[31] W. Tress, N. Marinova, T. Moehl, S. M. Zakeeruddin, M. K. Nazeeruddin, M. Grätzel, *Energy & Environmental Science* **2015**, 8, 995.

[32] A. Kovalenko, J. Pospisil, J. Krajcovic, M. Weiter, A. Guerrero, G. Garcia-Belmonte, *Applied Physics Letters* **2017**, 111, 163504.

[33] A. Guerrero, G. Garcia-Belmonte, I. Mora-Sero, J. Bisquert, Y. S. Kang, T. J. Jacobsson, J.-P. Correa-Baena, A. Hagfeldt, *J. Phys. Chem. C* **2016**, 120, 8023.

[34] O. Almora, K. T. Cho, S. Aghazada, I. Zimmermann, G. J. Matt, C. J. Brabec, M. K. Nazeeruddin, G. Garcia-Belmonte, *Nano Energy* **2018**, 48, 63.

[35] H. Schmidt, K. Zilberberg, S. Schmale, H. Flügge, T. Riedl, W. Kowalsky, *Applied Physics Letters* **2010**, 96, 243305.

[36] A. Guerrero, G. Garcia-Belmonte, *Nanomicro Lett* **2017**, 9, 10.

[37] R. A. Kerner, B. P. Rand, *The Journal of Physical Chemistry Letters* **2017**, 8, 2298.

[38] C. Li, A. Guerrero, S. Huettner, J. Bisquert, *Nat. Commun.* **2018**, 9, 5113.

[39] S.-G. Kim, C. Li, A. Guerrero, J.-M. Yang, Y. Zhong, J. Bisquert, S. Huettner, N.-G. Park, *Journal of Materials Chemistry A* **2019**, 7, 18807.

[40] M. K. Gangishetty, R. W. J. Scott, T. L. Kelly, *Nanoscale* **2016**, 8, 6300.

[41] S. M. Sze, *Physics of Semiconductor Devices*, John Wiley and Sons, New York **1981**.

4.4. Supporting Information

Negative Capacitance and Inverted Hysteresis: Matching Features in Perovskite Solar Cells

Agustin O. Alvarez[1]; Ramón Arcas[1]; Clara A. Aranda[2,3*]; Loengrid Bethencourt[1,4]; Elena Mas-Marzá[1]; Michael Saliba[2,3]; Francisco Fabregat-Santiago[1*]

[1]*Institute of Advanced Materials (INAM), Universitat Jaume I, 12006 Castelló, Spain*

[2]*IEK-5 Photovoltaics, Forschungzentrum Jülich, 52425 Jülich, Germany*

[3]*Institute für Photovoltaik (IPV), Universität Stuttgart, 70569 Stuttgart, Germany*

[4]*Grupo de Desarrollo de Materiales y Estudios Ambientales, Departamento de Desarrollo Tecnológico, CURE, Universidad de la República, Ruta 9 Km 207, Rocha, Uruguay*

Email: fabresan@uji.es; caranda@uji.es

EXPERIMENTAL METHODS

1. *Solar cells fabrication*

Both, $MAPbI_3$ and $MAPbBr_3$ solar cells were fabricated as reported previously.[1],[2]

2. Optoelectronic characterization

For photovoltaic measures, an Abet Solar simulator equipped with 1.5 AM filter was used. The light intensity was adjusted to 100 $mWcm^{-2}$ using a calibrated Si solar cell. Devices were measured under room conditions using a mask to define an active area of 0.11 cm^2. In all the Cyclic Voltammetry (CV) measurements, forward scan starting at 0V was followed immediately by the reverse scan, without waiting time. In the study of scan-rate response dependent, the applied scan-rate were: 10, 25, 50, 100, 200, and 500 mV s^{-1}. All remaining CV were performed at 50 mV s^{-1}. Impedance Spectroscopy (IS) measurements were done in dark using an Autolab PGSTAT204 equipped with a FRA32M IS module. The bias potentials were ranged between 0 and 1.05 V for $MAPbI_3$ cells, and between 0 and 1.3 V for $MAPbBr_3$ cells. A 20 mV AC perturbation was applied ranging between 1 MHz and 10 mHz.

3. Humidity measurements

Moisture influence analysis on $MAPbI_3$ solar cells was performed using a homemade Dry Box (DB) and a Climatic Chamber (CC) CCK 70 model from Dycometal. DB atmosphere moisture was controlled with a dryer system that introduced the air in the box at values below 0.01 % R.H. During all the experiments, the temperature was established to be 25 ºC. To remove the moisture which could be absorbed by the TiO_2 layer, previous to $MAPbI_3$ layer deposition, substrates were heated at 120 ºC for 1 h. Once the cells were evaporated, all of them were introduced in a box with silica, brought to the DB, and stored there for 3 day assuring a R.H less than 0.2 %. After the 3 days, cyclic voltammetry and impedance in dark of $MAPbI_3$ solar cells were carried out at "0% RH" (actually in a humidity lower than 0.2 %). After that, the H.R. was changed to 30, 45, and 60 % (in that order). For every RH the solar cell stayed at the controlled conditions for 2h at and after that the electrochemical measurement were raped.

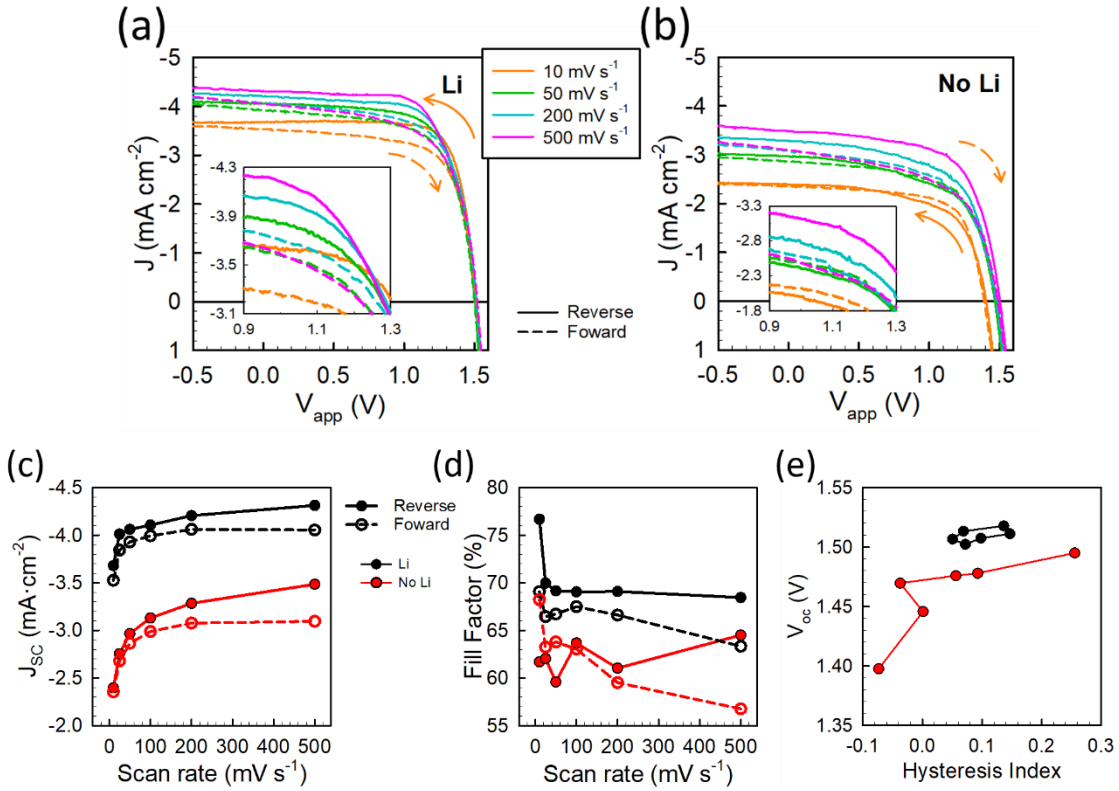

Figure S1. Cyclic voltammetry of Li (a) and No-Li (b) devices performed at different scan rates from 10 mV s^{-1} to 500 mV s^{-1}. (c) Short-circuit current and (d) Fill Factor *versus* scan rate. (e) Open-circuit voltage *versus* hysteresis index. Comparing both samples: black dots for doped and red dots for un-doped samples.

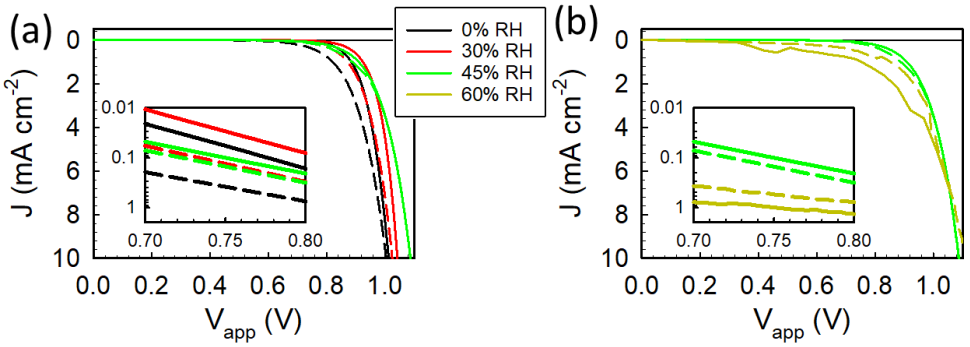

Figure S2. Cyclic voltammetry curves of regular $MAPbI_3$ solar cells (FTO/TiO_2/m-TiO_2/$MAPbI_3$/*spiro*-OMeTAD/Au) at different relative humidity (0, 30, 45 and 60 %), under dark conditions

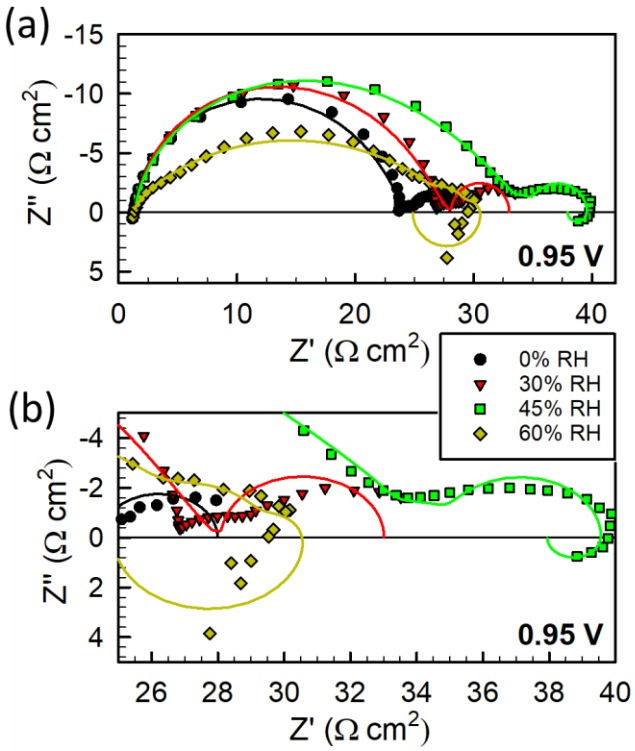

Figure S3. Impedance Spectroscopy plot of regular $MAPbI_3$ solar cells (FTO/TiO_2/m-TiO_2/$MAPbI_3$/*spiro*-OMeTAD/Au) at 0.95 applied voltage under dark conditions. Solid lines correspond to fits using the equivalent circuit detailed in Fig 1c. (b) is a zoom of the figure (a), which is Fig 3c in the main text.

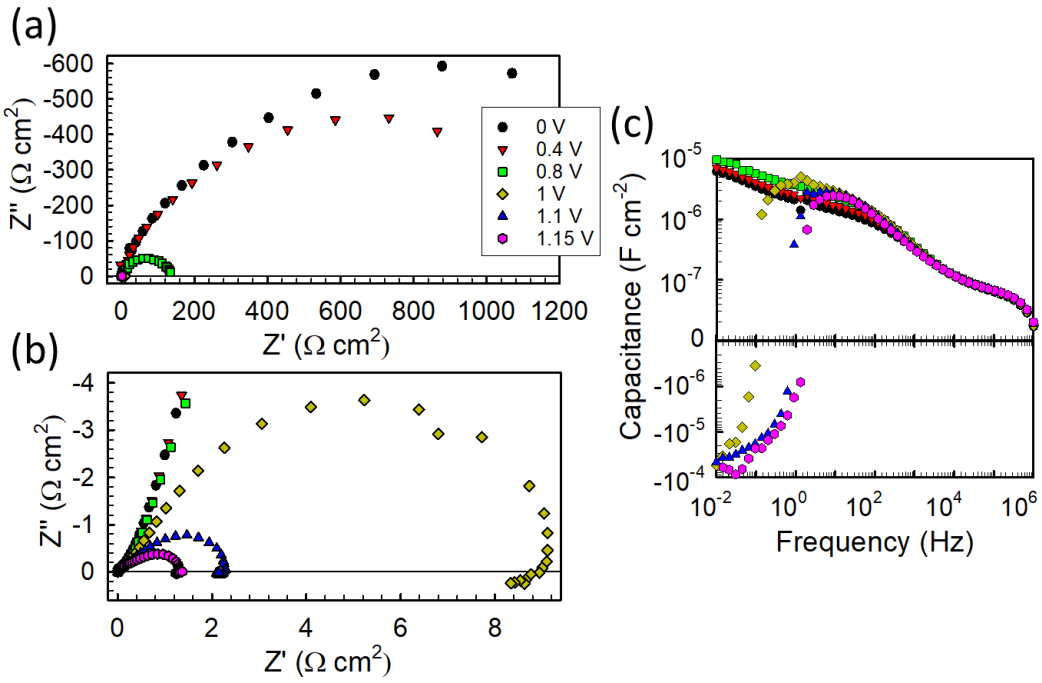

Figure S4. (a) and (b) impedance plots and corresponding (c) capacitance spectra, measured under dark conditions and at different voltages for a Li device.

R_L-L line effect onto the functioning of the EC established by the SPM

In an electronic circuit, an inductor (L) is typically a wire in the shape of a coil. When a change in voltage occurs, a magnetic field is generated by the inductor, which oppose to the change in the electric current flowing through it. This opposition is known as the inductance (the magnitude of L).

In the current model, the surface ionic accumulation provokes a delay defined by the kinetic relaxation time. This delay is correlated with the opposition to a change in the current in a typical inductor. When the delayed process occurs, the low-frequency arcs appears and so the negative capacitance, represented by the inductance. The delayed process, due to the ionic movement, leads to the additional recombination pathway represented by $R_{L.}$ Contrary, when there is not an accumulation of ions onto the surface, the main recombination pathway occurs through R_{rec}.

The AC impedance response corresponding to the model reads as follows:[3]

$$Z = \frac{\hat{V}}{\hat{\jmath}} = \left[i\omega C_d + \frac{1}{R_L + i\omega L} + \frac{1}{R_{rec}} + \frac{1}{R_C - i\frac{1}{\omega C_1}} \right]^{-1} \quad \text{(S1)}$$

$$R_{rec} = \frac{\beta k_B T}{q\bar{J}_{rec}} \quad \text{(S2)}$$

$$R_L = \frac{\gamma k_B T}{q\bar{J}_{rec}} \quad \text{(S3)}$$

$$L = \frac{R_L}{\tau_{kin}} \quad \text{(S4)}$$

$$R_C = \frac{b\tau_{kin}}{C_1} \quad \text{(S5)}$$

$$m_\beta = \frac{1}{\beta} \quad \text{(S6)}$$

$$m_\gamma = \frac{1}{\gamma} \quad \text{(S7)}$$

where $\bar{J}_{rec}$ is the recombination current at steady state, β and γ exponents are constants with values ≤ 1 which are related with the ideality factors m_β and m_γ; that may take values close to 1, 2 or 3 depending on the recombination mechanism; b is a correction factor for the fitting and $k_B T$ is the thermal energy.

Table S1: Values obtained from IS fitting for the $MAPbBr_3$ cells treated (Li) and no treated (No Li) with Lithium at the ETL/Perovskite interface, and the $MAPbI_3$ cell exposed to different relative humidity (0%, 30%, 45% and 60%).

Cell	V_{app} (V)	C_d ($F \cdot cm^{-2}$)	R_{rec} ($\Omega \cdot cm^2$)	C_1 ($F \cdot cm^{-2}$)	R_C ($\Omega \cdot cm^2$)	$\tau_C=R_CC_1$ (s)	L ($H \cdot cm^2$)	R_L ($\Omega \cdot cm^2$)	$\tau_{kin}=L/R_L$ (s)
Li	1.15	5.6×10^{-8}	1292	1.8×10^{-6}	1379	2.4×10^{-3}	8100	19928	**0.41**
	1.1	5.4×10^{-8}	2238	1.9×10^{-6}	1361	2.6×10^{-3}	2.1×10^{4}	29405	**0.72**
No	1.2	7.2×10^{-8}	553	4.4×10^{-6}	1684	7.5×10^{-3}	1.5×10^{4}	2459	**6.0**
Li	1.1	7.0×10^{-8}	1203	4.8×10^{-6}	823	3.9×10^{-3}	5.6×10^{4}	9900	**5.7**
0%	0.95	5.4×10^{-7}	17	3.3×10^{-2}	77	2.5			
30%	0.95	5.9×10^{-7}	30	5.7×10^{-3}	145	0.82			
45%	0.95	4.5×10^{-7}	38	4.1×10^{-4}	282	0.12	2.1×10^{4}	860	**24**
60%	1.05	8.7×10^{-8}	9	2.4×10^{-5}	16	3.7×10^{-4}	208	14	**15**
	1	5.5×10^{-8}	19	7.6×10^{-6}	22	1.7×10^{-4}	351	25	**14**
	0.95	2.34×10^{-7}	29	6.0×10^{-7}	48	2.9×10^{-5}	2991	68	**44**

Table S2: charge transfer and ideality factors from equation S2 and S3.

Cell	V (V)	β	γ	m_β	m_γ
Li		0.33	0.32	3.0	3.1
No-Li	≤ 0.95	0.41	0.31	2.4	3.2
	≥ 95	0.29	0.31	3.4	3.2
0%		0.44	--	2.3	--
30%		0.47	--	2.1	--
45%		0.45	--	2.2	--
60%	≤ 1.1	0.41	0.45	2.4	2.2
	≥ 1.1	0.32	0.45	3.2	2.2

References

[1] C. Aranda, C. Cristobal, L. Shooshtari, C. Li, S. Huettner, A. Guerrero, *Sustainable Energy & Fuels* **2017**, 1, 540.

[2] C. Aranda, A. Guerrero, J. Bisquert, *ACS Energy Letters* **2019**, 741.

[3] E. Ghahremanirad, A. Bou, S. Olyaee, J. Bisquert, *The Journal of Physical Chemistry Letters* **2017**, 8, 1402.

CHAPTER 5

Publication 2: Correcting unintended changes in electroluminescence perturbation for reliable light intensity modulated spectroscopies

Agustin O. Alvarez, Antonio Riquelme, Rosinda Fuentes-Pineda, Elena Mas-Marzá, Lluis F. Marsal, Osbel Almora, Juan A Anta, Francisco Fabregat-Santiago.

Measurement Science and Technology **2023**
Submitted.
Impact Factor 2023: 2.398.

5.1. Candidate's contribution

Nature of Contribution	Extent of Contribution
✓ Carried out all the measurements ✓ Developed the theoretical model and calculations ✓ Analysed the measurements ✓ Interpreted the results ✓ Preaped the first version of the figures ✓ Wrote the first draft	70%

5.2. Thesis context

In **CHAPTER 4** we made clear the power of IS. The remainder of this thesis is devoted to combining IS with intensity-modulated photocurrent spectroscopy (IMPS) and intensity-modulated photovoltage spectroscopy (IMVS), to gain an even better understanding of the functioning of photoconversion devices. This publication is the first step towards this combination, where we develop a protocol to properly measure IMPS and IMVS. Obtaining reliable measurements of IMPS and IMVS is, obviously, essential for the proper analysis with these techniques, avoiding misinterpretations, and is critical for the combination of the different techniques.

In this chapter, we show that the light sources used to measure these techniques can generate undesired fluctuations in the modulated light. This effect is ignored in some instruments used to measure these techniques, which we show can generate artefacts that lead to misinterpretation of the results. The protocol we present in this publication solves this problem by properly measuring these light modulation fluctuations and applying a simple correction to the measured spectra. This protocol will be applied to the measurements in the following chapters.

5.3. Published Manuscript

Correcting unintended changes in electroluminescence perturbation for reliable light intensity modulated spectroscopies

Agustin O. Alvarez,[1] Antonio Riquelme [2], Rosinda Fuentes-Pineda[3], Elena Mas-Marzá[1], Lluis F. Marsal[4], Osbel Almora[2,4], Juan A Anta[2], Francisco Fabregat-Santiago[1*]*

[1]Institute of Advanced Materials, Universitat Jaume I, Castellón de la Plana 12071, Spain
[2]Department of Physical, Chemical and Natural Systems, Universidad Pablo de Olavide, Sevilla 41013, Spain
[3]Saule Technologies, Wroclaw PL, 54-427, Poland
[4]Department of Electronic, Electric and Automatic Engineering, Universitat Rovira i Virgili, 43007 Tarragona, Spain
* oalmora@upo.es ,*fabresan@uji.es
Keywords: light modulation, impedance spectroscopy, light emitting diodes, perovskite solar cells

Keywords: light modulation, impedance spectroscopy, light emitting diodes, perovskite solar cells

Abstract

Light intensity modulated photocurrent and photovoltage spectroscopies, IMPS and IMVS respectively, are characterization techniques for studying charge carrier transport and recombination properties of photosensitive samples such as photovoltaic solar cells. In these techniques controlling the modulated light flux is key to obtaining accurate results. Typically, the electroluminescence of the light source is considered frequency-independent and therefore, it may be estimated from the modulated current delivered by the power source. However, some anomalies may appear when the experimental requirements demand large variations in the measurement conditions. Herein, an analysis is presented on the unusual low-frequency response of IMPS and IMVS which appears for some light sources at high illumination intensities. We found that a frequency-dependent modulation of the light source electroluminescence should be accounted for, rather than the traditional steady-state calibration of the setup, as it may affect the accuracy and even produce undesired artifacts during the measurements. A protocol for detecting the modulation of the electroluminescence is proposed, combining the simultaneous use of the IMPS of a reference photodiode and the impedance spectroscopy of the light source. Discerning whether these low-frequency signal "tails" are due to the measurement setup or the sample is of major importance to avoid misinterpretations in any study. This is particularly important for preventing misinterpretations in studies on perovskite solar cells whose instability and ion-conductivity phenomena relate to the low-frequency region of the spectra.

5.3.1. Introduction

Light-perturbated transient techniques[1-2] and spectroscopic technique methods[3] are commonly used to characterize photosensitive devises, such as photoelectrodes,[4] photodetectors[5] and photovoltaic (PV) cells,[6] based on a broad range of materials, including silicon[3, 7] to chalcopyrites,[8] dyes,[9] organic semiconductors,[10-11] perovskites,[12-13] and ternary oxide semiconductors.[14] Among the spectroscopic techniques, the intensity-modulated photocurrent and photovoltage spectroscopies, IMPS and IMVS, respectively, are commonly used to approach the transport properties and dissipation mechanisms[15-16] in photosensitive samples. In these techniques, at a given frequency (f), an alternating current (AC) mode small perturbation of photon flux ($\tilde{\phi}$) is superposed over the stationary, or direct current (DC) mode, background illumination. Then, the corresponding modulated current density ($\tilde{J}$) or voltage ($\tilde{V}$) signal is recorded at the sample for IMPS or IMVS, respectively. Commonly, IMPS and IMVS spectra are shown in Nyquist representation, where the respective transfer functions are plotted representing the negative imaginary parts $-Q''$ and $-W''$, as a function of the real parts, Q' and W' (see **Figure 1**). In this representation, most typical spectra include one or several arcs in the first quadrant[3-4, 17] and, in some cases, loops and/or tails in the second and/or the fourth quadrant.[18-19]

IMPS and IMVS have been used for long time, for the calculation of transport and recombination times.[15] In last years, significant progress has been reported on the analytic and numerical modelling of the IMPS and IMVS signals for different devices. For instance, for dye sensitized solar cells, Kant et al.,[20] proposed a theory for IMPS on rough and finite fractal dye sensitized solar cell which identifies three characteristic frequency regimes: (i) lifetime of charge carrier dependent low frequency (Lf) regime, (ii) surface irregularity dependent intermediate frequency (Mf) power-law regime and (iii) diffusion controlled high frequency (Hf) regime. For solid-state PV cells, Almora et al.[7] solved the transport equations with photocurrent and photovoltage response due to light perturbation for an abrupt-one-sided junction assuming homogeneous charge carrier generation. On the other hand, Bisquert et al.,[6, 12, 21-22] reported the solution for thicker absorber layers where the Beer-Lambert law is a better approximation. In the latter,[12, 21] a correlation was proposed between the Hf part of the IMPS and the diffusion parameters for the standard sandwich-contacts solar cells and quasi-interdigitated back-contact devices for lateral long-range diffusion.

Regarding equivalent circuit (EC) modelling, Alvarez et al.[23] demonstrated Donolato's[24] theorem of reciprocity for charge collection using the same EC to fit IMPS, IMVS and impedance spectroscopy experimental data. According to this study, having the excitation signals properly characterized was critical for enabling the combination of the three techniques. Moreover, Ravishankar et al.[25-27] simulated and experimentally observed "sign inversions/tails" of Q'' and W'' towards Lf in perovskite solar cells (PSCs). Furthermore, drift-diffusion numerical modelling by Bernhardsgrütter and Schmid[28] including ion migration simulated IMPS and IMVS spectra with two arcs in the Nyquist representation, associating the Hf and Lf features to electronic and ionic phenomena, respectively. Remarkably, they qualitatively reproduced spectra with ion-related "sign inversion/tails" of Q'' and W''.

Experimentally, not only the use of IMPS and IMVS continues to be customary,[17, 29-30] but also new approaches have been proposed. For instance, Almora et al.[3, 7] demonstrated the combination of IMPS and IMVS to acquire light intensity modulated impedance spectroscopy as an alternative to study recombination velocities at the interfaces of solid-state PV devices. More recently, Laird et al.[31] implemented IMPS in an imaging mode with microscopic resolution in back-contact PSCs. This microscopy-based IMPS is used to calculate spatial maps of the carrier ambipolar diffusion length in the Lf limit. Interestingly, Ravishankar et al.,[32] found that the instability of the PSCs can be the main reason behind apparent loops and/or "sign-inversion/tails" of Q''. Furthermore, Srivastava et al.[19] studied the IMPS spectra of perovskite–electrolyte and polymer-aqueous electrolyte interfaces. They reported that the electronic-ionic interaction in hybrid perovskites including the Lf ion/charge transfer and recombination kinetics at the interface leads to a spiral feature in IMPS Nyquist plot.

Regardless of the system, the literature is abundant on the analysis of IMVS/IMPS spectra with clear differences between the low and high-frequency domains. The higher the frequency, the faster the transport processes that are characterized, and the higher the presence of artifacts due to signal processing limitations. On the other hand, the lower the frequency, the closer the signal response to the steady state transport regime and the higher the $1/f$ noise artifacts. Particularly, the Lf range is key for the characterization of devices and materials as it is the domain in which instabilities and phenomena like ionic conductivity occurs in materials such as metal halide perovskites. However, care must be taken when exploring the Lf part of these spectra and attributing all the features to the sample.[19-20, 28, 32] For instance, **Figure 1** (darker dots) illustrates IMPS and IMVS spectra with sign inversion towards Lf of

Q'' and *W''*, respectively (see Figure S1 in the supporting information for the device structure and *J-V* curves of the PSC sample). Notably, the so-called "Lf tail" does not produce major changes in the frequency derivative of the absolute values (see Figure S1) which could be related to a frequency-dependent phase issue. Then, a question arises on whether it is a sample feature or an artifact due to the setup.

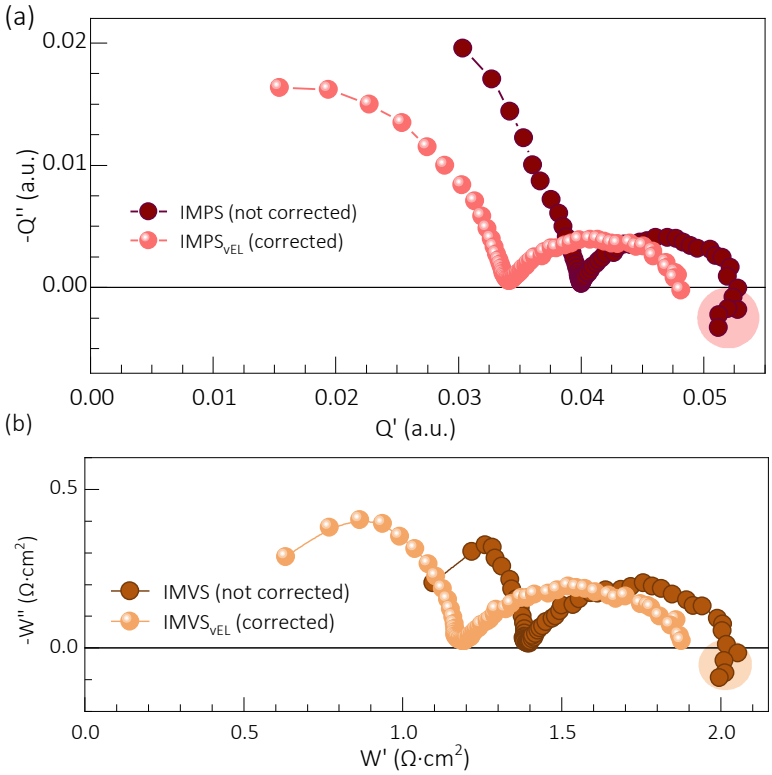

Figure 1. Different spectra of a perovskite solar cell: (a) IMPS, and (b) IMVS. The measurements were performed from 200 kHz to 0.1 Hz, at open-circuit condition (980 mV) and under a DC light intensity of 89 mWcm^{-2} from a blue LED (600mA, LXML-PB01-0040 Philips LUMILEDS).[33] The fabrication details and primarily characterization of the studied device can be found in our previous work[34] Darker dot colors indicate the pristine data assuming frequency-independent electroluminescence of the light source. The shadowed area highlights the apparent tails of the spectra. The subscript "vEL" and the lighter dot colors indicate a correction of the photon flux by considering the modulation-varied electroluminescence of the light source following the equations summarized in **Table 1**. The tails disappear thanks to the implementation of the proposed protocol.

In this work, the occurrence and origin of a characteristic sign inversion of the imaginary part of the IMPS and IMVS signals toward Lf is analyzed, regardless of instability issues. Several light emitting diodes (LEDs) and samples are characterized at different measurement conditions using light modulation techniques as well as potentiostatic impedance spectroscopy

(IS). Our findings indicate that some light sources present a frequency-dependent electroluminescence (EL) which requires an accurate calibration to acquire truthful measurements. Accordingly, a new calibration method is proposed that not only validates the qualitative analysis of unusual low-frequency tails in the spectra, but also quantitatively increase around 10% the accuracy in the estimation of derived physical magnitudes, such as the external quantum efficiency (EQE). Furthermore, it eliminates spurious effects that would otherwise yield misinterpretation of low frequency results which, in systems such as those including metal halide perovskites, are key to understand device performance and stability.

5.3.1. Theoretical formalism and methods

To further analyze the origin of the apparently anomalous signal we start by revisiting the experimental design and the formalisms of the light-modulated spectroscopy techniques. **Figure 2** shows two main configurations typically used for IMPS and IMVS. The current I_{LS} through the light source (e.g. a light emitting diode, LED) is typically used to control the photon flux ϕ at a distance L where a reference diode and the sample are placed. The calibration is most often based on the DC response of the reference photodiode whose current density J_d can be monitored.

The one-time DC calibration configuration is depicted in **Figure 2**a, where the photodiode and the sample are placed at a distance L from the light source, but only one DC calibration is set before the measurement. In this configuration, the illuminated area of the reference photodiode and the sample should be similar to simplify the setup (and reduce costs). Conveniently, a high homogeneity of the light intensity is not required. Yet, the one-time calibration does not account for temperature (T) changes and/or DC fluctuations in the electroluminescence of the light source and the sample during the DC+AC measurements and large samples may introduce artifacts. Furthermore, the perturbation can only be estimated throughout the modulation of the current across the light source, meaning that the AC components are assumed as $\tilde{I}_{LS} \propto \tilde{\phi}$.

The simultaneous DC calibration configuration is shown in **Figure 2**b, where not only the sample and the photodiode are placed at an equivalent distance L from the light source, but also the calibration and measurement are as simultaneous as possible. Notably, this approach requires additional potentiostat channels to simultaneously process the reference photodiode and the sample, and the light source should distribute the photon flux as

homogeneously as possible. Advantageously, this configuration permits the in-situ correction of thermal and/or DC fluctuations of the electroluminescence of the light source and the sample during the DC+AC measurements. In addition, depending on the equipment, the simultaneous calibration approach introduces the modulation of the photon flux by monitoring the current density across the reference diode. Accordingly, $\tilde{I}_{LS} \propto \tilde{\phi}$ and $\tilde{J}_d \propto \tilde{\phi}$ can be assumed and/or monitored, increasing the accuracy. For this configuration, the response time of the photodiode (its own $IMPS_{ref}$) should be considered. If this response from the photodiode is not fast enough, or departs from linearity, the apparent flux will need to be corrected at each frequency so that $\tilde{J}_d \propto \tilde{\phi} \cdot IMPS_{ref}$.

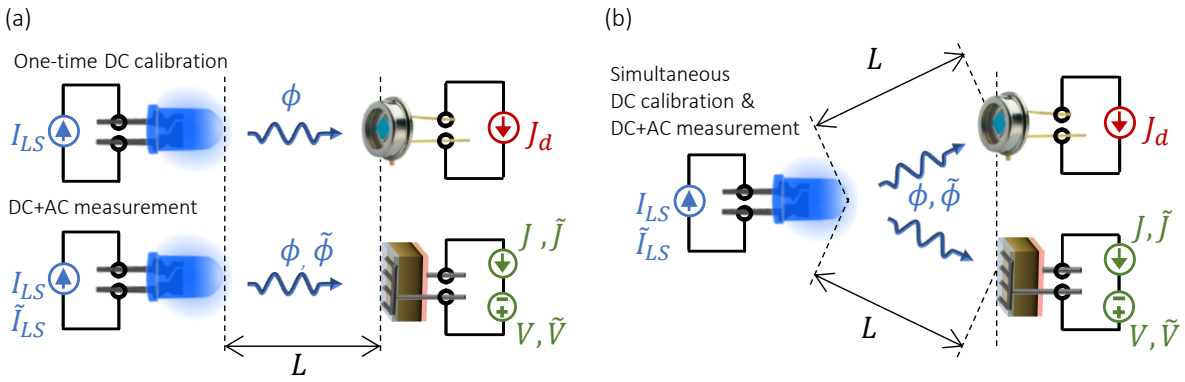

Figure 2. Scheme of setup configurations for IMPS and IMVS including the DC calibration with a reference photodiode and the measurement of DC+AC signals in the emitter and sample where the calibration can be (a) a one-time step before measurement or (b) a simultaneous.

Once the AC photon flux, $\tilde{\phi}$, and the AC photocurrent density extracted from the sample, $\tilde{\jmath}$, are obtained, the transfer function of IMPS may be calculated through

$$Q = \frac{\tilde{J}}{q\tilde{\phi}} \tag{1}$$

where q is the elementary charge and $\tilde{\phi}$ is the photon flux perturbation in units of $s^{-1}cm^{-2}$ that normalizes Q in dimensionless units. In the Lf limit, Q is the EQE.[25] The device external current may be considered with the opposite sign, in which case the definition of Q has a negative sign.[23] Alternatively, IMPS can be defined as the photocurrent responsivity $\Psi_J = \tilde{J}/\tilde{P}$ (in units of $A \cdot W^{-1}$), where $\tilde{P}$ is the light power density falling upon the sample.[3, 35]

Similarly, the modulated photovoltage signal $\tilde{V}$ from the sample is used to calculate the transfer function of IMVS, given by

$$W = \frac{\tilde{V}}{q\tilde{\phi}} \tag{2}$$

which results in units of $\Omega \cdot cm^2$. Otherwise, IMVS can be defined as photovoltage responsivity $\Psi_V = \tilde{V}/\tilde{P}$ (in units of $V \cdot W^{-1} \cdot cm^2$).[3, 35] In any electroluminescent system, one can define the DC electroluminescence rate (in units of $A^{-1}s^{-1}cm^{-2}=C^{-1}cm^{-2}$) through

$$\eta_{EL} = \frac{\phi}{I_{LS}} \tag{3}$$

indicating the number of emitted photons that reach the sample per unit area provided a current flow I_{LS} through the light source for a given set of conditions (e.g. L, T). For regular use, η_{EL} is typically provided by the equipment manufacturer with a given tolerance range (e.g. included in the software that performs the measurement). In other words, an already done one-time DC calibration reports a table of DC values of $\eta_{EL}(L,T)$ as a function of I_{LS}, from which $\phi(L,T)$ is estimated. In the event that η_{EL} is not provided, one can measure the current density at a reference photodiode whose DC photon-to-current responsivity S_d (in units of A·s) is known, then

$$\phi = \frac{J_d}{S_d} \tag{4}$$

For the one-time DC calibration (**Figure 2**a), the current in Equation (4) can be denoted as J_{d0} to highlight that the photodiode is measured in a "zero" state that does not necessarily match the measurement conditions of the sample. Note that when factory calibrations are used, especially after many hours of use or changes in the configuration of the measurement, the real J_d may differ from the original J_{d0}. Moreover, for monochromatic light sources with photon wavelength λ, then $S_d = hcS_\lambda\lambda^{-1}$, where h is the Plank's constant, c is the celerity of light in vacuum, and the sensitivity S_λ has units of $A \cdot W^{-1}$ (typically provided by the manufacturer of the photodiode). For non-monochromatic light sources with spectrum $\Gamma(\lambda)$ (units of $W \cdot nm^{-1}$), the sensitivity is $S_d = hc \int \Gamma S_\lambda \lambda^{-1} d\lambda \, (\int \Gamma d\lambda)^{-1}$.

Subsequently, one can combine equations (3) and (4) to obtain

$$\eta_{EL} = \frac{J_d}{I_{LS}\, S_d} \tag{5}$$

Relations (3)-(5) can be substituted in definitions (1) and (2) for IMPS and IMVS, respectively, assuming a proportionality between the calibrated reference DC values and the analogue AC signals ($\tilde{\phi} = \tilde{I}_{LS}\eta_{EL} = \tilde{J}_d/S_d$). However, this is not always the case and some instruments do not account for nonlinearities during modulation of the EL and thus the photon flux $\tilde{\phi}$.

Furthermore, the signal output from some commercial instruments does not have an internal assessment of the values of ϕ and the area A of the sample for estimating $\tilde{J} = \tilde{I}/A$ from definition in Equation (1). Hence, the dimensionless transfer function of the IMPS is reported as the uncalibrated ratio

$$Q_I = \frac{\tilde{I}}{\tilde{I}_{LS}} = q\ Q\ A\ \eta_{EL} \tag{6}$$

This expression can be combined with Equation (3) to provide the calibrated IMPS of Equation (1) as a simple normalization

$$Q = \frac{Q_I}{qA\eta_{EL}} \tag{7}$$

A similar normalization may be used for IMVS (in units of Ω). The value typically provided by many apparatuses is the uncalibrated IMVS given by

$$W_I = \frac{\tilde{V}}{\tilde{I}_{LS}} = q\ W\ \eta_{EL} \tag{8}$$

Analogously, using Equation (3) and assuming DC values of η_{EL}, Equation (8) can be used to obtain the IMPS as defined in Equation (2), which results in

$$W = \frac{W_I}{q\eta_{EL}} \tag{9}$$

The use of Equation (6) assuming η_{EL} as a real number is often found in the literature,[9, 17, 36] especially when the interest was focused only on extracting the characteristic time constants. In general, with those objectives this procedure give the impression to be correct unless the artifacts mentioned above emerge. In the following section, a discussion is presented on why and when a more accurate approach is required assuming the electroluminescence rate as a complex number.

5.3.1. Results and Discussion

The Lf quadrant inversion of the IMPS and IMVS spectra for PSCs, such as those in **Figure 1** (dark dots), has been found to occur only for incident light intensities higher than a threshold value. Figures S2-3 show the spectra obtained for the same PSC and measured with the same setup[33] used in **Figure 1**, but utilizing lower light intensities. In these cases, the Lf quadrant change is no longer present. Furthermore, similar experiments were conducted with a silicon photodiode (Hamamatsu S1133), instead of the PSCs, and a similar sign inversion was obtained for high illumination intensities (see Figure S4). The occurrence of this effect with the silicon photodiode discards extra possible contributions, such as device chemical and thermal instabilities, which are negligible in silicon-based devices. This suggests that the Lf dependency of the spectra is related to the photon flux $\tilde{\phi}(\omega)$, and not to the photocurrent and photovoltage responsivities.

A different setup,[35] following the scheme of **Figure 2**a, including a different light source, was also used to analyze the same silicon photodiode. These experiments are summarized in Figure S5. Accordingly, the frequency dependency of the photon flux is associated with the measurement setup (Autolab),[33] rather than the sample. This may lead to two main effects: the potentiostat could have an unaccounted frequency dependency in the current supply $\tilde{I}_{ls}(\omega)$ to the light source (i.e., the LED), and/or the light source could introduce a perturbation in the modulation of the electroluminescence which may result in a frequency-dependent electroluminescence rate $\eta_{EL}(f)$.

Note that η_{EL} is mostly assumed to be a magnitude whose value does not change upon modulation. However, if one takes the reference photodiode as the sample, i.e. $\tilde{I}$=$\tilde{I}_d$ in equations (5) and (6), the electroluminescence rate of the light source can be characterized as

$$\tilde{\eta}_{EL} = \frac{Q_{Id}}{A_d\, S_d} = \frac{Q_{Id}{}' + iQ_{Id}{}''}{A_d\, S_d} = \frac{|Q_{Id}|\exp[i\theta_d]}{A_d\, S_d} \tag{10}$$

where i is the imaginary number; Q_{Id} is the uncalibrated ratio from the reference photodiode; with its real part, imaginary part and modulus indicated by ´, ´´, and ‖, respectively; and the corresponding phase shift is θ_d. Accordingly, η_{EL} results in a complex number $\tilde{\eta}_{EL} = \eta'_{EL} + i \cdot \eta''_{EL} = |\eta_{EL}|\exp[i\theta_d]$ due to the unintended modulation observed in Q_{Id}. Subsequently, one can substitute Equation (10) in (6) for correcting the IMPS from the sample of area A_s, whose uncalibrated ratio is $Q_I = Q_I{}' + i \cdot Q_I{}'' = |Q_I|\exp[i\theta]$. Therefore, the final expressions for the definitions of IMPS (Equation 1) can be rewritten as shown in **Table 1**. Similarly, one can measure the uncalibrated ratio of IMVS as $W_I = W_I{}' + i \cdot W_I{}'' = |W_I|\exp[i\vartheta]$, and the respective expressions for correcting the modulation of the photon flux would be those summarized in **Table 1**.

Table 1. Set of equations for correcting modulation of the electroluminescence rate for a given DC current I_{LS} (at the light source) and a distance L between the sample and the light source.

Representation type	IMPS		IMVS	
	Q'	Q''	W'	W''
Modulus and phase of Q_I, W_I and η_{EL}	$\frac{1}{A_s q}\frac{\lvert Q_I\rvert}{\lvert\eta_{EL}\rvert}\sin[\theta-\theta_d]$	$\frac{1}{A_s q}\frac{\lvert Q_I\rvert}{\lvert\eta_{EL}\rvert}\cos[\theta-\theta_d]$	$\frac{\lvert W_I\rvert}{q\,\lvert\eta_{EL}\rvert}\sin[\vartheta-\theta_d]$	$\frac{\lvert W_I\rvert}{q\,\lvert Q_{Id}\rvert}\cos[\vartheta-\theta_d]$
Real and imaginary parts of Q_I, W_I and η_{EL}	$\frac{(Q_I{}'\eta_{EL}{}' + Q_I{}''\eta_{EL}{}'')}{A_s q(\eta_{EL}{}'^2 + \eta_{EL}{}''^2)}$	$\frac{(Q_I{}'\eta_{EL}{}'' - Q_I{}''\eta_{EL}{}')}{A_s q(\eta_{EL}{}'^2 + \eta_{EL}{}''^2)}$	$\frac{(W_I{}'\eta_{EL}{}' + W_I{}''\eta_{EL}{}'')}{q(\eta_{EL}{}'^2 + \eta_{EL}{}''^2)}$	$\frac{(W_I{}'\eta_{EL}{}'' - W_I{}''\eta_{EL}{}')}{q(\eta_{EL}{}'^2 + \eta_{EL}{}''^2)}$
Modulus and phase of Q_I, W_I and Q_{Id}	$\frac{A_d S_d}{A_s q}\frac{\lvert Q_I\rvert}{\lvert Q_{Id}\rvert}\sin[\theta-\theta_d]$	$\frac{A_d S_d}{A_s q}\frac{\lvert Q_I\rvert}{\lvert Q_{Id}\rvert}\cos[\theta-\theta_d]$	$\frac{A_d S_d}{q}\frac{\lvert W_I\rvert}{\lvert Q_{Id}\rvert}\sin[\vartheta-\theta_d]$	$\frac{A_d S_d}{q}\frac{\lvert W_I\rvert}{\lvert Q_{Id}\rvert}\cos[\vartheta-\theta_d]$
Real and imaginary parts of Q_I, W_I and Q_{Id}	$\frac{A_d S_d}{A_s q}\frac{(Q_I{}'Q_{Id}{}' + Q_I{}''Q_{Id}{}'')}{(Q_{Id}{}'^2 + Q_{Id}{}''^2)}$	$\frac{A_d S_d}{A_s q}\frac{(Q_I{}'Q_{Id}{}'' - Q_I{}''Q_{Id}{}')}{(Q_{Id}{}'^2 + Q_{Id}{}''^2)}$	$\frac{A_d S_d}{q}\frac{(W_I{}'Q_{Id}{}' + W_I{}''Q_{Id}{}'')}{(Q_{Id}{}'^2 + Q_{Id}{}''^2)}$	$\frac{A_d S_d}{q}\frac{(W_I{}'Q_{Id}{}'' - W_I{}''Q_{Id}{}')}{(Q_{Id}{}'^2 + Q_{Id}{}''^2)}$

The fully corrected measurements can be obtained by substituting the frequency dependent value of η_{EL} from **Table 1**, instead of the DC estimation from Equation (6), as illustrated in **Figure 1** with lighter spheres for the PSC. Not only have the Lf "tails" disappeared but also a small decrease in the real part of the spectra is evident from the

horizontal left-shift of the Nyquist plots of **Figure 1**. This indicates that the electroluminescence modulation of the LED is producing both a signal artifact toward Lf and an overestimation of the photocurrent and photovoltage responsivities of the sample. An illustrative comparison between the modulated electroluminescence rate and the DC value is presented in **Figure 3**a (for the same experimental conditions of I_{LS} and L of the spectra in **Figure 1**), where the Lf region related to the IMPS and IMVS signal quadrant inversion is light-red-highlighted.

Figure 3a shows that the calculation of Q and W with the DC value, instead of the method we are proposing here, can generate an overestimation of more than 10% at high frequencies, reaching 14% in the presented case (values of 1.14 on the right axis of **Figure 3**a).This relatively high divergence may be of low influence when the studies are aim to qualitatively assess characteristic time constants between different samples, like for instance transport times.[37-38] However, a proper modulation frequency normalization is required when the main objective is quantifying Q' and W'. Notably, on the latter, an estimation of S_d is recommended since most of the commercial LSs are LEDs with gaussian-like spectra whose standard deviation ranges from 20 nm to 100 nm.

The unintended electroluminescence modulation of the light source can also be illustrated by comparing the IS spectrum of the light source $Z(f)$ and that of the electroluminescence rate $\eta_{EL}(f)$. This is displayed in the Nyquist and Bode representations in **Figure 3**c,d, respectively. Toward low frequencies, the IS spectrum shows a well-defined process which is evident from the arc in **Figure 3**a and the Z'' maximum in **Figure 3**b. Similarly, the renormalized η_{EL}'' evidences a maximum at the exact frequency, which suggests that the Lf process of the LED is modifying the electroluminescence during the measurement.

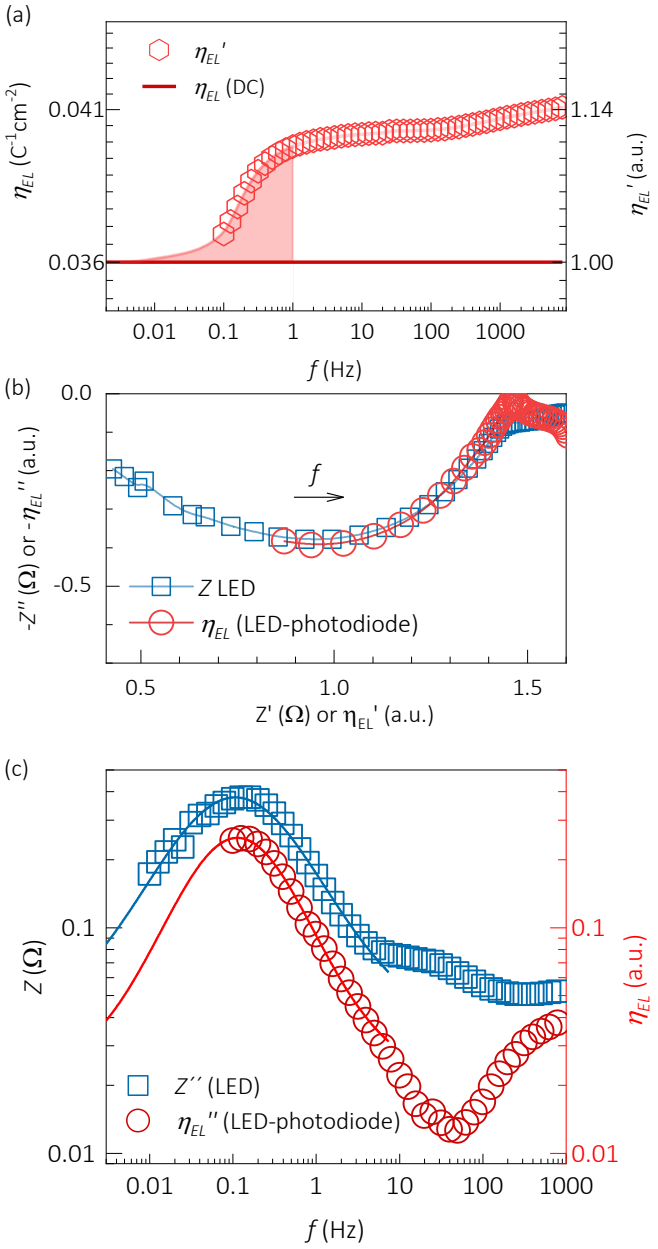

Figure 3. Comparisons between the modulated electroluminescence rate after calibration and that of the DC estimation in (a), and the impedance and electroluminescence rate spectra of the light source (LED LXML-PB01-0040 Philips LUMILEDS) are compared in Nyquist (b) and Bode (c) representations for the impedance check. The shadowed area in (a) indicates the frequency range of high frequency-dependency modulation for the electroluminescence rate, which is the same range of the signal peaks in (c). The coincidence between impedance and electroluminescence peaks in (c) suggests good agreement with the equations summarized in **Table 1**.

The variation of the electroluminescence rate of LEDs upon bias perturbation is well-known in the literature, although frequency domain experiments are seldom found. For instance, Lie-Feng et al.[39] not only documented a significant change in the relative light intensity of blue LEDs from 100 Hz to 10 mHz, but also correlated it with the recombination luminescence. Similarly, but on semipolar InGaN/GaN LEDs, Haggar et al.[40] showed how the higher the injection current to the LED, the lower the characteristic frequency for the EL response to transit and peak toward the steady state limit. On the other hand, in the time domain, the characterization of transient electroluminescence is more often reported.[41-42] For instance, Lupton and Klein[43] studied the transient EL of polyfluorene LEDs showing changes in the EL spectra distribution and intensity for different pulse durations from tens to hundreds of μs and bias offsets.

The variation of the electroluminescence rate of LEDs upon bias perturbation is well-known in the literature, although frequency domain experiments are seldom found. For instance, Lie-Feng et al.[39] not only documented a significant change in the relative light intensity of blue LEDs from 100 Hz to 10 mHz, but also correlated it with the recombination luminescence. Similarly, but on semipolar InGaN/GaN LEDs, Haggar et al.[40] showed how the higher the injection current to the LED, the lower the characteristic frequency for the EL response to transit and peak toward the steady state limit. On the other hand, in the time domain, the characterization of transient electroluminescence is more often reported.[41-42] For instance, Lupton and Klein[43] studied the transient EL of polyfluorene LEDs showing changes in the EL spectra distribution and intensity for different pulse durations from tens to hundreds of μs and bias offsets. The above analysis suggests that a proper calibration protocol is required before setting up light intensity modulated measurements. Accordingly, a set of steps is proposed here as a guideline for good practices, which is summarized in **Table 2**. These recommendations propose checking the AC properties of the light source to deliver reliable experimental practices. Moreover, **Figure 4** shows the schemed calibration and measurement procedures analogue to those of **Figure 1**, but now including the recommended protocol in **Table 2**. For the one-time calibration in **Figure 4**a, not only DC estimation of the photon flux but AC measurement of the IMPS of the reference diode and IS analysis of the light source (LED) is suggested before measurement of the sample. For the simultaneous calibration alternative in **Figure 4**b, a previous check of the IS spectra of the light source is suggested before the simultaneous AC and DC measurement of the reference photodiode and the sample.

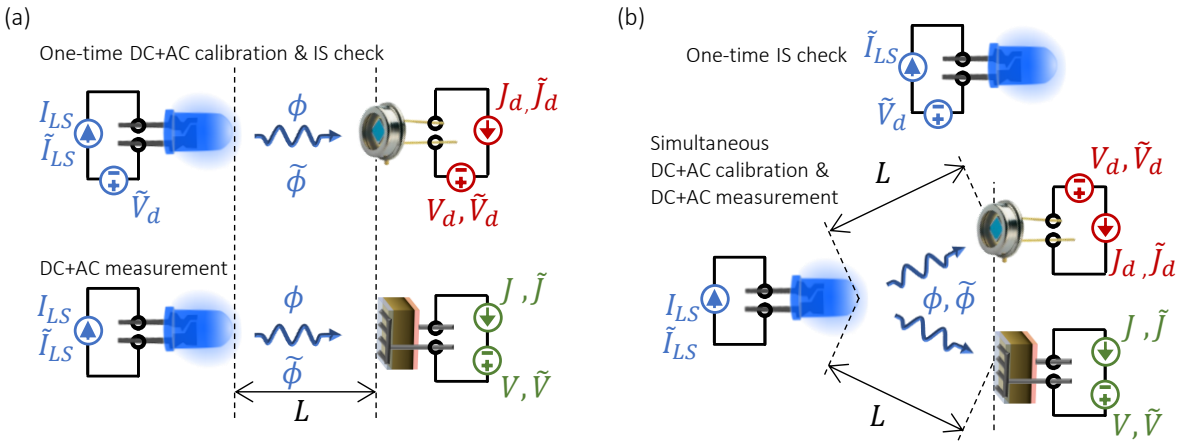

Figure 4. Schemed new proposed approach, as summarized in **Table 2**, for the one-time (a) and simultaneous (b) calibration modes, which respectively modifies the processes in **Figure 2**a,b.

Table 2. Recommended measurement protocol for IMPS and IMVS

No.	Procedure
1.	Calibration of DC photon flux value ϕ of photon flux using equivalent DC to equations (3)-(6) for a given distance L between the detector/sample and the light source: i. Place a calibrated detector at a fix distance L from the light source. ii. Apply a current I_{LS} to the light source. iii. Measure the photocurrent response in the photodetector J_d. iv. Calculate $\phi(I_{LS}) = J_d/S_d$, using the photon-to-current responsivity S_d.
2.	Measurement of the IMPS of a reference photodiode for estimating the frequency dependent values $\eta_{EL}(f)$ of the electroluminescence rate, using the expression in **Table 1**. In case of varying modulation effects (e.g. low frequency tails), the frequency-dependent $\eta_{EL}(f)$ should be used to correct the value $\phi(f)$ of the photon flux, and thus Q and W.
3.	Measurement of the impedance $Z''(f)$ of the light source (typically an LED) for comparison with the $\eta_{EL}''(f)$ spectrum. If there is no coincidence between these spectra, the features in the spectrum of the sample may be related to the sample.
4.	Verify thermal, optical and atmosphere stability during the measurement. For analyses on PSCs, repeat the measurement several times after polarization until equilibrium is reached.

An important direct implication/advantage of the proposed protocol relates to the accuracy of the EQE measurement in PV cells. From the EQE spectra, one can integrate the short-circuit current density ($J_{sc,EQE}$) under standard 1-sun illumination.[44] Provided the same measurement conditions,[45-47] the photocurrent values from the EQE and the current-voltage curve under the solar simulator ($J_{sc,JV}$) should match, i.e., $J_{sc,EQE} \approx J_{sc,JV}$. Therefore, when using IMPS for measuring the *EQE*, the light sources may be set to high DC illumination intensity in order to simulate the 1-sun standard. This condition may trigger the unintended electroluminescence modulation to be corrected with the protocol of **Table 2** (for equipment that generates the AC and DC signals with the same light source). Nevertheless, the AC modulation/chopping frequency[25, 48] and the DC background illumination intensity[45-47] are not the only modifying factors for the EQE measurement.[49-50] Device instability[51] can also be an issue. Overall, the accuracy of EQE spectra continues to be a subject of debate and even recent concern has arisen on reported high integrated photocurrent values for being above the detailed balance efficiency limit.[52-53]

5.3.1. Conclusions

In summary, IMPS and IMVS spectra of photosensitive samples should be analyzed in detail to discard measurement artifacts. This is particularly important for characterizing unstable and/or mixed electronic-ionic materials and devices such as the metal halide perovskite-based samples, where many anomalous behaviors are often found toward lower frequencies. A systematic check is required upon occurrence of characteristic sign inversion (quadrant change) in the spectra of the imaginary parts of the IMPS or IMVS transfer functions, also known as low-frequency tails. It is shown that the photon flux amplitude cannot always be assumed to be independent of the modulation frequency. Instead, the electroluminescence modulation of the light source should be measured and corrected accordingly. Moreover, we highlight how the impedance characterization of the light source can be useful to identify these artifacts that may be present at high illumination intensities and toward low perturbation frequencies.

Supplementary Material

IMPS, IMVS and IS spectra measured under different conditions and with several instruments for validation of the proposed correction.

ORCID iDs

Agustin O. Alvarez— http://orcid.org/0000-0002-0920-5390
Antonio Riquelme— https://orcid.org/0000-0003-2445-3664
Rosinda Fuentes-Pineda— https://orcid.org/0000-0003-2587-8795
Elena Mas-Marzá— http://orcid.org/0000-0002-2308-0635
Luis F. Marsal— https://orcid.org/0000-0002-5976-1408
Osbel Almora — https://orcid.org/0000-0002-2523-0203
Juan A. Anta— https://orcid.org/0000-0002-8002-0313
Francisco Fabregat-Santiago — https://orcid.org/0000-0002-7503-1245

Notes

The authors declare no competing financial interests.

Acknowledgement

The authors would like to acknowledge Dr Vivek Babu for his collaboration in the fabrication and transport of the perovskite solar cells. This work has received funding from the European Union's Horizon 2020 research and innovation program under the Photonics Public Private Partnership (www.photonics21.org) with the project PEROXIS under the grant agreement N° 871336. We acknowledge the Ministerio de Ciencia e Innovación of Spain, Agencia Estatal de Investigación (AEI) and EU (FEDER) under grants PID2019-110430GB-C22 and PCI2019-111839-2 (SCALEUP). O.A. thanks the Spanish State Research Agency (Agencia Estatal de Investigación) for the Juan de la Cierva 2021 grant.

References

[1] E. Palomares, N. F. Montcada, M. Méndez, J. Jiménez-López, W. Yang, G. Boschloo, *Chapter 7 - Photovoltage/photocurrent transient techniques* in *Characterization Techniques for Perovskite Solar Cell Materials*, (Eds: M. Pazoki, A. Hagfeldt, T. Edvinsson), Elsevier, **2020**.

[2] D. Walter, A. Fell, Y. Wu, T. Duong, C. Barugkin, N. Wu, T. White, K. Weber, *J. Phys. Chem. C* **2018**, 122, 11270.

[3] O. Almora, Y. Zhao, X. Du, T. Heumueller, G. J. Matt, G. Garcia-Belmonte, C. J. Brabec, *Nano Energy* **2020**, 75, 104982.

[4] A. O. Alvarez, M. García-Tecedor, L. Montañés, E. Mas-Marzá, S. Giménez, F. Fabregat-Santiago, *Sol. RRL* **2022**, 6, 2200826.

[5] S. Ma, G. Jang, S. Kim, H.-C. Kwon, S. Goh, H. Ban, J. H. Cho, J. Moon, *ACS Appl. Mater. Interfaces* **2020**, 12, 41674.

[6] J. Bisquert, M. Janssen, *J. Phys. Chem. Lett.* **2021**, 12, 7964.

[7] O. Almora, D. Miravet, G. J. Matt, G. Garcia-Belmonte, C. J. Brabec, *Appl. Phys. Lett.* **2020**, 116, 013901.

[8] C. J. Pereyra, Y. Di Iorio, M. Berruet, M. Vazquez, R. E. Marotti, *J. Mater. Sci.* **2020**, 55, 9703.

[9] A. J. Riquelme, V. M. Mwalukuku, P. Sánchez-Fernández, J. Liotier, R. Escalante, G. Oskam, R. Demadrille, J. A. Anta, *ACS Appl. Energy Mater.* **2021**, 4, 8941.

[10] P. Deb, R. T. Grimm, J. K. Grey, *ACS Appl. Mater. Interfaces* **2021**, 13, 5338.

[11] R. T. Grimm, P. Deb, D. J. Walwark, Jr., C. Viets, J. K. Grey, *J. Phys. Chem. C* **2020**, 124, 16838.

[12] A. Bou, A. Pockett, H. Cruanyes, D. Raptis, T. Watson, M. J. Carnie, J. Bisquert, *APL Mater.* **2022**, 051104.

[13] Z. Ye, J. Zhou, J. Hou, F. Deng, Y.-Z. Zheng, X. Tao, *Solar RRL* **2019**, 3, 1900109.

[14] I. Rodríguez-Gutiérrez, E. Djatoubai, M. Rodríguez-Pérez, J. Su, G. Rodríguez-Gattorno, L. Vayssieres, G. Oskam, *Electrochimica Acta* **2019**, 308, 317.

[15] L. M. Peter, *Chem. Rev.* **1990**, 90, 753.

[16] E. A. Ponomarev, L. M. Peter, *J. Electroanal. Chem.* **1995**, 396, 219.

[17] N. Parikh, S. Narayanan, H. Kumari, D. Prochowicz, A. Kalam, S. Satapathi, S. Akin, M. M. Tavakoli, P. Yadav, *Phys. Status Solidi RRL* **2022**, 16, 2100510.

[18] M. Antuch, *Curr. Opin. Electrochem.* **2022**, 35, 101043.

[19] P. Srivastava, R. Kumar, H. Ronchiya, M. Bag, *Sci. Rep.* **2022**, 12, 14212.

[20] R. Kant, N. R. Chowdhury, S. Srivastav, *J. Electrochem. Soc.* **2019**, 166, H3047.

[21] A. Bou, H. Āboliņš, A. Ashoka, H. Cruanyes, A. Guerrero, F. Deschler, J. Bisquert, *ACS Energy Lett.* **2021**, 6, 2248.

[22] J. Bisquert, *J. Phys. Chem. Lett.* **2022**, 13, 7320.

[23] A. O. Alvarez, S. Ravishankar, F. Fabregat-Santiago, *Small Methods* **2021**, 5, 2100661.

[24] C. Donolato, *Appl. Phys. Lett.* **1985**, 46, 270.

[25] S. Ravishankar, C. Aranda, P. P. Boix, J. A. Anta, J. Bisquert, G. Garcia-Belmonte, *J. Phys. Chem. Lett.* **2018**, 9, 3099.

[26] S. Ravishankar, C. Aranda, S. Sanchez, J. Bisquert, M. Saliba, G. Garcia-Belmonte, *J. Phys. Chem. C* **2019**, 123, 6444.

[27] S. Ravishankar, A. Riquelme, S. K. Sarkar, M. Garcia-Batlle, G. Garcia-Belmonte, J. Bisquert, *J. Phys. Chem. C* **2019**, 123, 24995.

[28] D. Bernhardsgrütter, M. M. Schmid, *J. Phys. Chem. C* **2019**, 123, 30077.

[29] M. A. Afroz, C. A. Aranda, N. K. Tailor, Yukta, P. Yadav, M. M. Tavakoli, M. Saliba, S. Satapathi, *ACS Energy Lett.* **2021**, 6, 3275.

[30] A. Pockett, M. Spence, S. K. Thomas, D. Raptis, T. Watson, M. J. Carnie, *Solar RRL* **2021**, 5, 2100159.

[31] J. S. Laird, S. Ravishankar, K. J. Rietwyk, W. Mao, U. Bach, T. A. Smith, *Small Methods* **2022**, 6, 2200493.

[32] S. Ravishankar, M. Garcia-Batlle, J. Bisquert, G. Garcia-Belmonte, J. Odrobina, C.-A. Schiller, *J. Phys. Chem. C* **2020**, 124, 15793.

[33] Metrohm Autolab B.V., *LED Driver User Manual*, https://www.metrohm.com/en.html. Accessed 25.10.2022.

[34] V. Babu, R. Fuentes Pineda, T. Ahmad, A. O. Alvarez, L. A. Castriotta, A. Di Carlo, F. Fabregat-Santiago, K. Wojciechowski, *ACS Appl. Energy Mater.* **2020**, 3, 5126.

[35] Zahner-Elektrik GmbH & Co. KG, *CIMPS*, https://zahner.de/products-details/photoelectrochemistry/cimps. Accessed 30.06.2023.

[36] A. Riquelme, F. E. Gálvez, L. Contreras-Bernal, H. Míguez, J. A. Anta, *J. Appl. Phys.* **2020**, 128.

[37] E. Guillén, F. J. Ramos, J. A. Anta, S. Ahmad, *J. Phys. Chem. C* **2014**, 118, 22913.

[38] A. Albadri, P. Yadav, M. Alotaibi, N. Arora, A. Alyamani, H. Albrithen, M. I. Dar, S. M. Zakeeruddin, M. Grätzel, *J. Phys. Chem. C* **2017**, 121, 24903.

[39] F. Lie-Feng, L. Ding, W. Cun-Da, Z. Guo-Yi, Y. Dong-Sheng, L. Wei-Fang, X. Peng-Fei, *Chinnese Phys. Lett.* **2011**, 28, 107801.

[40] J. I. H. Haggar, Y. Cai, S. S. Ghataora, R. M. Smith, J. Bai, T. Wang, *ACS Appl. Electron. Mater.* **2020**, 2, 2363.

[41] Q. Yuan, T. Wang, P. Yu, H. Zhang, H. Zhang, W. Ji, *Organic Electron.* **2021**, 90, 106086.

[42] H. Kajii, N. Takahota, Y. Sekimoto, Y. Ohmori, *Jpn. J. Appl. Phys.* **2009**, 48, 04C176.

[43] J. M. Lupton, J. Klein, *Synthetic Metals* **2003**, 138, 233.

[44] L. V. Mercaldo, E. Bobeico, A. De Maria, M. Della Noce, M. Ferrara, L. Lancellotti, A. Romano, G. V. Sannino, G. Nasti, A. Abate, P. Delli Veneri, *Energy Tech.* **2022**, 10, 2200748.

[45] D. J. Wehenkel, K. H. Hendriks, M. M. Wienk, R. A. J. Janssen, *Org. Electron.* **2012**, 13, 3284.

[46] X.-Z. Guo, Y.-H. Luo, C.-H. Li, D. Qin, D.-M. Li, Q.-B. Meng, *Current Appl. Phys.* **2012**, 12, e54.

[47] B. Swatowska, P. Panek, T. Stapinski, *Opt. Laser Technol.* **2021**, 137, 106830.

[48] G. Xue, X. Yu, T. Yu, C. Bao, J. Zhang, J. Guan, H. Huang, Z. Tang, Z. Zou, *J. Phys. D: Appl. Phys.* **2012**, 45, 425104.

[49] M. Saliba, L. Etgar, *ACS Energy Lett.* **2020**, 5, 2886.

[50] K. O. Brinkmann, T. Becker, F. Zimmermann, C. Kreusel, T. Gahlmann, T. Haeger, T. Riedl, *Solar RRL* **2021**, 5, 2100371.

[51] Y. Cheng, X. Liu, Z. Guan, M. Li, Z. Zeng, H.-W. Li, S.-W. Tsang, A. G. Aberle, F. Lin, *Adv. Mater.* **2021**, 33, 2006170.

[52] O. Almora, C. I. Cabrera, J. Garcia-Cerrillo, T. Kirchartz, U. Rau, C. J. Brabec, *Adv. Energy Mater.* **2021**, 11, 2100022.

[53] R. B. Dunbar, B. C. Duck, T. Moriarty, K. F. Anderson, Noel W. Duffy, C. J. Fell, J. Kim, A. Ho-Baillie, D. Vak, T. Duong, Y. Wu, K. Weber, A. Pascoe, Y.-B. Cheng, Q. Lin, P. L. Burn, R. Bhattacharjee, H. Wang, G. J. Wilson, *J. Mater. Chem. A* **2017**, 5, 22542.

5.4. Supporting Information

Correcting unintended changes in electroluminescence perturbation for reliable light intensity modulated spectroscopies

Agustin O. Alvarez,[1] Antonio Riquelme [2], Rosinda Fuentes-Pineda[3], Elena Mas-Marzá[1], Lluis F. Marsal[4], Osbel Almora[2,4], Juan A Anta[2], Francisco Fabregat-Santiago[1*]*

[1]Institute of Advanced Materials, Universitat Jaume I, Castellón de la Plana 12071, Spain
[2]Department of Physical, Chemical and Natural Systems, Universidad Pablo de Olavide, Sevilla 41013, Spain
[3]Saule Technologies, Wroclaw PL, 54-427, Poland
[4]Department of Electronic, Electric and Automatic Engineering, Universitat Rovira i Virgili, 43007 Tarragona, Spain
* oalmora@upo.es ,*fabresan@uji.es
Keywords: light modulation, impedance spectroscopy, light emitting diodes, perovskite solar cells

Keywords: light modulation, impedance spectroscopy, light emitting diodes, perovskite solar cells

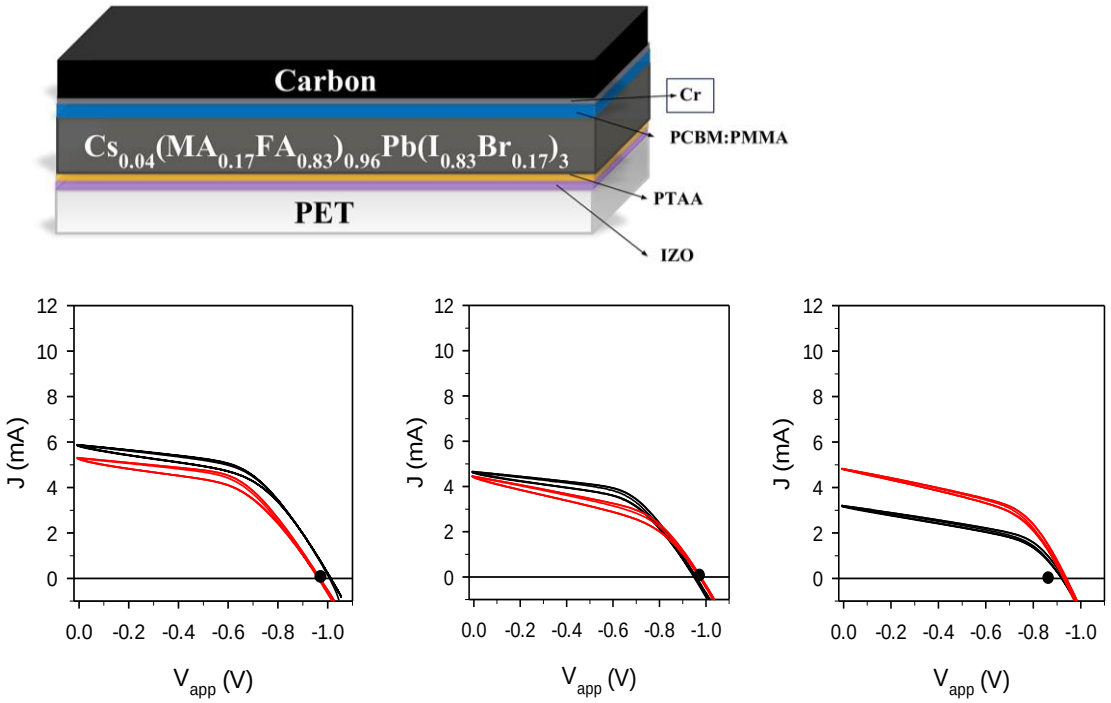

Figure S1. Cell structure of the perovskite solar cell and current density-voltage (*J*-*V*) curves before (black) and after (red) measurement of spectra (dot) under blue LED illumination: 89 mW cm^{-2} (600mA LED), 67 mW cm^{-2} (400mA LED), 39 mW cm^{-2} (200mA LED). Details of fabrication can be found in our previous work. [1]

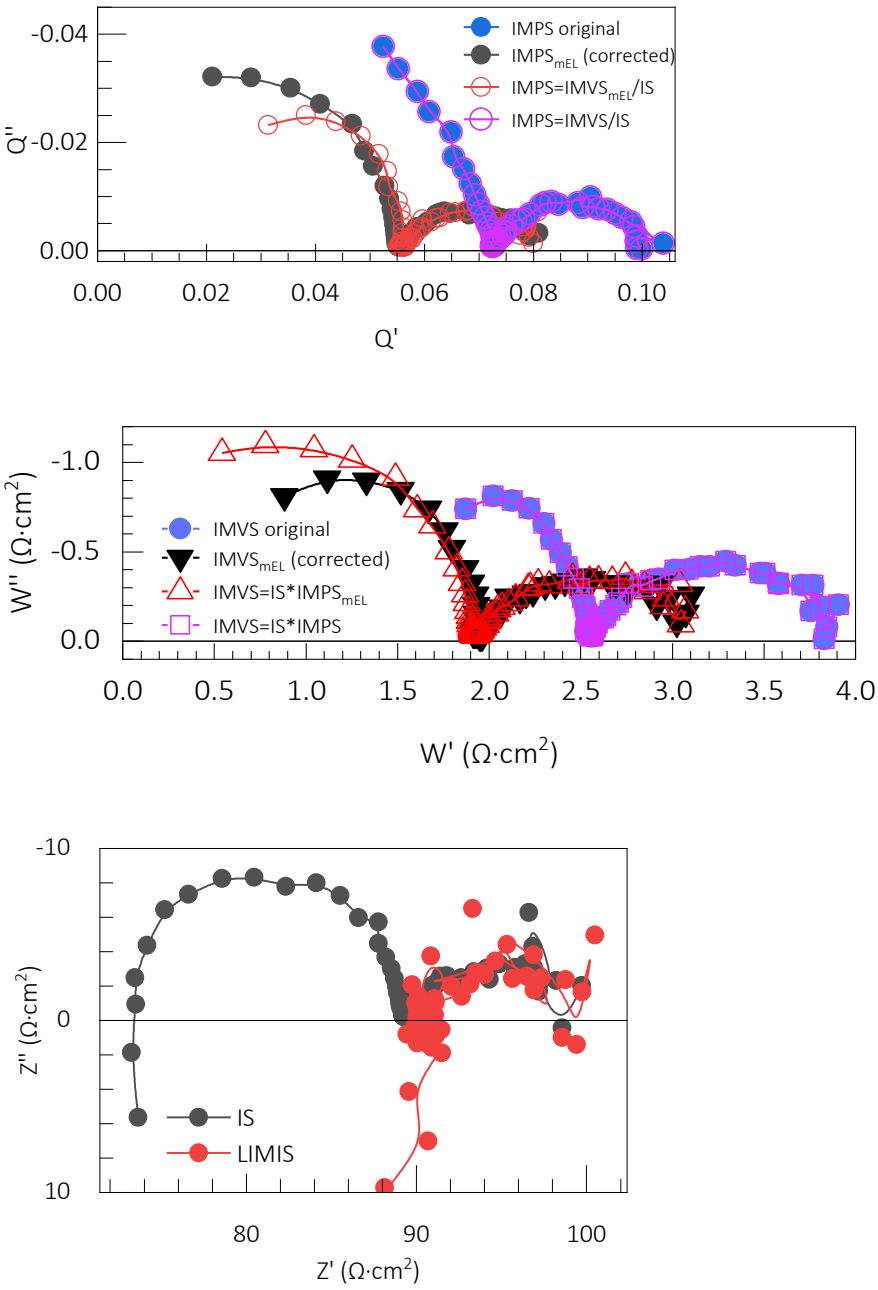

Figure S2. IMPS, IMVS and IS spectra under lower illumination intensity of the perovskite solar cell of Figure 1 in the main manuscript. The measurements were performed with frequencies from 200 kHz to 0.1 Hz, at open-circuit condition (975 mV) with a DC illumination of 67mWcm^{-2} from a blue LED (Philips LUMILEDS LXML-PB01-0040 with 470nm peak, @400mA) provided by Autolab.[2]

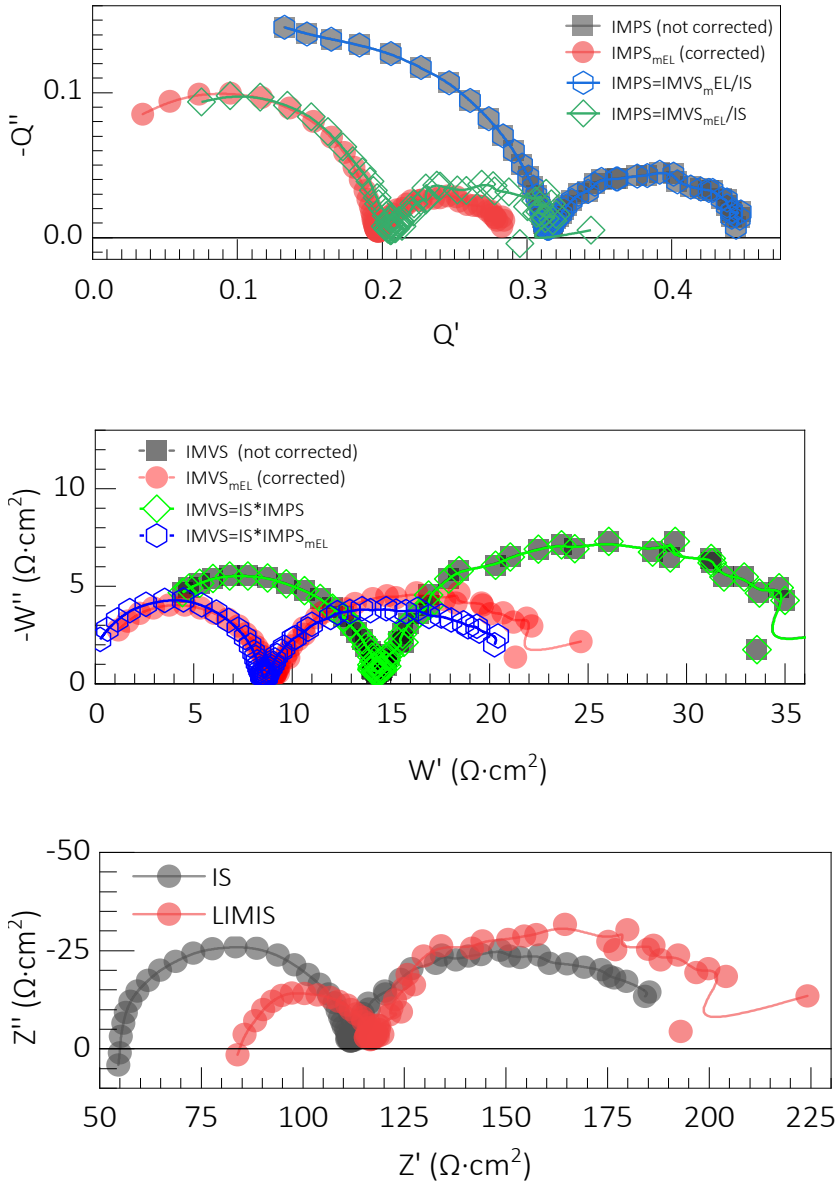

Figure S3. IMPS, IMVS and IS spectra under lower illumination intensity of the perovskite solar cell of Figure 1 in the main manuscript. The measurements were performed with frequencies from 200 kHz to 0.1 Hz, at open-circuit condition (850 mV) with a DC illumination of 39mWcm^{-2} from a blue LED (Philips LUMILEDS LXML-PB01-0040 with 470nm peak, @200mA) provided by Autolab.[2]

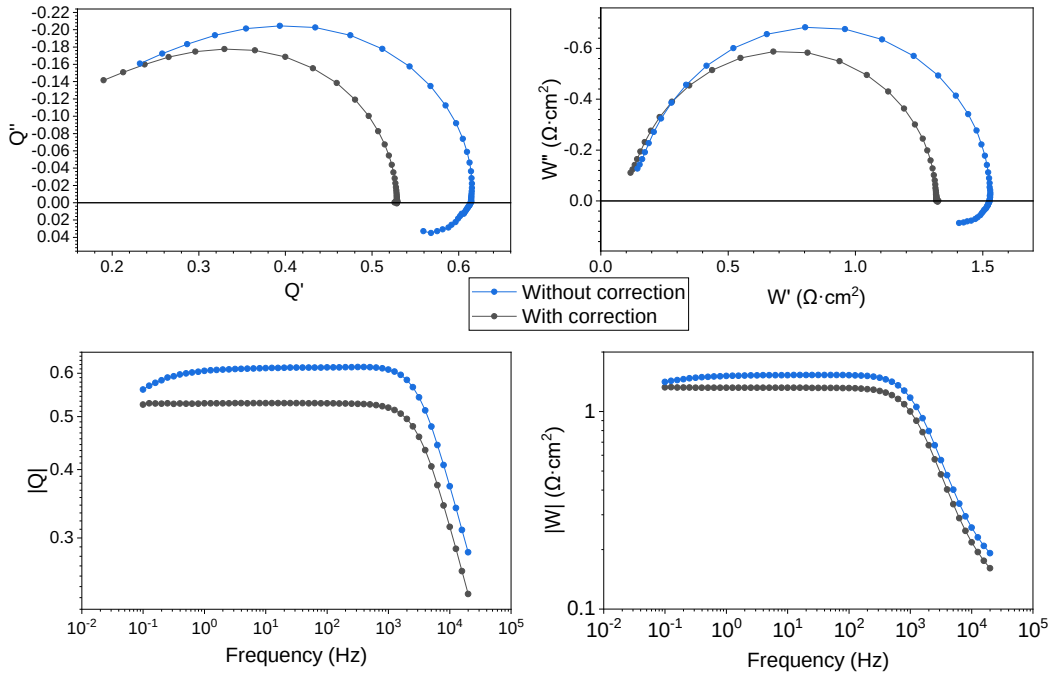

Figure S4. IMPS and IMVS spectra from the silicon photodiode Hamamatsu S1133 measured with the Zehnium Pro potentiostat from Zahner,[3] under 600 mW cm^{-2} at open-circuit condition (0.544 V). The data is shown with and without the MES correction.

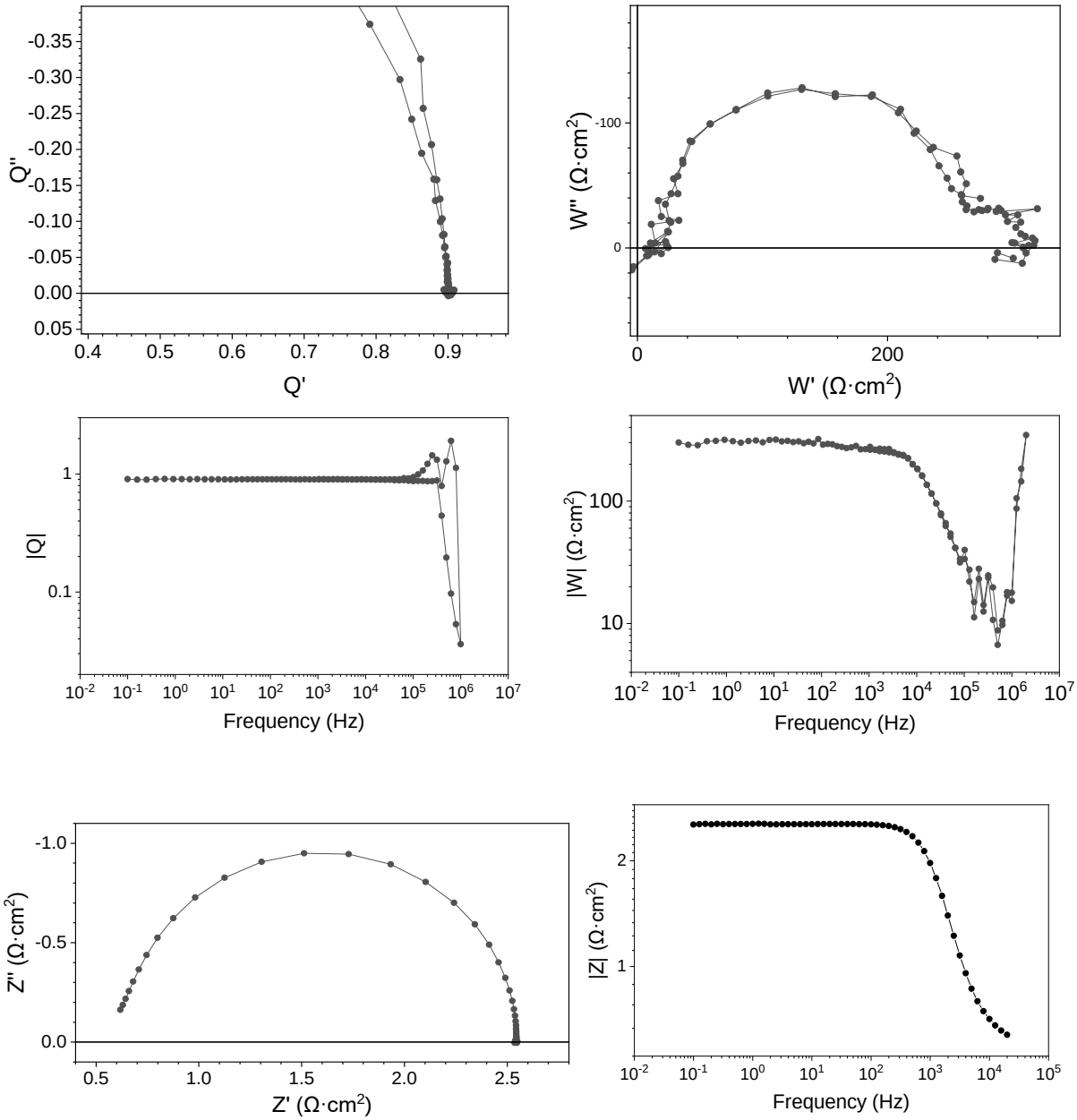

Figure S5. IMPS, IMVS and IS spectra from the silicon photodiode Hamamatsu S1133 measured with the Zehnium Pro potentiostat from Zahner,[3] under 8 mW cm^{-2} at open-circuit condition (1.009 V).

ORCID iDs

Agustin O. Alvarez— http://orcid.org/0000-0002-0920-5390
Antonio Riquelme— https://orcid.org/0000-0003-2445-3664
Rosinda Fuentes-Pineda— https://orcid.org/0000-0003-2587-8795
Elena Mas-Marzá— http://orcid.org/0000-0002-2308-0635
Luis F. Marsal— https://orcid.org/0000-0002-5976-1408
Osbel Almora — https://orcid.org/0000-0002-2523-0203
Juan A. Anta— https://orcid.org/0000-0002-8002-0313
Francisco Fabregat-Santiago — https://orcid.org/0000-0002-7503-1245

References

[1] V. Babu, R. Fuentes Pineda, T. Ahmad, A. O. Alvarez, L. A. Castriotta, A. Di Carlo, F. Fabregat-Santiago, K. Wojciechowski, *ACS Appl. Energy Mater.* **2020**, 3, 5126.

[2] Metrohm Autolab B.V., *LED Driver User Manual*, https://www.metrohm.com/en.html. Accessed 25.10.2022.

[3] Zahner-Elektrik GmbH & Co. KG, *CIMPS*, https://zahner.de/products-details/photoelectrochemistry/cimps. Accessed 30.06.2023.

CHAPTER 6

Publication 3: Combining Modulated Techniques for the Analysis of Photosensitive Devices.

Agustin O. Alvarez, Sandheep Ravishankar, Francisco Fabregat-Santiago.
Small Methods **2021**, *5*, 2100661.
DOI: 10.1002/smtd.202100661.
Impact Factor 2021: 15.367.

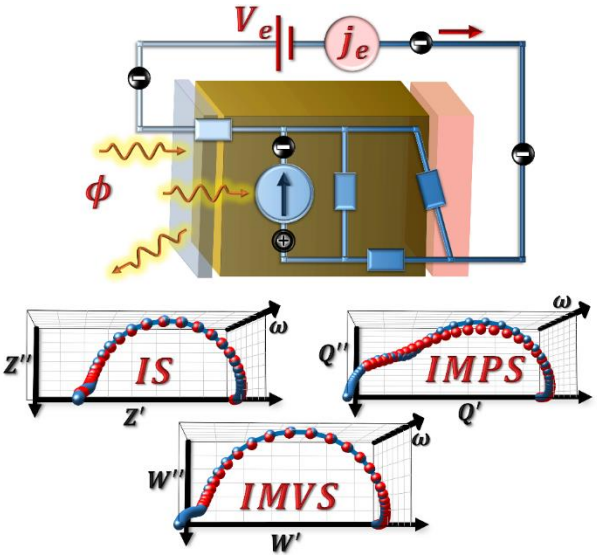

6.1. Candidate's contribution

Nature of Contribution	Extent of Contribution
✓ Carried out all the measurements ✓ Developed the theoretical model and calculations ✓ Carried out the simulations ✓ Analysed the measurements ✓ Interpreted the results ✓ Preaped all the figures ✓ Wrote manuscript drafts, incorporating the comments provided by the co-author and referees ✓ Wrote the first draft of the reply to the referees	70%

6.2. Thesis context

After developing the protocol to obtain reliable measurements of IMPS and IMVS, presented in the previous publication (**CHAPTER 5**), we focused on the key aspects needed to characterise optoelectronic devices by combining IS, IMPS and IMVS. In the following publication, we present a procedure to analyse the three techniques with an equivalent circuit (EC). We show that this procedure allows a better identification of the EC, solving, at least in part, one of the main problems of IS: different ECs can generate the same IS response. Moreover, we show, for the first time, that it is possible to analyse all three techniques with the same equivalent circuit. To demonstrate the potential of the experimental application of this procedure, we used a silicon photodiode, because of its stability and reproducibility. The results are presented in the most general way possible, thus inviting to apply this procedure to other photoconversion devices. Indeed, we are convinced that this procedure will allow a better description and understanding of the internal processes in whichever device is applied. As a result, we believe that this will help to improve the photoconversion devices and even develop new ones, in line with the objectives of this thesis.

6.3. Published Manuscript

Combining Modulated Techniques for the Analysis of Photosensitive Devices

Agustin O. Alvarez, Sandheep Ravishankar and Francisco Fabregat-Santiago**

A. O. Alvarez, Prof. F. Fabregat-Santiago
Institute of Advanced Materials
Universitat Jaume I
Castellón de la Plana 12071, Spain
E-mail: agalvare@uji.es; fabresan@uji.es

Dr. S. Ravishankar
IEK-5 Photovoltaik
Forschungzentrum Jülich
Jülich 52425, Germany

Keywords: IMPS, IMVS, impedance spectroscopy, charge separation efficiency, photodiode

Small-perturbation techniques such as impedance spectroscopy (IS), intensity-modulated photocurrent spectroscopy (IMPS), and intensity-modulated photovoltage spectroscopy (IMVS) are useful tools to characterize and model photovoltaic and photoelectrochemical devices. While the analysis of the impedance spectra is generally carried out using an equivalent circuit, the intensity-modulated spectroscopies are often analyzed through the measured characteristic response times. This makes the correlation between the two methods of analysis generally unclear. In this work, by taking into consideration the absorptance and separation efficiency, a unified theoretical framework and a procedure to combine the spectral analysis of the three techniques are proposed. Such a joint analysis of IS, IMPS, and IMVS spectra greatly reduces the sample space of possible equivalent circuits to model the device and allows obtaining parameters with high reliability. This theoretical approach is applied in the characterization of a silicon photodiode to demonstrate the validity of this methodology, which shows great potential to improve the quality of analysis of spectra obtained from frequency domain small-perturbation methods.

6.3.1. Introduction

Intensity-modulated photocurrent spectroscopy (IMPS), intensity-modulated photovoltage spectroscopy (IMVS) and impedance spectroscopy (IS) are powerful techniques to characterize electrochemical and solid-state light-to-energy conversion devices under operational conditions.[1-2] IMPS was extensively developed by L.M. Peter and co-workers[3-4] mainly in the characterization of carrier transport processes,[5-8] while IMVS has been mostly used in the study of recombination processes, though both techniques involve optical perturbations.[9-10] IS has been used to analyze transport and recombination processes together through the response of the device to an electrical perturbation.[11-12]

IMPS and IMVS techniques have been widely applied to study dye-sensitized solar cells,[13-14] photoelectrodes for water oxidation,[15-17] and recently are gaining attention in the field of perovskite solar cells (PSCs).[18-19] The analysis of the data obtained with these techniques is generally made through the characteristic time constants.[20-22] While such an analysis is very useful in certain cases, this strategy limits the amount of information that can be obtained from these techniques. With regard to IS, experimental data are usually analyzed by modelling the internal electrochemical processes of the study device using an equivalent circuit model (EC),[23] built from passive electrical elements such as resistances, capacitances and inductances.[24-26] These parameters in turn can provide key information regarding the nature of the operation of the device and its limitations. However, the choice of the correct EC could be a difficult task, because several ECs can reproduce the same experimental spectra. Therefore, there exists a need to combine the analysis methods of these three techniques to overcome their individual limitations and extract the maximum knowledge from the experimental data.

Before discussing how these techniques are related, we present a scheme of a photosensitive device showing the basic light to electricity conversion mechanism in Figure 1. In these systems, when a photon flux (ϕ) reaches the device, part of these photons can be absorbed, generating electron-hole pairs (represented by absorbed current, j_a). The pairs that do not recombine and are successfully separated, provide the free-photogenerated current (j_{ph}) in the light absorber material. Part of this current is lost as a recombination current (j_{rec}), and the remaining current ($j_e = j_{ph} - j_{rec}$) is extracted at the external contacts of the device. j_{rec}, and thus j_e, are functions of the external voltage (V_e).

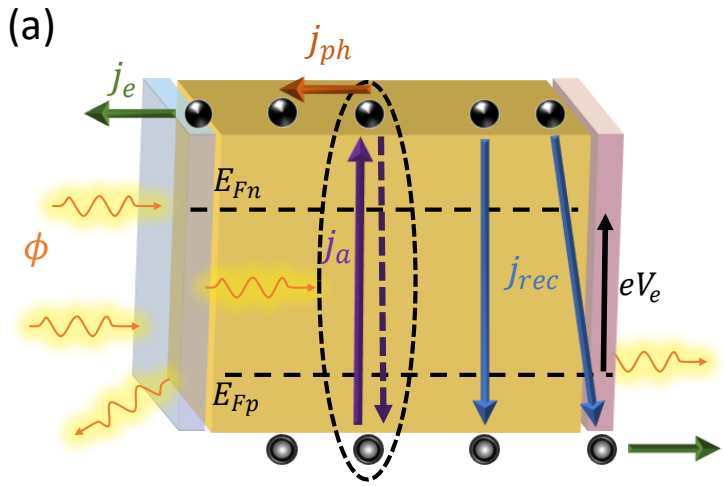

Figure 1. Scheme of the light to electricity conversion mechanism in a photovoltaic device. ϕ is a photon flux reaching the device. j_a, j_{ph}, j_{rec} and j_e are the absorbed, free-photogenerated, recombination and extracted currents respectively. E_{Fn} and E_{Fp} are the Fermi levels of electrons and holes respectively, e is the elementary charge and V_e the external voltage.

In Figure 2, the basic operation of IS, IMPS and IMVS is shown. Figure 2b, 2c and 2d show the excitation and measurement signals involved in IS, IMPS and IMVS respectively. Note that all variables with a tilde ($\tilde{}$) indicate AC perturbations, while variables with overbars ($\bar{}$) represent steady-state signals. Thus, the steady-state at which the measurements are performed is defined by $\bar{j}_\phi$, $\bar{V}_e$ and $\bar{j}_e$. As shown in Figure 2b, for IS (in potentiostatic mode), an AC small-perturbation in voltage ($\tilde{V}_e$) is applied and the corresponding AC external current ($\tilde{j}_e$) is measured. The IS transfer function is then

$$Z = \frac{\tilde{V}_e}{\tilde{j}_e} \tag{1}$$

Similarly, for IMPS and IMVS, a perturbation of incident photon current density ($\tilde{j}_\phi = e\tilde{\phi}$) is applied and $\tilde{j}_e$ and $\tilde{V}_e$ are measured respectively. If we define the generated photocurrent as negative and, consequently, the photovoltage as positive, then the IMPS and IMVS transfer functions are

$$Q = -\frac{\tilde{j}_e}{\tilde{j}_\phi} \tag{2}$$

$$W = \frac{\tilde{V}_e}{\tilde{j}_\phi} \tag{3}$$

Note that if we use the opposite notation (also very common), in which the generated photocurrent is positive and the photovoltage negative, [28] then the signs of IMPS and IMVS change yielding $Q = \tilde{j}_e/\tilde{j}_\phi$ and $W = -\tilde{V}_e/\tilde{j}_\phi$, while the definition of Z remains unchanged.

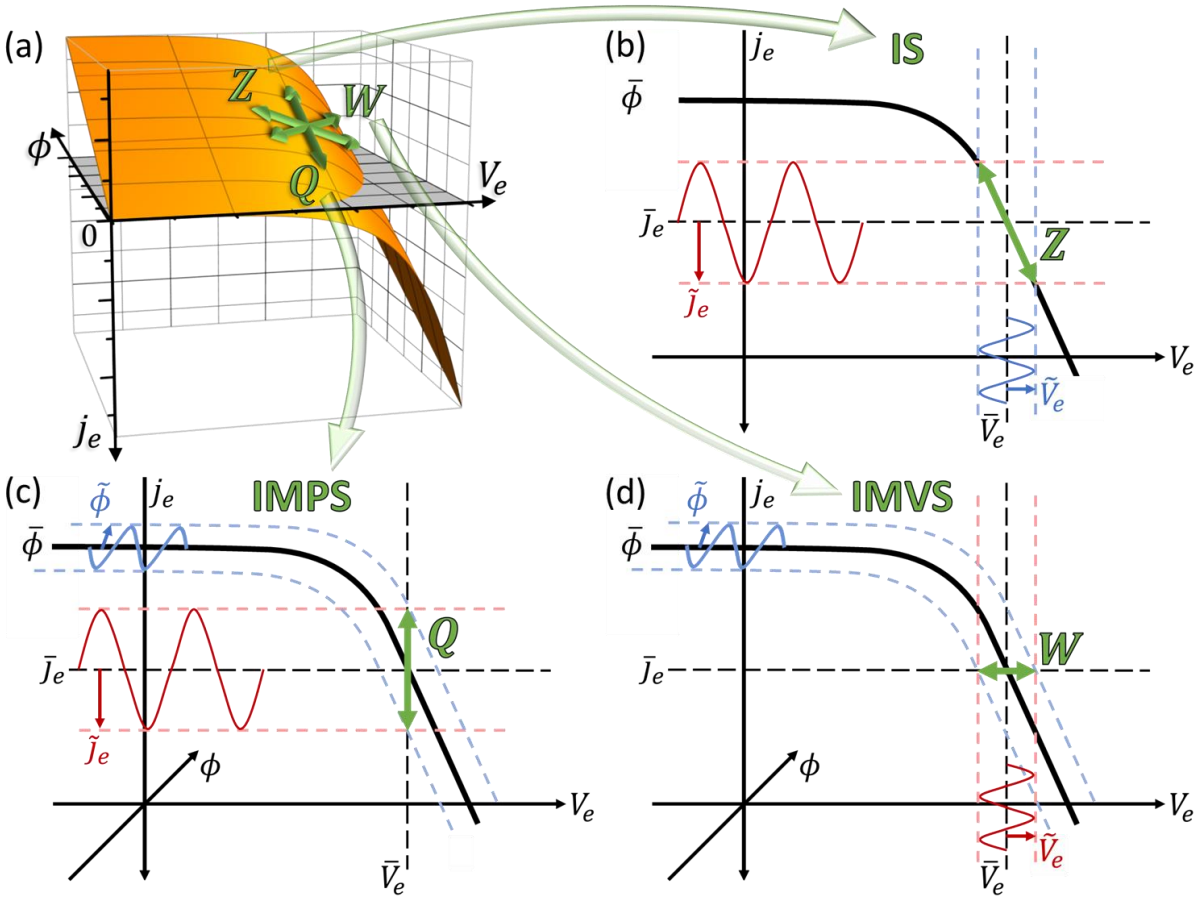

Figure 2. (a) Characteristic current - voltage - photon flux (j_e-V_e- ϕ) surface for a device as the one shown in Figure 1. (b), (c) and (d) represent the connection between the current-voltage curve and the transfer functions of IS (Z), IMPS (Q) and IMVS (W) respectively. The tilde represents AC signals on top of the DC values (represented by the overbar). The AC perturbation is shown in blue, the modulated response is shown in red and the corresponding transfer function is shown in green. The slope of the surface in the ϕ, V_e and j_e planes provide the DC limit of these transfer functions.

As shown in Figure 2, these three techniques are closely related. The basic relationship between the transfer funtions, derived step by step in Section 1.1 in the supporting information (SI), is

$$Z(\omega) = \frac{W(\omega)}{Q(\omega)} \qquad (4)$$

This relation was confirmed from measurements on different systems such as dye-sensitized solar cells[27], water splitting[2] and PSCs[28]. On the other hand, Almora et al. recently showed some particular cases where this relation might not be entirely valid.[29-30] Therefore, the validity of Equation (4) is unquestionable only after verification. It is worth highlighting the fact that to

be in the regime where Equation (4) is valid, strict conditions must be fulfilled: (i) The device is stable enough to ensure that the three techniques are performed in the same steady-state condition[31-32] and (ii) the different perturbations applied are small enough to ensure linearity of the system response. An additional point to take into consideration is that different Fermi-level distributions in the material during measurement of each spectra could affect this relation.

Other relations among these techniques have been previously made. Klotz et al. combined the three techniques and analyzed them by means of a distribution of relaxation times.[2] This procedure can be particularly useful to separate polarization processes, but its implementation is not straightforward. Bertoluzzi and Bisquert theoretically proposed for the first time that a common EC linking the three small-perturbation techniques should describe the same physical mechanisms occurring for a device.[1] Applying this theory and assuming perfect free-photogeneration ($j_\phi = j_{ph}$), Ravishankar et al. proposed an EC to describe the frequency-domain, small-perturbation response of PSCs.[33] In this last work, the authors measured IS and IMPS, reproducing both measured spectra with the EC proposed. However, some discrepancies were observed in the parameters obtained from the fitting of experimental spectra with the two techniques.

In the present work, we advance the state-of-the-art analysis by taking into account the contribution of the absorptance and the separation efficiency to accurately correlate the IMPS and IMVS responses with the IS response and their correspondences in the fitting of experimental spectra. We first introduce a general equivalent circuit (GEC) composed of generic impedance elements. Then, we derive the corresponding expressions for the IS, IMPS and IMVS transfer functions of this GEC and the inter-relation among these techniques, which allows combining and complementing the information obtained with the three techniques in a unified analysis procedure. These results may be applied to many different systems by just adapting the impedances in the GEC to the specific combination of elements needed to describe each device. Finally, to illustrate the validity and capacity of the method, we characterized a silicon photodiode with our developed theoretical framework. We started by combining the three techniques to narrow down the large number of potential equivalent circuits available to analyze the IS data using a selection method, identifying an appropriate equivalent circuit that models all three experimental spectra. Such an analysis leads to a consistent set of output parameters that combines the information obtained from each individual measurement technique, allowing for a more holistic analysis of the optoelectronic properties of the device.

6.3.2. Results and Discussion

6.3.2.1.Theory: General Equivalent Circuit

Theoretical framework

The photovoltaic external quantum efficiency (EQE_{PV}) relates the flux of collected electrons per incident photon ($j_e = EQE_{PV} j_\phi$) and can be expressed as the product of three terms

$$EQE_{PV} = a\,\eta_{sep}\eta_{col} \quad (5)$$

where a is the absorptance, also called light-harvesting efficiency (LHE or η_{LHE}), defined by the fraction of incident photons that are effectively absorbed ($j_a = a\,j_\phi$, see Figure 1). η_{sep} is the efficiency of charge separation from the generated electron-hole pairs to free-photogenerated carriers ($j_{ph} = \eta_{sep}\,j_a$). j_{ph} represents the current provided by the current generator in the equivalent circuit of the device. Finally, η_{col} is the collection efficiency that determines the fraction of free-photogenerated carriers that are extracted at the contacts ($j_e = \eta_{col}\,j_{ph}$).[34] The photovoltaic internal quantum efficiency (IQE_{PV}) is the ratio between collected electrons or holes and absorbed photons ($j_e = IQE_{PV}\,j_a$), so

$$IQE_{PV} = \eta_{sep}\,\eta_{col} \quad (6)$$

Similarly, the ratio of incident photons and free-photogenerated carriers can be expressed as the absorptance and separation efficiency

$$\eta_{a\cdot s} = a\,\eta_{sep} \quad (7)$$

which implies $j_{ph} = \eta_{a\cdot s}\,j_\phi$. Assuming that $\eta_{a\cdot s}$ is independent of the light intensity, the modulated photon flux and the free-photogenerated carriers are related by the relationship

$$\tilde{J}_{ph} = \eta_{a\cdot s}\,\tilde{J}_\phi \quad (8)$$

In homogeneous semiconductors with low-exciton binding energies, such as crystalline silicon (c-Si) or standard inorganic thin films, $\eta_{sep} \approx 1$ could be a good approximation.[34-35] In such cases, we can simplify $\eta_{a\cdot s} \approx a$, a parameter that can be measured directly. However, this is not the general case, especially in photoelectrochemical systems or solar cells that are in an optimization stage. Therefore, we will use $\eta_{a\cdot s}$ as a single parameter to describe the efficiency of absorption and separation.

Transfer Functions

Using Equation (8), the IMPS and IMVS transfer functions in Equation (2) and (3) can be rewritten as

$$Q = -\eta_{a\cdot s}\frac{\tilde{J}_e}{\tilde{J}_{ph}} \quad (9)$$

$$W = \eta_{a\cdot s}\frac{\tilde{V}_e}{\tilde{j}_{ph}} \tag{10}$$

Equations (9) and (10) have an important consequence as they allow combining and comparing light-modulated methods with voltag or current-modulated methods. Without proper normalization of the IMPS and IMVS transfer functions using the absorption and separation efficiency, any comparison of calculated parameters from these methods will be skewed from those measured by IS. Therefore, in systems where the separation efficiency is 1, the absorptance, which is a straightforward optical quantity that can be easily determined, is essential for an accurate normalization of the transfer functions. With these relations, we can now introduce an electrical model of the device. To be as general as possible, we assume the general equivalent circuit (GEC) model shown in Figure 3a. This model is made up of four general impedances (Z_S, Z_{rec}, Z_P and Z_f). The measurable variables (ϕ, V_e and j_e) are represented in blue while the free-photogenerated current (j_{ph}), which is directly unmeasurable, is in red. This GEC may be adapted to represent fundamental processes such as charge transport,[1] traps,[36] geometric and chemical[37] capacitances etc., depending on the studied system.

The transfer function of impedance spectroscopy for the equivalent circuit in Figure 3b may be obtained by considering a small perturbation of voltage (or current) on the GEC in Figure 3a and applying the superposition theorem and Kirchhoff's laws, which yields

$$Z = Z_S + \left(\frac{1}{Z_p} + \frac{1}{Z_{rec} + Z_f}\right)^{-1} \tag{11}$$

Similarly, the transfer function for IMPS (Figure 3c) is

$$Q = \frac{\eta_{a\cdot s}}{Z_S}\ \frac{Z_{rec}}{Z_{rec} + Z_f}\left(\frac{1}{Z_S} + \frac{1}{Z_p} + \frac{1}{Z_{rec} + Z_f}\right)^{-1} \tag{12}$$

and the IMVS transfer function (Figure 3d) is

$$W = \eta_{a\cdot s}\frac{Z_{rec}}{Z_{rec} + Z_f}\left(\frac{1}{Z_p} + \frac{1}{Z_{rec} + Z_f}\right)^{-1} \tag{13}$$

Alternative expressions and combinations of Equation (11) to (13) are shown in Section 1.2 of the SI. The low-frequency limit is also discussed in Section 1.3 of the SI, where it is shown that the GEC is reduced to Figure 3e and can be simplified to the EC in Figure 3f by defining the "total" equivalent series (R_S^T) and recombination (R_{rec}^T) resistances. Combining Equation (12) and (13) through Equation (4), Equation (11) is obtained again. Whenever Equation (4) is valid, all the information that can be extracted from the three techniques is contained in the combination of any two of them.

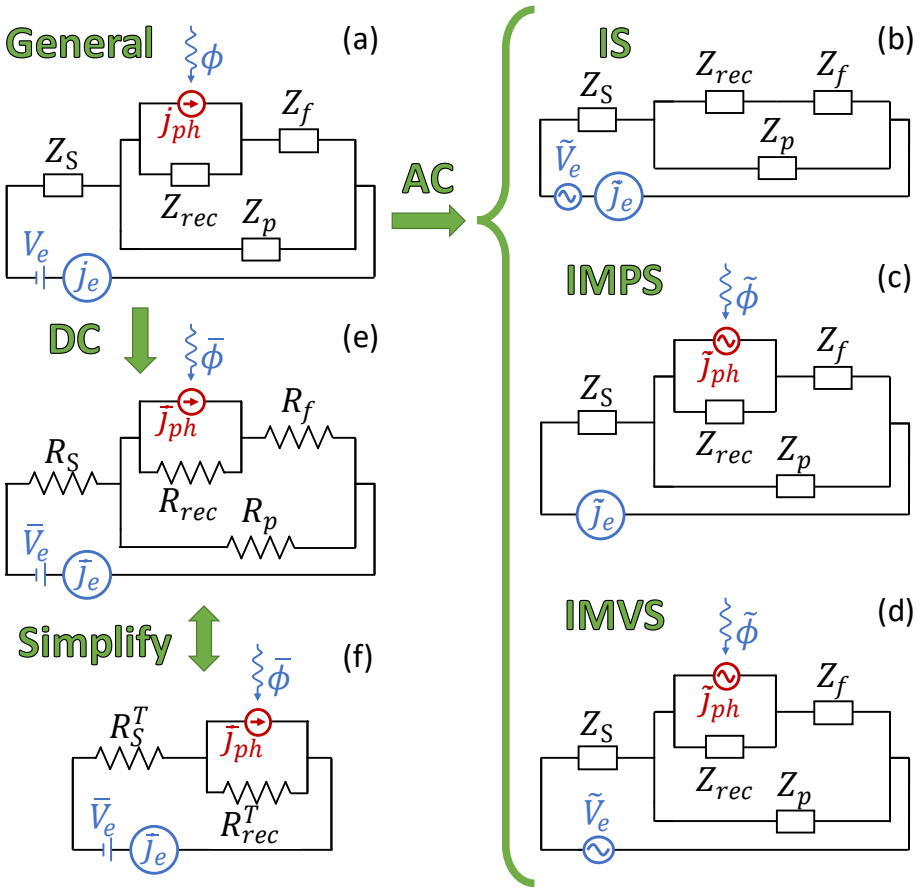

Figure 3. (a) General equivalent circuit, with the simplifications to (b) IS, (c) IMPS, (d) IMVS and (e-f) steady-state condition. ϕ is a photon flux reaching the device. j_{ph} and j_e are the free-photogenerated and extracted currents. Z_S, Z_{rec}, Z_P and Z_f are general impedances and V_e is the external voltage. The tilde and overbar represent the AC and DC signals respectively. The directly measurable variables are represented in blue while the free-photogenerated current is in red. The "total variables" in (f) are electrically equivalent to those they substitute in (e), see also Figure S1.

We will now explore a simplified case of the GEC with special implications that will be applied in the experimental part.

6.3.2.2.Case $Z_f = 0$ (or $Z_f \ll Z_{rec}$)

This case is very illustrative for the simplicity of the resulting equations. The most important consequence of considering $Z_f = 0$ is that Z_{rec} and Z_P may not be dissociated anymore and the two branches in Figure 3 reduce to a single "total recombination impedance"

$$Z_{rec}^T = \left(\frac{1}{Z_p} + \frac{1}{Z_{rec}}\right)^{-1} \quad (14)$$

The IS, IMPS and IMVS transfer functions in Equation (11) to (13) reduce to

$$Z = Z_S + Z_{rec}^T \quad (15)$$

$$Q = \frac{\eta_{a\cdot s}}{Z_S}\left(\frac{1}{Z_S} + \frac{1}{Z_{rec}^T}\right)^{-1} \quad (16)$$

$$W = \eta_{a\cdot s} Z_{rec}^T \quad (17)$$

Note that the GEC is reduced to only two impedances Z_S and Z_{rec}^T, and they can be separated using any couple of the experimental techniques plus $\eta_{a\cdot s}$ without making any further assumptions, through

$$Z_{rec}^T = \frac{W}{\eta_{a\cdot s}} = \frac{ZQ}{\eta_{a\cdot s}} \quad (18)$$

and

$$Z_S = W\left(\frac{1}{Q} - \frac{1}{\eta_{a\cdot s}}\right) = Z\left(1 - \frac{Q}{\eta_{a\cdot s}}\right) = Z - \frac{W}{\eta_{a\cdot s}} \quad (19)$$

These calculations represent clear progress for the definition of an accurate EC of the device. Therefore, the serial contributions of the impedance, such as contact or transport impedances, can be separated from those which are in parallel to the absorber and charge generator, such as recombination and some polarization processes. This is a key aspect to model and understand the operation and limitations of many optoelectronic and photovoltaic devices.[11, 38]

6.3.2.3.Experimental Demonstration: Silicon Photodiode

To illustrate our theoretical development with experimental results, we measured the IS, IMPS and IMVS spectra of a commercial silicon photodiode (Thorlabs FDS100), see black dots in Figure 4. Silicon photodiodes are well-known and stable systems that ensure the reliability of the three measurements (see the cyclic voltammetry in Figure S4 in the SI). The low-frequency limit used was 0.1 Hz because no more features were observed below this frequency. On the other hand, the high frequencies were instrumentally limited, reaching 310, 200 and 16 kHz for IS, IMPS and IMVS respectively. The measurements were performed at open-circuit, the most common condition for IMVS, very typical for IS and recently, also used for IMPS.[7, 28-29] In the Experimental Section, we provide further details of the experimental procedures.

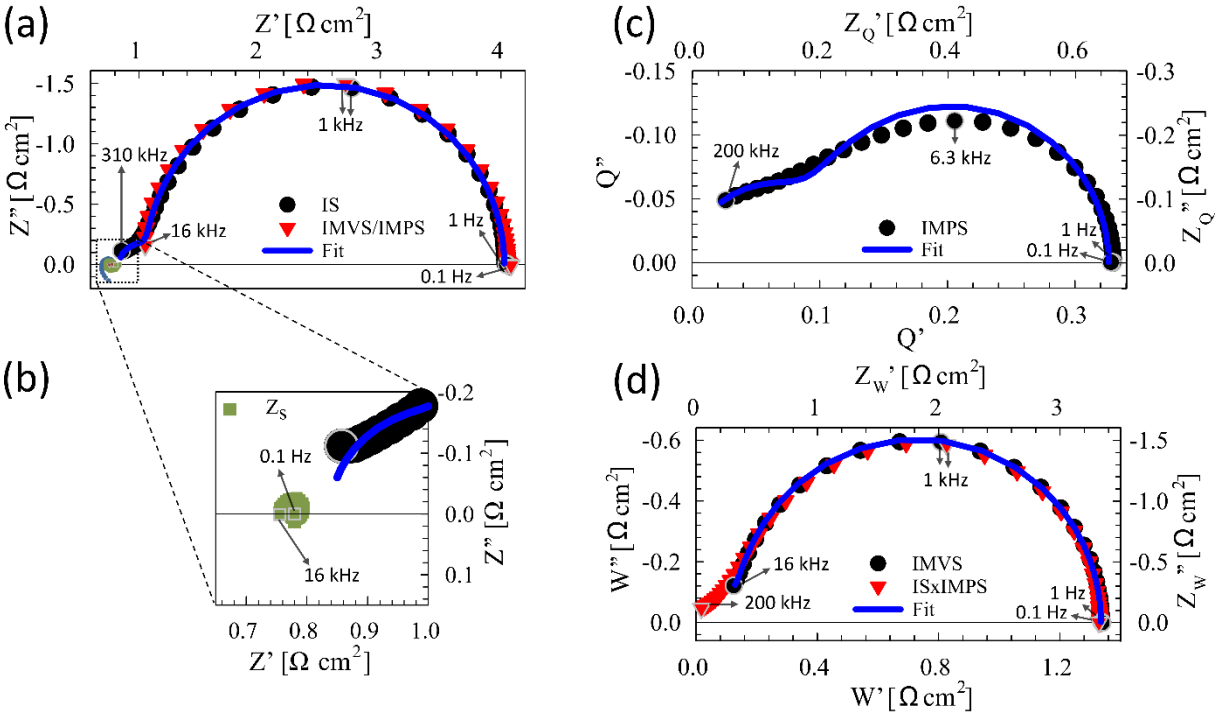

Figure 4. Black dots represent measured (a, b) IS, (c) IMPS and (d) IMVS spectra of a silicon photodiode, under open-circuit conditions and 89 mW/cm^2 blue LED illumination. Red triangles represent the quotient between IMVS and IMPS in (a) and the product between IS and IMPS in (d). The top and right axis of (c) and (d) represent $Z_Q = QR_S/\eta_{a\cdot s}$ and $Z_W = W/\eta_{a\cdot s}$, respectively as given by Equation (29) and (30). The blue lines are the fittings of (a, b) IS, (c) IMPS and (d) IMVS employing the simplified GEC in Figure 5h. The green squares in (b), inset of (a), is the series impedance (Z_S) obtained from the combination of IS with IMVS through Equation (19).

We first verified that our experimental data satisfied Equation (4) by calculating the quotient of W and Q for each frequency, see red triangles in Figure 4a. A very good match between the measured IS spectrum and the one obtained from IMPS and IMVS is observed.

Selection of the Equivalent Circuit

The IS spectrum of the silicon photodiode (Figure 4a) presents one large arc at low frequencies and a secondary process at high frequencies. In the IMPS spectrum (Figure 4c), we also observe two processes, although their characteristic frequencies appear closer than in the IS spectrum, resulting in more distorted arcs. In contrast, the IMVS spectrum (Figure 4d) shows only one large arc. However, as we mentioned above, IMVS could only be measured up to 16 kHz, so we speculate that one process is likely hidden in the IMVS spectrum at higher frequencies. The fact that the projection of the IMVS arc does not end at the origin of the W' and W'' axes support this assumption.

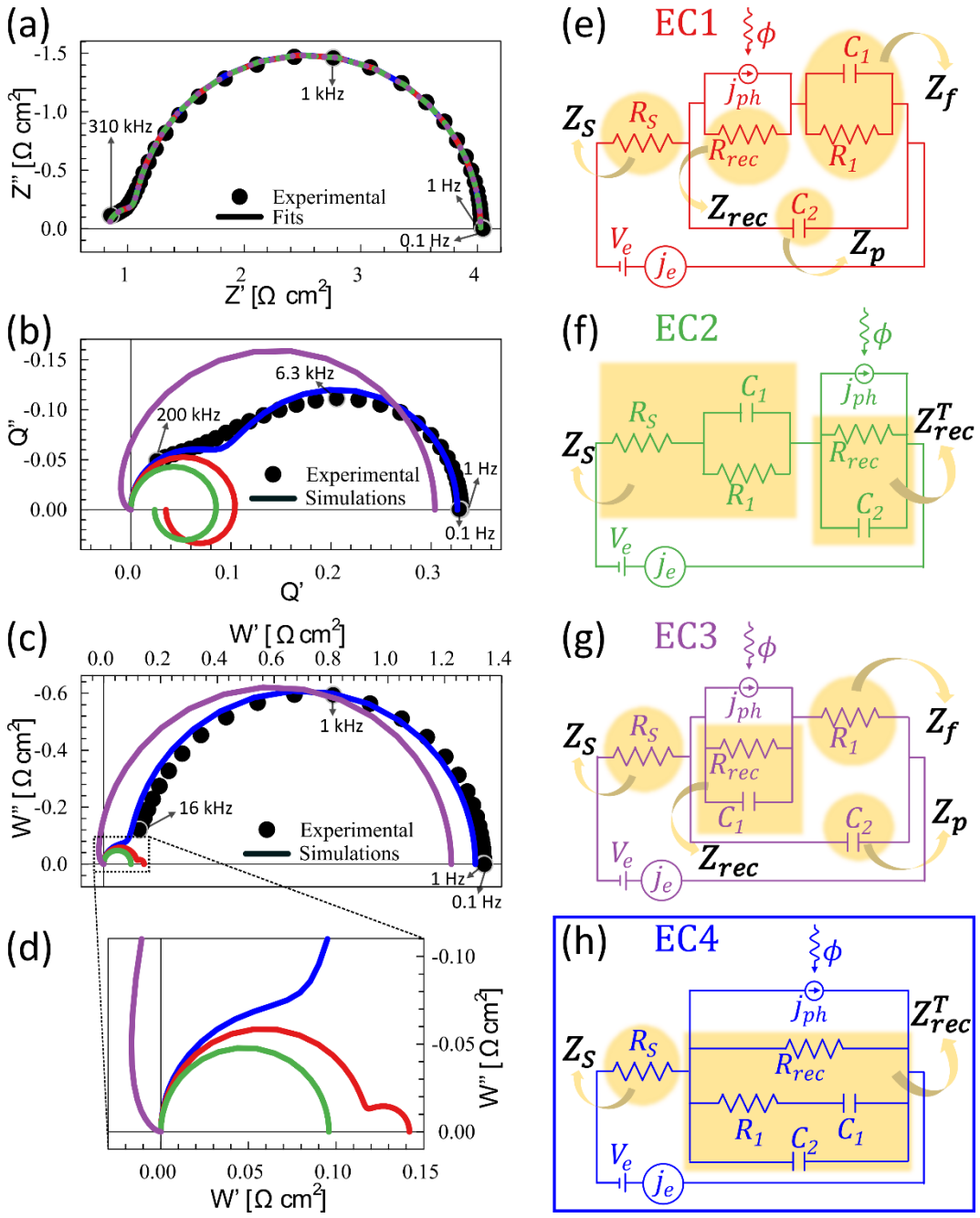

Figure 5. Black dots show measured (a) IS, (b) IMPS and (c) IMVS for a Silicon photodiode, under OC condition and 89 mW/cm^2 blue light (470nm peak), also shown in Figure 4. The different lines in (a) are the resulting fits employing the equivalent circuits in (e), (f), (g) and (h), respectively with the color. Following the same color pattern, the lines in (b), (c) and (d) are the IMPS and IMVS simulations corresponding to the IS fitting results and considering $\eta_{a\cdot s}$ in Table 1.

To analyze the obtained spectra with the developed theory, we must first reduce the GEC in Figure 3a to a particular case, replacing the general impedances (Z_S, Z_{rec}, Z_P and Z_f) by specific elements such as resistances and capacitances. This choice is complicated by the fact that

different circuits can reproduce the general spectral features of combinations of any two of IS, IMPS and IMVS.[39] This is shown in Figure 5 for fitting of the experimental IS spectra and simulations with the corresponding fitted parameters of IMPS and IMVS spectra using different ECs. For example, an R||C element in both Z_f (Figure 5e) and Z_S (Figure 5f) gives an arc in the lower quadrant of the IMPS spectrum (Figure 5b) while yielding two arcs also in the impedance spectrum (Figure 5a). However, when also considering the IMVS response (Figure 5d), we observe a difference in the generated spectra. We therefore use this logic to compare the response of different ECs with that of the experimental spectra of the three techniques to narrow down the number of ECs available for fitting the spectra. A detailed discussion of the different equivalent circuits in Figure 5 is provided in Section 2.1 of the SI. As an example of the method, we note that the ECs in Figure 5e, 5f and 5g have an R||C pair placed in Z_f, Z_S and Z_{rec}, respectively. The ECs in Figure 5e and 5f can be easily discarded because they present an arc in the bottom quadrant of the IMPS spectra (red and green lines respectively in Figure 5b) which is not present in the experimental spectrum. On the other hand, the IMPS and IMVS simulations corresponding to the circuit in Figure 5g (purple lines in Figure 5b, 5c and 5d) reach negative values of the real components which are also not present in the experimental spectrum.

The selected EC as a consequence of this procedure is shown in Figure 5f, where $Z_S = R_S$, $Z_f = 0$ and Z_{rec}^{T} is given by the combination of R_{rec}, R_1, C_1 and C_2, which reproduce the three spectra simultaneously (see blue lines in Figure 5). The condition $Z_f = 0$ (discussed in section 2.1.3) allows estimating Z_S and Z_{rec}^{T} through Equation (18) and (19). The Z_S spectra calculated by combining IS and IMVS data can be seen (green squares) in Figure 4a and, with more detail, in its inset plot in Figure 4b. It approaches very well to a single point on the real axis, the expected behavior of a resistor (R_S). This yields the rest of the impedance (the two arcs in Figure 4a) to Z_{rec}^{T}. We clarify that the chosen EC is not a unique equivalent circuit that fits all three spectra, an example of an alternative is shown in Section 2.2 in the SI. Our procedure serves to reduce the large number of EC options available for fitting by using the experimental spectra as a quality check. While providing general rules for identifying the correct EC is an attractive proposition, it is a very difficult goal due to the generality of the model, whose elements can be arbitrary combinations of passive elements. In addition, we note that the structure of the device must also be taken into consideration when choosing an equivalent circuit for devices that contain multiple layers in addition to that of the absorber, such as perovskite solar cells that employ selective contact layers. The generality of our developed model allows the inclusion of passive elements in different parts of the EC to easily model these additional layers in the device.

Fitting Results

As mentioned in the introduction, analysis of IMPS or IMVS beyond the calculation of characteristic times has been very uncommon until now.[29, 33] To the best of our knowledge, the fitting of IMPS and IMVS spectra with an equivalent circuit, in a similar way to what is done conventionally for IS spectra, has not been done previously. The main reason for this fact was the absence of a model that connected the IMPS or IMVS transfer functions to the electrical elements such as resistances and capacitances that are used for the analysis of the impedance. Here, the connection developed in the theoretical framework (Section 2.1) through $\eta_{a\cdot s}$ allows simultaneous fitting with the three techniques, after discarding (using our selection procedure) many potential equivalent circuits that do not provide compatible results. We show the potential of this method in the analysis of the particular case of a silicon photodiode through the EC in Figure 5h.

Provided the condition $Z_f = 0$ given by the photodiode and considering the EC of Figure 5h, the transfer functions in Equation (11), (12) and (13) reduce to

$$Z = R_S + Z_{rec}^T = R_S + \left(\frac{1}{R_{rec}} + \frac{1}{R_1 + (i\omega C_1)^{-1}} + i\omega C_2\right)^{-1} \tag{20}$$

$$Q = \frac{\eta_{a\cdot s}}{R_S}\left(\frac{1}{R_S} + \frac{1}{Z_{rec}^T}\right)^{-1} = \frac{\eta_{a\cdot s}}{R_S}\left(\frac{1}{R_S} + \frac{1}{R_{rec}} + \frac{1}{R_1 + (i\omega C_1)^{-1}} + i\omega C_2\right)^{-1} \tag{21}$$

$$W = \eta_{a\cdot s} Z_{rec}^T = \eta_{a\cdot s}\left(\frac{1}{R_{rec}} + \frac{1}{R_1 + (i\omega C_1)^{-1}} + i\omega C_2\right)^{-1} \tag{22}$$

IS data were fitted using standard software for IS analysis (ZView® in our case) using the equivalent circuit plot in Figure 5h, reduced to Figure S3e in the SI. Results of the fitting of these data are plotted as a blue curve in Figure 4a and the parameters obtained are shown in the "IS" column of Table 1.

Equation (21) shows that the transfer function of IMPS is simply the impedance of the parallel combination of R_S and Z_{rec}^T multiplied by a constant $\eta_{a\cdot s}/R_S$. Similarly, the transfer function of IMVS written in Equation (22) is just the impedance Z_{rec}^T multiplied by $\eta_{a\cdot s}$. Therefore, the same tools used to fit IS serve to fit the IMPS and IMVS spectra. To apply this analysis procedure, Equation (21) and (22) may be re-written as

$$Q = \left[\frac{1}{R_{rec}^Q} + \frac{1}{R_1^Q + \left(i\omega C_1^Q\right)^{-1}} + i\omega C_2^Q\right]^{-1} \tag{23}$$

and

$$W = \left[\frac{1}{R_{rec}^{W}} + \frac{1}{R_1^W + (i\omega C_1^W)^{-1}} + i\omega C_2^W\right]^{-1} \quad (24)$$

where the parameters with the superscripts Q and W can now be obtained directly from the fitting (see Figure S3f and S3h). These parameters are related to the resistances and capacitances in the EC of Figure 5h (obtained from IS) through

$$\frac{\eta_{a\cdot s}}{R_S} = \frac{C_1}{C_1^Q} = \frac{C_2}{C_2^Q} = \frac{R_1^Q}{R_1} = R_{rec}^Q\left(\frac{1}{R_S} + \frac{1}{R_{rec}}\right) \quad (25)$$

and

$$\eta_{a\cdot s} = \frac{C_1}{C_1^W} = \frac{C_2}{C_2^W} = \frac{R_1^W}{R_1} = \frac{R_{rec}^W}{R_{rec}} \quad (26)$$

Similarly, the relation between the parameters obtained from IMPS and IMVS is given by

$$R_S = \frac{C_1^Q}{C_1^W} = \frac{C_2^Q}{C_2^W} = \frac{R_1^W}{R_1^Q} \quad (27)$$

and

$$\eta_{a\cdot s} = \left(\frac{1}{R_{rec}^Q} - \frac{R_S}{R_{rec}^W}\right)^{-1} \quad (28)$$

Therefore, $\eta_{a\cdot s}$ and R_S can be obtained through the combination of any two of these techniques. The results of the IMPS and IMVS fits are represented in blue lines in Figure 4c and 4d, with the EC parameters and $\eta_{a\cdot s}$ obtained from Equation (25) to (28) in the "IMPS+IMVS" column of Table 1. Before discussion of the parameters, we introduce an alternate method of fitting the IMPS and IMVS spectra. We define pseudo-impedances of IMPS and IMVS as

Table 1. Parameters obtained from the fitting of IS, IMPS, and IMVS data in Figure 4 with the equivalent circuit in Figure 5h. The "IS" column corresponds to the direct fitting of impedance spectroscopy data in Figure 4a to the equivalent impedance shown in Figure S3e in the Supporting Information. The "IMPS+IMVS" column corresponds to the parameters obtained by combining the fittings of IMPS and IMVS with the ECs adapted for these techniques in Figure S3g,i in the Supporting Information, respectively

		IS	IMPS+IMVS	Direct measurements
R_S	[Ω cm^2]	0.82 ± 0.03	0.80 ± 0.06	--
R_{rec}	[Ω cm^2]	3.19 ± 0.01	3.2 ± 0.2	--
C_2	[μF cm^{-2}]	8.0 ± 0.4	8.0 ± 0.7	--
R_1	[Ω cm^2]	0.37 ± 0.01	0.42 ± 0.05	--
C_1	[μF cm^{-2}]	31.1 ± 0.4	28 ± 4	--
R_{DC}	[Ω cm^2]	4.01 ± 0.03	4.0 ± 0.2	4.1 ± 0.2 [a)]
$\tau_{LF}^{IS} = \tau_{LF}^{IMVS}$	[ms]	125 ± 2	116 ± 16	126 ± 24
τ_{LF}^{IMPS}	[ms]	25.5 ± 0.7	23 ± 3	25 ± 5
a	[%]	--	--	43 ± 2 [b)]
$\eta_{a\cdot s}$	[%]	--	41 ± 3	--
$\eta_{col-diff}$	[%]	79.6 ± 0.7	80 ± 7	--
η_{sep}	[%]	--	95 ± 8	--

[a)] The R_{DC} was obtained from the inverse of the slope of the current-voltage curve at the V_{OC} (see Figure S4 in the SI). [b)] The absorptance (a) was obtained from reflectance measurements.

$$Z_Q = Q\frac{R_S}{\eta_{a\cdot s}} \tag{29}$$

$$Z_W = \frac{W}{\eta_{a\cdot s}} \tag{30}$$

Using these impedances, we transformed the experimental spectra to a pseudo-impedance form, see top and right axis of Figure 4c and 4d. With these last transformations, the fitting of the data, through the EC in Figure S3g and S3i (see Section 3.2 in the SI), provides the same parameters as those obtained through IS, as can be seen in "Z_Q" and "Z_W" columns of Table S1 in the SI. These fits are plot as the blue lines in Figure 4c and 4d.

With the results of the fitting, the low-frequency characteristic times of each technique can be calculated. The derivation of the mathematical expressions is detailed in Section 4 of the SI,

the results are shown in Equations (S50), (S52) and (S55), and calculated in Table 1 and S1. Note that the low-frequency characteristic time of IS is the same as that of IMVS, but different from that of IMPS. These characteristic times were also obtained directly from the measured spectra (see Figure 4a, 4c and 4d and last column of Table 1).

Once all the elements of the EC in Figure 5h were obtained, it was possible to calculate further useful parameters, presented in Table 1 and S1. The DC resistance (R_{DC}) and collection efficiency ($\eta_{col-diff}$) were calculated from Equation (S20) and (S23), respectively. The differential external quantum efficiency $EQE_{PV-diff}$ was calculated from Equation (S15) as can be seen in columns "Z_Q" and "IMPS+IMVS" of Table S1, an alternative way from the low-frequency limit of the IMPS (see Figure 3c).[39] By directly measuring the absorptance (a) (last column of Table 1) it was possible to calculate η_{sep} from Equation (7) and $IQE_{PV-diff}$ from Equation (S24). For the silicon photodiode, η_{sep} is very close to 1 (indistinguishable, considering the error interval), which means that, as expected for this device, [34,35] the approximation of $\eta_{a\cdot s} \approx a$ is very reasonable.

All sets of results in the different columns of Table 1 and in Table S1 match very well, including those obtained from direct measurements with independent techniques. This match confirms our main assumption that the three spectra (IS, IMPS and IMVS) in Figure 4 correspond to the same internal process of the device. Secondly, it proves that we can model the three techniques with a simple equivalent circuit (i.e. Figure 5h). And last but not least, it validates the procedures developed to obtain the characteristic parameters of the device, such as time constants, capacitances and resistances. Furthermore, by combining any of these two techniques, these procedures allow calculating optoelectronic parameters such $\eta_{a\cdot s}$, $\eta_{col-diff}$, $EQE_{PV-diff}$, and together with absorptance measurements, η_{sep}, and $IQE_{PV-diff}$.

6.3.3. Conclusions

This work provides a strong framework for the analysis of solar cells and photoelectrochemical devices by combining different small-perturbation frequency-domain techniques, namely, IS, IMPS, and IMVS. First, we have shown that the three techniques are properly correlated only when accounting for the absorptance and separation efficiency. Using this relationship, we have developed a generalized equivalent circuit and its associated theoretical framework that can be used to model the response of all three techniques together. The potential of this tool was demonstrated experimentally for a silicon photodiode. Combining the experimental results of the three techniques, the selection of the equivalent circuit was narrowed down, leading to an equivalent circuit that accurately models all three experimental responses simultaneously. Additionally, we have developed a method to fit the three spectra with standard software for impedance analysis using the identified equivalent circuit, allowing to obtain high quality and reliability of the output parameters from the model. Furthermore, combining these techniques in pairs, electro-optical parameters such as the separation efficiency, together with differential external and internal quantum efficiencies were obtained that are inaccessible from individual use of any of the three techniques. The generality of the developed procedure allows easy extension to the analysis of other photosensitive devices.

6.3.4. Experimental Section/Methods

The IS, IMPS and IMVS measurements were performed on a commercial silicon photodiode (SiPh, Thorlabs FDS100). IS, IMPS, IMVS and CV were measured with an Autolab PGSTAT302 equipped with a FRA32M module and combined with the LED driver. The four techniques were performed under 89 mW/cm^2 light intensity generated by an array of three blue LEDs (Philips LUMILEDS LXML-PB01-0040 with 470nm peak). The CV was performed at 50 $mV\ s^{-1}$. For the IS measurement, a 20 mV AC perturbation was applied. For IMPS and IMVS, an AC perturbation equal to 10% of the light flux was applied. The low-frequency limit was 0.1 Hz for the three techniques and the high frequencies were instrumentally limited, reaching 310, 200 and 16 kHz for IS, IMPS and IMVS respectively. The measurements were performed at open-circuit. Analysis of all spectra was done using Zview software.

Supporting Information

Supporting Information is available from the Wiley Online Library or from the author.
Raw experimental data are available at public repository http://hdl.handle.net/10234/193441.

Acknowledgements

This project has received funding from the European Union's Horizon 2020 MSCA Innovative Training Network under grant agreement No. 764787. F.F.-S. acknowledges Ministerio de Economía y Competitividad (MINECO) from Spain under the project ENE2017-85087-C3-1-R and Generalitat Valenciana under the project PROMETEO/2020/028 for financial support. S.R. acknowledges funding from the Helmholtz association via the project PEROSEED.

ORCID

Agustin O. Alvarez: 0000-0002-0920-5390
Sandheep Ravishankar: 0000-0002-8118-0159
Francisco Fabregat-Santiago: 0000-0002-7503-1245

References

[1] L. Bertoluzzi, J. Bisquert, *J. Phys. Chem. Lett.* **2017**, 8, 172.

[2] D. Klotz, D. S. Ellis, H. Dotan, A. Rothschild, *PCCP* **2016**, 18, 23438.

[3] L. M. Peter, *Chem. Rev.* **1990**, 90, 753.

[4] J. Li, R. Peat, L. Peter, *J. Electroanal. Chem. Interfacial Electrochem.* **1984**, 165, 41.

[5] P. De Jongh, D. Vanmaekelbergh, *Phys. Rev. Lett.* **1996**, 77, 3427.

[6] J. Krüger, R. Plass, M. Grätzel, P. J. Cameron, L. M. Peter, *J. Phys. Chem. B* **2003**, 107, 7536.

[7] S. Ravishankar, A. Riquelme, S. K. Sarkar, M. Garcia-Batlle, G. Garcia-Belmonte, J. Bisquert, *J. Phys. Chem. C* **2019**, 123, 24995.

[8] A. Pockett, M. Spence, S. K. Thomas, D. Raptis, T. Watson, M. J. Carnie, *Sol. RRL* **2021**, 2100159.

[9] G. Schlichthörl, S. Y. Huang, J. Sprague, A. J. Frank, *J. Phys. Chem. B* **1997**, 101, 8141.

[10] R. Kern, R. Sastrawan, J. Ferber, R. Stangl, J. Luther, *Electrochim. Acta* **2002**, 47, 4213.

[11] F. Fabregat-Santiago, E. M. Barea, S. Giménez, J. Bisquert, *Impedance Spectroscopy in Molecular Devices* in *Molecular Devices for Solar Energy Conversion and Storage*, (Eds: H. Tian, G. Boschloo, A. Hagfeldt), Springer Singapore, Singapore **2018**, 12.

[12] J. Bisquert, F. Fabregat-Santiago, *Impedance spectroscopy: a general introduction and application to dye-sensitized solar cells* in *Dye-sensitized Solar Cells*, (Ed: K. Kalyanasundaram), CRC Press, Switzerland **2010**, 12.

[13] L. Dloczik, O. Ileperuma, I. Lauermann, L. Peter, E. Ponomarev, G. Redmond, N. Shaw, I. Uhlendorf, *J. Phys. Chem. B* **1997**, 101, 10281.

[14] J. Bisquert, V. S. Vikhrenko, *J. Phys. Chem. B* **2004**, 108, 2313.

[15] H. Cachet, E. M. M. Sutter, *J. Phys. Chem. C* **2015**, 119, 25548.

[16] J. E. Thorne, J.-W. Jang, E. Y. Liu, D. Wang, *Chem. Sci.* **2016**, 7, 3347.

[17] D. Cardenas-Morcoso, A. Bou, S. Ravishankar, M. García-Tecedor, S. Gimenez, J. Bisquert, *ACS Energy Lett.* **2019**, 5, 187.

[18] A. Todinova, J. s. Idígoras, M. Salado, S. Kazim, J. A. Anta, *J. Phys. Chem. Lett.* **2015**, 6, 3923.

[19] L. Contreras, J. Idígoras, A. Todinova, M. Salado, S. Kazim, S. Ahmad, J. A. Anta, *PCCP* **2016**, 18, 31033.

[20] E. Ponomarev, L. Peter, *J. Electroanal. Chem.* **1995**, 396, 219.

[21] L. M. Peter, *J. Solid State Electrochem.* **2013**, 17, 315.

[22] A. Riquelme, F. E. Gálvez, L. Contreras-Bernal, H. Míguez, J. A. Anta, *J. Appl. Phys.* **2020**, 128, 133103.

[23] J. Bisquert, S. Giménez, L. Bertoluzzi, I. Herraiz-Cardona, *Analysis of Photoelectrochemical Systems by Impedance Spectroscopy* in *Photoelectrochemical Solar Fuel Production*, (Eds: S. Giménez, J. Bisquert), Springer, Cham **2016**.

[24] V. Babu, R. Fuentes Pineda, T. Ahmad, A. O. Alvarez, L. A. Castriotta, A. Di Carlo, F. Fabregat-Santiago, K. Wojciechowski, *ACS Appl. Energy Mater.* **2020**, 3, 5126.

[25] A. O. Alvarez, R. Arcas, C. A. Aranda, L. Bethencourt, E. Mas-Marzá, M. Saliba, F. Fabregat-Santiago, *J. Phys. Chem. Lett.* **2020**, 8417.

[26] O. Almora, C. Aranda, G. Garcia-Belmonte, *J. Phys. Chem. C* **2018**, 122, 13450.

[27] J. Halme, *PCCP* **2011**, 13, 12435.

[28] A. Bou, A. Pockett, D. Raptis, T. Watson, M. J. Carnie, J. Bisquert, *J. Phys. Chem. Lett.* **2020**, 11, 8654.

[29] O. Almora, Y. Zhao, X. Du, T. Heumueller, G. J. Matt, G. Garcia-Belmonte, C. J. Brabec, *Nano Energy* **2020**, 75, 104982.

[30] O. Almora, D. Miravet, G. J. Matt, G. Garcia-Belmonte, C. J. Brabec, *Appl. Phys. Lett.* **2020**, 116, 013901.

[31] S. Ravishankar, M. Garcia-Batlle, J. Bisquert, G. Garcia-Belmonte, J. Odrobina, C.-A. Schiller, *J. Phys. Chem. C* **2020**, 124, 15793.

[32] G. Tumen-Ulzii, T. Matsushima, D. Klotz, M. R. Leyden, P. Wang, C. Qin, J.-W. Lee, S.-J. Lee, Y. Yang, C. Adachi, *Commun. Mater.* **2020**, 1, 31.

[33] S. Ravishankar, C. Aranda, S. Sanchez, J. Bisquert, M. Saliba, G. Garcia-Belmonte, *J. Phys. Chem. C* **2019**, 123, 6444.

[34] J. Bisquert, *The physics of solar cells: perovskites, organics, and photovoltaic fundamentals*, CRC press, Boca Raton **2017**.

[35] T. Kirchartz, J. Bisquert, I. Mora-Sero, G. Garcia-Belmonte, *PCCP* **2015**, 17, 4007.

[36] J. Bisquert, *ACS Energy Lett.* **2010**, 646, 43.

[37] J. Bisquert, *PCCP* **2003**, 5, 5360.

[38] S. R. Raga, E. M. Barea, F. Fabregat-Santiago, *J. Phys. Chem. Lett.* **2012**, 3, 1629.

[39] S. Fletcher, *J. Electrochem. Soc.* **1994**, 141, 1823.

6.4. Supporting Information

Combining Modulated Techniques for the Analysis of Photosensitive Devices

Agustin O. Alvarez, Sandheep Ravishankar, and Francisco Fabregat-Santiago**

A. O. Alvarez, Prof. F. Fabregat-Santiago
Institute of Advanced Materials
Universitat Jaume I
Castellón de la Plana 12071, Spain
E-mail: agalvare@uji.es; fabresan@uji.es

Dr. S. Ravishankar
IEK-5 Photovoltaik
Forschungzentrum Jülich
Jülich 52425, Germany

6.4.1. Transfer functions

6.4.1.1. Basic relationship

As shown in Figure 2, the variables j_e, V_e and ϕ are related in a way that they generate a surface in the three-dimentional space (j_e-V_e-ϕ). This surface could be parametrized by considering j_e as a funtion of V_e and ϕ, $j_e(V_e, e\phi)$. Then, a differential j_e can be written as

$$dj_e = \left(\frac{dj_e}{dV_e}\right)_{e\phi:cte} dV_e + \left(\frac{dj_e}{de\phi}\right)_{V_e:cte} de\phi \quad \text{(S1)}$$

It can be notted that the derivatives in Equation (S1) are related with the IS and IMPS transfer functions in Equation (1) and (2)

$$Z = \frac{\hat{V}_e}{\hat{j}_e} = \left(\frac{dV_e}{dj_e}\right)_{e\phi:cte} \quad \text{(S2)}$$

$$Q = \frac{-\hat{j}_e}{e\hat{\phi}} = -\left(\frac{dj_e}{de\phi}\right)_{V_e:cte} \quad \text{(S3)}$$

Substituting Equation (S2) and (S3) in Equation (S1)

$$dj_e = \frac{1}{Z} dV_e - Q de\phi \quad \text{(S4)}$$

If the derivative with respect to $e\phi$ is taken with j_e constant, we have

$$0 = \frac{1}{Z}\left(\frac{dV_e}{de\phi}\right)_{j_e:cte} - Q \quad \text{(S5)}$$

Finally, it has to be noted that the derivative in Equation (S5) is related with the IMVS transfer funtion in Equation (3)

$$W = \frac{\hat{V}_e}{e\hat{\phi}} = \left(\frac{dV_e}{de\phi}\right)_{j_e:cte} \quad \text{(S6)}$$

Substituiting Equation (S6) into Equation (S5), it can be rewritten as Equation (4)

$$Z = \frac{W}{Q} \quad \text{(S7)}$$

As mention in the main text, an alternative definition is $Q = \tilde{j}_e/\tilde{j}_\phi$ and $W = -\tilde{V}_e/\tilde{j}_\phi$. Making the corresponding sign changes in Equation (S3) to (S6), it can be easily shown that Equation (4) is also valid.

6.4.1.2. Alternative expressions for the transfer functions

Based on the general equivalent circuit (GEC) in Figure 3 in the main text, the general expression for the IS, IMPS and IMVS transfer functions are

$$Z = Z_S + \left(\frac{1}{Z_p} + \frac{1}{Z_{rec} + Z_f}\right)^{-1} \tag{S8}$$

$$\begin{aligned} Q &= \frac{\eta_{a\cdot s}}{Z_S}\frac{Z_{rec}}{Z_{rec} + Z_f}\left(\frac{1}{Z_S} + \frac{1}{Z_p} + \frac{1}{Z_{rec} + Z_f}\right)^{-1} \\ &= \eta_{a\cdot s} Z_{rec}\left[Z_S\left(1 + \frac{Z_f + Z_{rec}}{Z_p}\right) + Z_f + Z_{rec}\right]^{-1} \end{aligned} \tag{S9}$$

$$W = \eta_{a\cdot s}\frac{Z_{rec}}{Z_{rec} + Z_f}\left(\frac{1}{Z_p} + \frac{1}{Z_{rec} + Z_f}\right)^{-1} = \eta_{a\cdot s} Z_{rec}\left(1 + \frac{Z_f + Z_{rec}}{Z_p}\right)^{-1} \tag{S10}$$

Because the three transfer functions are related by Equation (4), we have only two independent equations and four general variables. Deciding which are the elements in each part of the GEC is not always straightforward. However, the combination of some constraints together with some training in the identification of the typical shapes of Z, Q and W may help to identify the best equivalent circuit needed to extract the physical parameters that describe the behavior of our device. Without considering any particular case, the relationships between the measurements and the general elements are:

$$Z_S = Z - \frac{W}{\eta_{a\cdot s}}\left(1 + \frac{Z_f}{Z_{rec}}\right) \tag{S11}$$

or

$$Z = Z_S + \frac{W}{\eta_{a\cdot s}}\left(1 + \frac{Z_f}{Z_{rec}}\right) \tag{S12}$$

which in terms of Q and W may be written as

$$\frac{1}{Q} = \frac{Z_S}{W} + \frac{1}{\eta_{a\cdot s}}\left(1 + \frac{Z_f}{Z_{rec}}\right) \tag{S13}$$

6.4.1.3. Low-Frequency Limit: Steady-State Condition

Once the transfer function at any frequency (ω) is obtained, it is possible to consider the particular case corresponding to its low-frequency limit, i.e. $\omega = 0$. In this limit, all the capacitances are blocking and inductances are short-circuited and therefore, only the resistances determine the response of the device. The most familiar case is the low-frequency limit of IS, which is a resistance, R_{DC}, that can also be obtained as the inverse of the slope of the $j_e - V_e$ curve (green arrow in Figure 2b)

$$Z(\omega = 0) = \frac{\tilde{V}_e(\omega = 0)}{\tilde{j}_e(\omega = 0)} = \frac{d\bar{V}_e}{d\bar{j}_e} = R_{DC} \quad \text{(S14)}$$

Similarly, as previously reported,[1-2] the low-frequency limit of the IMPS transfer function is given by the differential external quantum efficiency ($EQE_{PV-diff}$)

$$Q(\omega = 0) = \frac{\tilde{j}_e(\omega = 0)}{\tilde{j}_\phi(\omega = 0)} = \frac{d\bar{j}_e}{d\bar{j}_\phi} = EQE_{PV-diff} \quad \text{(S15)}$$

Finally, the low-frequency limit of the IMVS transfer function is[1]

$$W(\omega = 0) = \frac{\tilde{V}_e(\omega = 0)}{\tilde{j}_\phi(\omega = 0)} = \frac{d\bar{V}_e}{d\bar{j}_\phi} = R_{EQE} \quad \text{(S16)}$$

Combining Equation (S14) to (S16) in Equation (4), the relationship

$$R_{EQE} = R_{DC} EQE_{PV-diff} \quad \text{(S17)}$$

is obtained.

Similar to Equation (S14), the low-frequency limit of Z_S, Z_{rec}, Z_P and Z_f can be defined as R_S, R_{rec}, R_P and R_f, respectively. With these considerations, the low-frequency limit of the GEC in Figure 3a is plotted in Figure 3e. By using source transformation (see Figure S1), we show that Figure 3e is equivalent to Figure 3f, where the "total" equivalent series and recombination resistances are given by

$$R_S^T = R_S + \frac{R_f}{R_{rec} + R_f}\left(\frac{1}{R_p} + \frac{1}{R_{rec} + R_f}\right)^{-1} \quad \text{(S18)}$$

$$R_{rec}^T = \frac{R_{rec}}{R_{rec} + R_f}\left(\frac{1}{R_p} + \frac{1}{R_{rec} + R_f}\right)^{-1} \quad \text{(S19)}$$

Then, the IS, IMPS and IMVS low-frequency limit can be obtained from Figure 3f or directly from Equation (33), (34) and (35)

$$R_{DC} = R_S^T + R_{rec}^T \quad \text{(S20)}$$

$$R_{EQE} = \eta_{a\cdot s}\, R_{rec}^T \quad \text{(S21)}$$

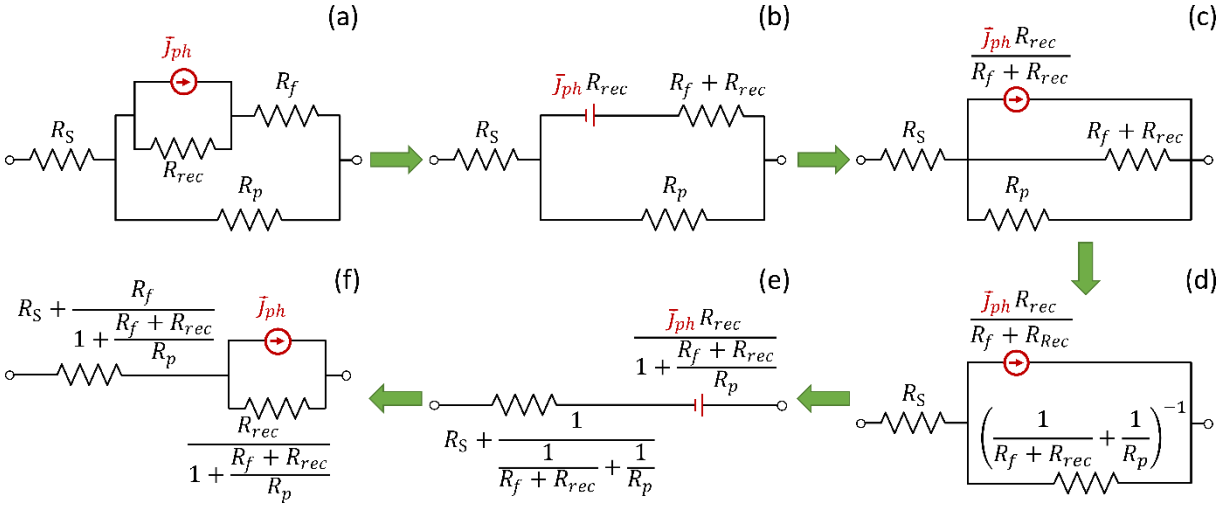

Figure S1. Step by step calculation of the equivalency between Figure 3e and 3f using source transformation.

Combining Equations (S17) and (S21), we get

$$EQE_{PV-diff} = \eta_{a\cdot s}\frac{R_{rec}^{T}}{R_{DC}} \tag{S22}$$

Equation (S22), combined with Equation (5) and (7) allows the identification of the differential collection efficiency ($\eta_{col-diff} = d\bar{J}_e/d\bar{J}_{ph}$) as

$$\eta_{col-diff} = \frac{R_{rec}^{T}}{R_{DC}} \tag{S23}$$

Provided our initial assumption that $\eta_{a\cdot s}$ is independent of light intensity, $\eta_{col-diff}$ moderates the differences between EQE_{PV} and $EQE_{PV-diff}$. Note that in the case $\eta_{sep} = 1$, according to Equation (28), $\eta_{col-diff}$ is equal to the differential internal quantum efficiency

$$IQE_{PV-diff} = \eta_{sep}\,\eta_{col-diff} = \frac{EQE_{PV-diff}}{a} \tag{S24}$$

On the other hand, the IMVS low-frequency limit together with $\eta_{a\cdot s}$ provides an indirect measure of R_{rec}^{T}. Combining this result with the IS low-frequency limit through equation (S27), R_S^T can be calculated. Identifying and separating the contribution of series and recombination resistances is key to understand the operation and limitations of solar and photoelectrochemical cells.[11] Simplified cases of the GEC in Figure 3 are discussed in the next sections for their special significance.

6.4.1.4.Case $Z_f = 0$ ($Z_f \ll Z_{rec}$)

In this particular case, described in Section 2.1.3. of the main text, the DC limits of the impedance elements reduce to

$$R_S^T = R_S \tag{S25}$$

$$R_{rec}^T = \left(\frac{1}{R_p} + \frac{1}{R_{rec}}\right)^{-1} \tag{S26}$$

6.4.1.5. Case $R_p \to \infty$

If leakage currents associated with R_p are negligible, then this resistance may be eliminated in Equation (S18) and (S19), and the low-frequency limit simplifies to

$$R_S^T = R_S + R_f \tag{S27}$$

$$R_{rec}^T = R_{rec} \tag{S28}$$

which allows the identification of R_{rec} by combining the IMVS low-frequency limit with $\eta_{a\cdot s}$ through Equation (S21)

$$R_{rec} = \frac{R_{EQE}}{\eta_{a\cdot s}} \tag{S29}$$

or combining $\eta_{a\cdot s}$ with the direct measurement of R_{DC} and $EQE_{PV-diff}$ using Equation (S17)

$$R_{rec} = \frac{R_{DC}\, EQE_{PV-diff}}{\eta_{a\cdot s}} \tag{S30}$$

where R_{DC} may be obtained from the inverse of the slope of the current-voltage curve. This allows the calculation of the total series resistance contribution

$$R_S^T = R_{DC} - R_{rec} \tag{S31}$$

Again, we can use these results to distinguish the series and recombination contributions or, alternatively, if we already know R_S or R_{rec}, to estimate $\eta_{a\cdot s}$.

6.4.2. Alternative Equivalent Circuits: IS fitting with corresponding IMPS and IMVS simulations

6.4.2.1. Equivalent circuit selection method

The silicon photodiode shows two arcs for the IS, only one appreciable arc for IMVS, and also a second one for IMPS. The number of ECs that may fulfill the IS behavior is large, but the number of equivalent circuits that can reproduce the three spectra simultaneously is much smaller. We will use this fact to make a general review of the effect that the positions of the different elements in the circuit have on the IS, IMVS and IMPS spectra.

For simplicity, we first fitted the different potential equivalent circuits to the IS spectrum and then use the parameters obtained to simulate the corresponding IMPS and IMVS spectra, see Figure . Finally, once the right circuit was chosen, we fitted the circuit to each of the techniques' spectra as shown in Figure 4, Table 1 and Table S1.

A first choice, plotted as a red line in Figure 5a to 5d, shows that a process in Z_f, represented by an R||C pair in the equivalent circuit in Figure 5e, generates a low-frequency arc in the lower quadrant of the IMPS spectra, as previously shown by Ravishankar et. al.,[33] but not observed here, which eliminates this circuit.

In the second choice, shown in Figure 5f, we have considered that, as described by Equation (13) in the main text, W is independent of Z_S, so at most, the high-frequency process might be in Z_S, because only one low-frequency process is observed in the measured IMVS spectrum. In green in Figure 5 is presented the effect of a process in Z_S represented by an R||C pair in series to R_S (see Figure 5f). The IMVS shape (an arc) was obtained, but the size was more than one order of magnitude smaller and the measured spectra also present a positive displacement in the x-axis that was not reproduced. Even more clear, the simulated IMPS spectrum also presents a low-frequency arc in the lower quadrant which does not correspond with the experimental data. Both results discard the use of this circuit, despite the good match with IS spectrum. Thus, for our case, we reduce Z_S to a single series resistance ($Z_S = R_S$).

Comparing the red and green results in Figure 5, we can note that for these cases, IS and IMPS fit and simulations do not allow easy identification of whether a process is in the parallel or the series branch of the EC. However, the IMVS simulations of these circuits are clearly different, which provides an easy way to differentiate them.

In our third choice - violet lines in Figure 5a to 5d, we show the result of using the combination of an R||C pair in parallel to the photogenerated current, one capacitance in Z_P and one resistance in Z_f, see Figure 5g, to account for the two processes found for IS. Unlike the two previous circuits, in this case, the simulated IMPS and IMVS spectra have the same order of magnitude as the measured spectra. However, the shapes are clearly different, reaching negative values in the real component at high frequencies. We conclude then that both processes should be combined in Z_{rec} or Z_P, with $Z_f = 0$, the particular case discussed in section 2.1.3 of the main text, where Z_{rec} and Z_P are indistinguishable. We, therefore, reduce the circuit to a resistor in Z_S and two processes in Z_{rec}^T shown in Figure 5h, which can reproduce the measured spectra accurately, as shown by simulations in Figure 5a to 5c (blue lines) and the fitting in Figure 4.

6.4.2.2. Limitations of the equivalent circuit selection method

While the procedure explained in the previous section could be very useful to select the EC more appropriately, it has some limitations. Figure 5 in the main paper shows that the combination of the small-perturbation techniques (IS,IMPS and IMVS) is useful to differentiate the location of the different general processes in the EC. However, Figure S2 shows the limitations of this method where for different equivalent circuits, we cannot differentiate the specific arrangement of elements for each general impedance (Z_S, Z_{rec}, Z_P and Z_f). The equivalent circuit in Figure S2d as shown in Figure 5h has only a series resistance and two processes in Z_{rec}^T, given by

$$Z_{rec}^T = \eta_{a\cdot s}\left(\frac{1}{R_{rec}} + \frac{1}{R_1 + (i\omega C_1)^{-1}} + i\omega C_2\right)^{-1} \quad \text{(S32)}$$

The equivalent circuit in Figure S2e has also a series resistance and two processes in Z_{rec}^T, but in this case are given by a different arrangement of the resistances and capacitances

$$\dot{Z}_{rec}^T = \eta_{a\cdot s}\left(\frac{1}{\dot{R}_{rec1} + \frac{1}{\left(\dot{R}_{rec2}\right)^{-1} + i\omega\dot{C}_1}} + i\omega\dot{C}_2\right)^{-1} \quad \text{(S33)}$$

As expected, both circuits can fit the IS spectra equally well (see Figure S2a), but when the resulting parameters are employed to simulate the IMPS and IMVS spectra (see Figure S2c and S2c) the EC generates also the same spectra. This could be understood by noting that Z_{rec}^T and $\dot{Z}_{rec}^T$ are degenerate impedances as shown by Fletcher,[3] this means that they generate the same impedance response as long as the following relationships are fulfilled

$$\dot{R}_{rec1} = \left(\frac{1}{R_1} + \frac{1}{R_{rec}}\right)^{-1} \quad \text{(S34)}$$

$$\dot{R}_{rec2} = \frac{{R_{rec}}^2}{R_1 + R_{rec}} \quad \text{(S35)}$$

$$C_1 = \dot{C}_1 \left(1 + \frac{R_1}{R_{rec}}\right)^{-1} \quad \text{(S36)}$$

Finally, because the three transfer functions depend on the total recombination resistance (Z_{rec}^T), as shown in Equation (15) to (17), it is not possible to differenctiate between Z_{rec}^T and $\dot{Z}_{rec}^T$ by combining these techniques.

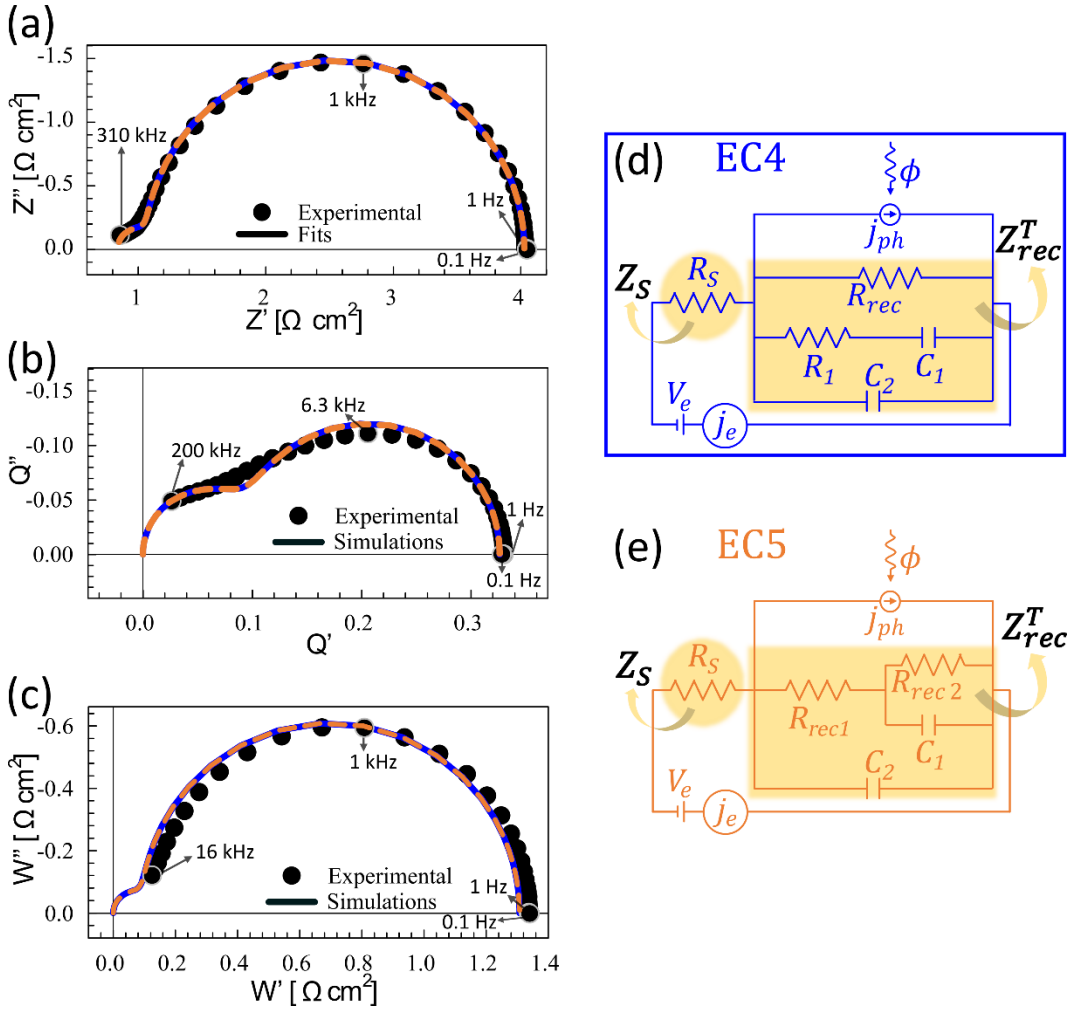

Figure S2. In black dots, measured (a) IS, (b) IMPS and (c) IMVS for a Silicon photodiode, under OC condition and 89 mW/cm^2 blue light (470nm peak). The high-frequency limits are 310, 200 and 16 kHz for IS, IMPS and IMVS, respectively, and the low-frequency limit is 0.1 Hz for every technique. The lines in (a) are the resulting fit employing the equivalent circuits in (d) and (e), respectively with the color. Following the same color pattern, the lines in (b) and (c) are the IMPS and IMVS simulations corresponding to the IS fitting results and considering $\eta_{a\cdot s}$ in Table 1 of the main text, from 10 mHz to 100 MHz. The equivalent circuit

in (d) is utilized for fitting the IS, IMPS and IMVS spectra (see Figure 4 and 5h). Both equivalent circuits are a particular case of the general equivalent circuit in Figure 3a, with the reduced general impedances in yellow. The only difference is in the arrangement of resistances and capacitances in Z_{rec}^{T} and as a consequence, both ECs generate the same IMPS and IMVS spectra when they are simulated with the corresponding IS fit parameters.

6.4.3. Fitting IMPS and IMVS with standard software for IS analysis

This section describes two procedures for the analysis of IMPS and IMVS spectra by fitting them using standard software for IS analysis. The EC for our system is shown in Figure 5h, however, the following analysis can be extended to any other EC as well. Our EC reduces to Figure S3b, S3c and S3d for IS, IMPS and IMVS respectively. The EC in Figure S3b can be directly used as Figure S3e to fit the IS spectra. However, for the fitting of IMPS and IMVS spectra, some transformations need to be done to their transfer function before implementing such an analysis.

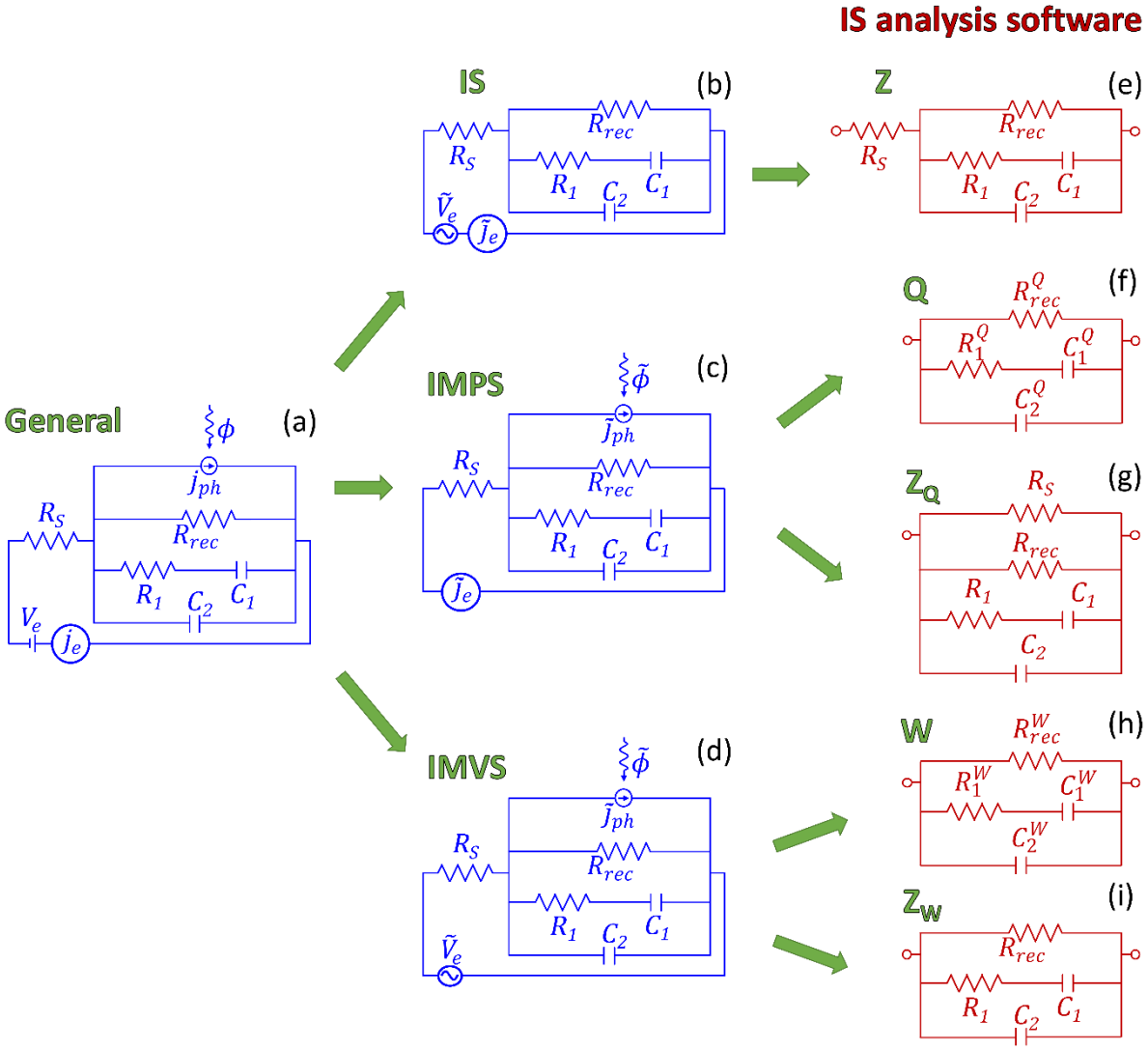

Figure S3. (a) The equivalent circuit used to describe the silicon photodiode. Simplifications of the general model applied specifically for (b) IS, (c) IMPS and (d) IMVS and (e) to (i) their corresponding conversion to the equivalent circuits used for the fitting with standard IS analysis software.

6.4.3.1. Combining IMPS and IMVS

In this section, we will describe a method where the IMPS and IMVS responses are fitted without any external parameters, but the fitting results need to be combined to get the parameters of interest. The IMPS and IMVS transfer functions can be written as shown in Equation (45) and (46) of the main text (corresponding to Figure S3f and S3h), reproduced again here

$$Q = \left[\frac{1}{R_{rec}^{Q}} + \frac{1}{R_1^{Q} + \left(i\omega C_1^{Q}\right)^{-1}} + i\omega C_2^{Q}\right]^{-1} \tag{S37}$$

$$W = \left[\frac{1}{R_{rec}^{W}} + \frac{1}{R_1^{W} + (i\omega C_1^{W})^{-1}} + i\omega C_2^{W}\right]^{-1} \tag{S38}$$

where the parameters with the superscripts Q and W are defined in Equation (25) and (26) of the main text. It is worth mentioning that the "resistances" and "capacitances" in Equation (S37) do not have their standard units, they are only a mathematical artifact to generate the circuit in Figure S3f. Combining Equation (25) and (26), the EC parameters and $\eta_{a\cdot s}$ are obtained (see "IMPS+IMVS" column of Table 1) as

$$R_S = \frac{R_1^{W}}{R_1^{Q}} = \frac{C_1^{Q}}{C_1^{W}} = \frac{C_2^{Q}}{C_2^{W}} \tag{S39}$$

$$\eta_{a\cdot s} = \left(\frac{1}{R_{rec}^{Q}} - \frac{R_S}{R_{rec}^{W}}\right)^{-1} \tag{S40}$$

$$R_{rec} = \frac{R_{rec}^{W}}{\eta_{a\cdot s}} = \frac{R_S}{\eta_{a\cdot s}}\left(\frac{1}{R_{rec}^{Q}} - \frac{1}{\eta_{a\cdot s}}\right)^{-1} \tag{S41}$$

$$R_1 = \frac{R_1^{W}}{\eta_{a\cdot s}} = \frac{R_S}{\eta_{a\cdot s}} R_1^{Q} \tag{S42}$$

$$C_1 = \eta_{a\cdot s} C_1^{W} = \frac{\eta_{a\cdot s}}{R_S} C_1^{Q} \tag{S43}$$

$$C_2 = \eta_{a\cdot s} C_2^{W} = \frac{\eta_{a\cdot s}}{R_S} C_2^{Q} \tag{S44}$$

6.4.3.2. A separate analysis of IMPS and IMVS

If we already know $\eta_{a\cdot s}$ and R_S, the IMPS and IMVS transfer functions can be transformed into "impedance" functions following Equation (29) and (30), which yields

$$Z_Q = Q\frac{R_S}{\eta_{a-s}} = \left[\frac{1}{R_S} + \frac{1}{R_{rec}} + \frac{1}{R_1 + (i\omega C_1)^{-1}} + i\omega C_2\right]^{-1} \tag{S45}$$

$$Z_W = \frac{W}{\eta_{a-s}} = \left(\frac{1}{R_{rec}} + \frac{1}{R_1 + (i\omega C_1)^{-1}} + i\omega C_2\right)^{-1} \tag{S46}$$

This allows direct fitting of the resulting Z_Q and Z_W data with the circuit in Figure S3g and S3i, through standard software for IS analysis. The resistances and capacitances obtained are the ones extracted from the fit of IS (see "Z_Q" and "Z_W" columns of Table S1).

6.4.4. Time constants

In this section, we derive the mathematical expressions for the low-frequency characteristic times of IS, IMPS and IMVS, corresponding to the EC in Figure 5h. The IS transfer function (Equation (20)) is

$$Z = R_S + \left(\frac{1}{R_{rec}} + \frac{1}{R_1 + (i\omega C_1)^{-1}} + i\omega C_2\right)^{-1} \quad \text{(S47)}$$

At low frequencies ($\omega \ll \omega_1 = 1/R_1C_1$), the central term in Equation (S47) can be approximated as

$$\frac{1}{R_1 + (i\omega C_1)^{-1}} \sim i\omega C_1 \quad \text{(S48)}$$

Therefore, the IS transfer function of Equation (S47) at low enough frequencies reduces to

$$Z \sim R_S + \left(\frac{1}{R_{rec}} + i\omega(C_1 + C_2)\right)^{-1} \quad \text{(S49)}$$

Yielding a single arc with a characteristic time

$$\tau_{LF}^{IS} = R_{rec}(C_1 + C_2) \quad \text{(S50)}$$

Similarly, we can calculate the characteristic time of the IMPS transfer function in Equation (21) at $\omega \ll \omega_1$

$$Q \sim \frac{\eta_{a\cdot s}}{R_S}\left[\frac{1}{R_S} + \frac{1}{R_{rec}} + i\omega(C_1 + C_2)\right]^{-1} \quad \text{(S51)}$$

then

$$\tau_{LF}^{IMPS} = \frac{C_1 + C_2}{\frac{1}{R_S} + \frac{1}{R_{rec}}} = R_{rec}^{Q}\left(C_1^{Q} + C_2^{Q}\right) \quad \text{(S52)}$$

Finally, the IMVS transfer (Equation (22)) function at low frequency is given by

$$W \sim \eta_{a\cdot s}\left(\frac{1}{R_{rec}} + i\omega(C_1 + C_2)\right)^{-1} \quad \text{(S53)}$$

The characteristic time in this conditions is

$$\tau_{LF}^{IMVS} = R_{rec}(C_1 + C_2) = R_{rec}^{W}(C_1^{W} + C_2^{W}) \quad \text{(S54)}$$

Comparing Equation (S50) and (S54), we obtain

$$\tau_{LF}^{IMVS} = \tau_{LF}^{IS} \quad \text{(S55)}$$

6.4.5. Current-voltage scans

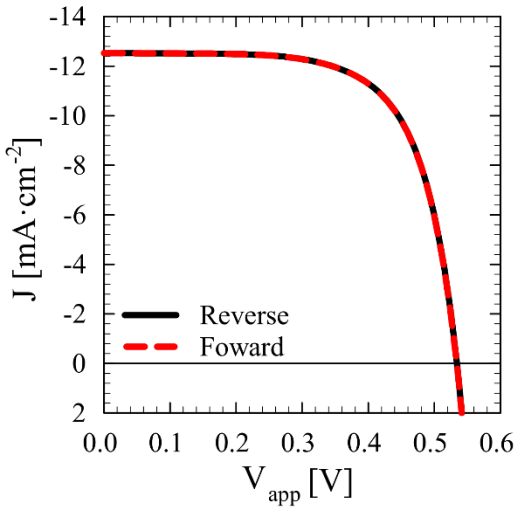

Figure S4. Forward and reverse current-voltage scans were performed at 50 mV s^{-1} under 89 mW/cm^2 blue light (470nm peak).

6.4.6. Fitting results: Parameters

Table S1. Extended results from the fitting of Figure 4a (IS), 4c (IMPS) and 4d (IMVS) data with the equivalent circuit in Figure 5h (reduced table shown in Table 1 in the main paper). The "IS" column corresponds to the direct fitting of impedance spectroscopy data in Figure 4a to the equivalent impedance shown in Figure S3e. The "IMPS+IMVS" column corresponds to the parameters obtained by combining the fittings of IMPS and IMVS with the ECs adapted for these techniques in Figure S3f and S3h respectively. The "Z_Q" column corresponds to the fitting of the IMPS impedance, Z_Q, obtained through Equation (51), with the EC in Figure S3g. The "Z_W" column corresponds to the fitting of the IMVS impedance Z_W,obtained through Equation (52), with the EC in Figure S3i. The low-frequency time constants correspond to the evaluation of Equation (S50) and (S52). The $EQE_{PV-diff}$ and $\eta_{col-diff}$ correspond to the differential external quantum efficiency and differential collection efficiency respectively (see Section 1.3 in the SI). The results are compared with direct measurements in the last column.

		IS	IMPS+IMVS	Z_Q	Z_W	Direct measurements
R_S	[Ω cm^2]	0.82 ± 0.03	0.80 ± 0.06	0.8 ± 0.3	0.7 ± 0.2 [a)]	--
R_{rec}	[Ω cm^2]	3.19 ± 0.01	3.2 ± 0.2	3.3 ± 0.2	3.3 ± 0.2	--
C_2	[μF cm^{-2}]	8.0 ± 0.4	8.0 ± 0.7	7.3 ± 0.5	7.7 ± 0.7	--
R_1	[Ω cm^2]	0.37 ± 0.01	0.42 ± 0.05	0.42 ± 0.04	0.56 ± 0.06	--
C_1	[μF cm^{-2}]	31.1 ± 0.4	28 ± 4	21.0 ± 1.2	29 ± 6	--
R_{DC}	[Ω cm^2]	4.01 ± 0.03	4.0 ± 0.2	4.1 ± 0.2	--	4.1 ± 0.2 [d)]
$\tau_{LF}^{IS} = \tau_{LF}^{IMVS}$	[ms]	125 ± 2	116 ± 16	--	121 ± 3	126 ± 24
τ_{LF}^{IMPS}	[ms]	25.5 ± 0.7	23 ± 3	18.6 ± 0.3	--	25 ± 5
$\eta_{a\cdot s}$	[%]	--	41 ± 3	42 ± 2 [b)]	42 ± 1 [c)]	--
$\eta_{col-diff}$	[%]	79.6 ± 0.7	80 ± 7	80 ± 6	--	--
$EQE_{PV-diff}$	[%]	--	32.6 ± 0.2	33 ± 4	--	32.3 ± 0.4 [e)]
a	[%]	--	--	--	--	43 ± 2 [f)]
			IMPS+IMVS+a	IMPS+IS+a	IMVS+IS+a	$EQE_{PV-diff}$ +a
η_{sep}	[%]	--	95 ± 8	98 ± 7	98 ± 5	--
$IQE_{PV-diff}$	[%]	--	76 ± 9	77 ± 9	--	75 ± 4

[a)]Obtained from R_{DC} (IS) minus R_{rec}. [b)]Obtained from the fitting of Q and Z through Equation (47). [c)]Obtained from the fitting of W and Z through equation(48). [d)]The R_{DC} was obtained

from the inverse of the slope of the current-voltage curve at the V_{OC} (see Figure S4). [e)]The $EQE_{PV-diff}$ was measured by applying the same DC light intensity and perturbation amplitude as in IMPS and IMVS (see Experimental Methods Section), also at a steady-state voltage bias corresponding to the open-circuit voltage. [f)]The absorptance (a) was obtained from reflectance measurements.

References

[1] L. Bertoluzzi, J. Bisquert, *J. Phys. Chem. Lett.* **2017**, 8, 172.

[2] S. Ravishankar, C. Aranda, P. P. Boix, J. A. Anta, J. Bisquert, G. Garcia-Belmonte, *J. Phys. Chem. Lett.* **2018**, 9, 3099.

[3] S. Fletcher, *J. Electrochem. Soc.* **1994**, 141, 1823.

CHAPTER 7

Publication 4: New Views on Carrier Diffusion and Recombination by Combining Small Perturbation Techniques: Application to BiVO4 Photoelectrodes

Agustin O. Alvarez, Miguel García-Tecedor, Laura Montañés, Elena Mas-Marzá, Sixto Giménez, Francisco Fabregat-Santiago.

Solar RRL **2022**, 2200826.
DOI: 10.1002/solr.202200826.
Impact Factor 2021: 9.173.

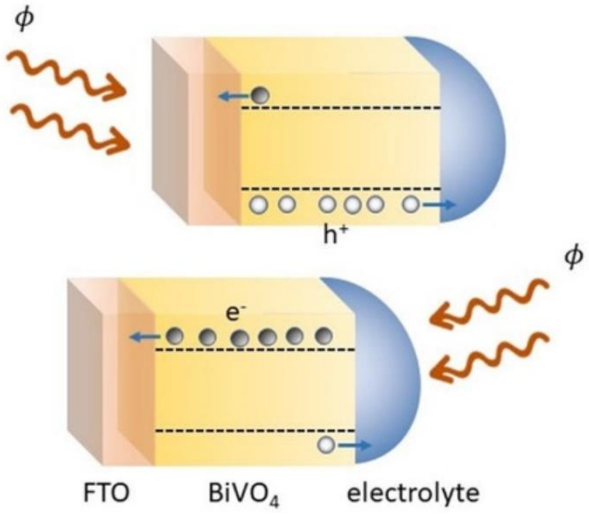

7.1. Candidate's contribution

Nature of Contribution	Extent of Contribution
✓ Carried out all the measurements ✓ Developed the theoretical model and calculations ✓ Carried out the simulations ✓ Analysed the measurements ✓ Interpreted the results ✓ Preaped all the figures ✓ Wrote manuscript drafts, incorporating the comments provided by the co-author and referees ✓ Wrote the first draft of the reply to the referees	75%

7.2. Thesis context

In this publication, we built on the procedure presented in **CHAPTER 6** to analyse in detail the functioning of a photoelectrochemical cell (PEC) that used a Zr:$BiVO_4$ photoanode for hydrogen generation. The aim of this analysis is, first, to corroborate that the main limitation of this system is the extraction of the photogenerated charges and, if so, to decipher the causes of this limitation. We measured the IS, IMPS, and IMVS techniques for this system using the protocol from **CHAPTER 5**. From these responses, we could first notice that the extraction of the photogenerated charges is limited by their diffusion and recombination within the absorber material device.

To further investigate the internal processes of this system, we have extended the procedure in **CHAPTER 6**, presenting an equivalent circuit (EC) based on the fundamental equations describing distributed photogeneration, recombination, and diffusion. We demonstrate that this EC allows the simultaneous analysis of the IS, IMPS, and IMVS responses of this PEC. Our results showed that both electron and hole diffusion limit the charge extraction when the device is illuminated from the hole and electron collector contact, respectively. However, we expose that the main limitation to the performance of this PEC is the charge separation efficiency of the Zr:$BiVO_4$.

These results are also a validation of the power of combining IS, IMPS and IMVS, exposing the main limitations of the devices, thus indicating the target for improving its performance.

7.3. Published Manuscript

New Views on Carrier Diffusion and Recombination by Combining Small Perturbation Techniques: Application to $BiVO_4$ Photoelectrodes

Agustin O. Alvarez,[a] Miguel García-Tecedor,[b] Laura Montañés,[a] Elena Mas Marzá,[a] Sixto Giménez,[a] and Francisco Fabregat-Santiago[a]**

[a]Institute of Advanced Materials, Universitat Jaume I, Castellón de la Plana 12006, Spain
[b]Photoactivated Processes Unit, IMDEA Energy Institute. Av. Ramón de la Sagra, 3. 28935 Móstoles, Spain.

E-mail: agalvare@uji.es; fabresan@uji.es

Keywords: IMPS, IMVS, impedance spectroscopy, Water Splitting, $BiVO_4$

Impedance Spectroscopy (IS), Intensity-Modulated Photocurrent Spectroscopy (IMPS) and Intensity-Modulated Photovoltage Spectroscopy (IMVS) are well-established powerful modulated techniques to characterize optoelectronic devices. Their combined use has proven to provide an understanding of the behaviour and performance of these systems, far beyond the output obtained from their independent analysis. However, this combination has shown to be challenging when applied to complex systems. In this work, IS, IMPS and IMVS were cooperatively employed, for the first time, to study the distributed photogeneration, diffusion and recombination processes in a photoanode of zircon-doped bismuth vanadate. The use of this methodology reveals that the carriers that determine the response of the device are the electrons when the device is illuminated from the hole-collector side (electrolyte), and the holes when the illumination reaches the device from the electron-collector side (FTO). Detailed quantitative information was obtained for each carrier, including recombination lifetime, diffusion coefficient, collection and separation efficiencies, identifying the latter as the main limitation of this device. This methodology is a powerful tool that can be used for the characterization and understanding of the operating processes of other photoconversion devices.

7.3.1. Introduction

Photoconversion devices, including photovoltaic and photoelectrochemical cells, are gaining increasing attention over time, standing as some of the main systems that will help to overcome the global dependence on fossil fuels. Photovoltaic devices are already generating electrical energy from sunlight massively in the world. The conversion of sunlight into fuels and chemicals is also an attractive and growing field,[1] mainly driven by the photoelectrochemical production of H_2 from the oxidation of H_2O.[2]

During the operation of photoconversion devices, the overall performance is determined by several optoelectronic processes (carrier generation, transport, recombination and charge transfer). Consequently, an appropriate characterization of these processes is essential for a reliable understanding of the operation mechanism. This knowledge makes it possible to identify the limitations of the system, thus favouring their optimisation and even the development of new devices. Impedance Spectroscopy (IS),[3-5] Intensity-Modulated Photocurrent Spectroscopy (IMPS)[6-8] and Intensity-Modulated Photovoltage Spectroscopy (IMVS)[9-10] have been extensively used for this purpose.

These three techniques were developed independently and their results are often analysed with different procedures, thus limiting the information that can be obtained from the characterisation. IS data is generally analysed with an equivalent circuit (EC), where the internal processes are modelled with passive electrical elements such as resistances, capacitances, and inductances.[11-12] On the other hand, IMPS and IMVS data are usually limited to the analysis of the characteristic times.[13-14] The combination of the three techniques has gained interest in recent years, exposing the intrinsic relationship among them. However, their experimental application has been challenging.[15-16] Klotz et al. combined the three techniques (IS, IMPS, IMVS) to analyze the charge carrier dynamics in hematite photoanodes by employing a distribution of relaxation times. This procedure can be particularly useful to separate polarization processes, but its implementation is not straightforward.[17] Bertoluzzi and Bisquert proposed an EC for a water-splitting system, reporting the corresponding simulated spectra for IS, IMPS and IMVS.[18] Subsequently, Ravishankar et al. proposed an EC to fit the IS and the IMPS responses of a perovskite solar cell, although some discrepancies were observed between both results.[19] Following these results, we have recently proposed an improved characterisation procedure by combining the three techniques, for a generic photoconversion device. This procedure was applied to analyse the response of a silicon photodiode using a common model for IS, IMPS and IMVS. This combination proved to maximise the information obtained from the device, both qualitatively and quantitatively and

at the same time, allows accessing new information that cannot be obtained using the techniques individually.[20]

In that previous work, it is considered that photogeneration can be separated from the other processes in the device. This can be appropriate for many systems, as exemplified with a silicon photodiode. But there are other systems where the photogeneration is distributed within a space where transport and recombination may also be non-uniform. This is the scenario of more complex systems, such as distributed photogeneration in a thin film with coupled diffusion and recombination. These processes determine the performance of many photoconversion devices, including photovoltaic devices such as dye-sensitized solar cells,[21] perovskite solar cells;[22] and photoelectrochemical devices,[23] so their understanding is key to optimizing the system behaviour.

IS was widely used to characterize such devices, allowing the extraction of quantitative parameters such as diffusion length and recombination frequency.[12, 23-25] These applications were widespread by the developments made mainly by Bisquert and co-workers, which includes the determination of the IS transfer function from fundamental equations and the presentation of the corresponding equivalent circuit (EC).[26-28] Although these developments have shown to be a game-changer in the characterization of optoelectronic devices, in some cases, the IS spectra are not clear enough to characterize properly the diffusive process.[29] Even when the analysis is possible, there are intrinsic limitations such as identifying if the diffusive carriers are electrons, holes or even ions.

Similarly, the IMPS transfer function was also deduced from fundamental equations. This theoretical development was mainly carried out by Peter and his co-workers. These authors also showed the experimental application in dye-sensitised solar cells.[21] Recently, this development was also experimentally applied to analyse the IMPS response of a perovskite solar cell.[22] Following these theoretical equations, the IMVS transfer function was also developed from fundamental equations.[30] Finally, the three transfer functions were deduced from a proposed EC for dye-sensitized solar cells, including other internal processes.[31-32] However, this EC has not been used for the practical analysis of devices combining IS, IMPS and IMVS spectra, yet.

In this work, we will show that it is possible to combine IS, IMPS and IMVS techniques to improve the characterization of systems with distributed photogeneration, diffusion and recombination processes. We will consider a general theoretical framework for these devices, from which the transfer functions are derived. Simulations of these transfer functions will be discussed to describe the possible spectra expected for these processes. Finally, this

information will be employed for the practical characterization of a water oxidation photoelectrode, with Zircon-doped $BiVO_4$ (Zr:$BiVO_4$) as an active layer.

While Zr:$BiVO_4$ is a promising photoanode material for water splitting,[33-36] it also suffers from poor charge transport, slow water oxidation kinetics and high surface recombination.[37-38] We will show that our methodology can help in understanding these internal processes behind performance losses, improving previous approaches used to investigate these electrodes,[39-40] including the separate use of IS,[41-44] IMPS[45-49] and IMVS.[50-52]

7.3.2. Theory: Transfer functions

Figure 1a illustrates the basic light conversion mechanism occurring in a photoconversion device, where the photogeneration is distributed over the light absorber layer (AL), and the charges must diffuse to be extracted, whilst recombination can take place along the layer. As depicted, when a photon flux (ϕ) reaches the device, only part of the photons will reach the absorber material ($\phi_{int}=\eta_{opt}\phi$, with η_{opt} the optical efficiency) and the rest will be lost, for example, by reflectance at the contacts. The absorbed current can be defined by $j_a=qa\phi_{int}$, where q is the elementary charge and $a=e^{-\alpha d}$, the absorptance, is the fraction of ϕ_{int} that generates electron-hole pairs, where α is the absorption coefficient and d is the thickness of the absorber. The pairs can be successfully separated in the active material to generate free-photogenerated charges in the AL ($j_{ph}=\eta_{sep}j_a$, with η_{sep} as the separation efficiency). Depending on whether the illumination is incident from the electron-collector side (ES) or the hole-collector side (HS), the position-dependent probability of generating free charges can be expressed as

$$G^{HS}(x) = \eta_{sep}\eta_{opt}\alpha\phi e^{\alpha(x-d)} \quad (1)$$

$$G^{ES}(x) = \eta_{sep}\eta_{opt}\alpha\phi e^{-\alpha x} \quad (2)$$

Then, the diffusion of the carriers toward the contacts takes place. During diffusion, part of the carriers is lost as recombination current (j_{rec}), which depends on the internal voltage ($qV_{int} = E_{Fn} - E_{Fp}$). The charges that reach the contact and are successfully extracted generate the extracted current ($j_{ext} = j_{ph} - j_{rec} = \eta_{col} j_{ph}$, with η_{col} the collection efficiency). Therefore, the current that is extracted from the device can be written as

$$j_{ext} = q\, a\, \eta_{col}\, \eta_{sep}\, \eta_{opt}\, \phi \quad (3)$$

is a function of V_{int} which is determined by the externally applied (or measured) voltage ($V_{ext} = V_{int} + R_s j_{ext}$).

Note that in literature there is a variety in the notation of the variables involved in this article, which may become an obstacle for the follow-up and comparison of publications. In the Supporting Information (SI) we present **Table S1** with a summary of the notations used on some relevant papers in the field to ease help with this problem.

To apply any of the small-perturbation techniques (IS, IMPS or IMVS) to a specific device, a steady-state condition is needed. Additionally, the combination of IS, IMPS or IMVS for a complementary analysis, imposes that these three small-perturbation techniques are applied in the same steady-state condition. The steady-stated conditions are defined by the light ($\bar{\phi}$), applied voltage ($\bar{V}_{ext}$) and extracted current ($\bar{J}_{ext}$), where the variables with overbars ($\bar{}$)

indicate DC signals. In particular, to measure IS, an AC small-perturbation in voltage ($\tilde{V}_{ext}$) is applied and the corresponding AC extracted current density ($\tilde{j}_{ext}$) is measured, where the variables with a tilde ($\tilde{}$) indicate AC perturbations. The IS transfer function is defined by:

$$Z = -\frac{\tilde{V}_{ext}}{\tilde{J}_{ext}} \tag{4}$$

Here, the sign of the current is a convention. In the case of IS, the current is usually considered positive when it flows into the device. In our case, we denoted this convention as the injected current ($\tilde{j}_{inj} = -\tilde{j}_{ext}$).[20, 53]

Similarly, to measure IMPS or IMVS, a small perturbation is applied in the light ($\tilde{\phi}$) and the $\tilde{j}_{ext}$ or $\tilde{V}_{ext}$ responses are measured, respectively. The corresponding transfer functions are defined by:

$$Q = \frac{\tilde{J}_{ext}}{q\tilde{\phi}} \tag{5}$$

$$W = \frac{\tilde{V}_{ext}}{q\tilde{\phi}} \tag{6}$$

Note that from Equation (3) it may be deduced that a small perturbation of the photon flux provides $\tilde{j}_{ext} = q\ a\ \eta_{col}\ \eta_{sep}\ \eta_{opt}\ \tilde{\phi}$, which is key for relating the parameters obtained from IS, IMPS and IMVS.[20]

From the definitions of the transfer functions, the relationship

$$W = Z \times Q \tag{7}$$

emerges intuitively. This relationship has been explored theoretically in multiple studies,[18, 20, 32] but experimentally it has been shown that this is not always fulfilled.[15-16, 29] Therefore, we emphasize the importance of verifying this relationship for each case under study, before combining the three techniques.[20, 32]

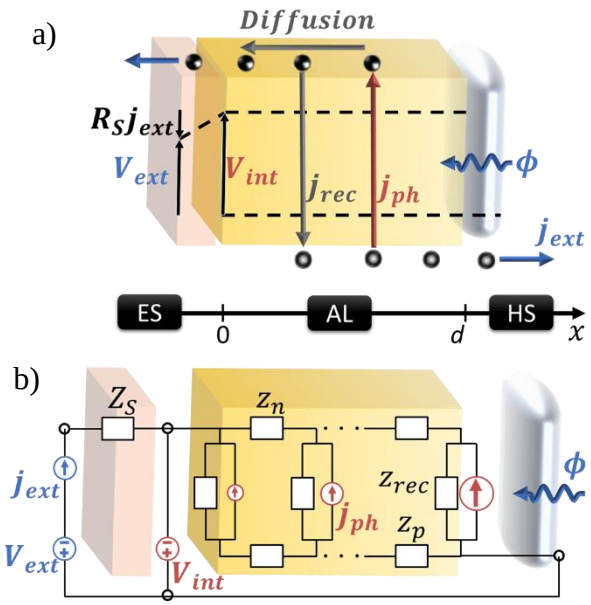

Figure 1. a) Scheme of the basic processes occurring in a photoconversion device with distributed photogeneration, recombination and diffusion. AL is the light absorber layer with thickness *d*, while ES and HS are the electron- and hole-collector sides, respectively. ϕ is the photon flux, j_{ph}, j_{rec} and j_{ext} are the free-photogenerated, recombination and extracted currents, respectively. V_{app} is the externally applied voltages, V_{int} the internal voltage in the film and R_S is a series resistance. b) Equivalent circuit modelling the device schematized in a), where z_n and z_p are impedance per unit length, while z_{rec} is an impedance length. Z_S is a series impedance, illustrated here on the ES layer, but it can contain other processes such as transport in the HS layer and interfacial processes.

7.3.2.1.Transmission Line Equivalent Circuit

Figure 1b shows a transmission line-based equivalent circuit (EC) for the analysis of the device schematized in **Figure 1a**. $z_n = Z_n/d$ and $z_p = Z_p/d$ are impedance per unit length, accounting respectively for the electron and hole transport processes within the AL. On the other hand, $z_{rec} = Z_{rec}d$ is an impedance length accounting for interaction processes between these two species, such as recombination and accumulation. Z_S is a series impedance, illustrated in **Figure 1b** as the ES layer impedance, although Z_S can account for alternative processes such as transport in the HS layer as well as interfacial processes. The acquisition of the IS, IMPS and IMVS transfer functions from a simpler EC was exposed in our previous work,[20] and although the current complexity, the basic idea to obtain the transfer functions is similar. As explained above, $\tilde{\phi} = 0$ when IS is measured, which is equivalent to removing j_{ph} from the EC (**Figure 1b**). Then, from the simplified EC, the impedance of the transmission line was solved in previous works,[54-55] and we reformulate it as:

$$Z_{D-R} = \frac{\tilde{V}_{int}}{\tilde{j}_{inj}} = \frac{Z_n\, Z_p}{Z_n + Z_p}\left(1 + \frac{2}{\Gamma\, sinh(\Gamma)}\right) + \frac{Z_n^2 + Z_p^2}{Z_n + Z_p}\,\frac{coth(\Gamma)}{\Gamma} \tag{8}$$

where:

$$\Gamma = \sqrt{\frac{Z_n + Z_p}{Z_{rec}}} \tag{9}$$

is a dimensionless parameter related to the effective constraints on charge extraction (or injection), tending to zero when the transport impedances (Z_n and Z_p) do so, as well as when the recombination impedance (Z_{rec}) tends to infinity.

Finally, considering the effect of Z_S, the IS transfer function is:

$$Z = Z_S + Z_{D-R} \tag{10}$$

Similarly, considering the effect of the conversion parameters from irradiance to the photogeneration,[19] provided by Equation (3) and the resulting distributed photogeneration (j_{ph}) on the EC, together with the IMPS and IMVS transfer functions solved in previous works,[30-32] we can obtain:

$$Q = \frac{\eta_{opt}\eta_{sep}\left(\eta_\Gamma^n Z_n + \eta_\Gamma^p Z_p\right)\left(Z_n + Z_p\right)}{\left[Z_S\left(Z_n + Z_p\right) + Z_n\, Z_p\right]\frac{\Gamma}{coth(\Gamma)} + \frac{2\, Z_n\, Z_p}{cosh(\Gamma)} + Z_n^2 + Z_p^2} \tag{11}$$

$$W = \eta_{opt}\eta_{sep}\left[\eta_\Gamma^n Z_n + \eta_\Gamma^p Z_p\right]\frac{coth(\Gamma)}{\Gamma} \tag{12}$$

These transfer functions are written as a function of impedance (Z, Γ), optical elements (η_{opt}, η_{sep}) and mixed elements as η_Γ^n and η_Γ^p. The specific definition of η_Γ depends on whether the illumination is from HS or ES:

$$\eta_\Gamma^{n,HS} = \eta_\Gamma^{p,ES} = \frac{(a-1)\left(1+\frac{\Gamma}{A}tanh(\Gamma)\right)+\frac{1}{cosh(\Gamma)}}{1-\frac{\Gamma^2}{A^2}} \quad (13)$$

$$\eta_\Gamma^{p,HS} = \eta_\Gamma^{n,ES} = \frac{1-\frac{\Gamma}{A}tanh(\Gamma)+\frac{a-1}{cosh(\Gamma)}}{1-\frac{\Gamma^2}{A^2}} \quad (14)$$

where $A = -log(1-a) = \alpha d$ the absorbance and the superscripts *n* and *p* denote electrons and holes, respectively. **Figure S1** shows the possible values that can be taken for these functions in the low-frequency limit ($\omega \longrightarrow 0$). As can be noted, η_Γ is equal to a when $\Gamma = 0$ and it decreases as Γ increases.

Writing the transfer functions Z, Q and W using the same parameters is key, as it allows the simultaneous analysis of experimental data.

7.3.2.2. Single Carrier Diffusion

In this section, it will be considered that only one species (for example electrons) is limiting the performance of a device, which implies that the other species (holes in this case) are more efficiently extracted. In this case, the electron carrier density (*n*) can be described by:

$$\frac{dn}{dt} = D\frac{d^2n}{dx^2} - \frac{n}{\tau_{rec}} + G(x,t) \quad (15)$$

Where *D* is the diffusion coefficient and τ_{rec} is the lifetime of the diffusion carriers. The case where the diffusive carriers are holes (*p*) instead of electrons (*n*) is described by the same equation. The differences between these two cases are the boundary conditions, as shown in **Section 7.4.1** in the SI.

In the case of IS, $G(x,t)$ is eliminated in Equation (15) and the IS transfer function is

$$Z_{D-R} = R_{tr}\, coth(\Gamma)/\Gamma \quad (16)$$

as previously obtained by Bisquert.[26] with

$$\Gamma = \sqrt{\frac{\omega_{rec}+i\omega}{\omega_D}} \quad (17)$$

where $\omega_{rec} = 1/\tau_{rec}$ and $\omega_D = D/d^2$ are the recombination and diffusion frequencies, and R_{tr} is defined as the diffusion resistance.

Finally, if it is considered that the series impedance is a single series resistance, R_S, the total (measurable) impedance becomes:

$$Z = R_S + Z_{D-R} \tag{18}$$

The effect of incorporating a series resistance R_S, modifies the IMPS and IMVS transfer functions obtained from Equation (15) providing:[9, 22, 29-30]

$$Q = \eta_{opt}\eta_{sep}\eta_{\Gamma}\left[1 + \frac{R_S}{Z_{D-R}}\right]^{-1} \tag{19}$$

$$W = \eta_{opt}\eta_{sep}\eta_{\Gamma}Z_{D-R} \tag{20}$$

where η_{Γ} is defined by Equation (13) or (14) depending on whether the diffusing species are electrons or holes and whether the illumination is from HS or ES.

The equivalent circuit corresponding to Equations (18), (19) and (20) is shown in **Figure 2a**, which is a particular case of the EC in **Figure 1b** (see more details in **Section 7.4.3** of the SI). This EC provides the following equivalences: for the transport resistance $R_{tr} = r_{tr}\, d$, for the recombination resistance $R_{rec} = r_{rec}/d = R_{tr}\omega_D\tau_{rec}$ and for the chemical capacitance $C_{\mu} = c_{\mu}\, d = 1/R_{rec}\omega_{rec}$. The diffusion length, which is key to explain carrier collection in photoelectrochemical devices, and can be obtained from the parameters provided though $L = d\sqrt{\omega_D\tau_{rec}} = d\sqrt{R_{rec}/R_{tr}}$.[12,27] With these definitions, Equation (17) provides that at the low frequency limit, $\Gamma(\omega \longrightarrow 0) = d/L$. Note that for good carrier collectors $L/d >> 1$, which implies that at the low-frequency limit $\Gamma \longrightarrow 0$.

Considering explicitly the optical efficiency, the differential external and internal quantum efficiencies can be expressed as:[20, 56]

$$EQE_{PV-Diff} = a\,\eta_{sep}\,\eta_{col}\,\eta_{opt} \tag{21}$$

$$IQE_{PV-Diff} = \frac{EQE_{PV-Diff}}{\eta_{opt}a} \tag{22}$$

The $EQE_{PV-Diff}$ corresponds to the low-frequency limit of Q. Then, comparing Equations (19) and (21), we have:

$$\eta_{col} = \frac{\eta_{\Gamma}(\omega \longrightarrow 0)}{a}\left[1 + \frac{R_S}{Z_{D-R}(\omega \longrightarrow 0)}\right]^{-1} \tag{23}$$

This equation points out the dependence of $EQE_{PV-Diff}$ and thus $IQE_{PV-Diff}$, on the diffusion length (through η_{Γ}),[57] but also on the ratio between the series resistance and the low-frequency limit of Z_{D-R}.

At this point is worthwhile to mention that the three transfer functions theoretically obtained comply with the relationship given in Equation (7), in all the scenarios presented in

this study. Therefore, the parameters obtained from the fitting of experimental data should be the same for the three modulated techniques.

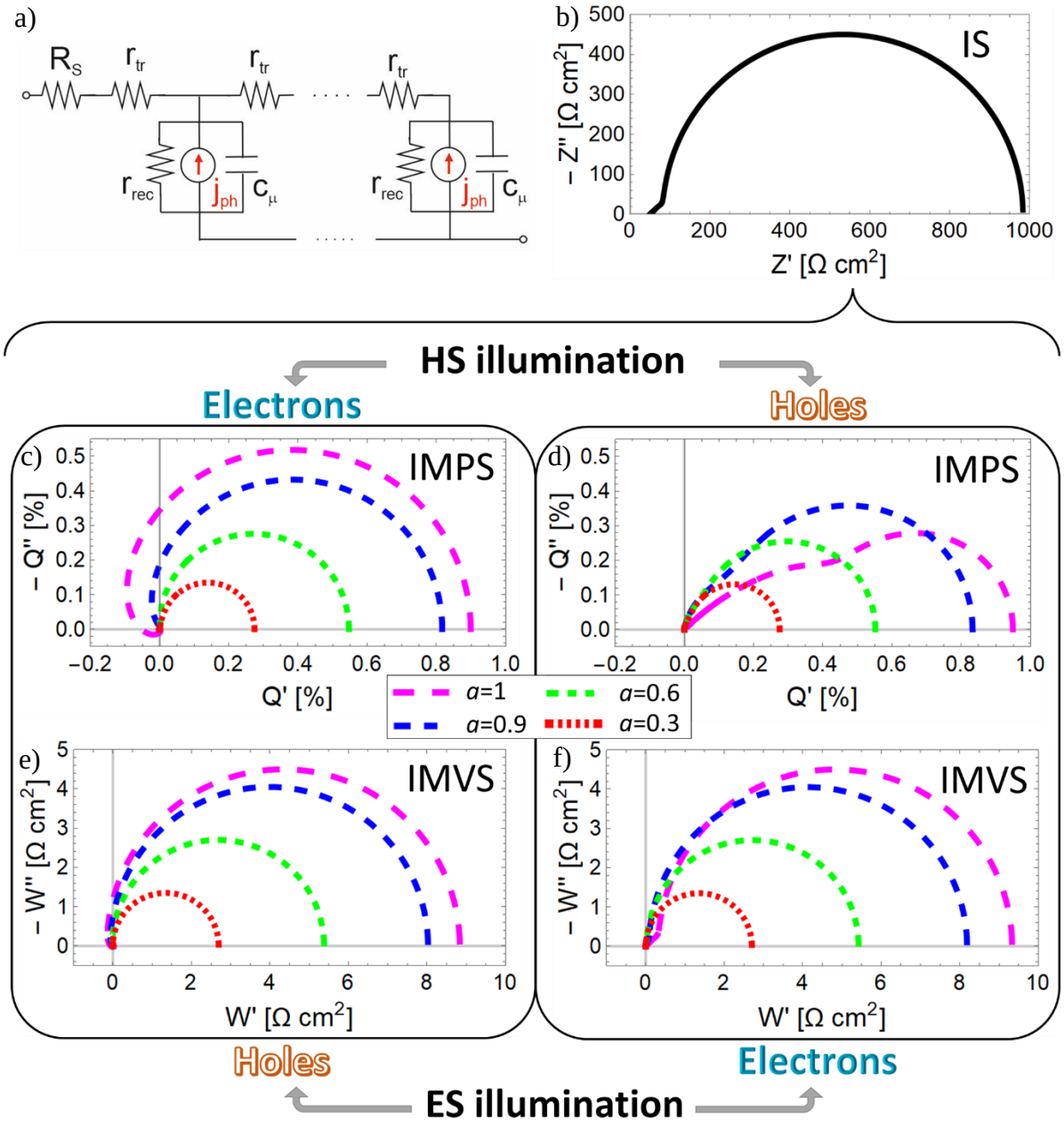

Figure 2. a) Equivalent circuit model for single carrier transport and recombination with distributed absorption, used to simulate b) IS, c)-d) IMPS and e)-f) IMVS spectra, with R_S = 50 Ω cm^2, R_{tr} = 100 Ω cm^2, ω_D = 450 rad/s, ω_{rec} = 50 rad/s and $\eta_{sep}\eta_{opt}$ = 100%. Considering either electrons or holes as diffusing species, with light reaching the device from the electron or hole collector sides ("ES" and "HS", respectively). The different plots represented in IMVS and IMPS correspond to different absorptance (a) as indicated in the legend.

7.3.3. Simulation of Transfer Functions

Figure 2b shows a typical spectrum of the IS response of the EC in **Figure 2a**, given by Equation (18). It is important to highlight that the shape of the IS spectrum is independent of parameters such as the absorptance (a), the illumination side and even the carrier species (electrons or holes), as long as the resistances (R_{tr}, R_{rec} and R_S) and the characteristic frequencies (ω_{rec} and ω_D) are kept constant.

Figure 2c to **2f** show the IMPS and IMVS simulations of Equations (19) and (20) for different absorptances. Considering HS illumination and electron diffusion and recombination, a characteristic feature is observed for the IMPS and IMVS responses (**Figure 2c** and **2e**): Q' and W' reach negative values at high frequencies. In contrast, for the same HS illumination, but for hole diffusion and recombination, the IMPS and IMVS spectra (**Figure 2d** and **2f**) do not present this characteristic feature. For this case, these spectra are more similar to the IS spectrum (**Figure 2b**), especially the IMVS spectrum. The electron and hole responses for ES illumination are inverted from those obtained for HS illumination. Thus, the diffusion and recombination of holes produce the spectra with Q' and W' entering the negative region at high frequencies (**Figure 2c** and **2e**), while for the electrons this feature is not present (**Figure 2d** and **2f**).

The effect of the decrease of a is clear in both IMPS simulations (**Figure 2c** and **2d**), mainly reducing the value of the low-frequency limit, as expected because this limit is the $EQE_{PV\text{-}Diff}$, see Equation (21).[20, 56] a has a similar effect on the IMVS simulations (**Figure 2e** and **2f**), as expected since the IS spectrum is independent of a, see Equation (7).

One of the most interesting results of **Section 7.3.2.1** is that, when both electrons and holes are diffusing, the IMVS transfer function, Equation (12), is the combination of both η_Γ^n and η_Γ^p, weighed by Z_n and Z_p respectively. From a practical point of view, this means that the IMVS spectra will be the sum of both **Figure 2e** and **Figure 2f**, multiplied by the electron and hole transport resistances, respectively. Something equivalent accounts for the IMPS spectra. This observation allows a qualitative characterization to identify the dominant diffusive species, by observing the IMPS and IMVS spectra, particularly if one of these resistances is much smaller than the other.

7.3.4. Experimental Results

In this section, we combine IS, IMPS and IMVS to characterize the optoelectronic properties of a porous Zr:$BiVO_4$ electrode used in a photoelectrochemical cell for water oxidation. **Figure 3** shows the cyclic voltammetry curves without illumination (black line) and under blue illumination (470 nm at 89 mW cm^{-2}, blue lines), for ES (solid lines) and HS (dashed lines) illumination. In this device, the ES illumination corresponds to illumination from the FTO side, while the HS illumination corresponds to illumination from the electrolyte side. **Figure S2** compares these measurements with the measurements made under 1 sun illumination (yellow lines). Under blue illumination, a higher j_{ext} is obtained since almost all the light is absorbed by the material (see **Figure S3**). Regardless of illuminating with 1 sun or with blue light, a higher j_{ext} is obtained for ES illumination, in good agreement with previous studies in $BiVO_4$ photoanodes.[58] We will show that the characterisation combining IS, IMPS and IMVS allows a deep understanding of the operating processes, and the differences between ES and HS lighting. In this work, we have performed this characterization under the same blue light illumination at 1.2 V vs RHE (grey line in **Figure 3**) and in the presence of 0.1 M Na_2SO_3 as hole scavenger in 0.1 M KPi buffer (pH=7.5).

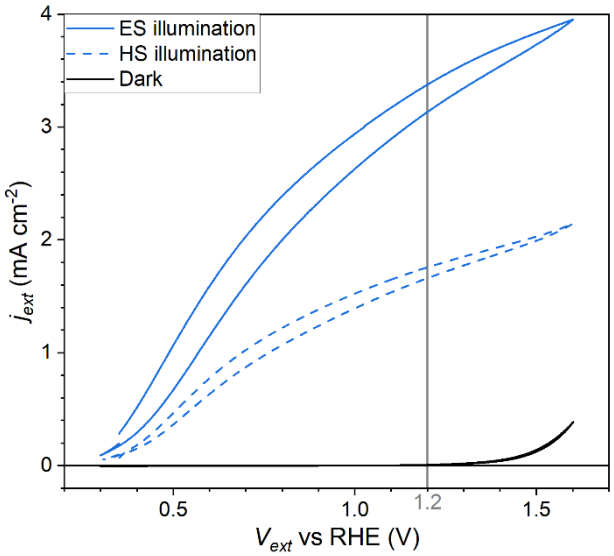

Figure 3. Cyclic voltammetry curves of a Zr:$BiVO_4$ electrode used in water splitting photoelectrochemical cell: without illumination (black line) and 89 mW cm^{-1} of blue light (blue lines); from the electron-collector side (ES, continues lines) and the hole-collector side (HS, dashed lines). IS, IMPS and IMVS are measured under the same illumination conditions and at 1.2 V vs RHE (grey line).

Figure 4 shows (solid black circles) the IS, IMPS and IMVS measured spectra of the Zr:$BiVO_4$ photoelectrochemical cell, exposed to HS illumination (a, c and e, respectively) and ES illumination (b, d and f, respectively). In all the spectra the frequency range is 5 kHz to 1 Hz. In **Figure 4e** and **Figure 4f**, the comparison of *W* with the product of *Z* and *Q* (see Equation (7)) is presented (empty red squares). In general, the experimental data are in good agreement with Equation (7). The major difference between *W* with the product of *Z* and *Q* is observed at lower frequencies, but this is not a limitation for our analysis because we are interested in the processes taking place at high frequencies. For this reason, we will focus on the experimental data until 20 Hz for our analysis.

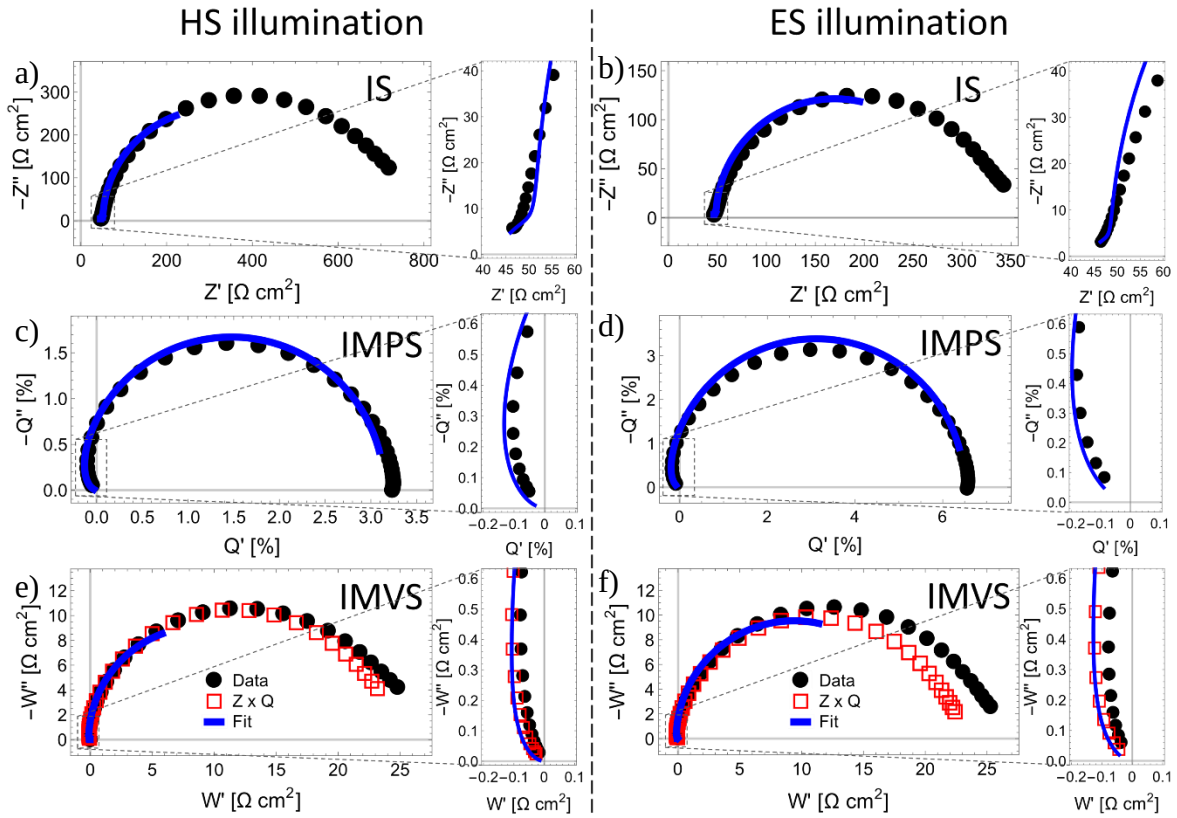

Figure 4. a) IS, c) IMPS and e) IMVS (with their respective zooms) measurement results (solid black circles) of a Zr:$BiVO_4$ electrochemical cell illuminated from the HS (see **Figure 1**). The spectra in b), d) and f) are the corresponding measurements for ES illumination. In e) and f) are compared *W* with the product of *Z* and *Q* (see Equation (7)), in red empty squares. The blue lines represent the simultaneous fittings of each set of measurements (IS, IMPS and IMVS), with the EC in **Figure 2a**. The measurements were performed at 89 mW cm^{-2} blue light (470nm) and 1.2 V vs RHE. The frequency range is, in all the spectra, from 5 kHz to 1 Hz.

Independently of the illumination side, the shapes of IS, IMVS and IMPS spectra (**Figure 4**), exhibit the same features, presenting the characteristic trend, reaching negative values at high frequencies for Q' and W'. The main differences between the experimental spectra for the different illumination sides relate to the low-frequency values obtained for IS and IMPS, which correspond to total resistance and the $EQE_{PV\text{-}Diff}$, respectively.[20, 56] By comparing **Figure 4** with **Figure 2** is not surprising that the experimental IS spectra are similar, since this technique gives the same response for the different scenarios. But, by comparing the experimental IMPS and IMVS spectra in **Figure 4** with the simulations in **Figure 2**, we can conclude that the extraction of electrons is determining the device performance when the illumination is reaching the device from the HS, while when the illumination is from the ES, the limiting carriers are the holes. This means that the other carrier species (holes for HS illumination and electrons for ES illumination) are transported well enough to have no significant effect on the IMPS and IMVS spectra, see Equation (12) and the corresponding discussion in **Section 7.3.3**. These results could be attributed to the fact that the carriers that dominate the spectral response have to travel longer distances as they are, on average, generated farther away from their extracting contact, while the other species can be more easily extracted.

Therefore, we analysed all the experimental spectra with the equivalent circuit in **Figure 2a**, whose transfer functions are given by Equations (18) and (16) for IS, and Equations (19) and (20) for IMPS and IMVS, restricted to $\eta_{I'}$ given by Equation (13). We used these equations to fit simultaneously the three measurements (IS, IMPS and IMVS), using Wolfram Mathematica software. The fitting results are shown as blue lines in **Figure 4**, having an excellent match with the experimental results. The extracted parameters, with variable errors below 10% and R^2 values above 0.999, are presented in **Table S2** and summarized in **Table 1**.

Table 1 Resulting parameters from the simultaneous fitting of the IS, IMPS and IMVS spectra for both HS and ES illumination in **Figure 4**, with the EC in **Figure 2a** and a = 98% obtained from direct measurement.

Illumination		HS	ES
Diffusion Species		Electrons	Holes
R_S	[Ω cm^2]	41.3 ± 0.2	43.2 ± 0.1
R_{tr}	[Ω cm^2]	31 ± 2	16.4 ± 0.4
D	[cm^2 s^{-1}]	(3.7 ± 0.3)× 10^{-6}	(5.7 ± 0.2)× 10^{-6}
ω_{rec}	[rad/s]	87 ± 4	155 ± 3
R_{rec}	[Ω cm^2]	520 ± 50	240 ± 10
C_μ	[μF cm^{-2}]	22 ± 2	27 ± 1
L	[μm]	2060 ± 70	1920 ± 30
η_{col}	[%]	90 ± 4	83 ± 2
η_{sep}	[%]	4.4 ± 0.2	10.9 ± 0.2
$IQE_{PV\text{-}Diff}$	[%]	4.0 ± 0.2	8.8 ± 0.3
$EQE_{PV\text{-}Diff}$	[%]	3.1 ± 0.1	6.5 ± 0.1

Comparing the parameters from the fitting of each illumination side in **Table 1**, we can first notice that the R_S values are practically identical, these resistances corresponding to the high-frequency limit of **Figure 4a** and **Figure 4b**. This is an expected result because this quantity is associated to transport properties external to the AL, which should be, in principle, independent of the illumination conditions.

Data obtained from the fitting of measurements with ES and HS illuminations indicate that the holes are transported more efficiently than the electrons, since they have a considerably lower R_{tr}, higher ω_D and consequently, a higher diffusion coefficient. In contrast, ω_{rec} of holes almost doubles that of electrons, which implies that they have almost half the lifetime of electrons. While chemical capacitance is similar, a bit larger for holes, the large difference in ω_{rec} is associated with the large difference observed in recombination resistance, which is much smaller for holes, indicating larger recombination. As consequence, the diffusion length, ~ 4 times the film thickness, is very similar in the two cases, slightly larger for the electrons.

These results are consistent with previous studies. In fact, ω_{rec} has been measured for $BiVO_4$ photoanodes using IMPS, achieving values around 100 rad/s, which are in good agreement with the values reported in Table 1.[45, 59] D is proportional to the carrier mobility (μ) trough the equation $D = kT\mu/q$, whereby we obtained electron and hole mobility values of 1.4×10^{-4} and 2.2×10^{-4} $cm^2\ V^{-1}\ s^{-1}$, respectively (see **Table S2**). Similar values were reported by Abdi and co-workers for the mobility of W-doped $BiVO_4$, suggesting that Zr and W doping could have a similar effect on the photoanode. Furthermore, in that work, lower mobility values for HS illumination (~30%) were also reported.[60] However, the corresponding characteristic times in that article were in the ns order, which yields to diffusion lengths in the nm order, which in our case would yield to the impossibility of collecting current because our thickness is several orders of magnitude greater. Those measurements were performed on films, without selective contacts, and this difference could be the reason for a much shorter carrier lifetime than the one presented in **Table 1**.

Table 1 shows, in both cases, η_{col} smaller than 100%, which is the value usually considered under hole scavenger conditions (the present case).[23] For illumination from the ES, η_{col} is smaller than from HS, in good agreement with diffusion length. This result might suggest a smaller j_{ext} for ES illumination which is contrary to the experimental measurements (**Figure 3**). The reason for this behaviour is that, as seen in **Table 1**, the charge separation efficiency for HS illumination is only 4.4% while for ES it reaches a value of 10.9%. Therefore, as the absorptance is 98% in both cases and the difference in the optical efficiency is very small (see **Table S2** in SI), it can be concluded that the main limitation to extract absorbed light is η_{sep}. As a result, see Equation (21), the $EQE_{PV\text{-}Diff}$, is only 6.5% and 3.1% for ES and HS illumination, respectively, which is in line with the low-frequency limit of the IMPS spectra observed in **Figure 3**. Similar values have been reported in the literature for the *EQE* of these devices for blue light (470nm).[23]

A possible origin of the differences between the η_{sep} obtained in each case may be related to the presence of structural defects, mainly oxygen vacancies, on the surface of $BiVO_4$, as it has been extensively reported.[61-63] These defects can act as recombination centres, known as surface traps, that could ultimately decrease the η_{sep}.[64-66] Indeed, surface recombination was been reported as the main limiting process on the performance of $BiVO_4$ photoanodes.[45, 67] When illuminating from the HS, the photogeneration is higher near this trap-rich interface which could act as internal recombination centres, thus reducing η_{sep}. Another possible origin is the higher conductivity found for holes which could help to separate carriers more

efficiently. A more detailed analysis of the origin of the differences in η_{sep} is beyond the scope of this paper and will be the target of future works.

In summary, we have shown here that the combination of the IS, IMPS and IMVS measurements, followed by an appropriate analysis method, allows a detailed characterization of the optoelectronic processes in the Zr:$BiVO_4$ photoanodes. This procedure can be used for the characterization of other photoconversion devices and electrodes, and it can be also extended for the analysis of the changes produced by varying the external voltage, the current or the illumination conditions.

7.3.5. Conclusions

In this work, we establish the theoretical basis and a practical method for combining IS, IMPS and IMVS to characterise photoconversion devices with distributed photogeneration, recombination and diffusion. The potential for this combination was demonstrated by comparing the possible responses of the three techniques for such devices. The practical application of this method is based on the simultaneous fitting of the experimental data, using the same model and parameters. The relationship between the optical and electrical properties is key for this analysis. The application of this method to a Zr:$BiVO_4$ photoanode allowed, first, to identify the electrons as the carrier controlling the response of the device when the illumination arrives from the hole-collector side (the electrolyte), while the holes assume this role when the sample is illuminated from the electron-collector side (the FTO). Then, it provided a detailed quantitative characterisation of the photoconversion parameters, that served to identify the separation efficiency as the main limitation to the performance of this device, which was 10.9% for electron- and 4.4% for hole-collector side illumination. Other parameters, such as the recombination, transport resistance, diffusion coefficient and diffusion length of each carrier, showed to play a minor role in the differences in device performance, including extracted current and external quantum efficiency found for each illumination side.

7.3.6. Experimental Section

Zr:$BiVO_4$ electrodes were prepared through a previously reported two-step method.[23, 68] The first step is the electrodeposition of metallic Bi on fluorine-doped tin oxide (FTO, 14 Ω sq^{-1})-coated glass substrate. The second step is the addition of the vanadium precursor by drop casting technique. According to a previous optimization process, 2.5 mol% of $ZrCl_2 \cdot 8H_2O$ (Sigma-Aldrich) was added to the Bi^{3+} plating bath.[69]

The optical properties were measured in a Lambda 1050+ spectrophotometer (Perkin Elmer), with $BaSO_4$ as a white reference. The optical efficiencies were calculated as

$$\eta_{opt}^{HS} = T_{Quartz}(1 - R_{HS})$$

$$\eta_{opt}^{ES} = T_{Quartz}(1 - R_{ES})(1 - a_{FTO})$$

where the superscript refers to the HS and ES illuminations, T_{Quartz} is the transmittance of the quartz cuvette, a_{FTO} is the absorptance of the FTO, R_{HS} and R_{ES} are the reflectances of the measured film when light reaches from HS and ES, respectively. On the other hand, the absorptance (a) was calculated by considering the photons that are not reflected or absorbed in the FTO

$$a = 1 - \frac{T_{HS}}{1 - R_{HS}} \frac{1}{1 - a_{FTO}}$$

with T_{HS} the transmittance of the measured film when light reaches from HS. These variables are shown in **Figure S3**.

The photoelectrochemical characterization of the electrodes was performed in the dark and under illumination (100 mW cm^{-2} of white light and 89 mW cm^{-2} of blue light) in a 0.1 M Potassium phosphate buffer solution of pH 7.5, including 0.1 M Na_2SO_3 solution as a hole scavenger. The electrochemical cell was composed of the working electrode, an Ag/AgCl (3 M KCl) reference electrode and a Pt wire as a counter electrode. All the potentials were referred to the RHE through the Nernst equation:

$$V_{RHE} = V_{Ag/AgCl} + V_{Ag/AgCl}^{0} + 0.059pH$$

where

$$V_{Ag/AgCl}^{0}(3\ M\ KCl) = 0.199V$$

The IS, IMPS and IMVS measurements were performed with an Autolab PGSTAT302 equipped with a FRA32M module and combined with the LED driver. The three techniques were measured under 89 mW/cm^2 light intensity generated by an array of three blue LEDs (Philips LUMILEDS LXML-PB01-0040 with 470nm peak). For the IS measurement, a 20 mV AC perturbation was applied. For IMPS and IMVS, an AC perturbation equal to 10% of the light flux was applied. The frequency range was for the three techniques from 5 kHz to 1

Hz. The measurements were performed at a bias voltage of 1.2 V vs RHE. The analysis of all spectra was done using MultiNonlinearModelFit function of Wolfram Mathematica software.

The morphology of the sample, including the thickness, was examined by field-emission scanning electron microscopy (FE-SEM) with a JSM-700F JEOL FEG-SEM system (Tokyo, Japan) equipped with an INCA 400 Oxford EDS analyser (Oxford, UK) operating at 15 kV. Before the FE-SEM experiment, the samples were sputtered with a 2 nm thick layer of Pt.

Supporting Information

Supporting Information is available from the Wiley Online Library or from the authors. Raw experimental data are available in a public repository.

Author contributions

F.F.S. provided the original idea and supervised the research. A.O.A. carried out the calculations, simulations, experimental measurements, data analysis and wrote the first version of the manuscript. L.M.G. fabricated the samples. F.F.S., E.M.M., M.G.T. and S.G. contributed to validating, reviewing and editing the manuscript.

Acknowledgements

This project has received funding from the European Union's Horizon 2020 MSCA Innovative Training Network under grant agreement No. 764787. The authors thank the support from project PID2020-116093RB-C41 funded by MCIN/AEI/10.13039/501100011033/ and from Generalitat Valenciana under the project PROMETEO/2020/028 for financial support. Dr Ana Gutiérrez-Blanco and Serveis Centrals at UJI (SCIC) are also acknowledged for SEM characterization.

ORCID

Agustin O. Alvarez: 0000-0002-0920-5390

Miguel García-Tecedor: 0000-0002-9664-4665

Laura Montañés: 0000-0002-1076-013X

Elena Mas Marzá: 0000-0002-2308-0635

Sixto Giménez: 0000-0002-4522-3174

Francisco Fabregat-Santiago: 0000-0002-7503-1245

References

[1] J. H. Montoya, L. C. Seitz, P. Chakthranont, A. Vojvodic, T. F. Jaramillo, J. K. Nørskov, *Nat. Mater.* **2017**, 16, 70.

[2] M. G. Walter, E. L. Warren, J. R. McKone, S. W. Boettcher, Q. Mi, E. A. Santori, N. S. Lewis, *Chem. Rev.* **2010**, 110, 6446.

[3] A. O. Alvarez, R. Arcas, C. A. Aranda, L. Bethencourt, E. Mas-Marzá, M. Saliba, F. Fabregat-Santiago, *J. Phys. Chem. Lett.* **2020**, 11, 8417.

[4] N. Klipfel, A. O. Alvarez, H. Kanda, A. A. Sutanto, C. Igci, C. Roldán-Carmona, C. Momblona, F. Fabregat-Santiago, M. K. Nazeeruddin, *ACS Appl. Energy Mater.* **2022**, 5, 1646.

[5] V. Babu, R. Fuentes Pineda, T. Ahmad, A. O. Alvarez, L. A. Castriotta, A. Di Carlo, F. Fabregat-Santiago, K. Wojciechowski, *ACS Appl. Energy Mater.* **2020**, 3, 5126.

[6] L. M. Peter, *Chem. Rev.* **1990**, 90, 753.

[7] S. Ravishankar, A. Riquelme, S. K. Sarkar, M. Garcia-Batlle, G. Garcia-Belmonte, J. Bisquert, *J. Phys. Chem. C* **2019**, 123, 24995.

[8] A. Riquelme, F. E. Gálvez, L. Contreras-Bernal, H. Míguez, J. A. Anta, *J. Appl. Phys.* **2020**, 128, 133103.

[9] G. Schlichthörl, S. Y. Huang, J. Sprague, A. J. Frank, *J. Phys. Chem. B* **1997**, 101, 8141.

[10] R. Kern, R. Sastrawan, J. Ferber, R. Stangl, J. Luther, *Electrochim. Acta* **2002**, 47, 4213.

[11] F. Fabregat-Santiago, E. M. Barea, S. Giménez, J. Bisquert, *Impedance Spectroscopy in Molecular Devices* in *Molecular Devices for Solar Energy Conversion and Storage*, (Eds: H. Tian, G. Boschloo, A. Hagfeldt), Springer Singapore, Singapore **2018**, 12.

[12] J. Bisquert, F. Fabregat-Santiago, *Impedance spectroscopy: a general introduction and application to dye-sensitized solar cells* in *Dye-sensitized Solar Cells*, (Ed: K. Kalyanasundaram), CRC Press, Switzerland **2010**, 12.

[13] E. Ponomarev, L. Peter, *J. Electroanal. Chem.* **1995**, 396, 219.

[14] L. M. Peter, *J. Solid State Electrochem.* **2013**, 17, 315.

[15] O. Almora, D. Miravet, G. J. Matt, G. Garcia-Belmonte, C. J. Brabec, *Appl. Phys. Lett.* **2020**, 116, 013901.

[16] O. Almora, Y. Zhao, X. Du, T. Heumueller, G. J. Matt, G. Garcia-Belmonte, C. J. Brabec, *Nano Energy* **2020**, 75, 104982.

[17] D. Klotz, D. S. Ellis, H. Dotan, A. Rothschild, *PCCP* **2016**, 18, 23438.

[18] L. Bertoluzzi, J. Bisquert, *J. Phys. Chem. Lett.* **2017**, 8, 172.

[19] S. Ravishankar, C. Aranda, S. Sanchez, J. Bisquert, M. Saliba, G. Garcia-Belmonte, *J. Phys. Chem. C* **2019**, 123, 6444.

[20] A. O. Alvarez, S. Ravishankar, F. Fabregat-Santiago, *Small Methods* **2021**, 5, 2100661.

[21] L. Dloczik, O. Ileperuma, I. Lauermann, L. Peter, E. Ponomarev, G. Redmond, N. Shaw, I. Uhlendorf, *J. Phys. Chem. B* **1997**, 101, 10281.

[22] A. Bou, H. Āboliņš, A. Ashoka, H. Cruanyes, A. Guerrero, F. Deschler, J. Bisquert, *ACS Energy Lett.* **2021**, 6, 2248.

[23] M. N. Shaddad, D. Cardenas-Morcoso, P. Arunachalam, M. García-Tecedor, M. A. Ghanem, J. Bisquert, A. Al-Mayouf, S. Gimenez, *J. Phys. Chem. C* **2018**, 122, 11608.

[24] W. Choi, H.-C. Shin, J. M. Kim, J.-Y. Choi, W.-S. Yoon, *J. Electrochem. Sci. Technol* **2020**, 11, 1.

[25] W. Peng, C. Aranda, O. M. Bakr, G. Garcia-Belmonte, J. Bisquert, A. Guerrero, *ACS Energy Lett.* **2018**, 3, 1477.

[26] J. Bisquert, *J. Phys. Chem. B* **2002**, 106, 325.

[27] J. Bisquert, G. Garcia-Belmonte, F. Fabregat-Santiago, N. S. Ferriols, P. Bogdanoff, E. C. Pereira, *J. Phys. Chem. B* **2000**, 104, 2287.

[28] F. Fabregat-Santiago, J. Bisquert, G. Garcia-Belmonte, G. Boschloo, A. Hagfeldt, *Sol. Energ. Mat. Sol. C.* **2005**, 87, 117.

[29] A. Bou, A. Pockett, H. Cruanyes, D. Raptis, T. Watson, M. J. Carnie, J. Bisquert, *APL Materials* **2022**, 10, 051104.

[30] J. Halme, K. Miettunen, P. Lund, *J. Phys. Chem. C* **2008**, 112, 20491.

[31] L. Bay, K. West, *Sol. Energ. Mat. Sol. C.* **2005**, 87, 613.

[32] J. Halme, *PCCP* **2011**, 13, 12435.

[33] T. W. Kim, K.-S. Choi, *Science* **2014**, 343, 990.

[34] J. Su, L. Guo, N. Bao, C. A. Grimes, *Nano Lett.* **2011**, 11, 1928.

[35] J. K. Cooper, S. Gul, F. M. Toma, L. Chen, P.-A. Glans, J. Guo, J. W. Ager, J. Yano, I. D. Sharp, *Chem. Mater.* **2014**, 26, 5365.

[36] A. Walsh, Y. Yan, M. N. Huda, M. M. Al-Jassim, S.-H. Wei, *Chem. Mater.* **2009**, 21, 547.

[37] W. Qiu, S. Xiao, J. Ke, Z. Wang, S. Tang, K. Zhang, W. Qian, Y. Huang, D. Huang, Y. Tong, S. Yang, *Angew. Chem. Int. Ed.* **2019**, 58, 19087.

[38] Y. Ma, A. Kafizas, S. R. Pendlebury, F. Le Formal, J. R. Durrant, *Adv. Funct. Mater.* **2016**, 26, 4951.

[39] B. J. Trześniewski, I. A. Digdaya, T. Nagaki, S. Ravishankar, I. Herraiz-Cardona, D. A. Vermaas, A. Longo, S. Gimenez, W. A. Smith, *Energ. Environ. Sci.* **2017**, 10, 1517.

[40] C. Cheng, Q. Fang, S. Fernandez-Alberti, R. Long, *J. Phys. Chem. Lett.* **2021**, 12, 3514.

[41] X. Shi, I. Herraiz-Cardona, L. Bertoluzzi, P. Lopez-Varo, J. Bisquert, J. H. Park, S. Gimenez, *PCCP* **2016**, 18, 9255.

[42] M. Zhou, J. Bao, Y. Xu, J. Zhang, J. Xie, M. Guan, C. Wang, L. Wen, Y. Lei, Y. Xie, *ACS Nano* **2014**, 8, 7088.

[43] D. Cardenas-Morcoso, R. Ifraemov, M. García-Tecedor, I. Liberman, S. Gimenez, I. Hod, *J. Mater. Chem. A* **2019**, 7, 11143.

[44] F. S. Hegner, I. Herraiz-Cardona, D. Cardenas-Morcoso, N. López, J.-R. Galán-Mascarós, S. Gimenez, *ACS Appl. Mater. Inter.* **2017**, 9, 37671.

[45] C. Zachäus, F. F. Abdi, L. M. Peter, R. van de Krol, *Chem. Sci.* **2017**, 8, 3712.

[46] R. Irani, P. Plate, C. Höhn, P. Bogdanoff, M. Wollgarten, K. Höflich, R. van de Krol, F. F. Abdi, *J. Mater. Chem. A* **2020**, 8, 5508.

[47] E. Y. Liu, J. E. Thorne, Y. He, D. Wang, *ACS Appl. Mater. Inter.* **2017**, 9, 22083.

[48] M. Antuch, P. Millet, A. Iwase, A. Kudo, *Appl. Catal. B-Environ.* **2018**, 237, 401.

[49] D. Cardenas-Morcoso, A. Bou, S. Ravishankar, M. García-Tecedor, S. Gimenez, J. Bisquert, *ACS Energy Lett.* **2020**, 5, 187.

[50] Z. Tian, P. Zhang, P. Qin, D. Sun, S. Zhang, X. Guo, W. Zhao, D. Zhao, F. Huang, *Adv. Eng. Mater.* **2019**, 9, 1901287.

[51] Y. Zhang, X. Chen, F. Jiang, Y. Bu, J.-P. Ao, *ACS Sustain. Chem. Eng.* **2020**, 8, 9184.

[52] M. Kan, D. Xue, A. Jia, X. Qian, D. Yue, J. Jia, Y. Zhao, *Appl. Catal. B-Environ.* **2018**, 225, 504.

[53] A. Bou, A. Pockett, D. Raptis, T. Watson, M. J. Carnie, J. Bisquert, *J. Phys. Chem. Lett.* **2020**, 11, 8654.

[54] J. Bisquert, G. Garcia-Belmonte, F. Fabregat-Santiago, P. R. Bueno, *J. Electroanal. Chem.* **1999**, 475, 152.

[55] J. Bisquert, G. Garcia-Belmonte, F. Fabregat-Santiago, A. Compte, *Electrochem. Commun.* **1999**, 1, 429.

[56] S. Ravishankar, C. Aranda, P. P. Boix, J. A. Anta, J. Bisquert, G. Garcia-Belmonte, *J. Phys. Chem. Lett.* **2018**, 9, 3099.

[57] L. Bertoluzzi, S. Ma, *PCCP* **2013**, 15, 4283.

[58] Y. Liang, T. Tsubota, L. P. A. Mooij, R. van de Krol, *J. Phys. Chem. C* **2011**, 115, 17594.

[59] J. A. Seabold, K. Zhu, N. R. Neale, *PCCP* **2014**, 16, 1121.

[60] F. F. Abdi, T. J. Savenije, M. M. May, B. Dam, R. van de Krol, *J. Phys. Chem. Lett.* **2013**, 4, 2752.

[61] N. Österbacka, F. Ambrosio, J. Wiktor, *J. Phys. Chem. C* **2022**, 126, 2960.

[62] W. Wang, P. J. Strohbeen, D. Lee, C. Zhou, J. K. Kawasaki, K.-S. Choi, M. Liu, G. Galli, *Chem. Mater.* **2020**, 32, 2899.

[63] R. Fernández-Climent, S. Giménez, M. García-Tecedor, *Sustainable Energy Fuels* **2020**, 4, 5916.

[64] Q. Shi, S. Murcia-López, P. Tang, C. Flox, J. R. Morante, Z. Bian, H. Wang, T. Andreu, *ACS Catal.* **2018**, 8, 3331.

[65] F. Tang, W. Cheng, H. Su, X. Zhao, Q. Liu, *ACS Appl. Mater. Inter.* **2018**, 10, 6228.

[66] S. Selim, E. Pastor, M. García-Tecedor, M. R. Morris, L. Francàs, M. Sachs, B. Moss, S. Corby, C. A. Mesa, S. Gimenez, A. Kafizas, A. A. Bakulin, J. R. Durrant, *J. Am. Chem. Soc.* **2019**, 141, 18791.

[67] D. K. Zhong, S. Choi, D. R. Gamelin, *J. Am. Chem. Soc.* **2011**, 133, 18370.

[68] D. Kang, Y. Park, J. C. Hill, K.-S. Choi, *J. Phys. Chem. Lett.* **2014**, 5, 2994.

[69] M. N. Shaddad, M. A. Ghanem, A. M. Al-Mayouf, S. Gimenez, J. Bisquert, I. Herraiz-Cardona, *ChemSusChem* **2016**, 9, 2779.

7.4. Supporting Information

New Views on Carrier Diffusion and Recombination by Combining Small Perturbation Techniques: Application to $BiVO_4$ Photoelectrodes

Agustin O. Alvarez,[a] Miguel García-Tecedor,[b] Laura Montañés,[a] Elena Mas Marzá,[a] Sixto Giménez,[a] and Francisco Fabregat-Santiago[a]**

[a]Institute of Advanced Materials, Universitat Jaume I, Castellón de la Plana 12006, Spain
[b]Photoactivated Processes Unit, IMDEA Energy Institute. Av. Ramón de la Sagra, 3. 28935 Móstoles, Spain.

E-mail: agalvare@uji.es; fabresan@uji.es

7.4.1. Single Carrier Diffusion

As mentioned in **Section 7.3.2.2**, in a device with distributed photogeneration and limited by the diffusion and recombination of electrons, the electron carrier density (n) can be described by:

$$\frac{dn}{dt} = D\frac{d^2n}{dx^2} - \frac{n}{\tau_{rec}} + G(x,t) \quad \text{(S1)}$$

Where D is the diffusion coefficient, τ_{rec} is the lifetime of the diffusion carriers and $G(x,t)$ is the probability of generating free charges for the incident light. The three small-perturbation techniques are measured in the small-perturbation regime, denoted by $\tilde{}$. Considering totally reflecting boundary condition at the hole-collector side interface ($x = d$)[1]

$$\frac{d\tilde{n}}{dx}(x = d) = 0 \quad \text{(S2)}$$

The extracted electrical current density (measured externally) is given by[2]

$$\tilde{j}_{ext} = qD\frac{d\tilde{n}}{dx}(x = 0) \quad \text{(S3)}$$

As mentioned in the main text, the internal voltage is the difference between the electron and hole Femi levels ($V_{int} = E_{Fn} - E_{Fp}$). Here we are considering that holes can be extracted much better than electrons, whereby the small perturbation only changes the charge density of the electrons an thus its Fermi level, therefore[1, 2]

$$\tilde{V}_{int} = \tilde{E}_{Fn}/q = k_{vol}\tilde{n}(x = 0) \quad \text{(S4)}$$

where k_{vol} is a constant which, for the final result we can substitute it by

$$R_{tr} = \frac{d\ k_{vol}}{q\ D} \quad \text{(S5)}$$

If the species that dominate transport and recombination are the holes instead of the electrons, the hole carrier density (p) can be described similarly to Equation (15):

$$\frac{dp}{dt} = D\frac{d^2p}{dx^2} - \frac{p}{\tau_{rec}} + G(x,t) \quad \text{(S6)}$$

But the boundary conditions are modified. The totally reflecting boundary condition, in this case, is in the electron-collector side interface ($x = 0$)

$$\frac{d\tilde{p}}{dx}(x = 0) = 0 \quad \text{(S7)}$$

The electrical current density and the internal voltage becomes

$$\tilde{j}_{ext} = qD\frac{d\tilde{p}}{dx}(x = d) \quad \text{(S8)}$$

$$\tilde{V}_{int} = -\tilde{E}_{Fp}/q = k_{vol}\tilde{p}(x = d) \quad \text{(S9)}$$

In both cases, the applied voltage (measured) and the internal voltage can generally be correlated with the external current by a general impedance

$$Z_s\tilde{J}_{ext} = \tilde{V}_{int} - \tilde{V}_{app} \quad \text{(S10)}$$

7.4.2. "Effective Absorptance"

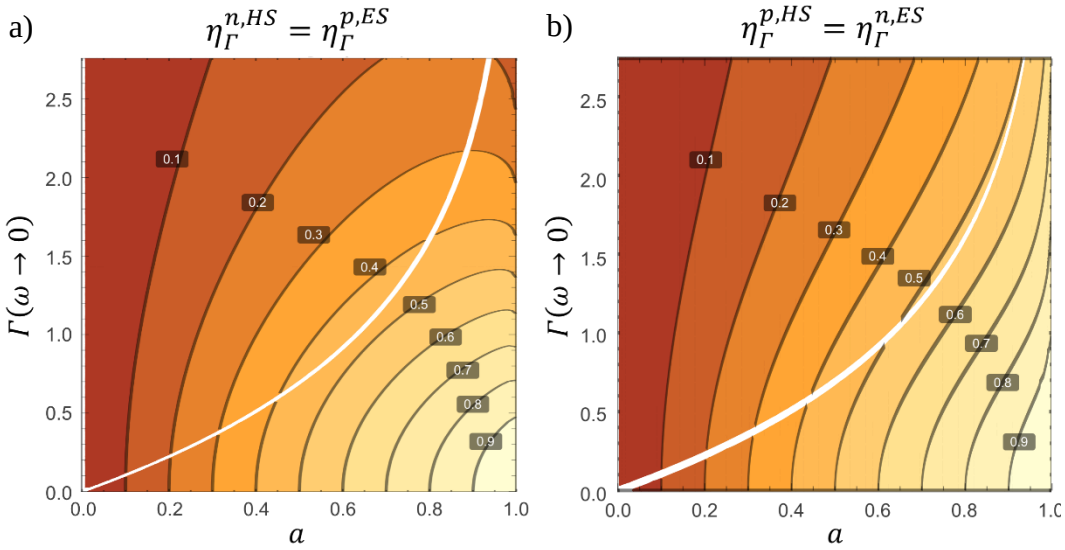

Figure S1. Simulations of the low-frequency limit of a) $\eta_\Gamma^{n,HS} = \eta_\Gamma^{p,ES}$ and b) $\eta_\Gamma^{p,HS} = \eta_\Gamma^{n,ES}$ defined by Equations (13) and (14), respectively. The white line represents the limit $\Gamma = A = -log(1-a)$, where η_Γ are not defined in equations (12) and (13).

7.4.3. Equivalences Between Transfer Functions

7.4.3.1. Within this article

When the general impedances in **Figure 1b** are reduced to

$$Z_S = R_S \tag{S11}$$

$$z_p = Z_p/d = 0 \tag{S12}$$

$$z_n = Z_n/d = r_{tr} \tag{S13}$$

$$z_{rec} = Z_{rec}d = \left(\frac{1}{r_{rec}} + i\omega c_\mu\right)^{-1} \tag{S14}$$

with d the film thickness, the equivalent circuit in **Figure 2a**, is obtained.

The relationships between total (capital letters) and distributed (lower case letters) transport resistance, recombination resistance and chemical capacitance with the recombination and diffusion frequencies are given by

$$R_{tr} = r_{tr}d \tag{S15}$$

$$R_{rec} = \frac{r_{rec}}{d} = R_{tr}\frac{\omega_D}{\omega_{rec}} = R_{tr}\omega_D\tau_{rec} \tag{S16}$$

$$C_\mu = c_\mu d = \frac{d}{r_{rec}\omega_{rec}} \tag{S17}$$

The diffusion coefficient is given by

$$D = \omega_D d^2 \tag{S18}$$

The Diffusion length may be obtained from several combinations of these parameters

$$L = d\sqrt{\omega_D\tau_{rec}} = d\sqrt{\frac{\omega_D}{\omega_{rec}}} = d\sqrt{\frac{R_{rec}}{R_{tr}}} \tag{S19}$$

and, according to Equation (17), it is related to the low-frequency limit of Γ through

$$L = \frac{d}{\Gamma(\omega \to 0)} \tag{S20}$$

7.4.3.2.With previous articles

Table S1 Comparison of notation used in different articles. Here: Z, total impedance, $Z_{D\text{-}R}$, impedance of the diffusion and recombination model; Q, IMPS transfer function; W, IMVS transfer function; ϕ, photon flux; α, absorption coefficient; j_{inj}, injected current density; L, carrier diffusion length; ω_D, carrier diffusion frequency or transport frequency; z_n and z_p, distributed electron and hole impedance per unit length; z_{rec}, distributed recombination impedance length; ω_k, recombination frequency; a, absorptance; η_{sep} and η_{col}, separation and collection efficiencies. In other papers: i, current[2-5] but also photon flux[6]; i_p, local photogeneration current. A, surface area; k_{ext}, extraction rate constant.

Here	***Peter[7]***	***Bisquert[2, 3]***	***West[6]***	***Halme[4, 5]***	***Bisquert21[8]***
Z	-	-	-	Z_{CELL}	-
$Z_{D\text{-}R}$	-	Z	Z_{EC}	Z_{TiO2}	-
Q^*	Φ, J_{photo}[9]	-	$IMPS$	F^*_{IMPS}	Q
W	δV_{photo}[9]	-	$IMVS$	F^*_{IMVS}	-
ϕ, ϕ_{int}	- , I_0	-	i_0, -	Φ, -	ϕ, -
G	$\alpha I_0 e^{-\alpha x}$	-	i_p/q	g	G
α	α	-	A	$\alpha = \alpha_D$	α
d	d	L	l	d	d
$j_{ext} = -j_{inj}$	j	-i_0/A,[3] -i/A[2]	$i_e(0)$	i_{CELL}/A	j_e
V_{app}	V	φ_T,[3] E[2]	π/φ	$-V_{CELL}$	-
L	L	L_n	L_n	L	L_n
D	D	D_1, D_e,[3] D[2]	D_n	D	D_n
ω_D	-	ω_d	-	-	ω_d
z_n, z_p	-	χ_1, χ_2,[3] χ_m[2]	Z_e, Z_i	-	-
z_{rec}	-	ζ,[3] ζ_m[2]	Z_S	-	-
r_{rec}, c_μ	-	r_k, c_m	R_S, C_S	r_{REC}, c_μ	-
r_{tr}**	-	r_1, r_2,[3] r_m[2]	R_e, R_i	r_T	-
R_{rec}, C_μ, R_{tr}	-	R_k, C_f, R_W	-	R_{REC} , - , R_T	-
$\tau_{rec} = \frac{1}{\omega_{rec}}$	τ	$\tau_n = \frac{1}{k} = \frac{1}{\omega_k}$	τ_n	τ	$\tau_n = \frac{1}{\omega_{rec}}$
Γ	$d\,\gamma$	L/λ	$\alpha\, l$	$d\,\gamma$	$z\frac{d}{L_n}$
a	-	-	-	η_{LH}	-
η_{sep}, η_{col}	-	-	B, -	η_{INJ},η_{COL}	-
k_{vol}	-	$\left(\frac{dE}{dc}\right)_0$	-	-	-
$\frac{k_{vol}}{qZ_S} = \frac{R_{tr}D}{Z_S d}$	k_{ext}	-	-	k_{EXT}	-

* Other notations for IMPS are used, such as H.[10]

** Despite not specifically indicated, r_{tr} refers to electrons or holes depending on the case discussed in the text

7.4.4. Cyclic voltammetry

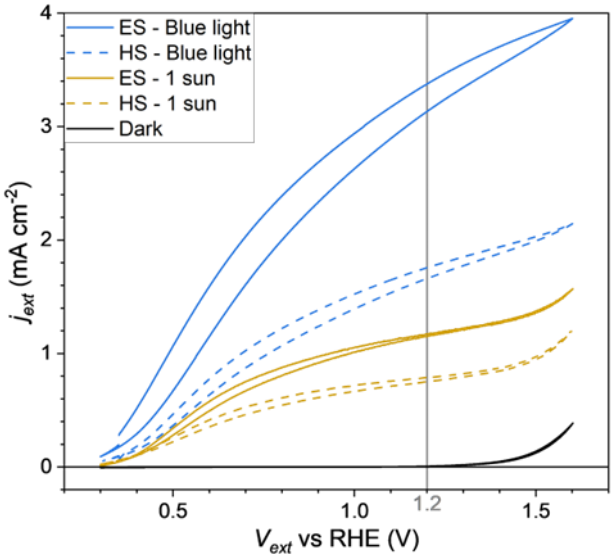

Figure S2. Cyclic voltammetry curves of a Zr:$BiVO_4$ electrode used in water splitting photoelectrochemical cell: without illumination (black line), illuminating with 1 sun (yellow lines) and 89 mW cm^{-1} of blue light (blue lines); from the electron-collector side (ES, continues lines) and the hole-collector side (HS, dashed lines). IS, IMPS and IMVS are measured under the same blue illumination conditions and at 1.2 V vs RHE (grey line).

7.4.5. Absorption, Transmittance and Reflectance

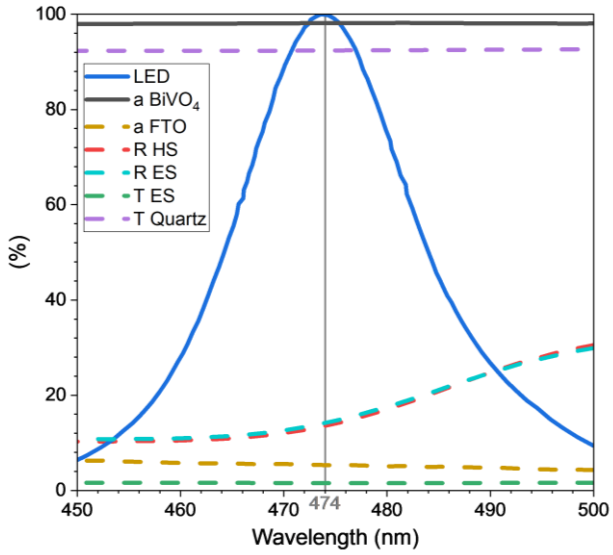

Figure S3. Absorptance (black line), reflectance (read and cyan dashed line) and transmittance (green dashed line) of the Zr:$BiVO_4$, where ES and HS refer to the illumination incidence. The absorbance of the FTO (yellow dashed line), the transmittance of the quartz cuvette (purple dashed line) and the emission peak of the LED used to measure IS, IMPS and IMVS (blue line).

7.4.6. SEM image

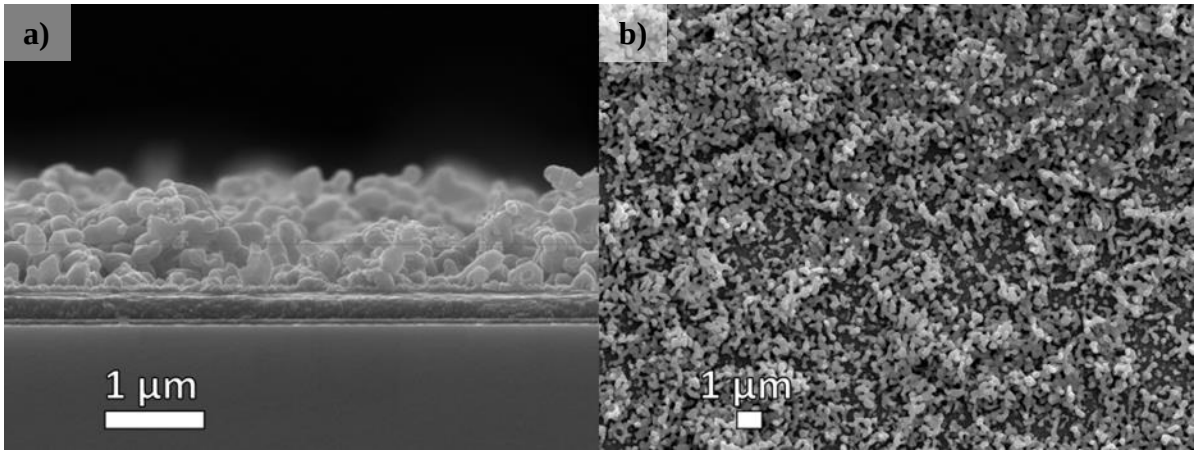

Figure S4. a) Cross-section and b) top-view SEM image of the Zr:$BiVO_4$ film.

7.4.7. Fitting Parameters

Table S2 Resulting parameters from the simultaneous fitting of the IS, IMPS and IMVS spectra for both cases HS and ES illumination in **Figure 4**, with the EC in **Figure 2a**.

Illumination		HS	ES
Diffusion Species		Electrons	Holes
R_S	[Ω cm^2]	41.3 ± 0.2	43.2 ± 0.1
R_{tr}	[Ω cm^2]	31 ± 2	16.4 ± 0.4
R_{rec}	[Ω cm^2]	520 ± 50	240 ± 10
C_μ	[μF cm^{-2}]	22 ± 2	27 ± 1
ω_{rec}	[rad/s]	87 ± 4	155 ± 3
τ_{rec}	[ms]	11.5 ± 0.5	6.4 ± 0.14
ω_D	[rad/s]	1480 ± 120	2290 ± 80
L/d	[ ]	4.1 ± 0.1	3.8 ± 0.1
D	[cm^2 s^{-1}]	(3.7 ± 0.3)× 10^{-6}	(5.7 ± 0.2)× 10^{-6}
L	[nm]	2060 ± 70	1920 ± 30
μ	[cm^2 V^{-1} s^{-1}]	(1.44 ± 0.12)× 10^{-4}	(2.22 ± 0.08)× 10^{-4}
a	[%]	98.2 ± 0.1	
η_{opt}	[%]	79.9 ± 0.1	75.1 ± 0.1
η_{col}	[%]	90 ± 4	83 ± 2
η_{sep}	[%]	4.4 ± 0.2	10.9 ± 0.2
$IQE_{PV\text{-}Diff}$	[%]	4.0 ± 0.2	8.8 ± 0.3
$EQE_{PV\text{-}Diff}$	[%]	3.1 ± 0.1	6.5 ± 0.1

The absorptance (a) and the optical efficiency (η_{opt}) were obtained as detailed in **7.3.6. Experimental Section** of the main text and shown in **Figure S3**. The series (R_S) and transport (R_{tr}) resistances, the recombination (ω_{rec}) and diffusion (ω_D) frequencies, and the separation efficiency (η_{sep}) were obtained directly from the fitting of each set of measurements (IS, IMPS and IMVS). With these parameters the recombination resistances

(R_{rec}), chemical capacitances (C_{μ}), diffusion lengths (L) and diffusion coefficients (D) were calculated as described in **Section 7.4.1**, by considering the absorber thickness $d = 500\,nm$ (the mean value from the SEM image in **Figure S4**). Finally, the collection efficiency (η_{col}) and the differential external ($EQE_{PV\text{-}Diff}$) and internal ($IQE_{PV\text{-}Diff}$) quantum efficiencies were calculated from Equations (23), (21) and (22) in the main text.

References

[1] J. Bisquert, G. Garcia-Belmonte, F. Fabregat-Santiago, P. R. Bueno, *J. Electroanal. Chem.* **1999**, *475*, 152.

[2] J. Bisquert, *J. Phys. Chem. B* **2002**, *106*, 325.

[3] J. Bisquert, G. Garcia-Belmonte, F. Fabregat-Santiago, A. Compte, *Electrochem. Commun.* **1999**, *1*, 429.

[4] J. Halme, K. Miettunen, P. Lund, *J. Phys. Chem. C* **2008**, *112*, 20491.

[5] J. Halme, *PCCP* **2011**, *13*, 12435.

[6] L. Bay, K. West, *Sol. Energ. Mat. Sol. C.* **2005**, *87*, 613.

[7] L. Dloczik, O. Ileperuma, I. Lauermann, L. Peter, E. Ponomarev, G. Redmond, N. Shaw, I. Uhlendorf, *J. Phys. Chem. B* **1997**, *101*, 10281.

[8] A. Bou, H. Āboliņš, A. Ashoka, H. Cruanyes, A. Guerrero, F. Deschler, J. Bisquert, *ACS Energy Lett.* **2021**, *6*, 2248.

[9] L. M. Peter, K. G. U. Wijayantha, *Electrochem. Commun.* **1999**, *1*, 576.

[10] A. J. Riquelme, V. M. Mwalukuku, P. Sánchez-Fernández, J. Liotier, R. Escalante, G. Oskam, R. Demadrille, J. A. Anta, *ACS Appl. Energy Mater.* **2021**, *4*, 8941.

CHAPTER 8

Final Remarks - Observaciones Finales

In this chapter, we will make the final remarks of this thesis. The first section will be the general conclusions of the thesis. And we will devote the second section to future perspectives, where we will discuss some ideas that we believe would be interesting to address as a continuation of the results obtained in this thesis. To make this thesis more accessible, and also to apply for the "international doctorate" mention, this chapter, as well as the abstract, is written in English and Spanish.

En este capítulo, haremos las observaciones finales de esta tesis. El primer apartado serán las conclusiones generales de la tesis. Y el segundo apartado lo dedicaremos a las perspectivas de futuro, donde discutiremos algunas ideas que creemos que sería interesante abordar como continuación de los resultados obtenidos en esta tesis. Para hacer esta tésis más accesible, y además solicitar la mención de "doctorado internacional", este capítulo y el resumen, están escritos en inglés y en castellano.

8.1. General Conclusions

In this thesis, we have developed tools, based on modulated (or small perturbation) techniques, that allow a depth understanding of the internal mechanisms involved in the operation of different photoconversion devices. We have tried to explain these tools as clearly and generally as possible so that they can be easily applied to any optoelectronic device. As we have been able to demonstrate experimentally, a detailed understanding of the operation of these devices allows the identification of their main limitations, paving the way for future optimisations and improvements in their performance. With these results, we hope to have contributed to the energy transition towards sustainable energies, thus reducing global warming.

Specifically, the results obtained in this thesis can be divided into two groups:

i. We have established for the first time the **relationship** between the presence of a **negative capacitance** measured with impedance spectroscopy (IS) with the presence of an **inverted hysteresis** in the cyclic voltammetry curves.
   a. We have demonstrated that this relationship is universal, i.e. any device presenting inverted hysteresis must also present negative capacitance. We have proven this relationship experimentally for different perovskite solar cell compositions and under different conditions.
   b. For the investigated devices, we have observed that the characteristic time of the process that generates these phenomena corresponds to the interaction between the perovskite ions/vacancies and the contacts. Furthermore, this interaction generates an additional recombination path, that reduces the overall resistance of the device and, therefore, its performance.

ii. We have developed a **methodology to investigate** in depth the internal processes that occur during the operation of **photoconversion devices**, and thus identify their main performance limitations. This methodology is based on the **combination of** three modulated techniques: **IS**, intensity-modulated photocurrent spectroscopy (**IMPS**) and intensity-modulated photovoltage spectroscopy (**IMVS**). We can divide this result into three steps:

   1st. We have developed a **measurement protocol** to obtain reliable **IMPS and IMVS** spectra.
      a. This protocol involves the **measurement of the modulated electroluminescence** of the light source used to measure IMPS and IMVS, as a function of the frequency, and a procedure to correct the IMPS and IMVS spectra.
      b. With this measurement, we have detected a decrease in the modulated electroluminescence at low frequencies in a LED used by default as a light source. The omission of this effect generates artefacts in the IMPS and IMVS measurements, leading to misinterpretations of the results.

2nd. We have developed a **procedure** for a combined **analysis** of **IS, IMPS and IMVS** responses. This procedure is based on the use of **a single equivalent circuit** (EC) for the analysis of the three techniques. As a result of this procedure, we have shown that:
   a. A better description of the internal processes occurring during the operation of the photoconversion devices is achieved, compared to the individual analysis of each technique. In particular, additional parameters, such as the separation efficiency, could be obtained.
   b. The combination of these techniques allows the identification of an EC that models more adequately the investigated photoconversion device. **Solving**, at least in part, **one of the main problems of IS**: different ECs can generate the same IS spectrum.
   c. For the first time, we have **fitted** the **IS, IMPS and IMVS** spectra **with the same equivalent circuit**.
   d. We have demonstrated experimentally the potential of this procedure for a silicon photodiode.

3rd. We have extended the latter **procedure to characterise** photoconversion devices with **distributed photogeneration, recombination and diffusion** along the absorbent material.
   a. We have demonstrated the potential of this procedure by experimentally **applying it to a** Zr:$BiVO_4$ **photoanode**.
   b. This methodology, based on the combination of IS, IMPS and IMVS, has allowed us to:
      1. Identify the electrons as the carriers that control the response of the device when illumination arrives from the hole collector contact, while holes assume this role when the sample is illuminated from the electron collector contact.
      2. Obtain a detailed quantitative characterisation of the photoconversion parameters, identifying the separation efficiency as the main performance limitation of this device.

8.2. Future Perspectives

The global warming predictions are alarming, so it is urgent to join even more efforts to alleviate and mitigate this process. To this end, we believe that one promising approach is solar energy conversion, where great advances have been made recently, with technologies such as perovskite solar cells and hydrogen generation, and where there is still much room for improvement. To further improve these technologies, it is necessary to continue enhancing the understanding of the internal mechanisms involved in their operation. For this purpose, the combination of techniques, particularly modulated techniques, may be very useful, as shown in this thesis. The information extracted from the combination of techniques will always be greater than the sum of the information extracted from each technique. Such a combination is in fact necessary in most cases to validate any hypothesis. Therefore, it is essential to further explore different combinations, bringing together as many techniques as possible. Accordingly, we believe that it would be very interesting to explore other modulated techniques, such as modulated electroluminescence spectroscopy (MELS), also presented in this thesis, and try to combine them with IS, IMPS and IMVS.

Specifically, following the results obtained in this thesis, we believe it would be interesting to explore the subsequent lines of research:

i. Attempt to describe in more detail and precision the internal processes that generate negative capacity and inverted hysteresis. To this end, we propose:
    a. Seek experimentally both effects in other devices, as has recently been observed in memristors.
    b. Study devices that exhibit these effects with additional techniques.
ii. Analyse different photoconversion devices with the procedures developed in this thesis, based on the combination of IS, IMPS and IMVS. This will allow a deeper understanding of the performance of these devices and at the same time will corroborate the potential of such a combination.
    a. We have already started to implement this methodology in perovskite solar cells.

8.3. Conclusiones Generales

En esta tesis hemos desarrollado herramientas, basadas en técnicas moduladas (o de pequeñas perturbaciones), que permiten comprender en profundidad los mecanismos internos implicados en el funcionamiento de diferentes dispositivos de fotoconversión. Hemos compartido estas herramientas de la forma más clara y general possible para que fácilmente puedan aplicarse a cualquier dispositivo optoelectrónico. Como hemos podido demostrar experimentalmente, la comprensión en detalle del funcionamiento de estos dispositivos permite identificar sus principales limitaciones, allanando el camino para futuras optimizaciones y mejora de su funcionamiento. Con estos resultados, esperamos haber contribuido a la transición energética hacia energías sostenibles, para reducir así el calentamiento global.

Específicamente, los resultados obtenidos en esta tesis se pueden dividir en dos grupos:

i. Hemos establecido por primera vez la **relación** entre la presencia de una **capacitancia negativa** medida con la espectroscopia de impedancia (IS) con la presencia de una **histéresis invertida** en las curvas de voltamperometría cíclica.
   a. Hemos demostrado que esta relación es universal, cualquier dispositivo que presente histéresis invertida debe también presentar capacidad negativa. Experimentalmente hemos demostrado esta relación para diferentes composiciones de células solares de perovskita y en diferentes condiciones.
   b. Para los dispositivos investigados, hemos observado que el tiempo característico del proceso que genera estos fenómenos se corresponde con la interacción entre los iones/vacantes de la perovskita y los contactos. Además, esta interacción genera un camino de recombinación adicional, que reduce la resistencia total del dispositivo y, por lo tanto, su rendimiento.

ii. Hemos desarrollado una **metodología para investigar** en profundidad los procesos internos que ocurren durante el funcionamiento de los **dispositivos de fotoconversión**, y de esta forma identificar las principales causas que limitan su rendimiento. Esta metodología está basada en la **combinación de** tres técnicas de pequeña perturbación: **IS**, espectroscopia de fotocorriente de intensidad-modulada (**IMPS**) y espectroscopia de fotovoltaje de intensidad-modulada (**IMVS**). Podemos dividir este resultado en tres pasos:
   1º. Hemos desarrollado un **protocolo de medida** para obtener espectros de **IMPS e IMVS** fiables.
      a. Este protocolo implica la **medición de la electroluminiscencia modulada** de la fuente de luz utilizada para medir IMPS e IMVS, en función de la frecuencia, y un procedmiento para corregir los espectros de IMPS e IMVS.
      b. Con esta medición, hemos detectado una disminución de la electroluminiscencia modulada a bajas frecuencias en un LED usado por defecto como fuente de luz. La omision de este efecto, genera artefactos en las medidas de IMPS e IMVS, que conducen a malas interpretaciones de los resultados.

2º. Hemos desarrollado un **procedimiento** para el **análisis** combinado de las respuestas de **IS, IMPS e IMVS**. Este procedimiento está basado en el uso de **un único circuito equivalente** (EC) para el análisis de las tres técnicas. Como resultado de este procedimiento, hemos mostrado que:
   a. Se consigue una mejor descripción de los procesos internos que ocurren durante el funcionamiento de los dispositivos de fotoconversión, en comparación con el análisis de cada técnica por separado. En particular, se pueden obtener parámetros adicionales, como la eficiencia de separación.
   b. La combinación de estas técnicas permite la identificación de un EC que modela más adecuadamente el dispositivo de fotoconversión investigado. **Resolviendo**, al menos en parte, **uno de los principales problemas de la IS**: diferentes ECs pueden generar el mismo espectro de IS.
   c. Por primera vez, hemos **ajustado** los espectros **IS, IMPS e IMVS con el mismo circuito equivalente**.
   d. Hemos demostrado experimentalmente el potencial de este procedimiento para un fotodiodo de silicio.

3º. Hemos extendido este último **procedimiento para caracterizar** dispositivos de fotoconversión que presentan **fotogeneración, recombinación y difusión distribuidas** a lo largo del material absorbente.
   a. Hemos demostrado el potencial de este procedimiento **aplicándolo** experimentalmente **a un fotoánodo** de Zr:$BiVO_4$.
   b. Esta metodología, basada en la combinación de IS, IMPS e IMVS, nos ha permitió:
      1. Identificar los electrones como los portadores que controlan la respuesta del dispositivo cuando la iluminación llega desde el contacto colector de huecos, mientras que los huecos asumen este papel cuando la muestra es iluminada desde el contacto colector de electrones.
      2. Obtener una caracterización cuantitativa detallada de los parámetros de fotoconversión, que permitió identificar la eficiencia de separación como la principal limitación del rendimiento de este dispositivo.

8.4. Perspectivas Futuras

Los pronósticos del calentamiento global son alarmantes, por lo que es urgente sumar aún más esfuerzos con el fin del paliar y mitigar dicho proceso. Para esto, creemos que un enfoque muy prometedor es la conversión de la energía solar, donde se han hecho grandes avances últimamente, con tecnologías tales como las celdas solares de perovskita y la generación fotoelectroquímica de hidrogeno, y donde todavía existe mucho por mejorar. Para mejorar aún más estas tecnologías es necesario continuar aumentando la comprensión de los mecanismos internos involucrados en su funcionamiento. Para ello, puede ser de gran utilidad la combinación de técnicas, particularmente las técnicas moduladas, como mostramos en esta tesis. La información extraída de la combinación de técnicas será siempre mayor que la suma de la información extraída con cada técnica. Dicha combinación es de hecho necesaria en la mayoría de los casos para validad cualquier hipótesis. Por lo tanto, es esencial seguir explorando distintas combinaciones, juntando la mayor cantidad posibles de técnicas. En consecuencia, creemos que sería muy interesante explorar otras técnicas moduladas, como la espectroscopia de electroluminiscencia modulada (MELS), también presentada en esta tesis, e intentar combinarlas con IS, IMPS e IMVS.

Específicamente, como continuación de los resultados obtenidos en esta tesis creemos que sería interesante explorar las siguientes líneas de investigación:

i. Intentar describir con mayor detalle y precisión los procesos internos que generan la capacidad negativa y la histéresis invertida. Para ello proponemos:
    a. Buscar experimentalmente ambos efectos en otros dispositivos, como se ha observado recientemente en memristores.
    b. Estudiar los dispositivos que presentan estos efectos con técnicas adicionales.
ii. Analizar diferentes dispositivos de fotoconversión con los procedimientos desarrollados en esta tesis, basados en la combinación de IS, IMPS e IMVS. Esto permitirá entender el funcionamiento de dichos dispositivos en mayor profundidad y a la vez corroborará el potencial de dicha combinación.
    a. Por nuestra parte, ya hemos comenzado con la implementación de esta metodología en celdas solares de perovskitas.